

Understanding Structural Representation in Foundation Models for Polymers

Nathaniel H. Park^{1*}, Eduardo Soares², Victor Shirasuna²,
Tiffany J. Callahan¹, Sara Capponi¹, Emilio Vital Brazil^{2*}

¹IBM Research Almaden, 650 Harry Rd., San Jose, 95120, CA, United States of America.

²IBM Research Brazil, Street, Rio de Janeiro, 10587, RJ, Brazil.

*Corresponding author(s). E-mail(s): npark@us.ibm.com;
evital@br.ibm.com;

Contributing authors: eduardo.soares@ibm.com; vshirasuna@ibm.com;
tiffany.callahan@ibm.com; sara.capponi@ibm.com;

Abstract

From the relative scarcity of training data to the lack of standardized benchmarks, the development of foundation models for polymers face significant and multi-faceted challenges. At the core, many of these issues are tied directly to the structural representation of polymers and here, we present a new foundation model using a SMILES-based polymer graph representation. This approach allows representation of critical polymer architectural features and connectivity that are not available in other SMILES-based representations. The developed polymer foundation model exhibited excellent performance on 28 different benchmark datasets. Critical evaluation of the developed representation against other variations in control experiments reveals this approach to be a highly performant method of representing polymers in language-based foundation models. These control experiments also reveal a strong invariance of all SMILES representations, with many variations achieving state-of-the-art or near state-of-the-art performance—including those which are chemically or semantically invalid. Examination of error sources and attention maps for the evaluated representations corroborate the findings of the control experiments, showing that chemistry language models based on SMILES interpolate over all sequence space for prediction tasks, not only those of semantically valid inputs. Overall, this work highlights the importance of control experiments as a check on human-imposed assumptions that can limit rational design of both chemistry foundation models and their underlying structural representations.

1 Introduction

Foundational artificial intelligence (AI) models hold immense promise for revolutionizing rational design of polymeric materials owing to their ability to interpolate over large regions of chemical space, providing considerable predictive capabilities for a variety of downstream tasks. Despite numerous reports on the development of predictive and generative models for polymers[1–4], none have demonstrated significant academic and industrial impact in manner analogous to AlphaFold[5]. In contrast to proteins, creation of foundation models for polymers face major and frequently intractable challenges. Data for training and benchmarking deep-learning models for polymers is scarce[6], restrictively licensed[7–10], and comes from only a handful of sources (Fig. 1c)—limiting both model development and their use in commercial applications. Moreover, existing datasets are often incomplete and lack many critical structural descriptors[11–15], such as dispersity, number-average molecular weight, or processing conditions that play important roles in determining polymer properties. Structural representations in these datasets are overwhelmingly based on variations of SMILES (Fig. 1b)[12–15], which are then featurized using various strategies. These approaches include fingerprinting[8, 16, 17], conversion to graphs[18–22], tokenization of SMILES line-notations[11, 22, 22–26], coarse grained representations[27, 28], images[29], 3D conformations[24], and others depending on the model architecture[30]. The lack of standardized benchmarks prevents accurate comparison of model architectures and many reports do not or cannot publish their benchmark data. Consequently, nearly every reported predictive or generative model for polymers looks the same (Fig. 1c and Fig. 1d) as they largely trained on the same data and use nearly equivalent polymer featurization strategies.

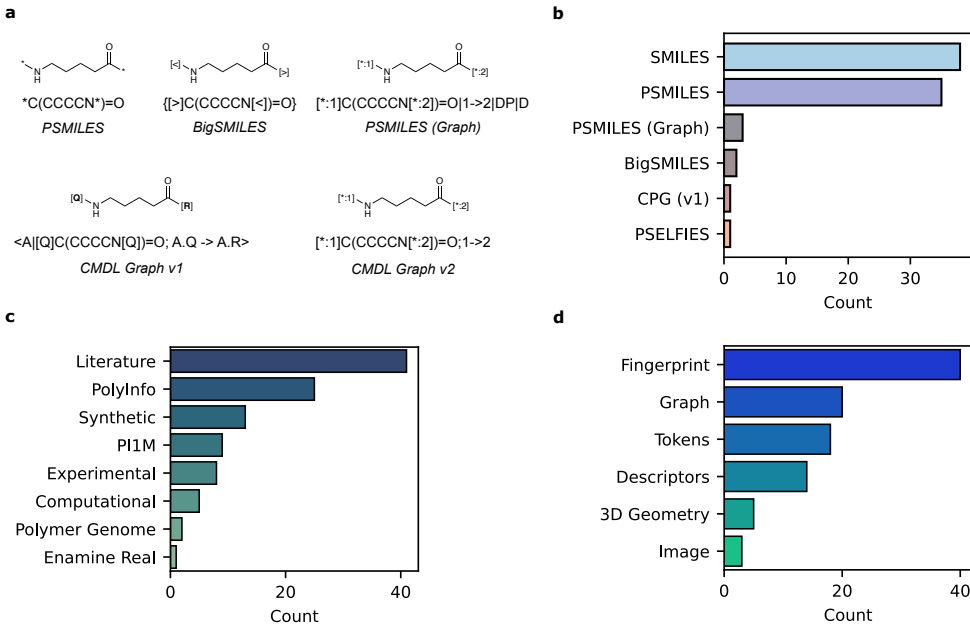


Fig. 1 **a.** Visual comparison of different string text representations for Nylon-6. **b.** Survey of polymer data structural representations in training datasets in polymer ML papers. **c.** Dataset source for recent polymer machine learning paper. **d.** Model input format from recent polymer machine learning papers. Data for **b**, **c**, and **d** were sourced from a survey of 80 machine learning papers in polymers published between 2018–2025.

The core of many issues surrounding foundation models for chemistry and materials revolves around structural representations which invariably involves the SMILES line notation and its derivatives. With regard to polymers, the inflexibility of SMILES to accurately represent critical architectural and compositional features of polymers has prompted development various extensions of SMILES to circumnavigate this issue, including modification of the SMILES grammar[29, 31–33], adjusting the connectivity of the SMILES string representing the repeat unit[34], concatenation of additional text information to SMILES[18, 22, 23], or the conversion of SMILES to SELFIES[26] (Fig. 1a). Each approach has reported some success in terms of downstream model performance on selected benchmarks. However, benchmark performance alone in the absence of control experiments is not conclusive evidence to demonstrate that representation modifications are indeed responsible for the observed performance increase. This naturally impedes any rational design of improved structural representations and at worst propagates potentially invalid assumptions regarding structural representation requirements. Thus, in order to critically evaluate the influence of polymer structural representation, we surmised that a minimal extension to the SMILES grammar would allow for both encoding of common polymer architectures and facilitate introspection of possible underlying mechanisms accounting for any observed change in

performance—providing valuable insight to further guide rational design of structural representations for polymers and other complex materials.

Previously, we have reported the use of a domain-specific programming language, the Chemical Markdown Language (CMDL) which represents polymers natively as graphs that can be compiled to a string representations for use in regression transformer models for polymer design[35]. Although this approach was experimentally validated, the serialized output of the polymer graph representation was not easily interoperable with existing datasets that are overwhelmingly denoted in SMILES or PSMILES (Fig. 1b) and necessitated a custom tokenizer[35]. However, the advantage of using a domain-specific language such as CMDL resides in its underlying mechanism for representing polymers as graphs of core structural components and flexibility to be compiled to a variety of serialized representations. We hypothesized that the CMDL graph representation could readily be applied to existing polymer datasets as a small extension of the SMILES grammar, allowing transmission of salient architectural information to the model affording an increase in performance on benchmark datasets.

2 Results

2.1 Polymer Representation

The core CMDL polymer graph representation is constructed on two principles: specifying the interconnections between core structural fragments of the polymer backbone and reduction of complexity via architectural symmetry. Each of the core polymer structural components was represented via a SMILES string containing non-atomic placeholders characters (Q, R) in brackets (Fig. 1a) and architectural symmetry was indicated via weights attached to edges between different structural components[35]. Most polymer datasets denoted in PSMILES consist of relatively simple homo-, random, or block copolymers, with little to no architectural symmetry present[12, 13, 18, 36]. Thus, we felt that the core features of the CMDL polymer graph representation could readily applied to such datasets with some minor adaptations. Rather than using non-atomic placeholder characters, numbered asterisks in brackets—which are part of the base SMILES grammar—could be used to map the connections between different components or within a component, with the edge definitions appended to the end of the SMILES string. Analogous representations have been used with different models for polymer property prediction, although these either were converted to a different internal representation prior to consumption by the model[18] or were tokenized directly including floating-point numbers for stoichiometry and dispersity[22].

The advantage of this approach to modeling polymer structure is that it inherently facilitates straightforward extension to cover a range of polymer architecture types, end groups, as well as blends or formulations. Importantly, this approach can readily distinguish between random and block copolymers via delineation of different edge connections (Fig. 1 and Supplementary Fig. 1). Such copolymers would appear identical to a chemistry language model using solely PSMILES representations, leading potentially erroneous associations between the copolymer structure and properties.

Additionally, this representation approach can accommodate mixtures of polymers or formulations of polymers and small-molecules, such as found in many polymer electrolyte datasets (Supplementary Fig. 1).

2.2 Model Development

Pre-training and benchmark datasets were sourced from openly available datasets[12, 18, 18, 21, 23, 36–42]. PSMILES and other representations from these datasets were converted in the CMDL polymer graph (CPG) representation prior to use in pre-training or benchmarking tasks. The pre-training process of the SMI-TED-POLYMER_{289M} model involves two key phases: i) Learning polymer token embeddings through a masking mechanism. ii) Mapping these embeddings into a unified latent space that represents the entire CPG string. This latent space captures the structural representation of the CPG but also enables the reconstruction of both individual polymer tokens and the complete CPG strings. Accordingly, the pre-training process utilizes two distinct loss functions: one associated with the token embeddings, driven by the masking process, and another targeting the encoder-decoder layer, focusing on token reconstruction. For encoder pre-training we use the masked language model method defined by Devlin et al. [43]. Initially 15% of the tokens are selected for possible learning. From that selection, 80% of the tokens are randomly selected and replaced with the <mask> token, 10% of the tokens are randomly selected to be replaced with a random token, while the remaining 10% of the tokens will be unchanged. The implementation of distinct pre-training strategies has positively impacted the model's efficiency, as demonstrated by the observed improvements in the corresponding loss functions. By optimizing the pre-training phases, we have developed a model that is both robust and highly adept at capturing and reconstructing SPG strings.

2.3 Experiments

To evaluate the latent space generated by our methodology, we tested the SMI-TED-POLYMER model on a slew of property prediction tasks on 28 different datasets (see Supplementary Information for details). For each benchmark dataset, care was taken to not mix datasets for the same property but from different sources to both minimize error propagation and facilitate comparison with previous work. For the assessment, we adopted a randomized 80:10:10 train/validation/test splits for all tasks (see Methods). The property prediction tasks fell across four principle categories electronic, physical, optical, and gas barrier properties (Table 1). In each of the categories, the SMI-TED-POLYMER model achieved or equaled state-of-the-art (SOTA) on given metrics (entries 2–5, 10–18, 20, 23, and 28, Table 1). In instances where the SMI-TED-POLYMER model did not improve upon the SOTA values, it frequently provided results very close to them with only the copolymer electron affinity and ionization potential showing significant deviations (entries 6 and 7, Table 1).

2.3.1 Representation Analysis

The results in Table 1 show the efficacy of utilizing the CPG representation to extend SMILES-based models for polymer property prediction tasks as compared to existing

Table 1 SMI-TED-POLYMER Benchmark Experiments

Entry	Dataset ¹	Data Source ²	Property Type	Metric	SOTA ³	STP
1	Chain Bandgap (E_{gc})[44]	DFT	Electronic	RMSE (↓)	0.44 [24]	0.49
2	Bulk Bandgap (E_{gb})[44]	DFT	Electronic	RMSE (↓)	0.50[24]	0.32
3	Electron Affinity (E_{ea})[44]	DFT	Electronic	RMSE (↓)	0.29 [24]	0.29
4	Ionization Energy (E_i)[44]	DFT	Electronic	RMSE (↓)	0.39[24]	0.37
5	Dielectric Constant (EPS)[44]	DFT	Electronic	RMSE (↓)	0.51[24]	0.39
6	Copolymer Electron Affinity[18]	DFTB	Electronic	RMSE (↓)	0.03 [18]	0.15
7	Copolymer Ionization Energy[18]	DFTB	Electronic	RMSE (↓)	0.03 [18]	0.16
8	Crystallization Tendency (X_c)[44]	DFT	Physical	RMSE (↓)	16.57 [44]	17.82
9	Refractive Index-I (N_c)[44]	Exp.	Optical	RMSE (↓)	0.09 [24]	0.12
10	Refractive Index-II[45]	Exp.	Optical	RMSE (↓)	0.031[45]	0.021
11	Conductivity-I[21]	Exp.	Physical	MAE (↓)	1.00[21]	0.89
12	Conductivity-II[46]	Exp.	Physical	RMSE (↓)	0.61 [23]	0.61
13	CO_2 Permeability[42]	Exp.	Barrier	MAE (↓)	0.29 [42]	0.29
14	CH_4 Permeability[42]	Exp.	Barrier	MAE (↓)	0.37[42]	0.35
15	N_2 Permeability[42]	Exp.	Barrier	MAE (↓)	0.38[42]	0.31
16	$CO_2:CH_4$ Selectivity[42]	Exp.	Barrier	MAE (↓)	5.34[42]	4.71
17	$CO_2:N_2$ Selectivity[42]	Exp.	Barrier	MAE (↓)	4.14[42]	3.89
18	CO_2 Permeability-II[36]	Exp.	Barrier	R^2 (↑)	0.90[36]	0.91
19	CH_4 Permeability-II[36]	Exp.	Barrier	R^2 (↑)	0.89 [36]	0.85
20	N_2 Permeability-II[36]	Exp.	Barrier	R^2 (↑)	0.91 [36]	0.91
21	H_2 Permeability[36]	Exp.	Barrier	R^2 (↑)	0.90 [36]	0.87
22	O_2 Permeability[36]	Exp.	Barrier	R^2 (↑)	0.92 [36]	0.89
23	He Permeability[36]	Exp.	Barrier	R^2 (↑)	0.91[36]	0.92
24	CO_2 Permeability-III[41]	Simulated	Barrier	R^2 (↑)	0.90 [41]	0.88
25	T_g -I (polyimides)[38]	Exp. and Synthetic	Thermal	MAE (↓)	24.4[38]	9.56
26	T_g -II (homopolymers)[37]	Exp.	Thermal	RMSE (↓)	19.4 [37]	27.7
27	T_g -III (homopolymers)[41]	Simulated	Thermal	R^2 (↑)	0.90 [41]	0.86
28	$T_{d,50\%}$ [41]	Simulated	Thermal	R^2 (↑)	0.92[41]	0.96

¹Reference citation indicates source of benchmark dataset²Indication of how data for polymers was collected, computational (DFT, DFTB), experimentally (Exp.), simulation (Simulated), or generated synthetically (Synthetic).³Reference citation indicates current SOTA performance

SOTA models. However, it cannot be determined from such experiments alone that the CPG representation is solely responsible for the observed performance improvements nor could the case be convincingly made that CPG is indeed superior to PSMILES or other line notations. Critical evaluation of the CPG representations necessitates running extensive control experiments, which are seldom performed and often incomplete. Indeed, most benchmark experiments for polymer models focus exclusively on model architecture or featurization method, not the structural representation system. Additionally, there exists many assumptions—both explicit and implicit—regarding both the requirements of a structural representation system for polymers and how it is interpreted by the model, without minimal experimental evidence to support such assumptions. Thus, in order to allow for rationale evolution in model and representation design, it is necessary to design control experiments to both systematically test

the performance of the CPG representation against other variations and challenge core underlying assumptions.

The advantage of using the SMI-TED model as base model for the SMI-TED-POLYMER, is that they share essentially identical overall architectures, tokenizers, SMILES vocabularies, and similar training histories[47]. This provides an ideal platform to perform controlled evaluation of the influence of structural representation on benchmark performance as only the SMI-TED-POLYMER model has seen SMILES strings containing asterisk tokens based on analysis of the pre-training data for both models (Supplementary Fig. 2). Here, we envisioned evaluation of both the CPG representation and PSMILES on selected benchmark datasets using both the frozen weights of SMI-TED and SMI-TED-POLYMER models as well as fine-tuned versions of both models using either CPG or PSMILES representations, affording six different models to use for comparison.

Comparing the performance of the CPG and PSMILES representations across SMI-TED and SMI-TED-POLYMER models alone is not illustrative; by default, there is an implicit assumption that asterisk containing tokens are important in modeling polymer structures using SMILES. Therefore, additional variations of the CPG and PSMILES representation must also be evaluated as negative controls wherein the asterisk character is systematically replaced with other atom tokens from the SMILES vocabulary. However, the systematic substitution of asterisk characters with other atoms in the input SMILES representation is a symmetric and self-consistent operation and therefore could potential introduce a systematic bias within these representation. Additionally, a core assumption in all CLMs using SMILES or another line-notation, is that the ordering of tokens is crucially important for performance—necessitating the use of positional encoding. While there are good reasons for making such an assumption, there exists no experimental evidence in either polymer or small-molecule models to support it. Thus, there is a need to evaluate both semantically and chemically invalid representations as well as randomly shuffled token orders as positive controls. This would mitigate potential systematic bias introduced from the atom substitutions and confirm the validity of assumptions regarding token order.

To systematically evaluate the influence structural representation, we selected a variety of replacement atoms that are part of the vocabularies of both the SMI-TED and SMI-TED-POLYMER models, this included lower-case, aromatic atoms that would result in semantically invalid SMILES strings (Supplementary Table 1). In each substitution, all asterisk characters in the CPG representation were replaced with the same atom for each variation in addition to dropping the numbered edge notations. Three different approaches to replacing the asterisk character in the CPG representation were adopted for each atom type: i. *all* where the entire bracketed and numbered asterisk character was replaced, ii. *bracket* where the asterisk and the number were replaced inside the pair of brackets, and iii. *star* were only the asterisk character was substituted inside the bracket (see Supplementary Methods). Additionally, some substitutions resulted in new SMILES strings which could be canonicalized into a different token order. In such cases, a separate dataset with newly canonicalized representations was created to evaluate in addition to the original token order following the atom substitution. Not all substitution methods were viable for all atoms.

Certain atoms used for substitution, such as metals, are only found inside of brackets in the SMILES vocabulary of both models. Non-bracketed versions are tokenized as having an *unknown* token which is in turn replaced by a *padding* token. As the insertion of the *padding* token resulted in mutually equivalent representations, only one example of such an input representation was evaluated (Supplementary Table 1). The SMI-TED model tokenizes the CPG representation in an identical manner as the SMI-TED-POLYMER model albeit the numbered asterisk tokens are replaced with the *padding* token as they are not part of the SMI-TED model vocabulary. Finally, randomized representations were also created where a random replacement atom was selected for each asterisk character, a randomly shuffled CPG representation, and a randomly shuffled SMILES string with randomly selected replacement atoms.

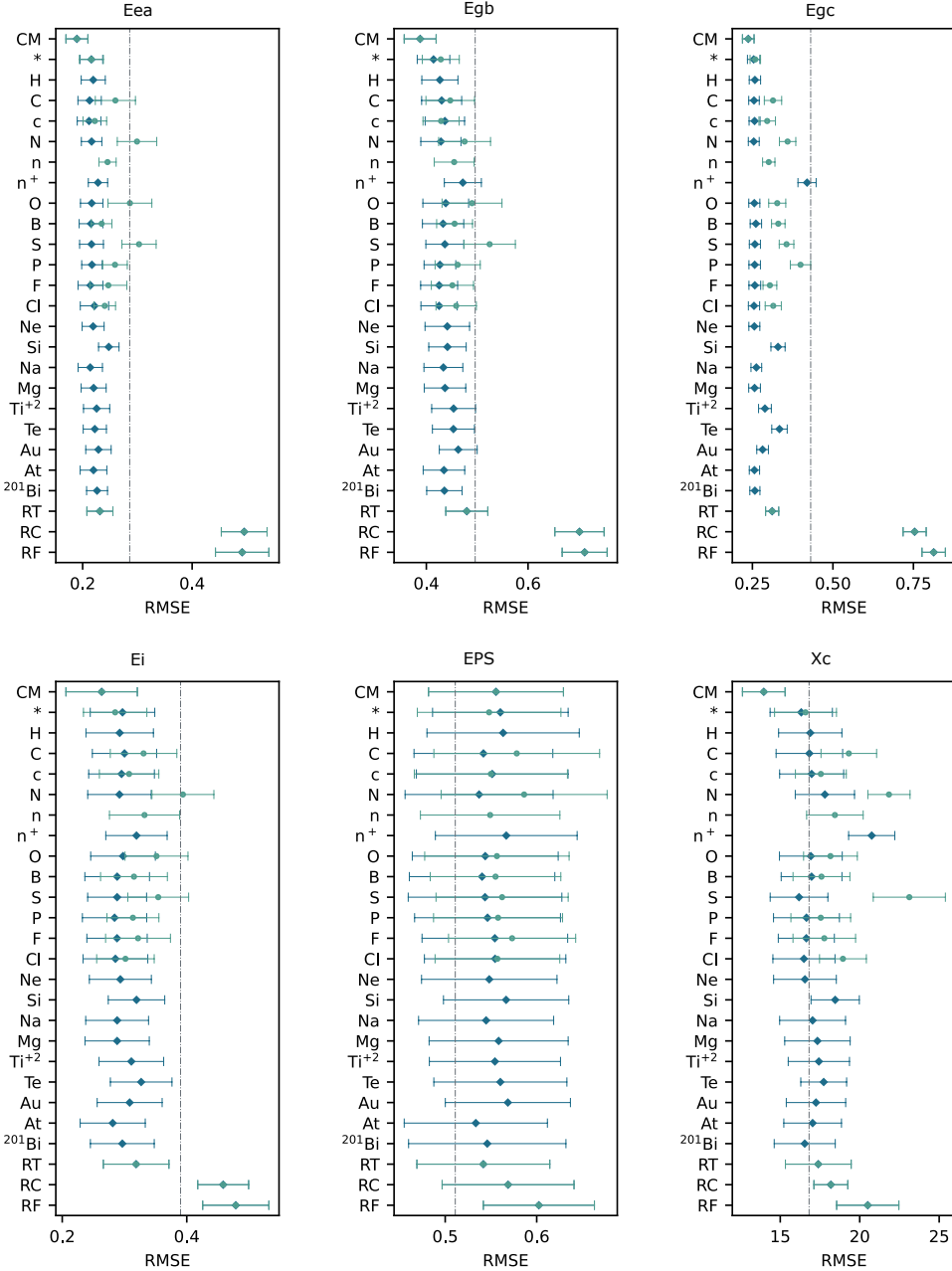


Fig. 2 Comparison of representation performance on repeated 5-fold cross-validation for six selected benchmark datasets using the SMI-TED model fine-tuned using the CPG representation. PSMILES representations are indicated with “*” and the CPG representation, the randomized token, randomized CPG, and fully randomized representations are indicated with CM, RT, RC, and RF, respectively. *Bracket* substitution method is indicated with blue markers, *all* substitution method are indicated with green markers, error bars indicate standard deviation of the results. Remainder of results from other models are in the Supplementary Information. Vertical dashed lines indicate reported SOTA performance.

The different representations were evaluated against the two frozen and four fine-tuned SMI-TED and SMI-TED-POLYMER models for selected benchmark datasets from Table 1. Identical train/valid/test splits as the original benchmark experiments (Table 1) were used to train and optimize XGBoost regression models for each representation system (see Methods for details). Additionally repeated five-fold cross-validation experiments, with each fold being repeated five times, were also performed for each representation system. Selected results comparing the loss of each representation across different models are shown in Fig. 2 and the full results are provided in the Supplementary Information (Supplementary Figures Section 2.6). The results in Fig. 2 demonstrate that that the CPG representation, PSMILES, and atom substituted representations performed nearly identically, with slight variation in performance depending on the dataset. Notably, the CPG representation performed well across all datasets despite having the numbered asterisk tokens being replaced with the *padding* in the base SMI-TED model (Fig. 2), including the frozen weight SMI-TED model where no fine-tuning was performed (see Supplementary Figures Section 2.6). For the most part, the randomly shuffled SMILES representations (RC and RT, Fig. 2) performed noticeably worse in most datasets. However, in several instances in using both fine-tuned models (EPS and X_c , Fig. 2) or frozen models (Supplementary Figures Section 2.6) the shuffled representations performance was not significantly different from other inputs and occasionally approached SOTA-level performance. Fine-tuning improved the performance of randomly shuffled representations in all cases, suggesting that fine-tuning boosts performance across all possible sequence inputs. Randomized token replacement for each asterisk character (RT) and semantically invalid substitutions (n, n+, c) all routinely had performance on par with CPG, PSMILES, and other substituted representations with some exceptions that are dataset dependent (Fig. 2, Supplementary Figures Section 2.6).

2.4 Error Analysis

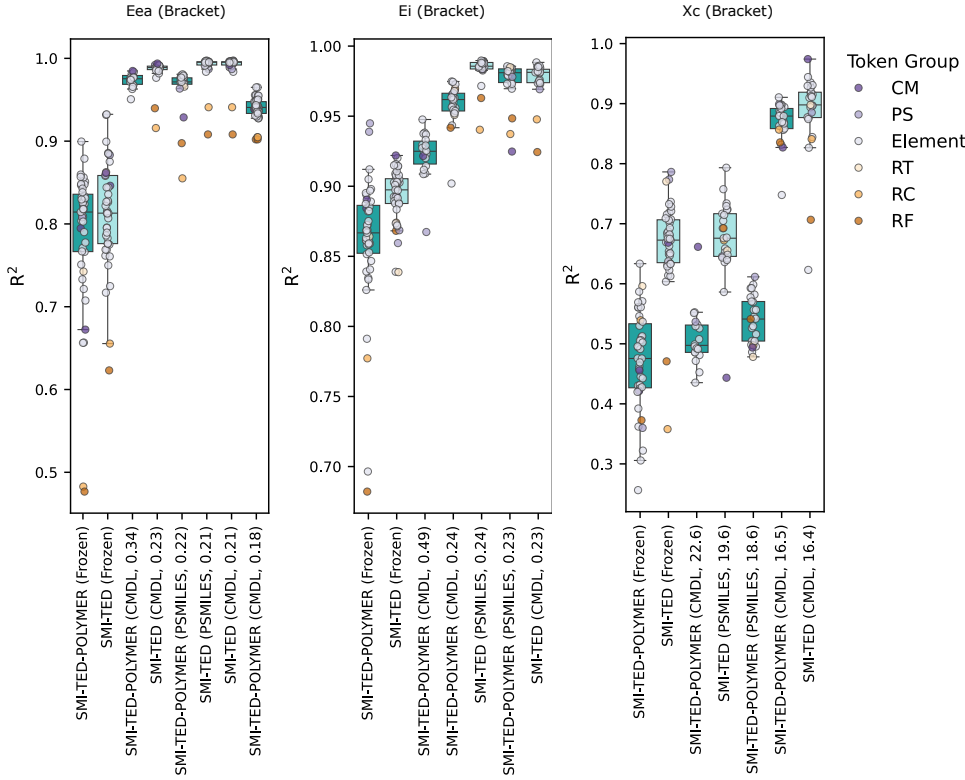


Fig. 3 Box plots of the R^2 from linear regression between the predicted property value of each candidate in the hold-out test set and the average true value from its top five nearest neighbors in the training set as a function of the model used. Fine-tuned models are labeled by their respective base model followed by the representation with which it was fine-tuned with and the associated loss for the checkpoint. All losses for fine-tuned models are RMSE unless indicated otherwise. Circular markers indicate individual data points of each representation system evaluated. Markers are colored according to their representation group, with CM = CPG representation, Elemental = indicates non-asterisk atom substitutions, RT = randomized token selection, RC = randomly shuffled CPG representation, and RF = randomly shuffled SMILES string with randomly selected replacement atoms.

The results from the representation analysis and the apparent invariance regarding the structural input made it imperative to better understand if prediction error is in any way correlated with structural representation. Prediction errors with deep-learning models can frequently be attributed their interpolative nature as well as systemic biases introduced from training and benchmark data. The interpolative nature of deep-learning models is well-understood and hence such models frequently struggle with out-of-distribution (OOD) tasks[48]—spurring efforts to ameliorate these performance deficits[49–51]. Additionally, extensive work has been done to understand

the effect of different dataset splitting techniques[52–54] on model performance, quantifying the uncertainty of model predictions[51, 55–57], and assessing the roughness of structure–property relationships as a function of representation[58]. In the context of this work, we were first interested in understanding the potential underlying sources of error as a function of random dataset splits, which are most commonly used in benchmark evaluations for polymer deep-learning models[11, 23–25]. Here, we opted to evaluate the potential correlation between training and test set predictions as dictated by latent embedding distance which is a function of chemical similarity. Chemical similarity based on atom-pair fingerprints has been shown previously to be highly explanatory of prediction error in previous studies on small-molecule drug datasets[59, 60].

For each representation system, we examined each candidate in the test set and compared it's predicted property value from the model to the average known property values of the top five nearest neighbors in the training set based on Euclidean distance between their embedding vectors. Each dataset of predicted versus averaged values was fitted with via linear regression and the resulting aggregated R^2 values are shown in Fig. 3 for selected benchmark datasets and with the remainder in the Supplementary Information (Supplementary Figs. 3–7). The results demonstrate a strong correlation between the predicted value for a test set candidate and the known values of its closest neighbors within the training dataset. Notably, the strength of the correlation increases for all representation types when more performant, fine-tuned models are used for the prediction (Fig. 3). This effect is maintained even when randomized representations are used (RT, RC, and RF, Fig. 3), highlighting the fact that fine-tuning will boost performance regardless of input representation. Switching from the Euclidean distance between the latent embeddings and using Morgan, MACCS, or atom-pair fingerprints (where possible, see Supplementary Information) and Dice similarity as the ranking metric dramatically reduced or eliminated any correlation between predicted and the average neighbor values (Supplementary Figs. 8 to 34).

2.5 Comparison of Attention Maps

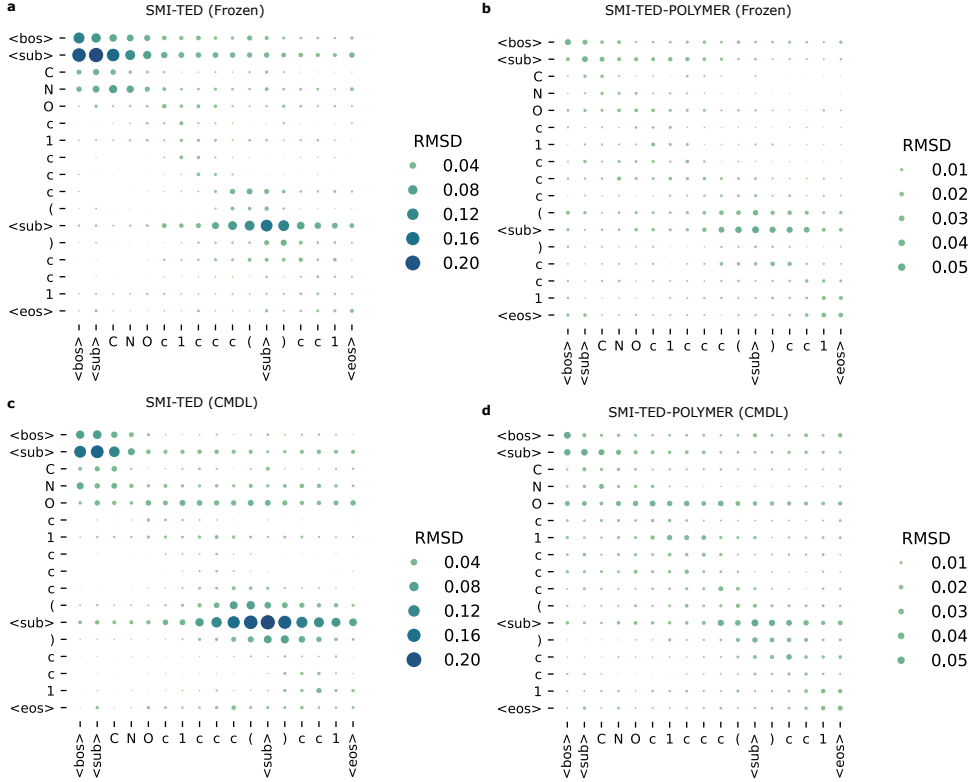


Fig. 4 Example RMSD attention maps for frozen (a and b) and CPG fine-tuned (c and d) SMI-TED and SMI-TED-POLYMER models showing the magnitude change in attention for different tokens between PSMILES and all other equivalent length atom substituted representations. The *sub* token indicates the location of within the SMILES string where atom-substitutions were made.

In addition to investigating the effects of dataset structure on prediction error, we also sought to understand the relationship between attention weights and performance across the different representation systems. Typically, interpretation of attention maps of SMILES CLMs from prior reports is often accompanied by an overeager chemistry-focused interpretation of the distribution of the attention weights to each token, which is assumed to be consistent with model learning chemistry from SMILES-based representations[11, 29, 61]. While the temptation to rationalize attention probabilities from a chemistry perspective is understandable, it lends to inject subjective interpretation of the observed distributions, conflating them with actual chemical meaning that is frequently at odds with the tokenization scheme employed. The advantage of

examining semantically or chemically invalid representations is that it forces us to dispense with subjective analysis from a chemistry perspective and focus on what the model is actually seeing: a sequence of tokens. Given the numerous different input representation formats evaluated and that comparing averaged attention maps by eye is challenging, we opted to utilize a different approach to examine attention maps. Here, we first averaged the attention weights across all 12 layers for each different input representation type for a given entity, then the root mean squared difference (RMSD) between the PSMILES representation average attention weights (X_p) and all other atom substituted representations (X_i) (Eq. 1).

$$\text{RMSD}(X_p, X) = \sqrt{\frac{\sum_{i=0}^{N-1} (X_p - X_i)^2}{N}} \quad (1)$$

This allows us to more broadly investigate the magnitude of change in attention for a given token across different atom substitutions representations. Figs. 4 show the aggregated attention maps from an example entity from the E_i benchmark dataset. The maps for the frozen weight models show a stark difference in the amount of attention given to different tokens in the same input sequence, where the SMI-TED model shows much more dramatic changes in attention for the substituted token in the SMILES representation (Fig. 4a and Fig. 4b). The same is also true in the models fine-tuned using the CPG representation (Figs. 4c and d), where again the SMI-TED model shows larger changes in attention for the substituted token. Example attention maps for the CPG and randomized representations which could not be included in the RMSD analysis are shown in Supplementary Figs. 35 and 36.

2.6 Comparison Against Historical Performance

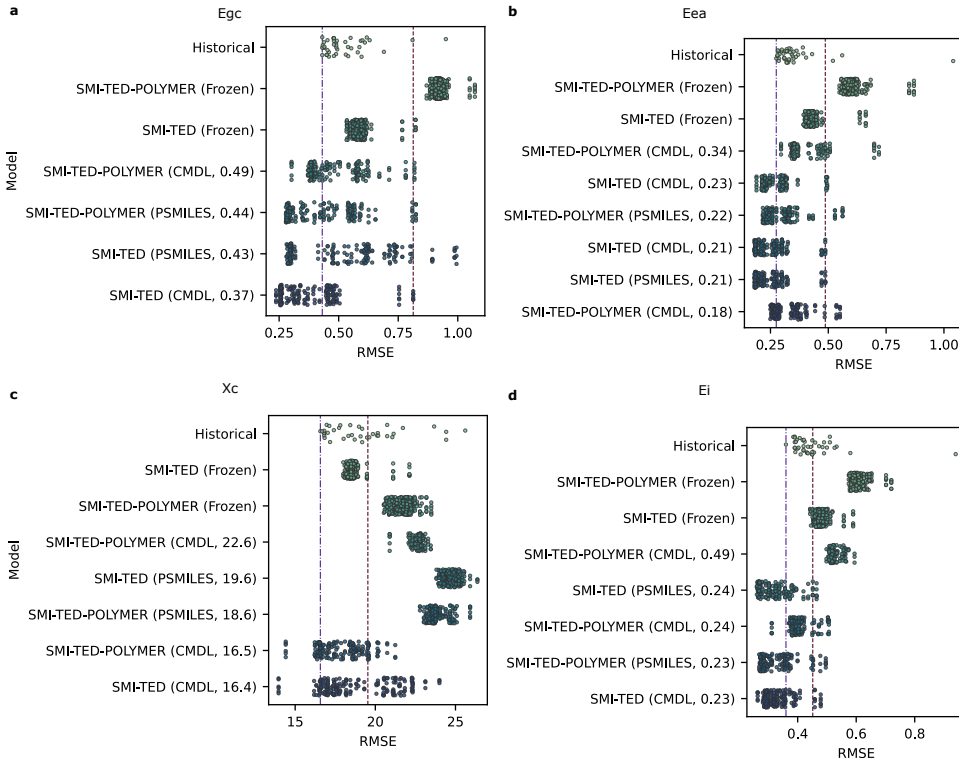


Fig. 5 Comparison of performance of SMI-TED-POLYMER and SMI-TED models with previously reported results. All values for SMI-TED-POLYMER and SMI-TED models are mean RMSE values from repeated five-fold cross-validation experiments.

Finally, we also compared the performance of all the representations and representation formats against all prior reported performances on the same benchmark datasets (Fig. 5 and Supplementary Fig. 37). Most prior reports in the development of AI models for polymers (or chemistry in general) only compare performance against solely SOTA values and/or a handful of other models as controls. To better understand how input representation influences performance, it is more illustrative to visualize comparisons against a broader set of previously reported performances. In many instances, a substantial number of input representations exceed the reported SOTA value (Figs. 5a, b, and d). Conversely, in many instances with both the SMI-TED, SMI-TED-POLYMER, and historical models failed to perform better than the best result from the fully randomized SMILES input (Fig. 5). These results highlight both

the highly performant nature of the SMI-TED models as well as the complex interplay between representation identity and the nature of the model (frozen vs. fine-tuned).

3 Discussion

The success of developing foundation models for polymers and polymer containing materials will hinge greatly on the development of improved datasets, accurate structural representations, and a thorough understanding of how a foundation model handles such information. While our initial hypothesis surrounding the effect on performance of the CPG representation has been partially validated, however, our results also show that, under commonly used benchmark and split protocols, strong performance can be achieved without chemically meaningful structural encodings. This suggests that current practice often measures interpolation within the training distribution more than mechanistic ‘understanding’ of chemistry. This effect is further confirmed by the strong observed correlation between predicted values and the nearest-neighbor average for all representation types, unequivocally demonstrating that model performance is arising from interpolation within latent space. Finally, while there is much more complexity in how attention weights translate into the formation of the latent space and model performance than presented here, the advantage of using invalid representations is that we can eliminate premature, chemistry-focused analysis of attention maps as a useful tool for inquiry. Overall, we have demonstrated the effectiveness of the CPG in enhancing the performance of a polymer foundation model as well as provided critical analysis of the performance of the CPG relative to other SMILES representations which can guide further improvements in the development of representations and datasets in AI for polymers.

4 Methods

4.1 Datasets

Pre-training data and benchmark datasets were sourced from commonly reported benchmark datasets for polymers as well as other published sources to cover a diversity of polymer properties. For each dataset, the SMILES-based structural representation was converted to the CPG representation before splitting into train/valid/test datasets.

4.2 Pre-training

Pre-training of the SMI-TED-POLYMER_{289M} model was conducted over 150 epochs using the curated CPG dataset, with a fixed learning rate of 1.6e-4 and a batch size of 256 molecules. The training was distributed across 4 NVIDIA V100 (16G) GPUs, parallelized into 4 nodes using DDP and *torch run*. The process involves two key phases: i) Learning polymer token embeddings through a masking mechanism. ii) Mapping these embeddings into a unified latent space that represents the entire CPG string. This latent space not only captures the structural representation of the

CPG but also enables the reconstruction of both individual polymer tokens and the complete CPG strings.

Accordingly, the pre-training process utilizes two distinct loss functions: one associated with the token embeddings, driven by the masking process, and another targeting the encoder-decoder layer, focusing on token reconstruction.

- In phase 1, the polymer token encoder is initially pre-trained using 95% of the available samples, while the remaining 5% is reserved for training the encoder-decoder layer. This partitioning is necessary as the polymer token embeddings may encounter convergence difficulties in the initial epochs, which could adversely affect the training of the encoder-decoder layer.
- In Phase 2, after the polymer token embeddings layer has converged, the pre-training process is scaled to leverage 100% of the available samples for both phases. This approach significantly enhances the performance of the encoder-decoder layer, particularly in improving polymer token reconstruction accuracy.

For encoder pre-training we use the masked language model method defined previously[43]. Initially 15% of the tokens are selected for possible learning. From that selection, 80% of the tokens are randomly selected and replaced with the [MASK] token, 10% of the tokens are randomly selected to be replaced with a random token, while the remaining 10% of the tokens will be unchanged. The implementation of distinct pre-training strategies has positively impacted the model's efficiency, as demonstrated by the observed improvements in the corresponding loss functions. By optimizing the pre-training phases, we have developed a model that is both robust and highly adept at capturing and reconstructing CPG strings.

4.3 Experiments

Benchmark Experiments

Benchmark experiments for Table 1 for SMI-TED-POLYMERS_{289M} were conducted using a randomized 80:10:10 train/valid/test split. For each benchmark dataset, the SMI-TED-POLYMER model was fine-tuned using the training and validation datasets. Using the fine-tuned model XGBoost regressor was created using the latent embedding (dim = 768) of the structure input and the regressor hyperparameters were optimized using the Optuna python package. Final performance of the XGBoost regressor was evaluated using the holdout test dataset. See Supplementary information for details on each dataset as well as sources for the benchmark SOTA.

Representation Analysis

Selected benchmark datasets from Table 1 were converted into a variety of alternative input representations, via replacement of asterisk tokens or randomization of token order. For consistency, the representation conversion was done from the CPG, not the original representation. This is due to the fact that the CPG representations were canonicalized once the numbered asterisks were inserted. For meaningful comparisons, this token order was maintained in all other input representations. Re-canonicalization of newly created input representation was also performed as a separate comparative

experiment, such that both the identical and different token orders could be compared. Depending on the atom used, re-canonicalization resulted in some or all the token orders of the input representation to be changed. Details on what percentage of each benchmark dataset for each input representation changed are available in the Supplementary Information.

For the evaluation of the new representations, both the frozen weight base model of SMI-TED and SMI-TED-POLYMERS were used in addition to fine-tuned versions for each benchmark dataset. Each base model (SMI-TED or SMI-TED-POLYMERS) was fine-tuned for 300 epochs using either the CPG or PSMILES input representation, resulting in four fine-tuned models for each benchmark dataset. Each input representation type for each benchmark dataset was evaluated against all six models (two frozen weight and four fine-tuned), wherein using the latent embeddings from the respective model and the same 80:10:10 train/valid/test split, a XGBoost regressor was created and its hyperparameters were optimized using the Optuna package for 300 rounds. A new XGBoost regressor was created using the identified optimal parameters and evaluated on the hold-out test set. The optimized hyperparameters for XGBoost regressor was also evaluated using a repeated 5-fold cross-validation, repeated for five times. Results from both the cross-validation and test set evaluation were used to compare the efficacy of each input representation.

Supplementary information.

Declarations

4.4 Data Availability

The benchmark data used to asses property prediction tasks is available from their respective published sources[12, 18, 18, 21, 23, 36–42]. See Supplementary Information for a detailed breakdown of each benchmark data source and additional information regarding each dataset.

4.5 Code Availability

Code used for generating the CPG graphs and the model will be released upon final publication of the manuscript.

References

- [1] Gao, L., Lin, J., Wang, L. & Du, L. Machine Learning-Assisted Design of Advanced Polymeric Materials. *Accounts of Materials Research* **5**, 571–584 (2024). <https://doi.org/10.1021/accountsmr.3c00288>.
- [2] Li, D. *et al.* Accelerating the design and development of polymeric materials via deep learning: Current status and future challenges. *APL Machine Learning* **1**, 021501 (2023). <https://doi.org/10.1063/5.0131067>.

- [3] Tran, H. *et al.* Design of functional and sustainable polymers assisted by artificial intelligence. *Nature Reviews Materials* 1–21 (2024). <https://www.nature.com/articles/s41578-024-00708-8>.
- [4] Yang, Q. *et al.* Artificial Intelligence for Conjugated Polymers. *Chemistry of Materials* (2024). <https://doi.org/10.1021/acs.chemmater.3c02358>.
- [5] Jumper, J. *et al.* Highly accurate protein structure prediction with AlphaFold. *Nature* **596**, 583–589 (2021). <https://www.nature.com/articles/s41586-021-03819-2>.
- [6] Zhao, Y., Chen, G. & Liu, J. Polymer Data Challenges in the AI Era: Bridging Gaps for Next-Generation Energy Materials. <http://arxiv.org/abs/2505.13494> (2025). [arXiv:2505.13494](https://arxiv.org/abs/2505.13494).
- [7] S. Otsuka, I. Kuwajima, J. Hosoya, Y. Xu & M. Yamazaki *PoLyInfo: Polymer Database for Polymeric Materials Design*, 22–29 (7-9 Sept. 2011).
- [8] Kim, C., Chandrasekaran, A., Huan, T. D., Das, D. & Ramprasad, R. Polymer Genome: A Data-Powered Polymer Informatics Platform for Property Predictions. *The Journal of Physical Chemistry C* **122**, 17575–17585 (2018). <https://doi.org/10.1021/acs.jpcc.8b02913>.
- [9] Walsh, D. J. *et al.* Community Resource for Innovation in Polymer Technology (CRIPT): A Scalable Polymer Material Data Structure. *ACS Central Science* **9**, 330–338 (2023). <https://doi.org/10.1021/acscentsci.3c00011>.
- [10] Kuenneth, C. *et al.* Bioplastic Design using Multitask Deep Neural Networks. <http://arxiv.org/abs/2203.12033> (2022). [arXiv:2203.12033](https://arxiv.org/abs/2203.12033).
- [11] Kuenneth, C. & Ramprasad, R. polyBERT: A chemical language model to enable fully machine-driven ultrafast polymer informatics. *Nature Communications* **14**, 4099 (2023). <https://www.nature.com/articles/s41467-023-39868-6>.
- [12] Doan Tran, H. *et al.* Machine-learning predictions of polymer properties with Polymer Genome. *Journal of Applied Physics* **128**, 171104 (2020). <https://aip.scitation.org/doi/10.1063/5.0023759>.
- [13] Volgin, I. V. *et al.* Machine Learning with Enormous “Synthetic” Data Sets: Predicting Glass Transition Temperature of Polyimides Using Graph Convolutional Neural Networks. *ACS Omega* **7**, 43678–43691 (2022). <https://doi.org/10.1021/acsomega.2c04649>.
- [14] Ma, R. & Luo, T. PI1M: A Benchmark Database for Polymer Informatics. *Journal of Chemical Information and Modeling* **60**, 4684–4690 (2020). <https://doi.org/10.1021/acs.jcim.0c00726>.

- [15] Xu, J., Liu, G., Guo, R., Jiang, M. & Luo, T. POINT²: A Polymer Informatics Training and Testing Database. <http://arxiv.org/abs/2503.23491> (2025). [arXiv:2503.23491](https://arxiv.org/abs/2503.23491).
- [16] Tao, L., Byrnes, J., Varshney, V. & Li, Y. Machine learning strategies for the structure-property relationship of copolymers. *iScience* **25**, 104585 (2022). <https://www.sciencedirect.com/science/article/pii/S2589004222008574>.
- [17] Lo, S., Seifrid, M., Gaudin, T. & Aspuru-Guzik, A. Augmenting Polymer Datasets by Iterative Rearrangement. *Journal of Chemical Information and Modeling* **63**, 4266–4276 (2023). <https://doi.org/10.1021/acs.jcim.3c00144>.
- [18] Aldeghi, M. & W. Coley, C. A graph representation of molecular ensembles for polymer property prediction. *Chemical Science* **13**, 10486–10498 (2022). <https://pubs.rsc.org/en/content/articlelanding/2022/sc/d2sc02839e>.
- [19] Antoniuk, E. R., Li, P., Kailkhura, B. & Hiszpanski, A. M. Representing Polymers as Periodic Graphs with Learned Descriptors for Accurate Polymer Property Predictions. *Journal of Chemical Information and Modeling* **62**, 5435–5445 (2022). <https://doi.org/10.1021/acs.jcim.2c00875>.
- [20] Gurnani, R., Kuenneth, C., Toland, A. & Ramprasad, R. Polymer Informatics at Scale with Multitask Graph Neural Networks. *Chemistry of Materials* **35**, 1560–1567 (2023). <https://doi.org/10.1021/acs.chemmater.2c02991>.
- [21] Bradford, G. *et al.* Chemistry-Informed Machine Learning for Polymer Electrolyte Discovery. *ACS Central Science* **9**, 206–216 (2023). <https://doi.org/10.1021/acscentsci.2c01123>.
- [22] Vogel, G. & M. Weber, J. Inverse design of copolymers including stoichiometry and chain architecture. *Chemical Science* **16**, 1161–1178 (2025). <https://pubs.rsc.org/en/content/articlelanding/2025/sc/d4sc05900j>.
- [23] Xu, C., Wang, Y. & Barati Farimani, A. TransPolymer: A Transformer-based language model for polymer property predictions. *npj Computational Materials* **9**, 1–14 (2023). <https://www.nature.com/articles/s41524-023-01016-5>.
- [24] Wang, F. *et al.* MMPolymer: A Multimodal Multitask Pretraining Framework for Polymer Property Prediction. <http://arxiv.org/abs/2406.04727> (2024). [arXiv:2406.04727](https://arxiv.org/abs/2406.04727).
- [25] Zhang, P. *et al.* Transferring a Molecular Foundation Model for Polymer Property Predictions. *Journal of Chemical Information and Modeling* **63**, 7689–7698 (2023). <https://doi.org/10.1021/acs.jcim.3c01650>.
- [26] Savit, A., Sahu, H., Shukla, S., Xiong, W. & Ramprasad, R. polyBART: A Chemical Linguist for Polymer Property Prediction and Generative Design. <http://arxiv.org/abs/2503.23491> (2025). [arXiv:2503.23491](https://arxiv.org/abs/2503.23491).

//arxiv.org/abs/2506.04233 (2025). arXiv:2506.04233.

- [27] Dobrynin, A. V., Stroujkova, A., Vatankhah-Varnosfaderani, M. & Sheiko, S. S. Coarse-Grained Artificial Intelligence for Design of Brush Networks. *ACS Macro Letters* **12**, 1510–1516 (2023). <https://doi.org/10.1021/acsmacrolett.3c00479>.
- [28] Webb, M. A., Jackson, N. E., Gil, P. S. & de Pablo, J. J. Targeted sequence design within the coarse-grained polymer genome. *Science Advances* **6**, eabc6216 (2020). <https://www.science.org/doi/10.1126/sciadv.abc6216>.
- [29] Qiu, H. & Sun, Z.-Y. Exploring SMILES and BigSMILES: Toward Efficient and Scalable Polymer Representations for Machine Learning. *Macromolecules* **58**, 7084–7093 (2025). <https://doi.org/10.1021/acs.macromol.5c00604>.
- [30] Huang, Q., Li, Y., Zhu, L., Zhao, Q. & Yu, W. Unified multimodal multidomain polymer representation for property prediction. *npj Computational Materials* **11**, 153 (2025). <https://www.nature.com/articles/s41524-025-01652-z>.
- [31] Lin, T.-S. *et al.* BigSMILES: A Structurally-Based Line Notation for Describing Macromolecules. *ACS Central Science* **5**, 1523–1531 (2019). <https://doi.org/10.1021/acscentsci.9b00476>.
- [32] Zou, W. *et al.* Extending BigSMILES to non-covalent bonds in supramolecular polymer assemblies. *Chemical Science* **13**, 12045–12055 (2022). <https://pubs.rsc.org/en/content/articlelanding/2022/sc/d2sc02257e>.
- [33] Schneider, L., Walsh, D., Olsen, B. & de Pablo, J. Generative BigSMILES: An extension for polymer informatics, computer simulations & ML/AI. *Digital Discovery* **3**, 51–61 (2024). <https://pubs.rsc.org/en/content/articlelanding/2024/dd/d3dd00147d>.
- [34] Yu, M. *et al.* Ring Repeating Unit: An Upgraded Structure Representation of Linear Condensation Polymers for Property Prediction. *Journal of Chemical Information and Modeling* **63**, 1177–1187 (2023). <https://doi.org/10.1021/acs.jcim.2c01389>.
- [35] Park, N. H. *et al.* Artificial intelligence driven design of catalysts and materials for ring opening polymerization using a domain-specific language. *Nature Communications* **14**, 3686 (2023). <https://www.nature.com/articles/s41467-023-39396-3>.
- [36] Yang, J., Tao, L., He, J., McCutcheon, J. R. & Li, Y. Machine learning enables interpretable discovery of innovative polymers for gas separation membranes. *Science Advances* **8**, eabn9545 (2022). <https://www.science.org/doi/10.1126/sciadv.abn9545>.
- [37] Hu, J., Li, Z., Lin, J. & Zhang, L. Prediction and Interpretability of Glass Transition Temperature of Homopolymers by Data-Augmented Graph Convolutional

- Neural Networks. *ACS Applied Materials & Interfaces* **15**, 54006–54017 (2023). <https://doi.org/10.1021/acsami.3c13698>.
- [38] Long, Z., Lu, H. & Zhang, Z. Large-Scale Glass-Transition Temperature Prediction with an Equivariant Neural Network for Screening Polymers. *ACS Omega* **9**, 5452–5462 (2024). <https://doi.org/10.1021/acsomega.3c06843>.
 - [39] Reis, M. *et al.* Machine-Learning-Guided Discovery of 19F MRI Agents Enabled by Automated Copolymer Synthesis. *Journal of the American Chemical Society* **143**, 17677–17689 (2021). <https://doi.org/10.1021/jacs.1c08181>.
 - [40] Arora, A. *et al.* Random Forest Predictor for Diblock Copolymer Phase Behavior. *ACS Macro Letters* **10**, 1339–1345 (2021). <https://doi.org/10.1021/acsmacrolett.1c00521>.
 - [41] Giro, R. *et al.* AI powered, automated discovery of polymer membranes for carbon capture. *npj Computational Materials* **9**, 1–11 (2023). <https://www.nature.com/articles/s41524-023-01088-3>.
 - [42] Tiwari, S. P. *et al.* Creation of Polymer Datasets with Targeted Backbones for Screening of High-Performance Membranes for Gas Separation. *Journal of Chemical Information and Modeling* **64**, 638–652 (2024). <https://doi.org/10.1021/acs.jcim.3c01232>.
 - [43] Devlin, J., Chang, M.-W., Lee, K. & Toutanova, K. Burstein, J., Doran, C. & Solorio, T. (eds) *BERT: Pre-training of Deep Bidirectional Transformers for Language Understanding*. (eds Burstein, J., Doran, C. & Solorio, T.) *Proceedings of the 2019 Conference of the North American Chapter of the Association for Computational Linguistics: Human Language Technologies, Volume 1 (Long and Short Papers)*, 4171–4186 (Association for Computational Linguistics, Minneapolis, Minnesota, 2019). <https://aclanthology.org/N19-1423/>.
 - [44] Kuenneth, C. *et al.* Polymer informatics with multi-task learning. *Patterns* **2**, 100238 (2021).
 - [45] Hatakeyama-Sato, K., Watanabe, S., Yamane, N., Igarashi, Y. & Oyaizu, K. Using GPT-4 in parameter selection of polymer informatics: Improving predictive accuracy amidst data scarcity and ‘Ugly Duckling’ dilemma. *Digital Discovery* **2**, 1548–1557 (2023).
 - [46] Schauser, N. S., Kliegle, G. A., Cooke, P., Segalman, R. A. & Seshadri, R. Database Creation, Visualization, and Statistical Learning for Polymer Li+-Electrolyte Design. *Chemistry of Materials* **33**, 4863–4876 (2021).
 - [47] Soares, E. *et al.* An open-source family of large encoder-decoder foundation models for chemistry. *Communications Chemistry* **8**, 193 (2025). <https://www.nature.com/articles/s42004-025-01585-0>.

- [48] Liu, J. *et al.* Towards Out-Of-Distribution Generalization: A Survey. <http://arxiv.org/abs/2108.13624> (2023). [arXiv:2108.13624](https://arxiv.org/abs/2108.13624).
- [49] Bradshaw, J. *et al.* Challenging Reaction Prediction Models to Generalize to Novel Chemistry. *ACS Central Science* **11**, 539–549 (2025). <https://doi.org/10.1021/acscentsci.5c00055>.
- [50] Toniato, A. *et al.* Fast Customization of Chemical Language Models to Out-of-Distribution Data Sets. *Chemistry of Materials* **35**, 8806–8815 (2023). <https://doi.org/10.1021/acs.chemmater.3c01406>.
- [51] Tang, H., Yue, T. & Li, Y. Assessing Uncertainty in Machine Learning for Polymer Property Prediction: A Benchmark Study. *Journal of Chemical Information and Modeling* **65**, 6585–6598 (2025). <https://doi.org/10.1021/acs.jcim.5c00550>.
- [52] Landrum, G. A. *et al.* SIMPD: An algorithm for generating simulated time splits for validating machine learning approaches. *Journal of Cheminformatics* **15**, 1–16 (2023). <https://jcheminf.biomedcentral.com/articles/10.1186/s13321-023-00787-9>.
- [53] Guo, Q., Hernandez-Hernandez, S. & Ballester, P. J. Scaffold Splits Overestimate Virtual Screening Performance. <http://arxiv.org/abs/2406.00873> (2024). [arXiv:2406.00873](https://arxiv.org/abs/2406.00873).
- [54] Steshin, S. Lo-Hi: Practical ML Drug Discovery Benchmark. <http://arxiv.org/abs/2310.06399> (2023). [arXiv:2310.06399](https://arxiv.org/abs/2310.06399).
- [55] Hirschfeld, L., Swanson, K., Yang, K., Barzilay, R. & Coley, C. W. Uncertainty Quantification Using Neural Networks for Molecular Property Prediction. *Journal of Chemical Information and Modeling* **60**, 3770–3780 (2020). <https://doi.org/10.1021/acs.jcim.0c00502>.
- [56] Scalia, G., Grambow, C. A., Pernici, B., Li, Y.-P. & Green, W. H. Evaluating Scalable Uncertainty Estimation Methods for Deep Learning-Based Molecular Property Prediction. *Journal of Chemical Information and Modeling* **60**, 2697–2717 (2020). <https://doi.org/10.1021/acs.jcim.9b00975>.
- [57] Varivoda, D., Dong, R., Omee, S. S. & Hu, J. Materials property prediction with uncertainty quantification: A benchmark study. *Applied Physics Reviews* **10**, 021409 (2023). <https://doi.org/10.1063/5.0133528>.
- [58] E. Graff, D., O. Pyzer-Knapp, E., E. Jordan, K., I. Shakhnovich, E. & W. Coley, C. Evaluating the roughness of structure–property relationships using pretrained molecular representations. *Digital Discovery* **2**, 1452–1460 (2023). <https://pubs.rsc.org/en/content/articlelanding/2023/dd/d3dd00088e>.

- [59] Sheridan, R. P. *et al.* Experimental Error, Kurtosis, Activity Cliffs, and Methodology: What Limits the Predictivity of Quantitative Structure–Activity Relationship Models? *Journal of Chemical Information and Modeling* **60**, 1969–1982 (2020). <https://doi.org/10.1021/acs.jcim.9b01067>.
- [60] Sheridan, R. P., Feuston, B. P., Maiorov, V. N. & Kearsley, S. K. Similarity to Molecules in the Training Set Is a Good Discriminator for Prediction Accuracy in QSAR. *Journal of Chemical Information and Computer Sciences* **44**, 1912–1928 (2004). <https://doi.org/10.1021/ci049782w>.
- [61] Dollar, O., Joshi, N., C. Beck, D. A. & Pfaendtner, J. Attention-based generative models for de novo molecular design. *Chemical Science* **12**, 8362–8372 (2021). <https://pubs.rsc.org/en/content/articlelanding/2021/sc/d1sc01050f>.

Understanding Structural Representation in Foundation Models for Polymers

Nathaniel H. Park^{1*}, Eduardo Soares², Victor Shirasuna²,
Tiffany J. Callahan¹, Sara Capponi¹, Emilio Vital Brazil²

¹IBM Research Almaden, 650 Harry Rd., San Jose, 95120, CA, United States of America.

²IBM Research Brazil, Street, Rio de Janeiro, 10587, RJ, Brazil.

*Corresponding author(s). E-mail(s): npark@us.ibm.com;
Contributing authors: eduardo.soares@ibm.com; vshirasuna@ibm.com;
tiffany.callahan@ibm.com; sara.capponi@ibm.com; evital@br.ibm.com;

Contents

1	Supplemental Methods	3
1.1	Representation Experiments	3
2	Supplemental Figures	5
2.1	Polymer Representation	5
2.2	Pre-Training Data	6
2.3	Error Analysis	6
2.3.1	Latent Embedding Distance	6
2.3.2	Fingerprint Similarity	11
2.4	Attention Figures	39
2.5	Historical Performance Comparisons	41
2.6	Representation Evaluation Results	41
2.6.1	Polymer Chain Bandgap (E_{gc}) CV Scores	43
2.6.2	Polymer Chain Bandgap (E_{gc}) Random Split Scores	46
2.6.3	Polymer Bulk Bandgap (E_{gb}) CV Scores	52
2.6.4	Polymer Bulk Bandgap (E_{gb}) Random Split Scores	55
2.6.5	Polymer Ionization Energy (E_i) CV Scores	61
2.6.6	Polymer Ionization Energy (E_i) Random Split Scores	64

2.6.7	Polymer Dielectric Constant (EPS) CV Scores	70
2.6.8	Polymer Dielectric Constant (EPS) Random Split Scores	73
2.6.9	Polymer Electron Affinity (E _{ea}) CV Scores	78
2.6.10	Polymer Electron Affinity (E _{ea}) Random Split Scores	81
2.6.11	Polymer Atomization Energy (E _{at}) CV Scores	86
2.6.12	Polymer Atomization Energy (E _{at}) Random Split Scores	89
2.6.13	Refractivity Index (N _c) CV Scores	94
2.6.14	Refractivity Index (N _c) Random Split Scores	97
2.6.15	Crystallization Tendency (X _c) CV Scores	103
2.6.16	Crystallization Tendency (X _c) Random Split Scores	106
2.6.17	Glass Transition Temperature (T _{g-II}) CV Scores	112
2.6.18	Glass Transition Temperature (T _{g-II}) Random Split Scores	115
2.6.19	CO ₂ Gas Permeability CV Scores	121
2.6.20	CO ₂ Gas Permeability Random Split Scores	124
2.6.21	N ₂ Gas Permeability CV Scores	129
2.6.22	N ₂ Gas Permeability Random Split Scores	132
2.6.23	CH ₄ Gas Permeability CV Scores	136
2.6.24	CH ₄ Gas Permeability Random Split Scores	139
2.6.25	CO ₂ :CH ₄ Gas Selectivity CV Scores	143
2.6.26	CO ₂ :CH ₄ Gas Selectivity Random Split Scores	146
2.6.27	CO ₂ :N ₂ Gas Selectivity CV Scores	150
2.6.28	CO ₂ :N ₂ Gas Selectivity Random Split Scores	153

1 Supplemental Methods

1.1 Representation Experiments

Atom Replacement Methods

As noted in the main text, we utilized three different approaches to transform the CPG representation into other SMILES strings, including PSMILES. The transformation was performed from benchmark data which had been converted into the CPG representation as opposed to the original data in order to ensure identical sequences of tokens for each entity were maintained. During conversion to the CPG notation, the SMILES strings had been canonicalized using RDKit, which resulted in new ordering in the SMILES strings as compared to the original data. The three replacement methods are:

- *All* – which replaces all characters including the brackets.
- *Bracket* – which replaces all characters inside the brackets.
- *Star* – which replaces only the asterisk character.

Following substitution, a separate copy of the converted dataset was canonicalized again for comparison, as some atom substitutions resulted in different canonical atom orders than the original.

Replacement Atoms

Below is a list of all the replacement atoms, which substitution methods were used, and whether a separate, re-canonicalized dataset was also created.

Table 1 Replacement Atoms for Input Representations

Atom	Methods	Canonicalization
*	<i>All</i> ¹ , <i>Star</i>	Yes
*	<i>Bracket</i> ¹	No ²
H	<i>Bracket</i>	Yes ³
C	<i>All</i> , <i>Bracket</i> , <i>Star</i>	Yes
c	<i>All</i> , <i>Bracket</i>	No
N	<i>All</i> , <i>Bracket</i>	Yes
n	<i>All</i>	No
n⁺	<i>Bracket</i>	No
O	<i>All</i> , <i>Bracket</i>	Yes
S	<i>All</i> , <i>Bracket</i>	Yes
P	<i>All</i> , <i>Bracket</i>	Yes
B	<i>All</i> , <i>Bracket</i>	Yes
Cl	<i>All</i> , <i>Bracket</i>	Yes
F	<i>All</i> , <i>Bracket</i>	Yes
Ne	<i>Bracket</i>	No
Si	<i>Bracket</i>	Yes
Na	<i>Bracket</i>	Yes
Mg	<i>Bracket</i>	Yes
Ti²⁺	<i>Bracket</i>	Yes
Au	<i>Bracket</i>	Yes
Te	<i>Bracket</i>	Yes
At	<i>Bracket</i>	Yes
²⁰¹Bi	<i>Bracket</i>	Yes

¹These replacement methods on the using the asterisk will afford the corresponding PSMILES representation

²Canonicalization of the asterisk inside a bracket removes the bracket, giving an equivalent representation as the *all* method

³Canonicaliztion of SMILES with the [H] token, removes the token entirely as hydrogen atoms are implicit in SMILES.

2 Supplemental Figures

2.1 Polymer Representation

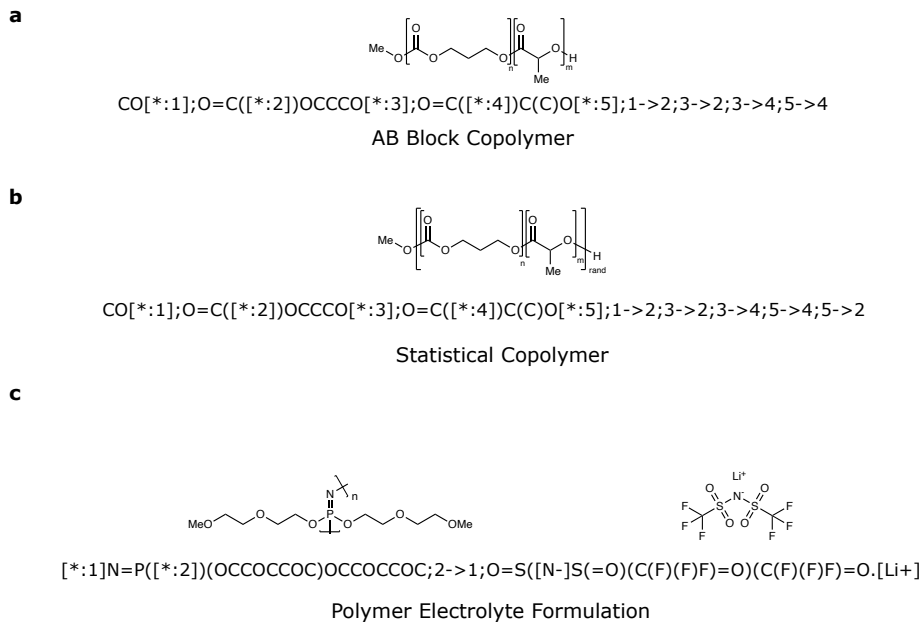


Fig. 1 Examples polymer structures and their corresponding CPG representation. **a.** Example of AB block copolymer represented using the CPG notation. **b.** Example of statistical copolymer containing identical components as **a**. Differentiation in the CPG representation is in the labeled edge connections. **c.** Example of a polymer electrolyte formulation containing a small-molecule lithium salt component.

2.2 Pre-Training Data

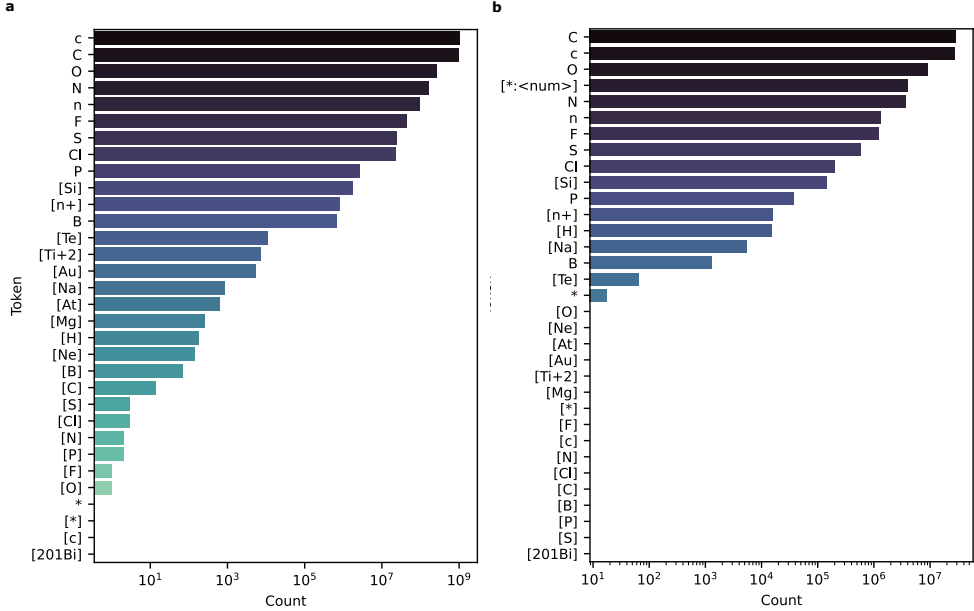


Fig. 2 Plots of token counts in the pre-training for the substituted tokens and asterisk containing tokens from Supplementary Table 1. **a.** Token counts from SMI-TED pre-training data. **b.** Token counts from further pre-training data used for SMI-TED-POLYMER. The token $[*: <\text{num}>]$ indicates the total for all numbered asterisk points e.g. $([:1], [:2]$, etc.).

2.3 Error Analysis

2.3.1 Latent Embedding Distance

Below are the remaining plots of the R^2 from linear regression between the predicted property value of each candidate in the hold-out test set and the average true value from its top five nearest neighbors in the training set as a function of the model used not included in the main manuscript. As in the main text, fine-tuned models are labeled by their respective base model followed by the representation with which it was fine-tuned with and the associated loss for the checkpoint. All losses for fine-tuned models are RMSE unless indicated otherwise. Circular markers indicate individual data points of each representation system evaluated. Markers are colored according to their representation group, with CM = CPG representation, Elemental = indicates non-asterisk atom substitutions, RT = randomized token selection, RC = randomly shuffled CPG representation, and RF = randomly shuffled SMILES string with randomly selected replacement atoms.

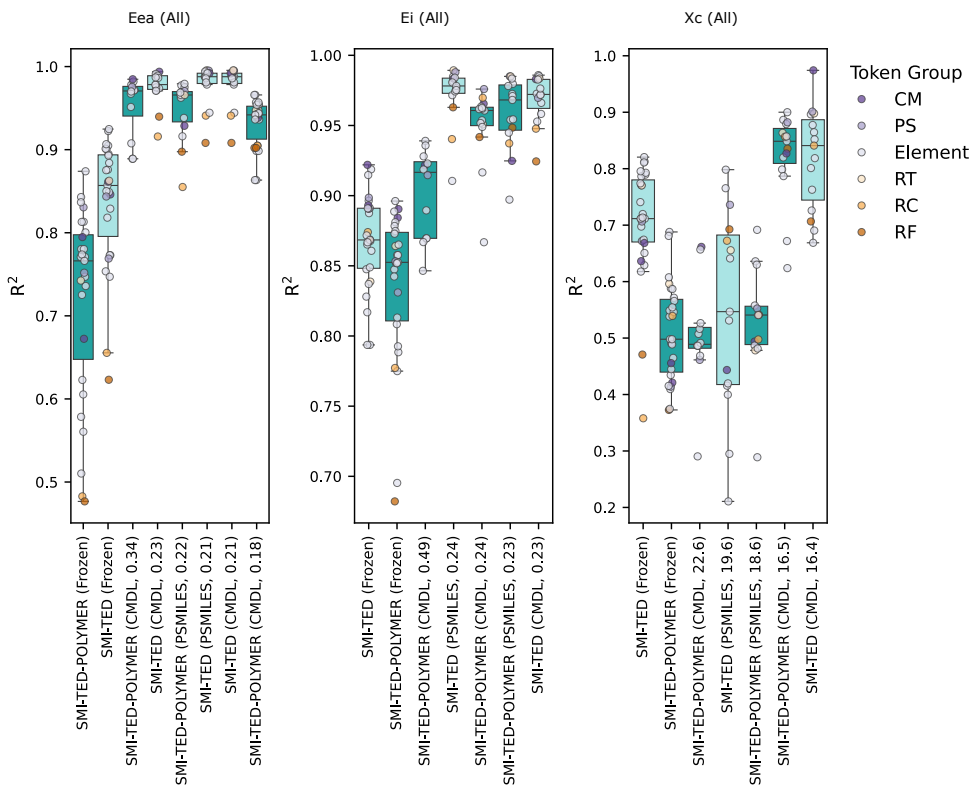


Fig. 3 Plots of R^2 value distributions for the benchmark datasets E_{ea} , E_i , and X_c using the *all* substitution strategy.

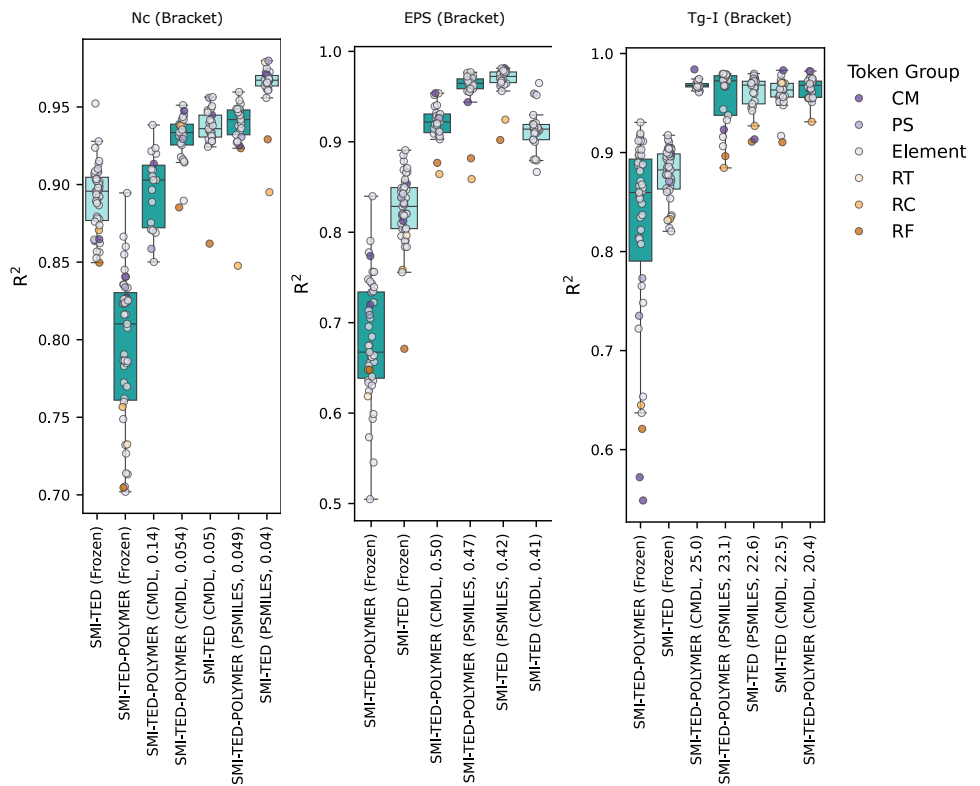


Fig. 4 Plots of R^2 value distributions for the benchmark datasets N_c , EPS , and $Tg-I$ using the bracket substitution strategy.

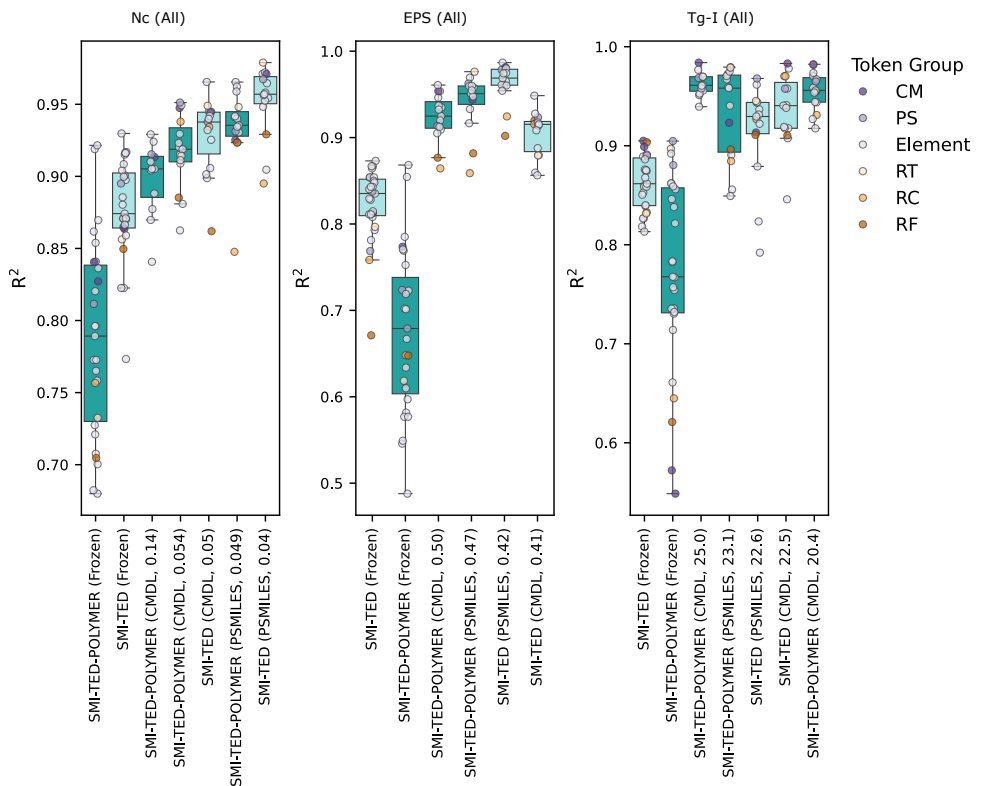


Fig. 5 Plots of R^2 value distributions for the benchmark datasets N_c , EPS , and $Tg\text{-}I$ using the *all* substitution strategy.

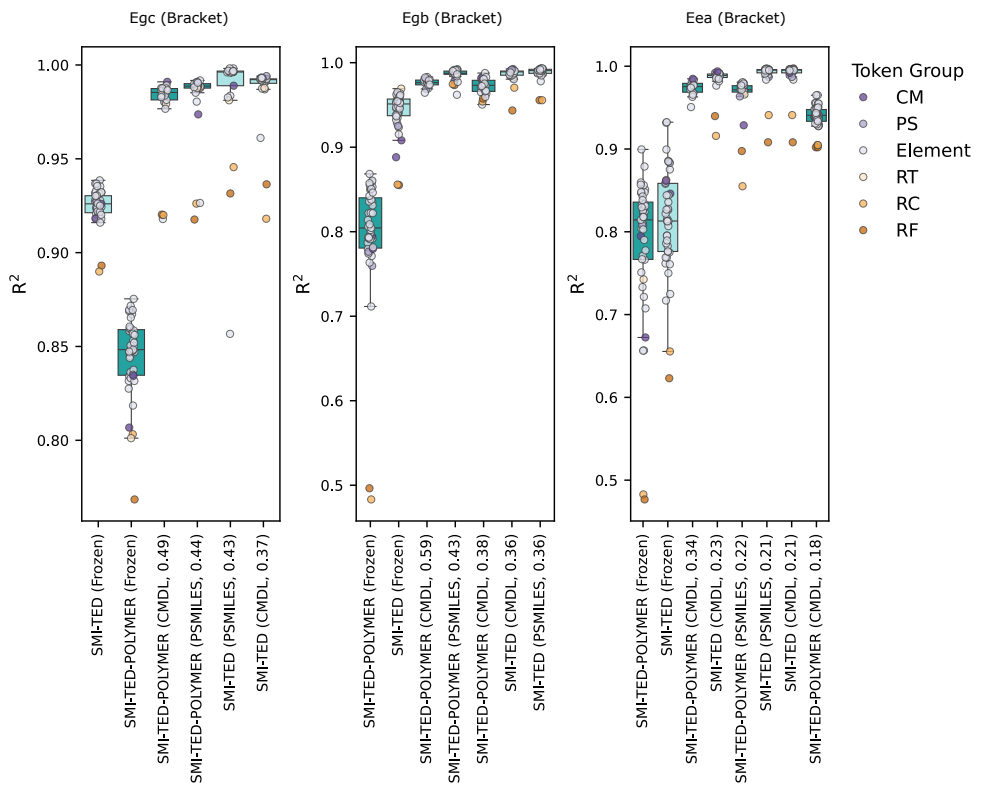


Fig. 6 Plots of R^2 value distributions for the benchmark datasets E_{gc} , E_{gb} , and E_{ea} using the *bracket* substitution strategy.

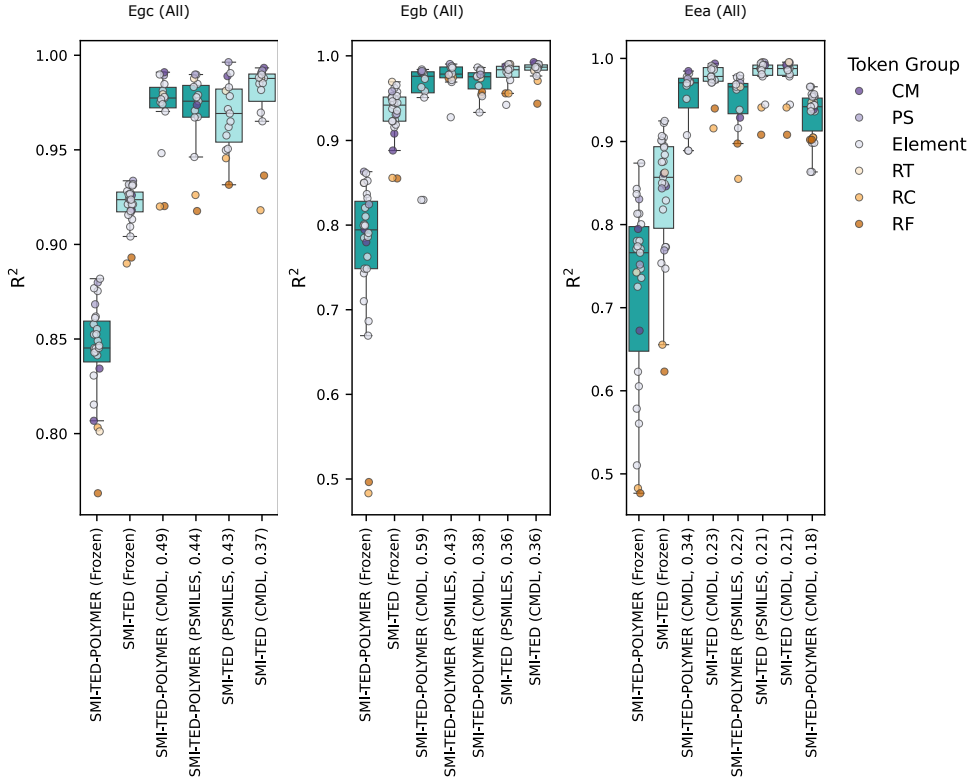


Fig. 7 Plots of R^2 value distributions for the benchmark datasets E_{gc} , E_{gb} , and E_{ea} using the *all* substitution strategy.

2.3.2 Fingerprint Similarity

Below are the plots of the R^2 from linear regression between the predicted property value of each candidate in the hold-out test set and the average true value from its top five nearest neighbors based on fingerprint chemical similarity in the training set as a function of the model used. Not all representations could be used to compute viable chemical fingerprints using the RDKit package. Substituted representations that resulted in an invalid SMILES or any of the randomly shuffled forms were not included in this analysis. Chemical similarity was computed using Dice similarity as reported previously. Fine-tuned models are labeled by their respective base model followed by the representation with which it was fine-tuned with and the associated loss for the checkpoint. All losses for fine-tuned models are RMSE unless indicated otherwise.

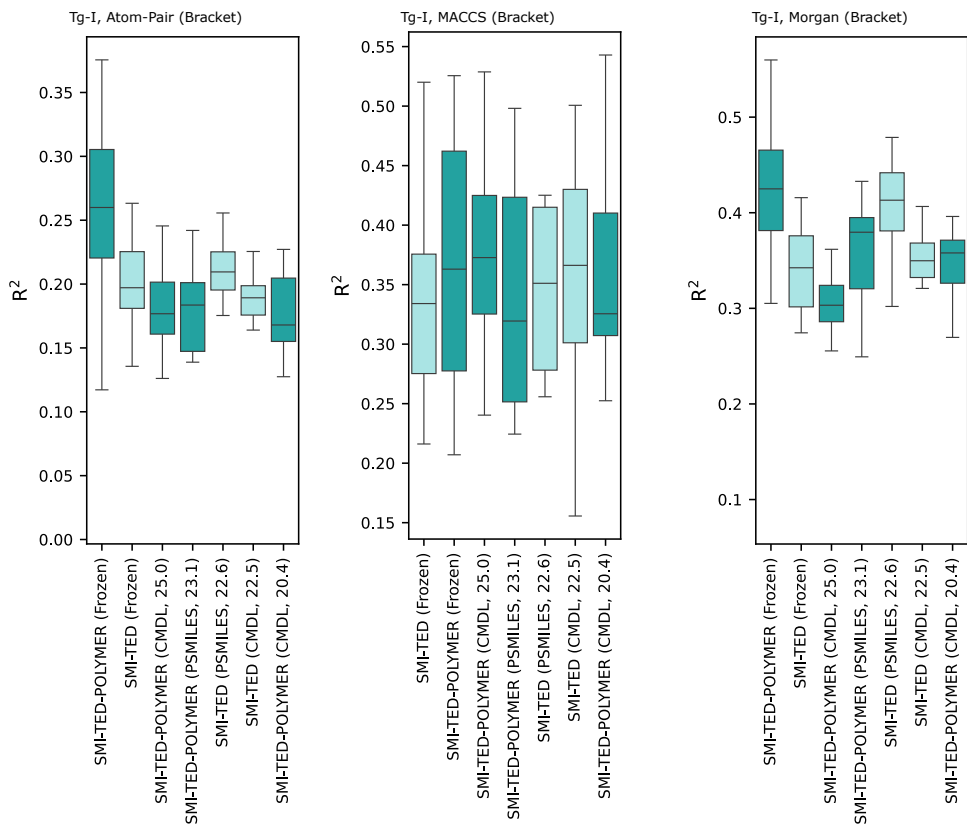


Fig. 8 Plots of fingerprint R^2 value distributions for the Tg-I benchmark dataset using the *bracket* substitution strategy.

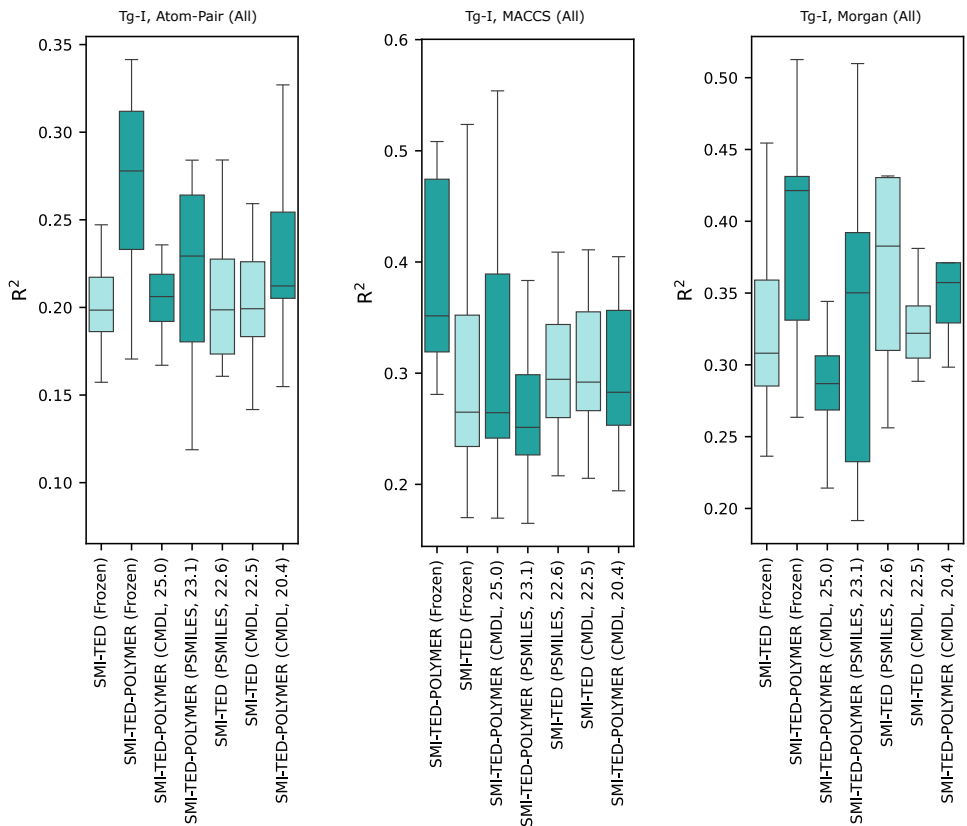


Fig. 9 Plots of fingerprint R^2 value distributions for the T_g-I benchmark dataset using the *all* substitution strategy.

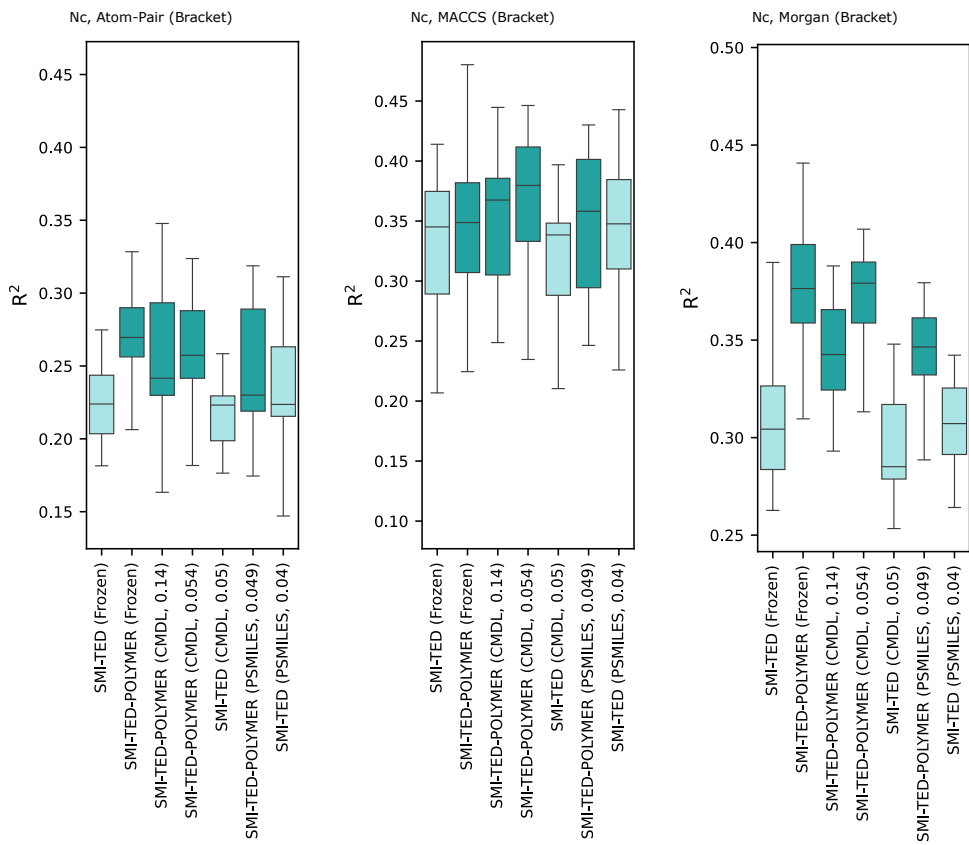


Fig. 10 Plots of fingerprint R^2 value distributions for the N_c benchmark dataset using the *bracket* substitution strategy.

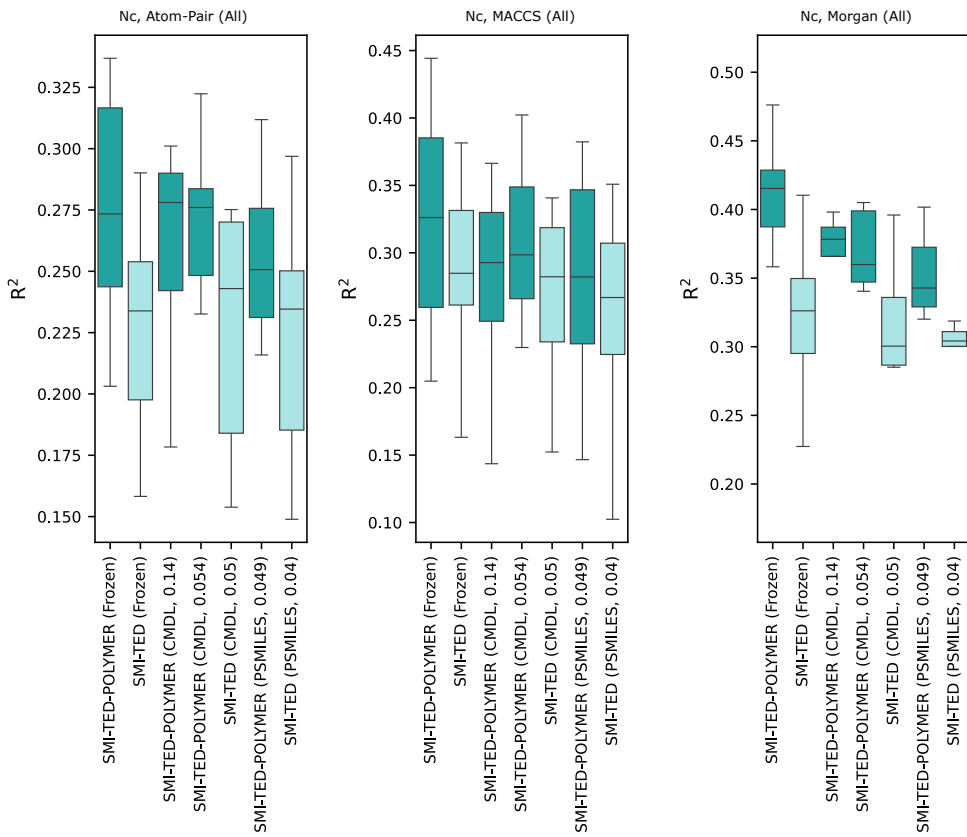


Fig. 11 Plots of fingerprint R^2 value distributions for the N_c benchmark dataset using the *all* substitution strategy.

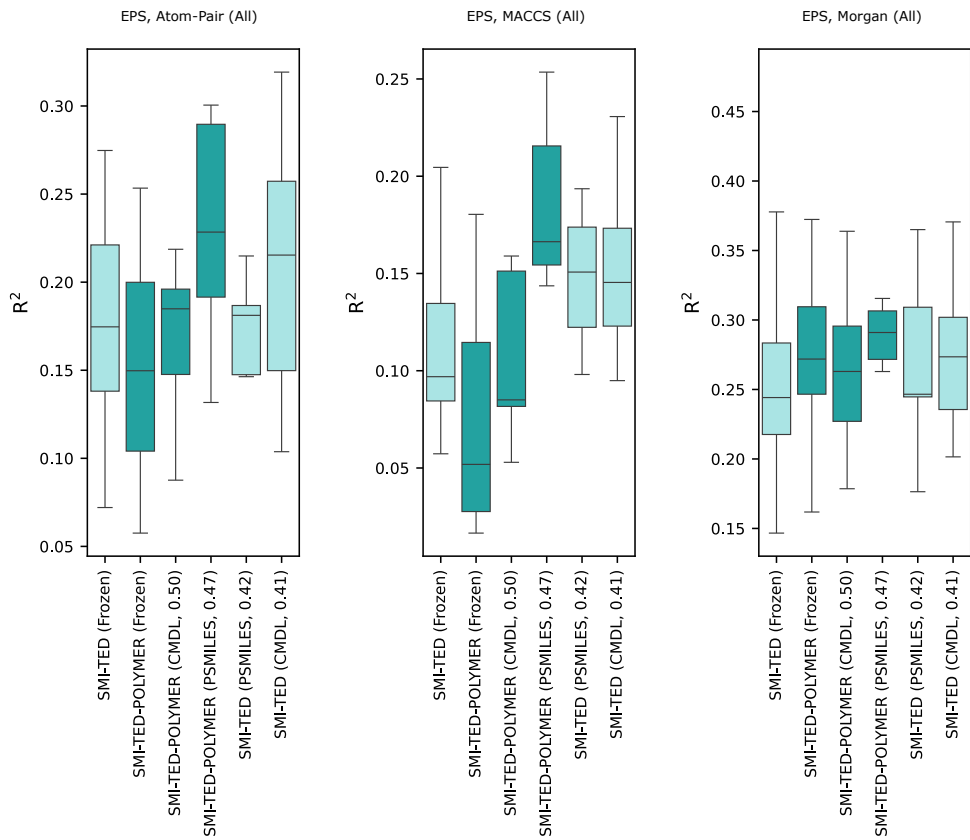


Fig. 12 Plots of fingerprint R² value distributions for the EPS benchmark dataset using the *all* substitution strategy.

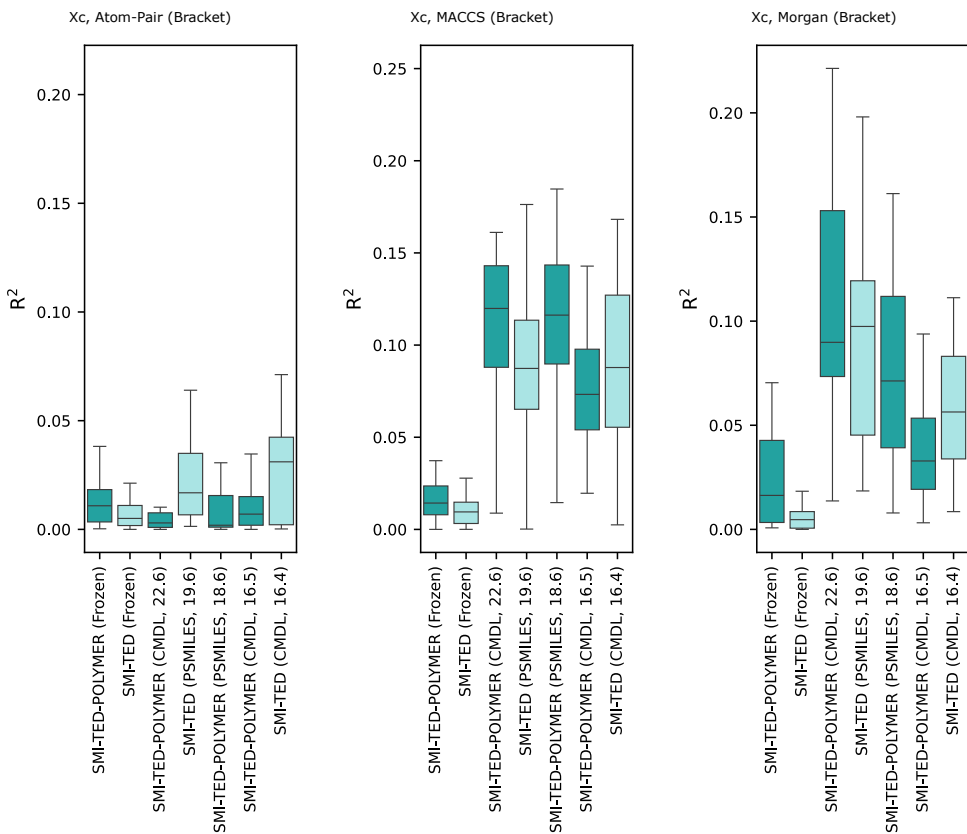


Fig. 13 Plots of fingerprint R^2 value distributions for the X_c benchmark dataset using the *bracket* substitution strategy.

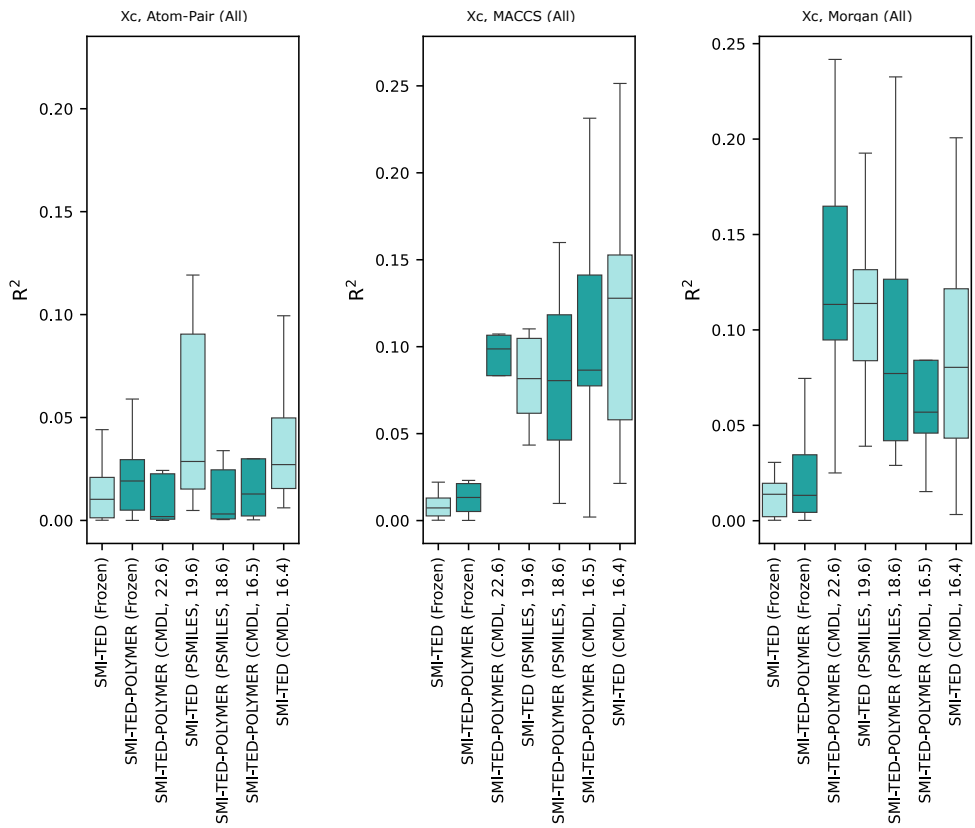


Fig. 14 Plots of fingerprint R^2 value distributions for the X_c benchmark dataset using the *all* substitution strategy.

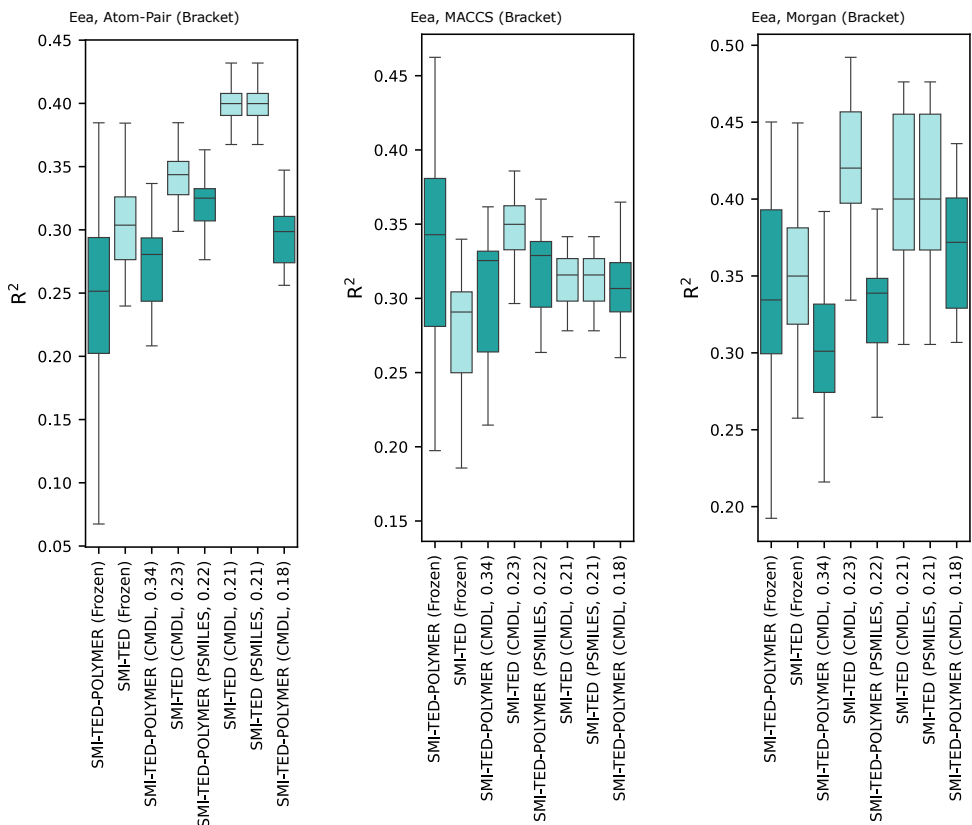


Fig. 15 Plots of fingerprint R^2 value distributions for the E_{ea} benchmark dataset using the *bracket* substitution strategy.

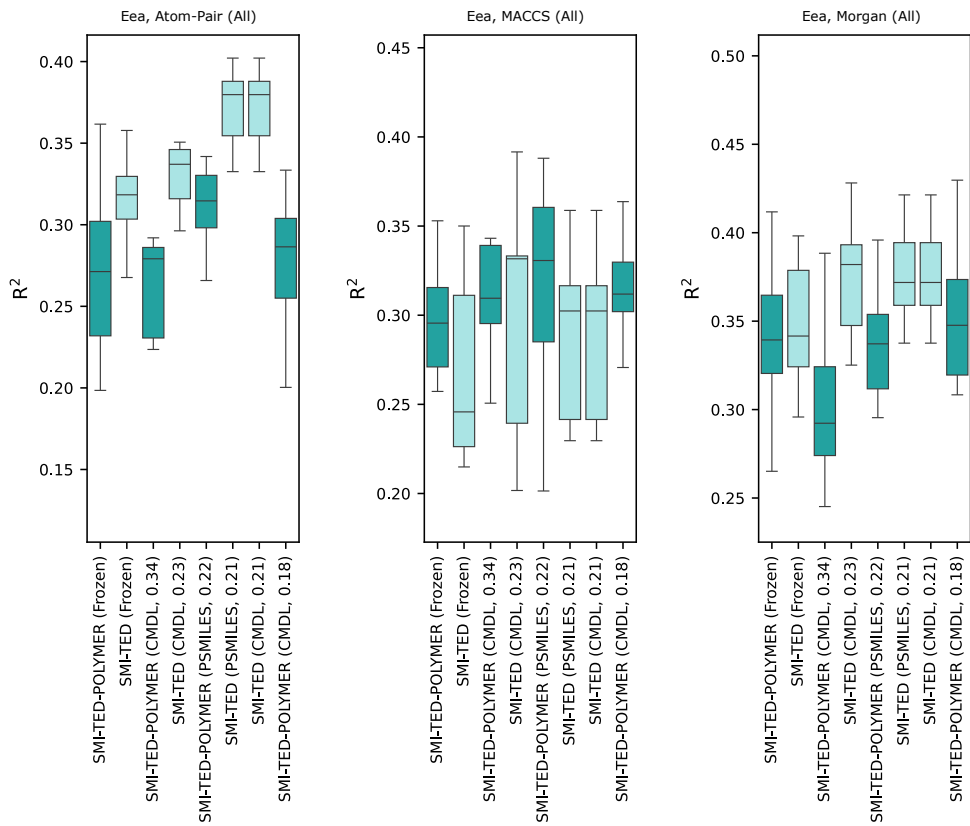


Fig. 16 Plots of fingerprint R^2 value distributions for the Eea benchmark dataset using the *all* substitution strategy.

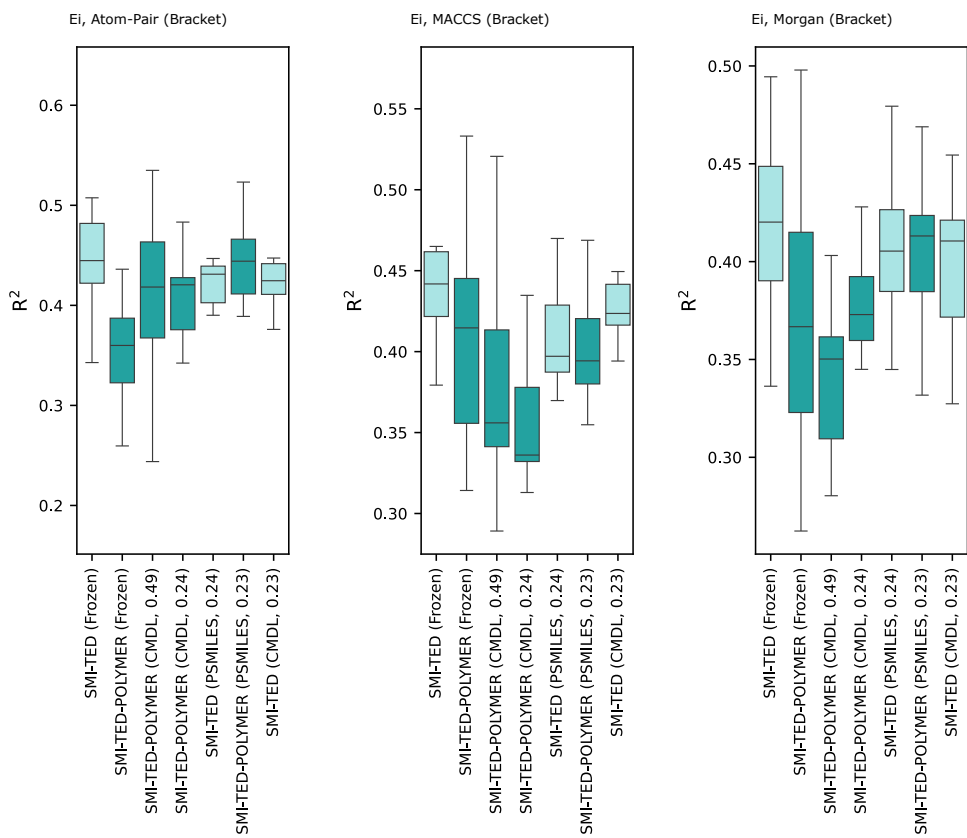


Fig. 17 Plots of fingerprint R^2 value distributions for the E_i benchmark dataset using the *bracket* substitution strategy.

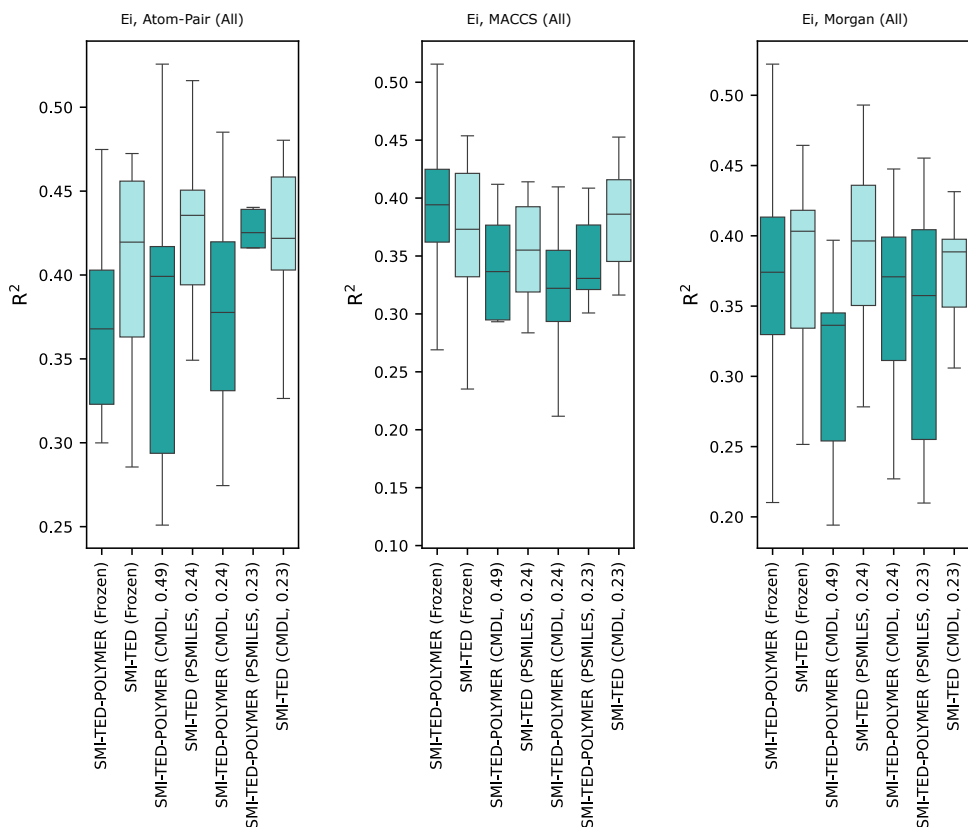


Fig. 18 Plots of fingerprint R^2 value distributions for the E_i benchmark dataset using the *all* substitution strategy.

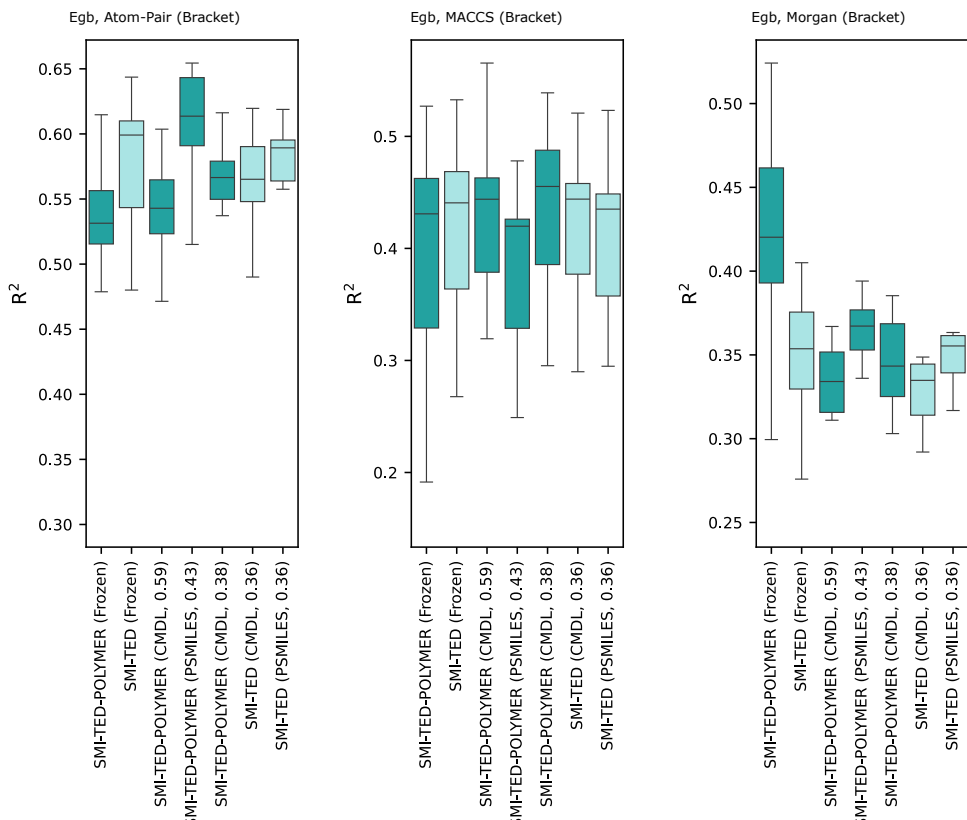


Fig. 19 Plots of fingerprint R^2 value distributions for the E_{gb} benchmark dataset using the *bracket* substitution strategy.

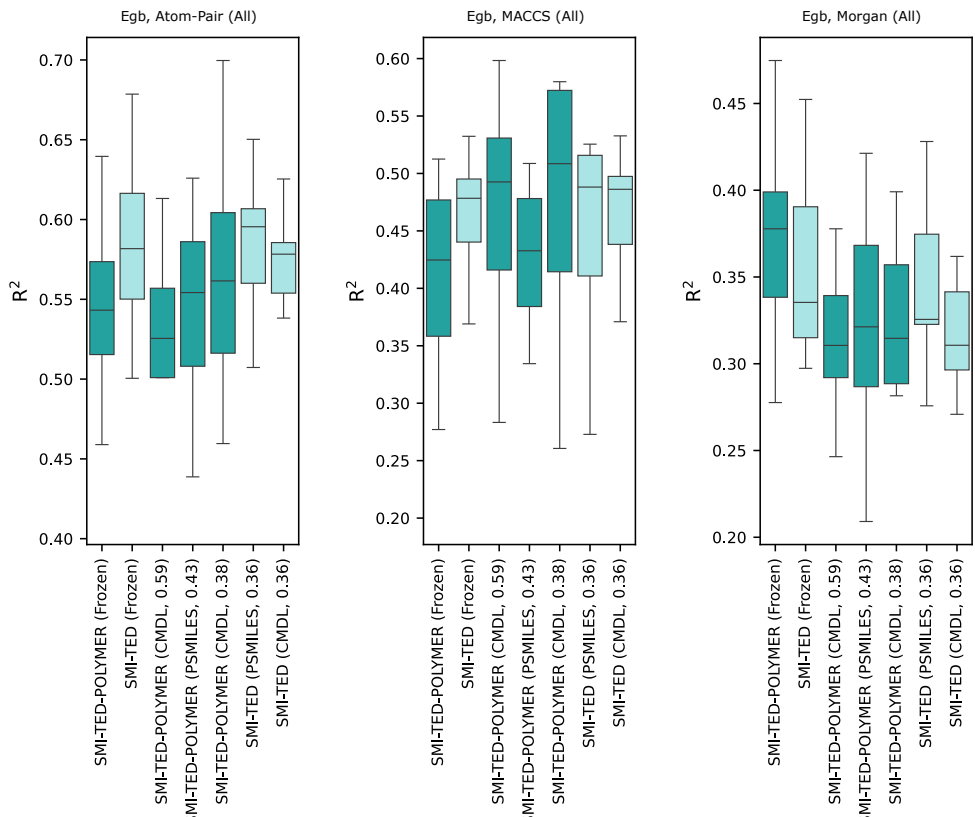


Fig. 20 Plots of fingerprint R^2 value distributions for the E_{gb} benchmark dataset using the *all* substitution strategy.

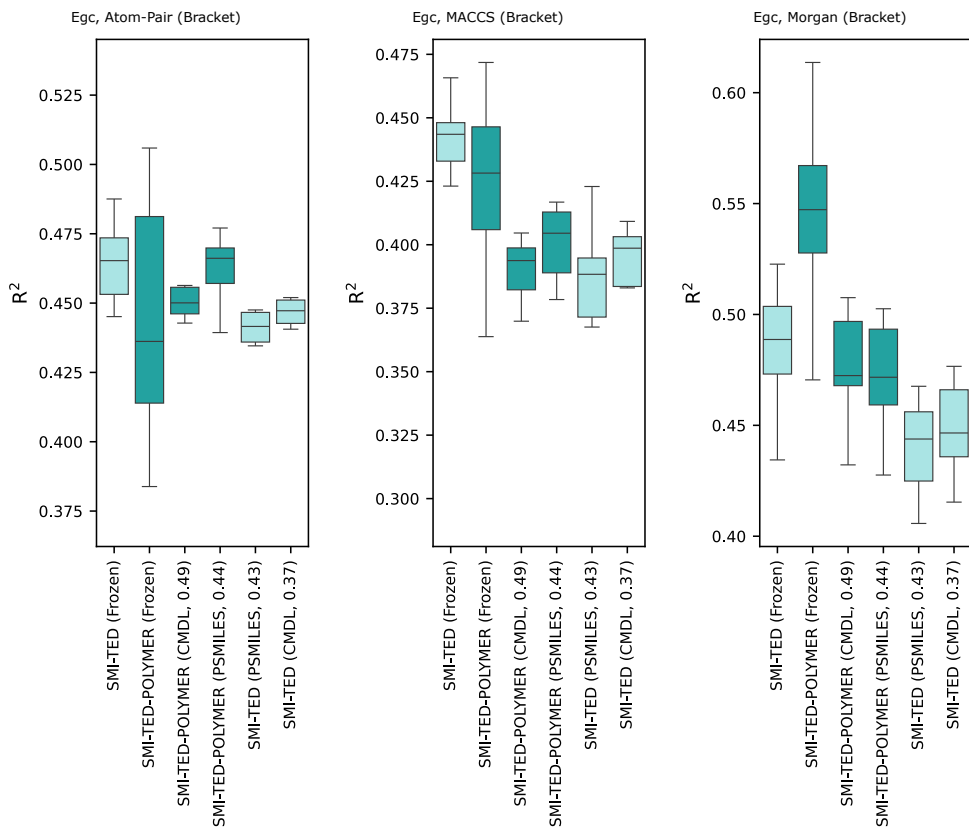


Fig. 21 Plots of fingerprint R^2 value distributions for the E_{gc} benchmark dataset using the *bracket* substitution strategy.

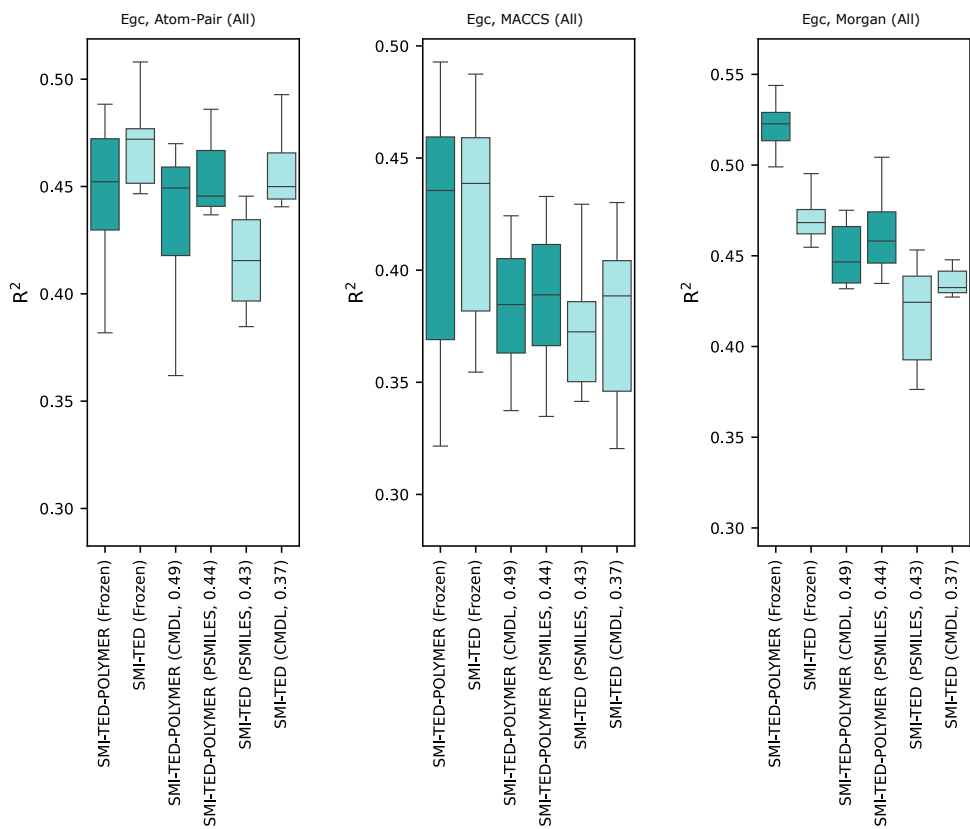


Fig. 22 Plots of fingerprint R^2 value distributions for the Egc benchmark dataset using the *all* substitution strategy.

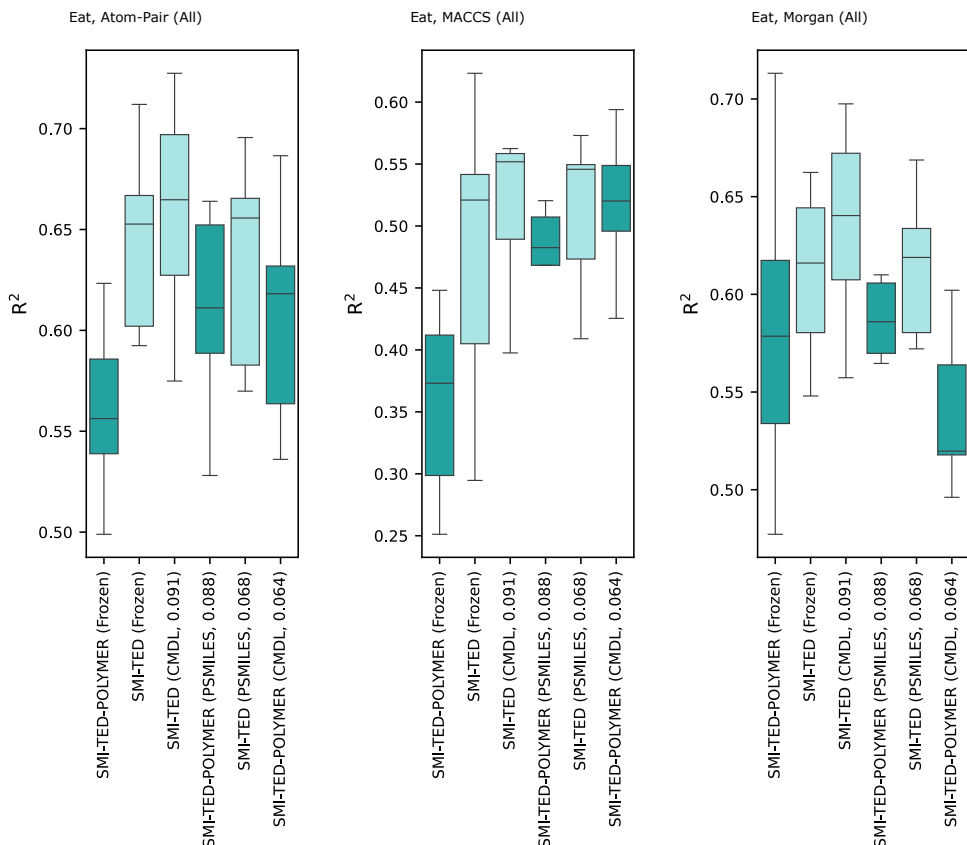


Fig. 23 Plots of fingerprint R^2 value distributions for the E_{at} benchmark dataset using the *all* substitution strategy.

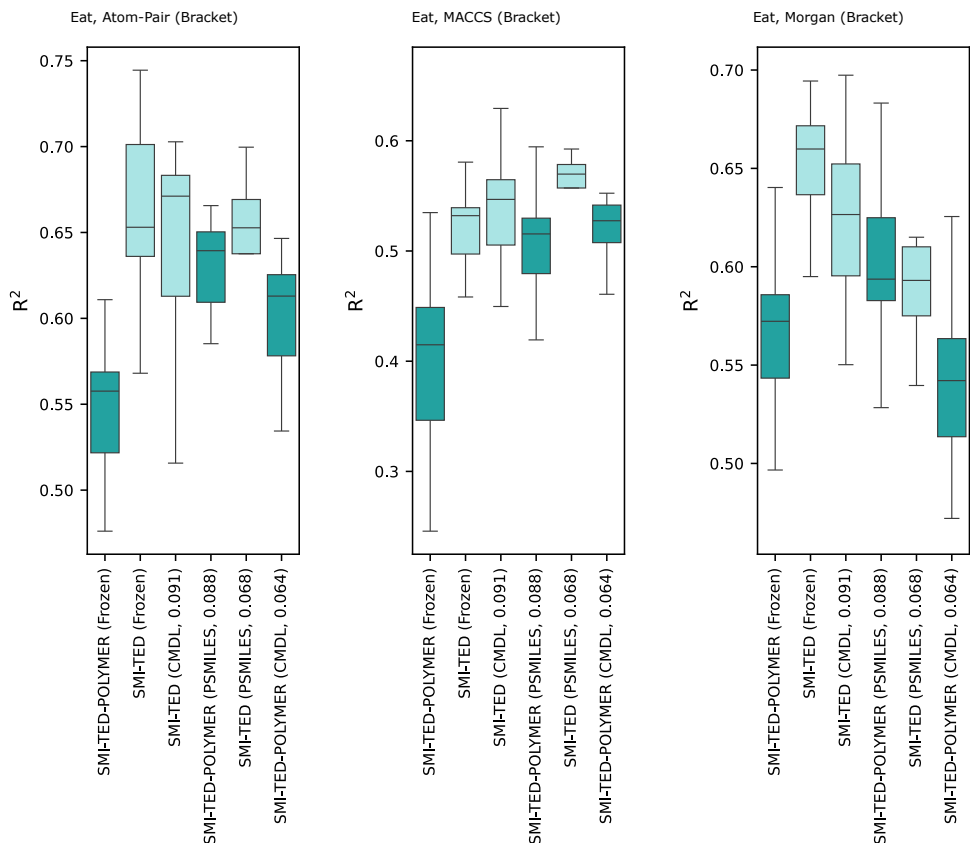


Fig. 24 Plots of fingerprint R^2 value distributions for the Eat benchmark dataset using the *bracket* substitution strategy.

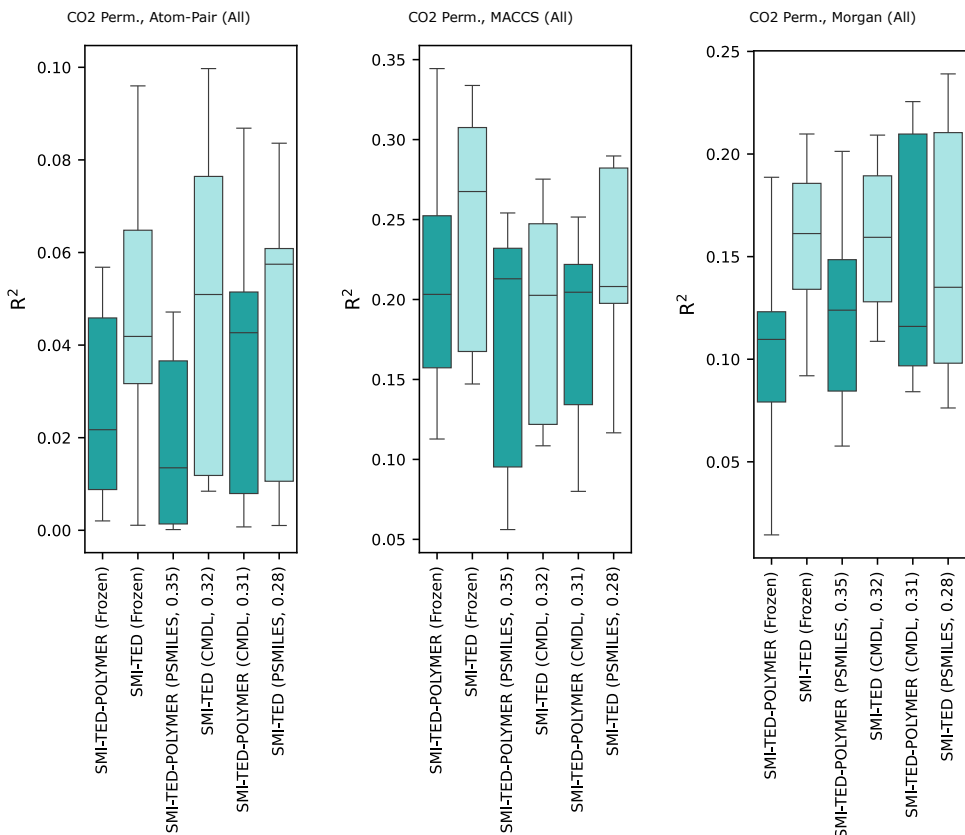


Fig. 25 Plots of fingerprint R^2 value distributions for the CO_2 permeability benchmark dataset using the *all* substitution strategy.

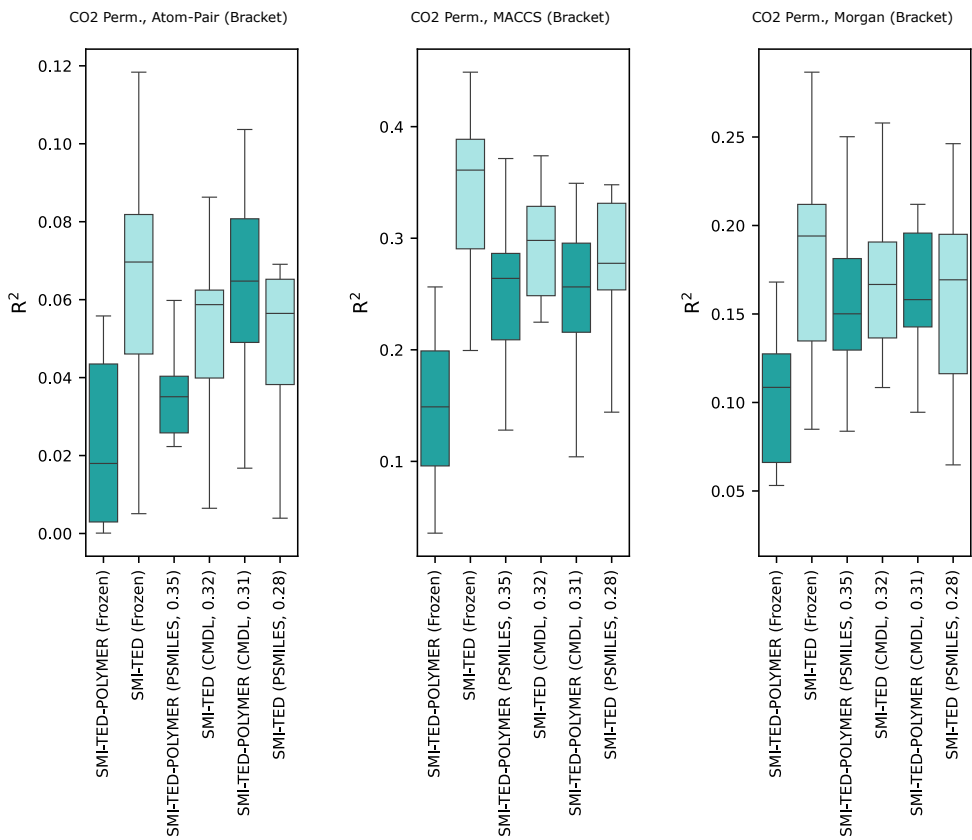


Fig. 26 Plots of fingerprint R^2 value distributions for the CO₂ permeability benchmark dataset using the *bracket* substitution strategy.

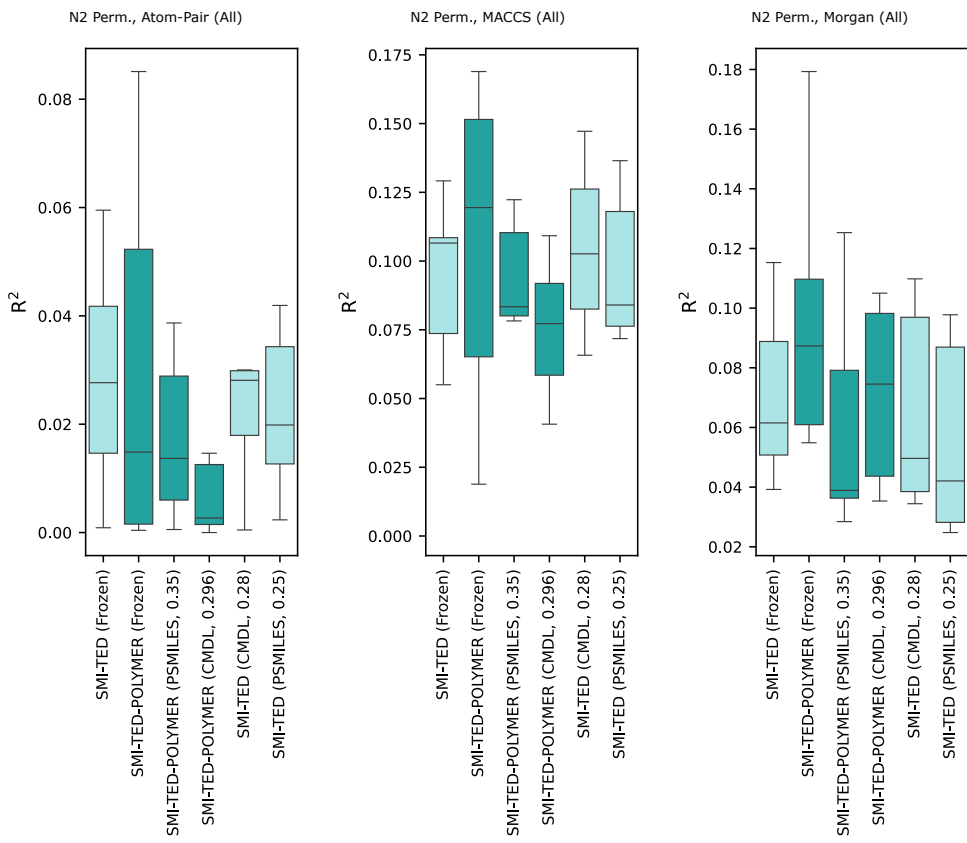


Fig. 27 Plots of fingerprint R^2 value distributions for the N₂ permeability benchmark dataset using the *all* substitution strategy.

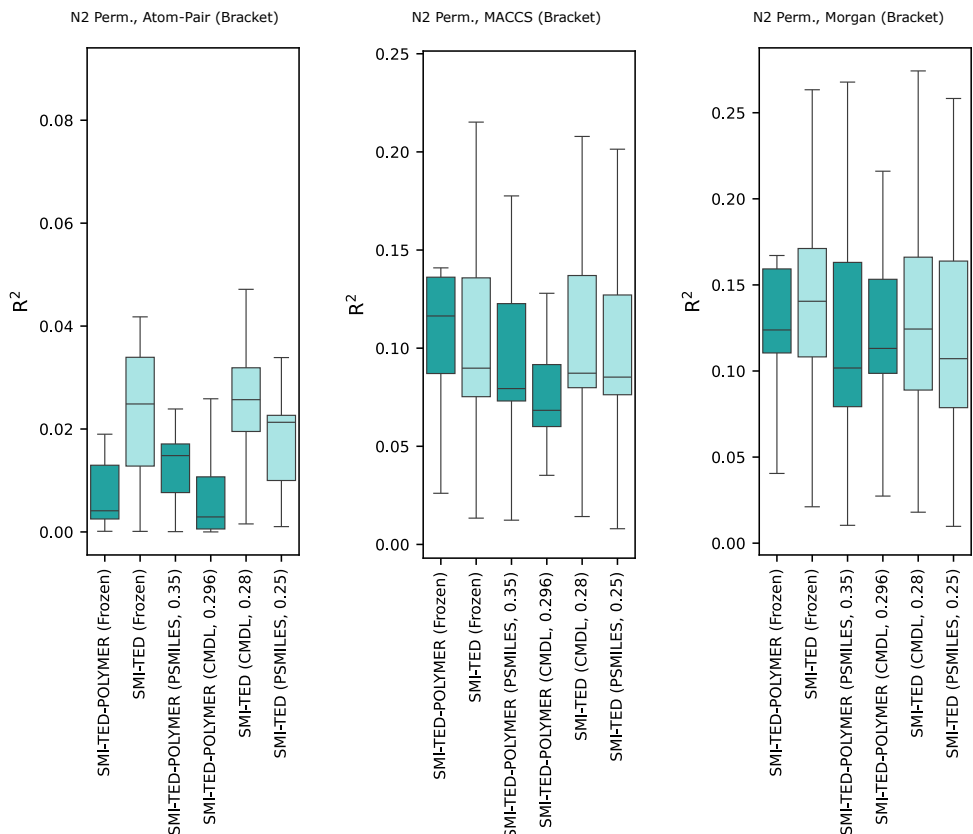


Fig. 28 Plots of fingerprint R^2 value distributions for the N_2 permeability benchmark dataset using the *bracket* substitution strategy.

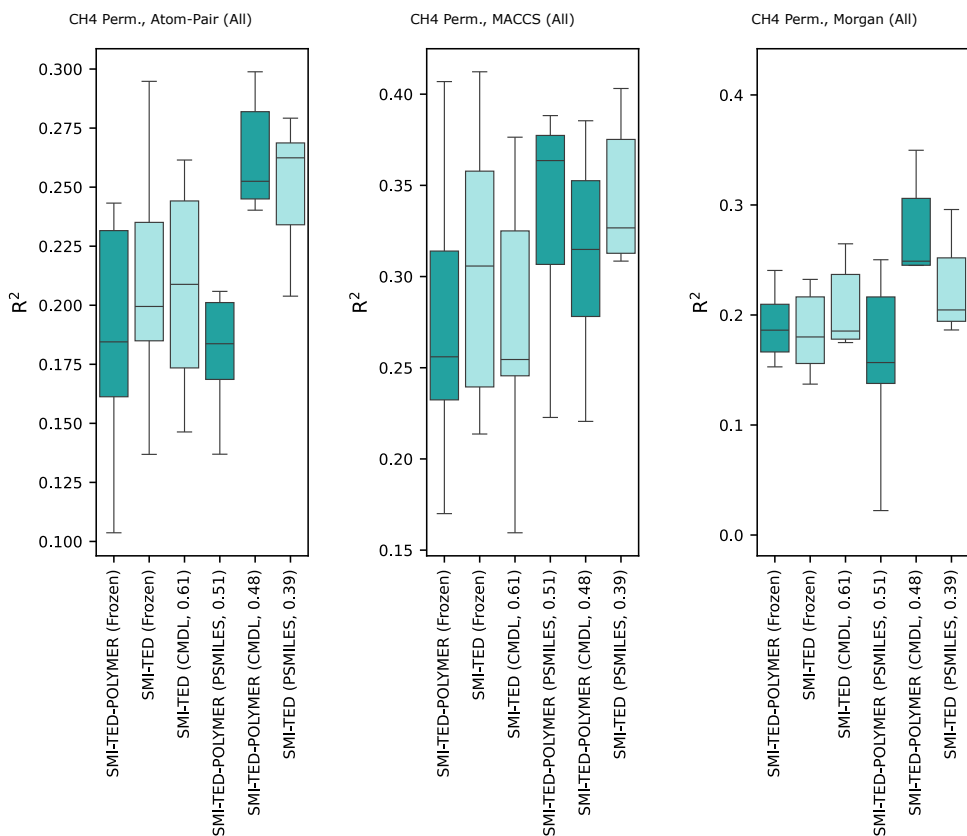


Fig. 29 Plots of fingerprint R^2 value distributions for the CH_4 permeability benchmark dataset using the *all* substitution strategy.

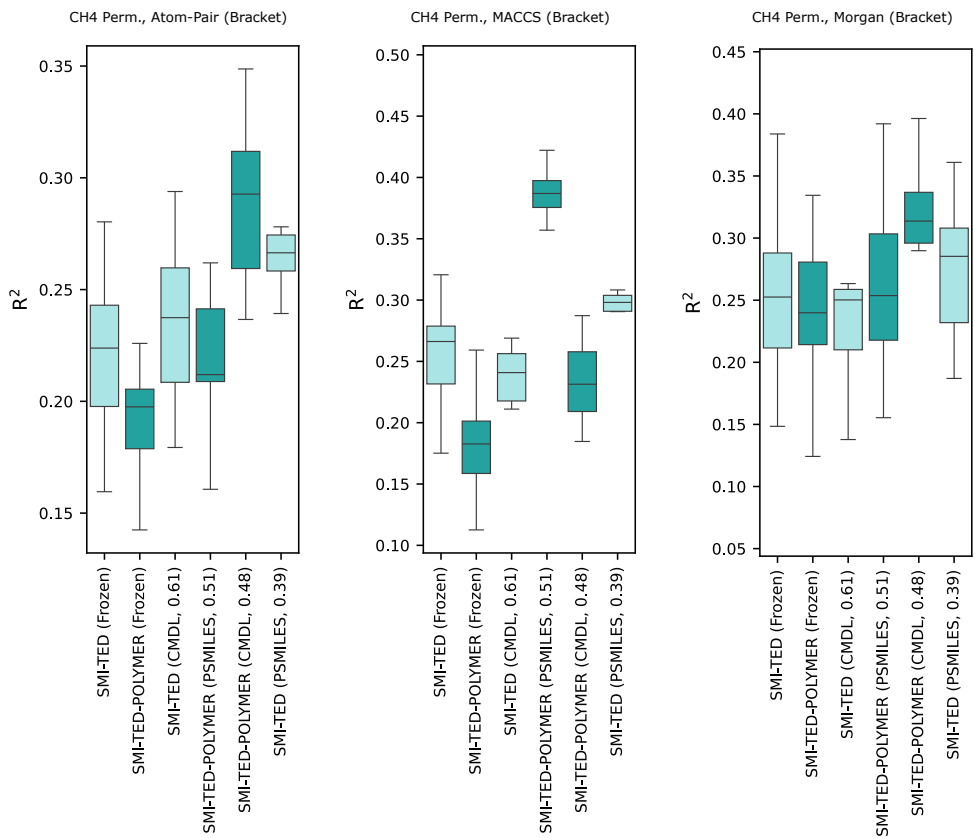


Fig. 30 Plots of fingerprint R^2 value distributions for the CH_4 permeability benchmark dataset using the *bracket* substitution strategy.

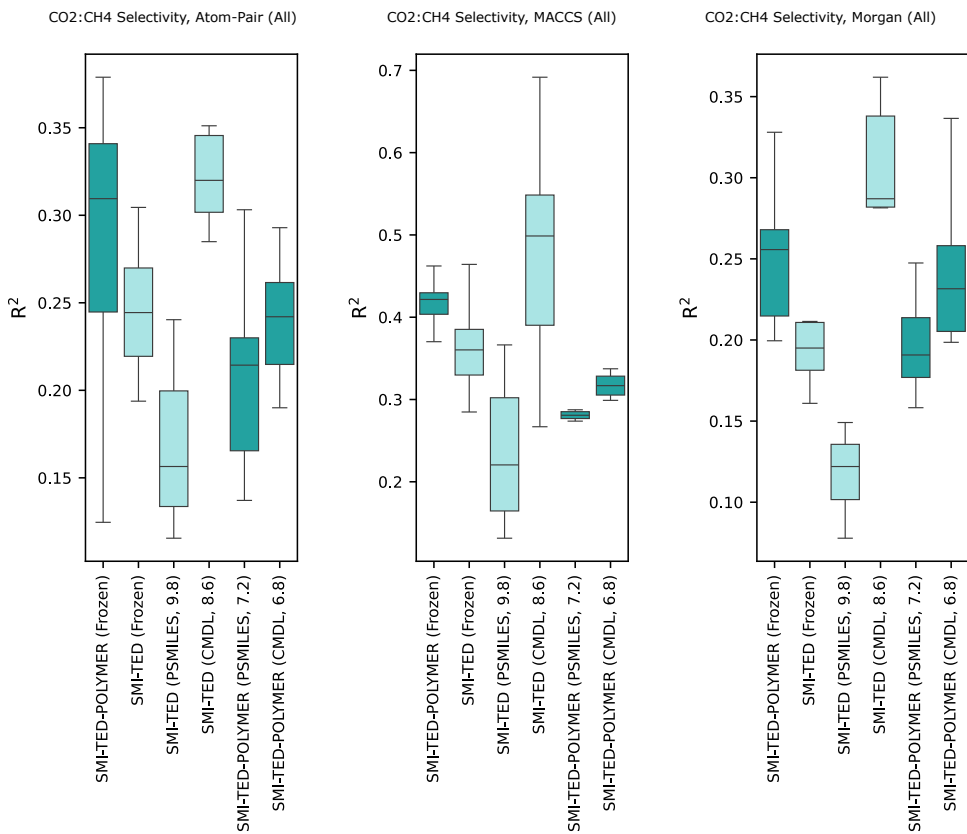


Fig. 31 Plots of fingerprint R^2 value distributions for the CO₂:CH₄ selectivity benchmark dataset using the *all* substitution strategy.

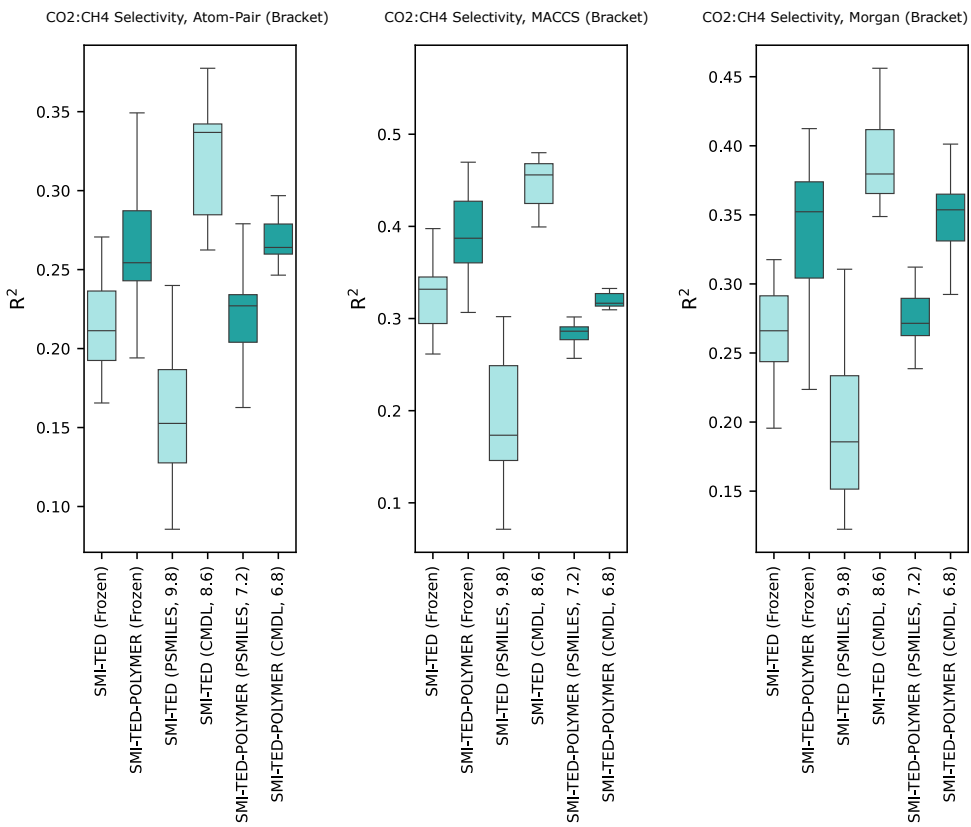


Fig. 32 Plots of fingerprint R^2 value distributions for the CO₂:CH₄ selectivity benchmark dataset using the *bracket* substitution strategy.

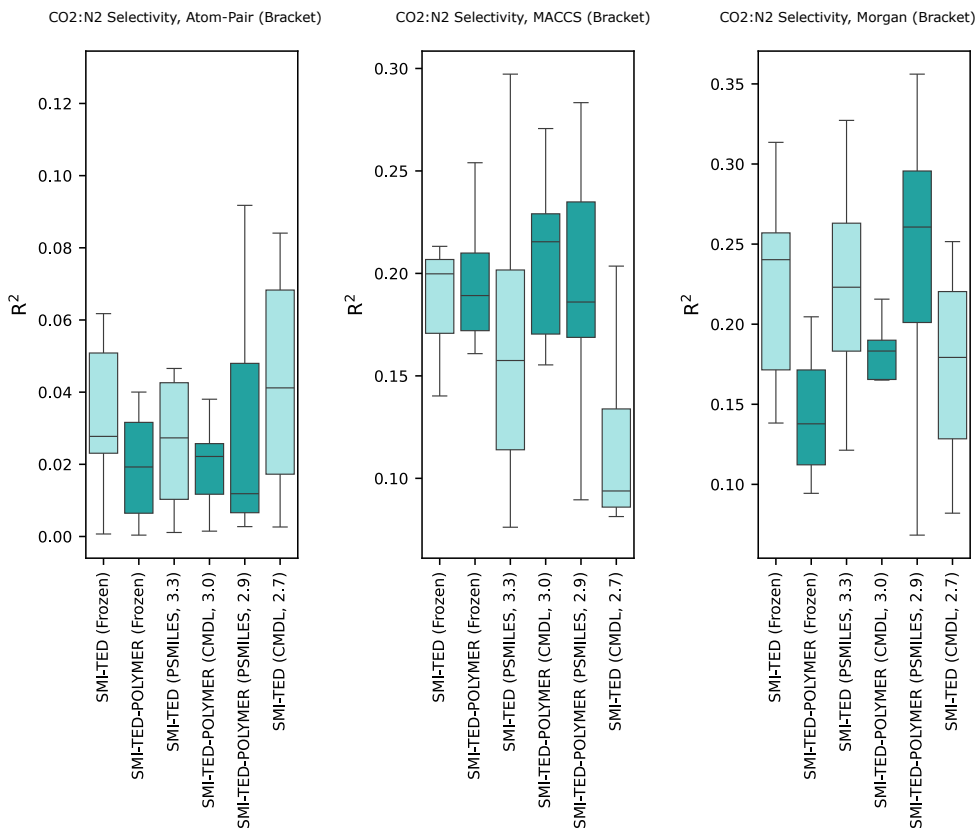


Fig. 33 Plots of fingerprint R^2 value distributions for the CO₂:N₂ selectivity benchmark dataset using the *all* substitution strategy.

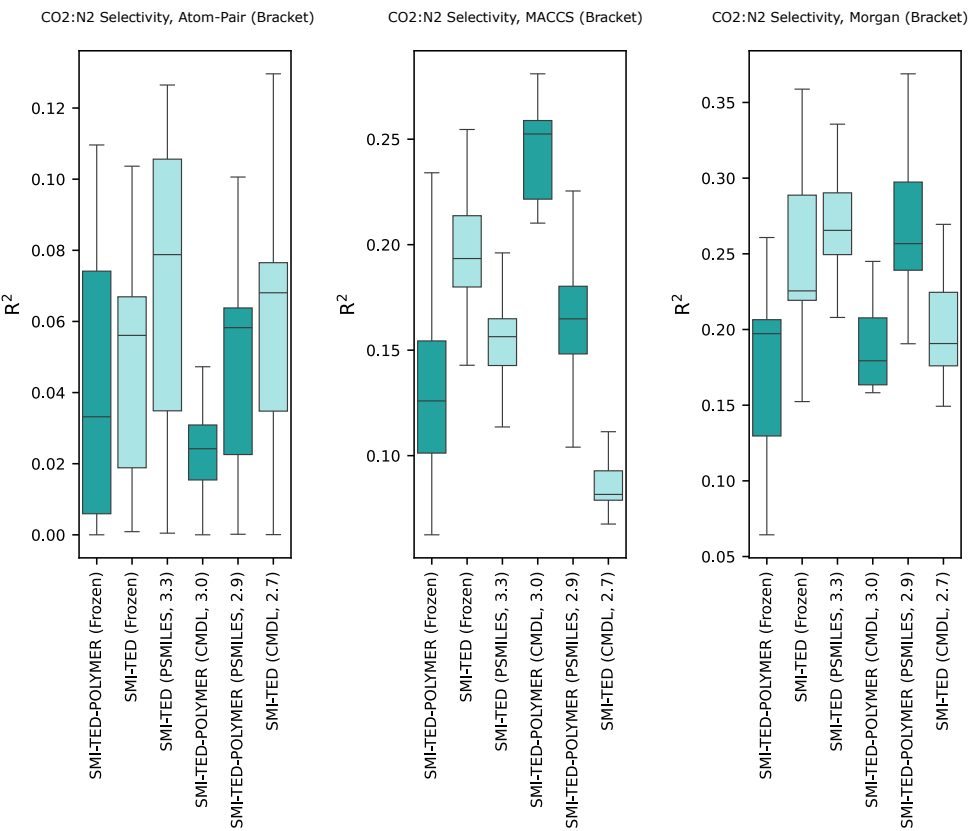


Fig. 34 Plots of fingerprint R^2 value distributions for the $\text{CO}_2:\text{N}_2$ selectivity benchmark dataset using the *bracket* substitution strategy.

2.4 Attention Figures

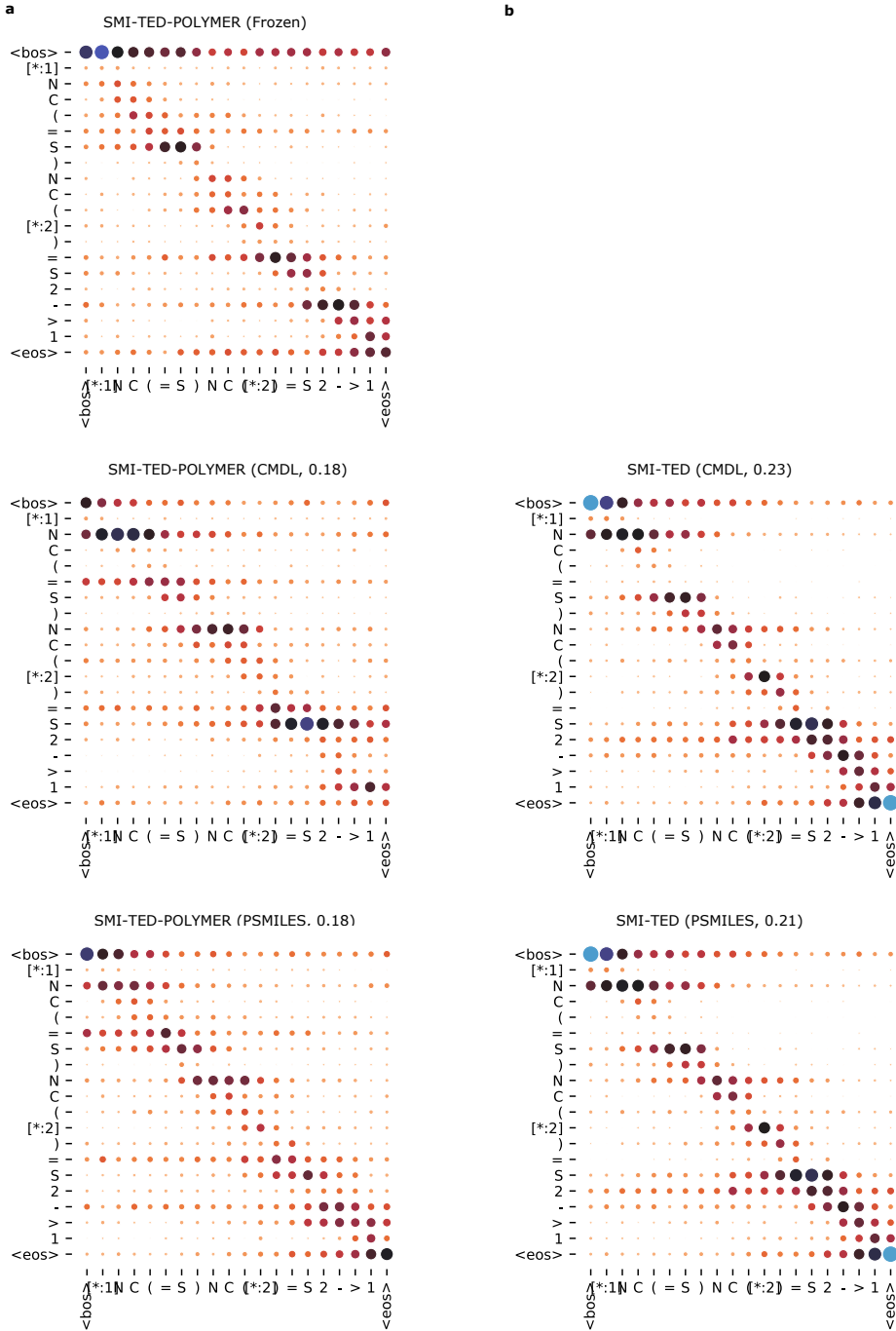


Fig. 35 Attention maps of CPG representations from the Eea dataset.

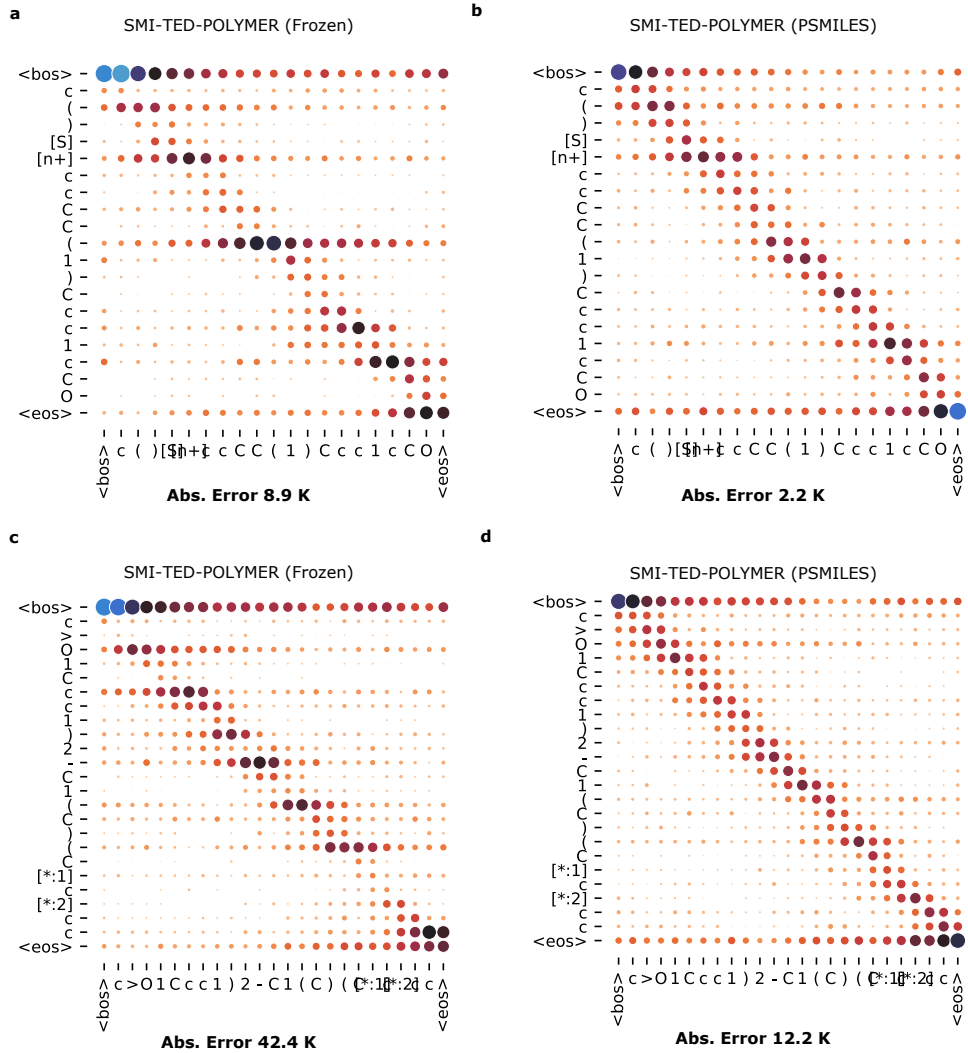


Fig. 36 Comparison of average attention probabilities for random representations

2.5 Historical Performance Comparisons

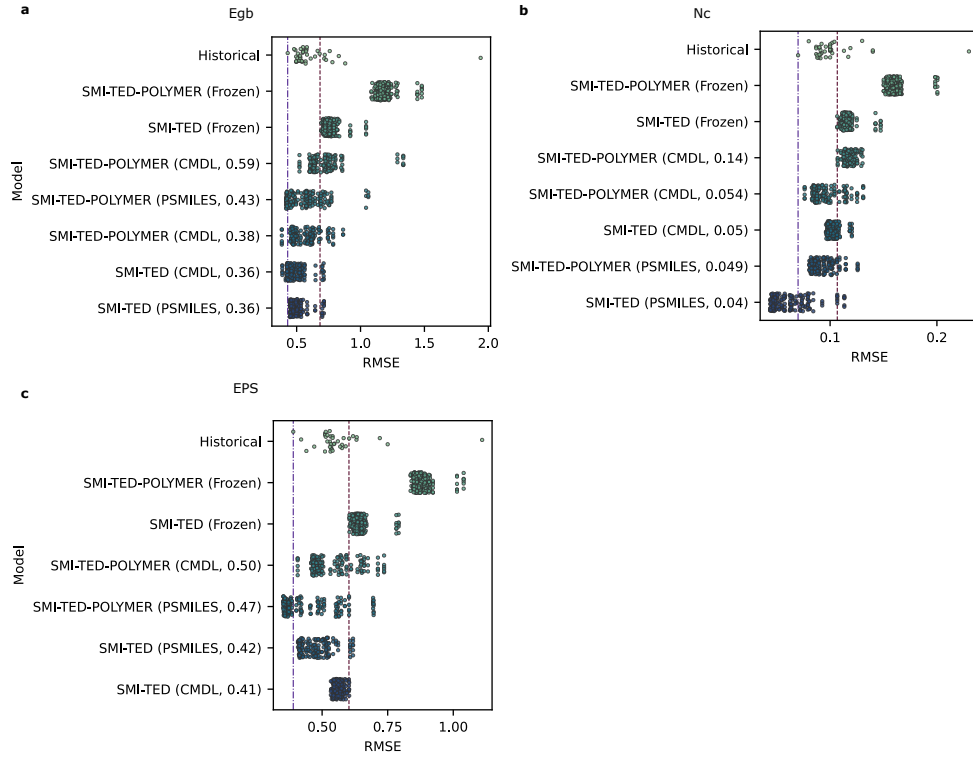


Fig. 37 Comparison of performance of SMI-TED models with reported historical values.

2.6 Representation Evaluation Results

CV Score Box Plot Notes

As noted above not all atom substitutions resulted in valid SMILES strings which cannot be canonicalized. Likewise, not all atom-substitution strategies were used for each replacement atom token (see Supplementary Info 1.1). Hence, no results are plotted in these instances. Special cases, such as the CPG representation, random token (RT), randomly shuffled CPG (RC), or randomly shuffled with random replacement token (RF) are included in all plots for reference. All box plots are plotted as facets of their respective substitution strategy (*all* or *bracket*) and whether or not the newly substituted representations were re-canonicalized (*True* or *False*).

Random Split Point Plot Notes

The point plots show the performance results of evaluation of the random 80:10:10 *train*, *valid*, and *test* splits of the benchmark dataset for each representation and substitution strategy using the hyperparameter optimized XGBoost model. As with the *CV Score Box Plots*, the point plots are plotted as facets, splitting the data by substitution strategy (*all* or *bracket*) and re-canonicalization (*True* or *False*). In all point plots the *train*, *valid*, and *test* results are indicated with blue diamond, black circle, and red square markers, respectively.

2.6.1 Polymer Chain Bandgap (E_{gc}) CV Scores

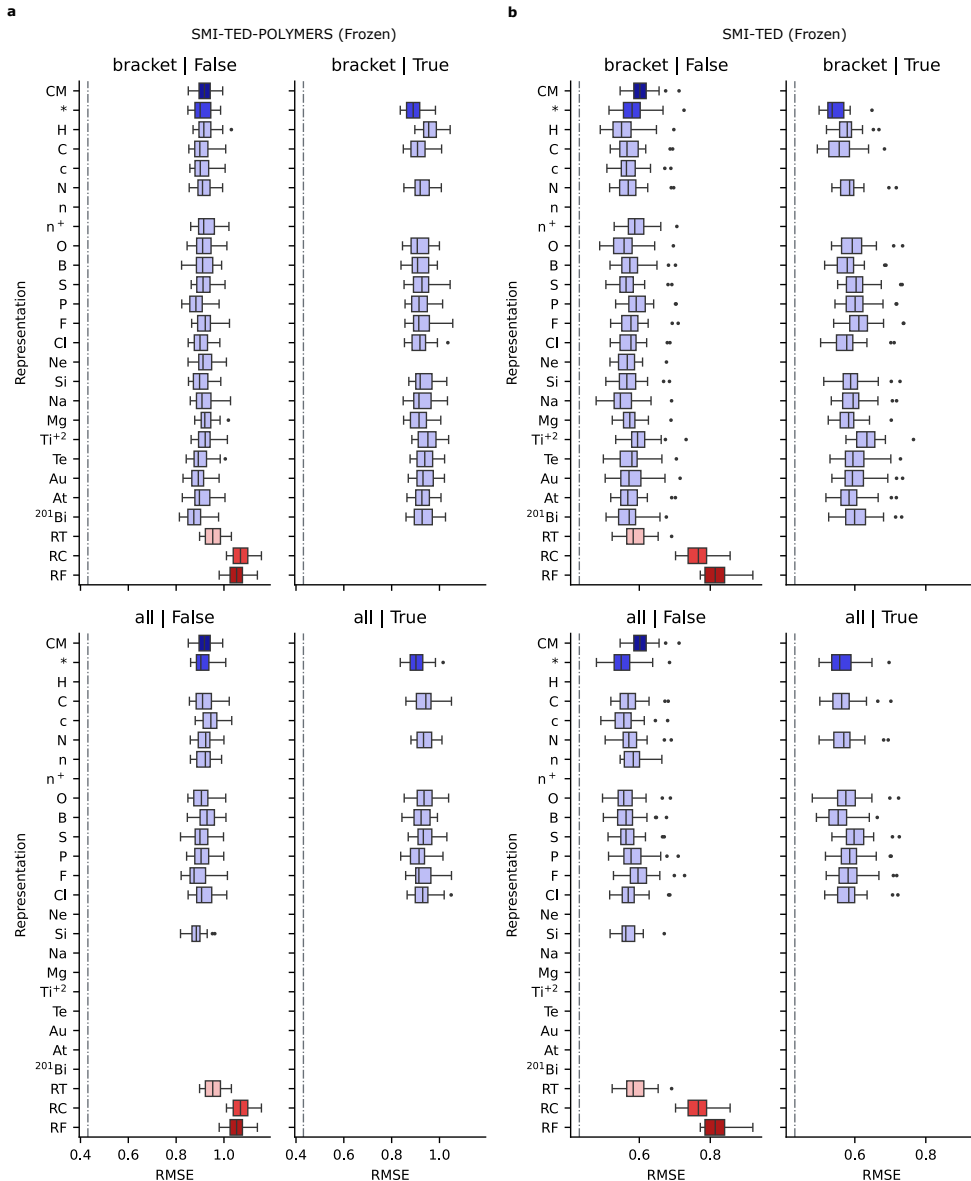


Fig. 38 Box plots for E_{gc} repeated cross-validation experiments for SMI-TED-POLYMER **(a)** and SMI-TED **(b)** models with frozen weights.

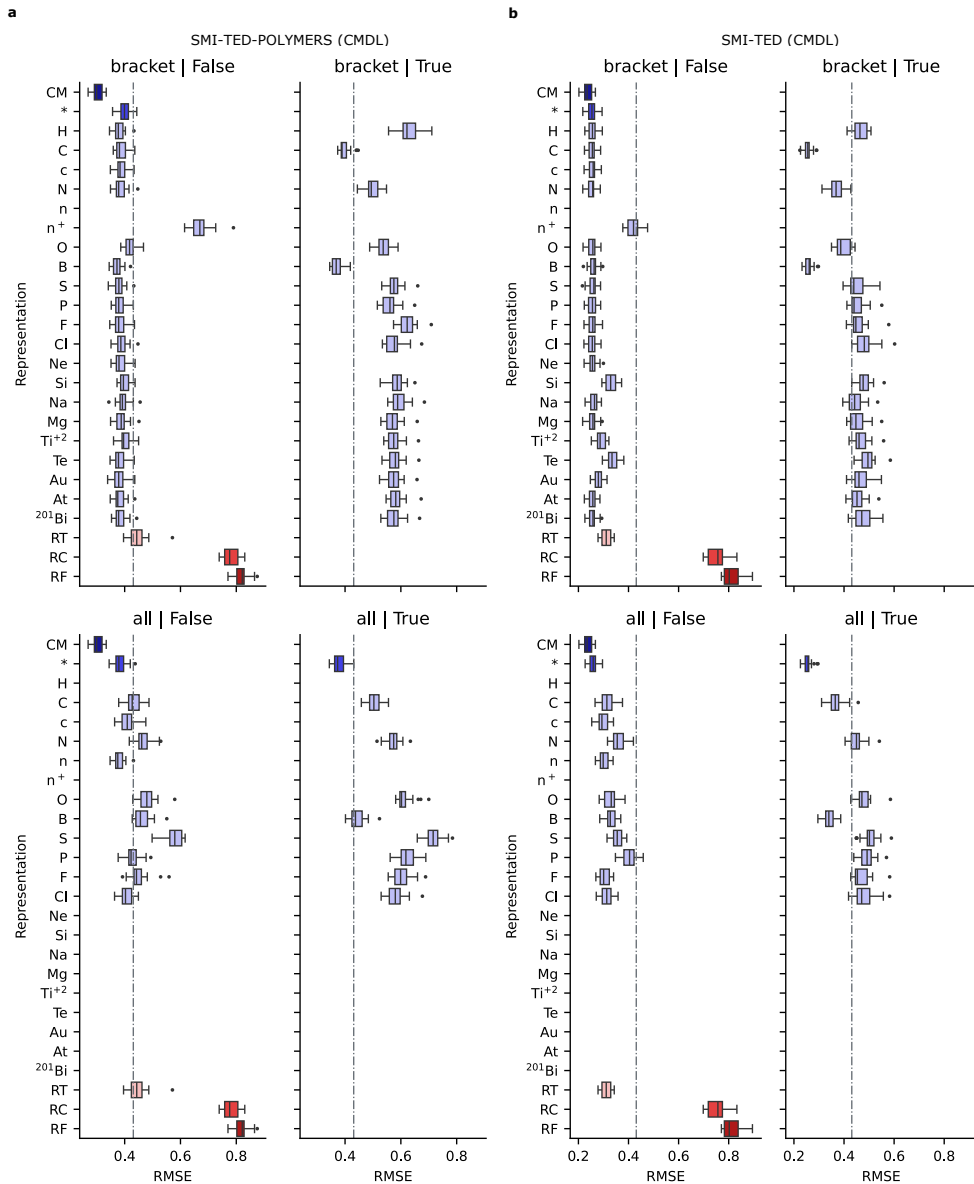


Fig. 39 Box plots for E_{gc} repeated cross-validation experiments for SMI-TED-POLYMER (a) and SMI-TED (b) models fine-tuned with the CPG polymer graphs.

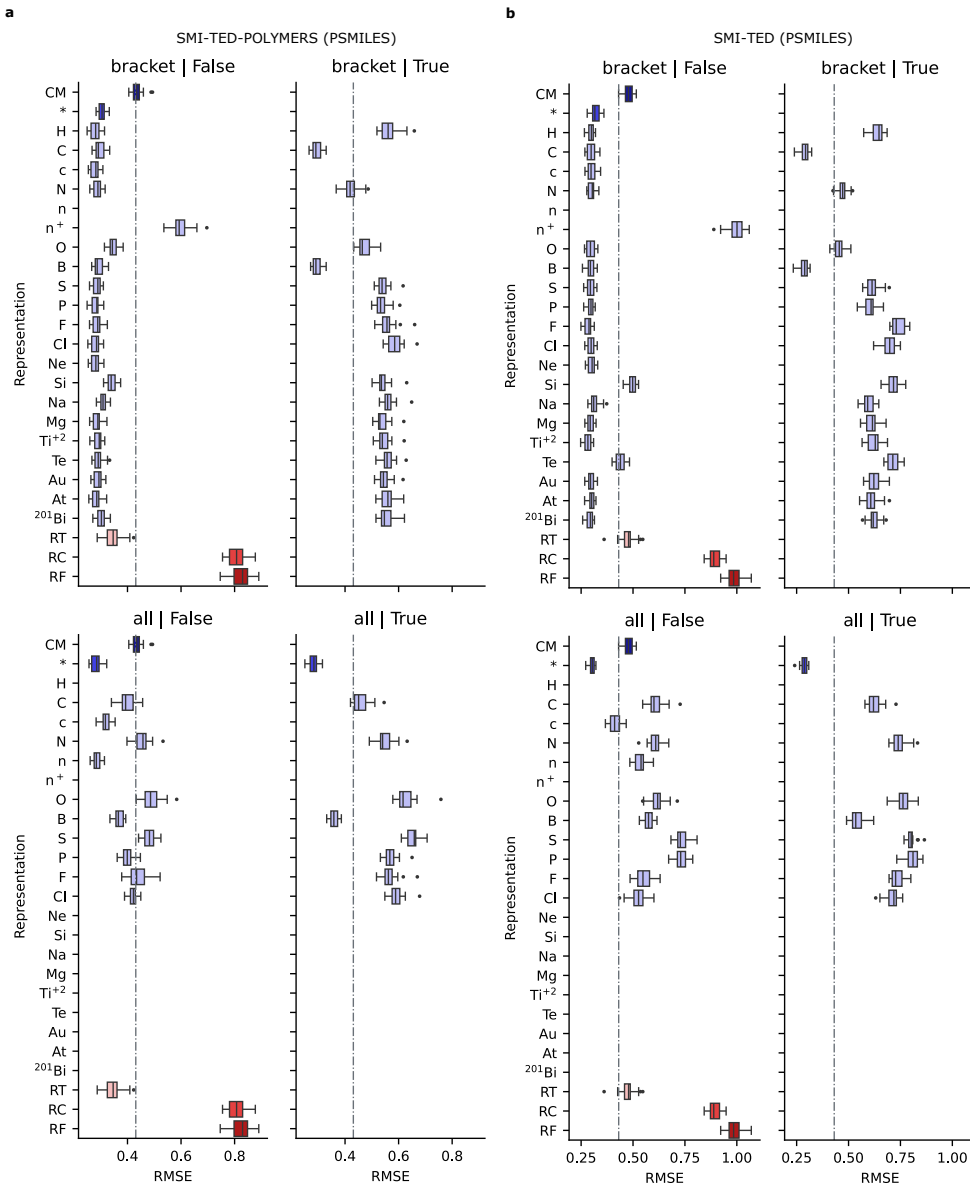


Fig. 40 Box plots for E_{gc} repeated cross-validation experiments for SMI-TED-POLYMER **(a)** and SMI-TED **(b)** models fine-tuned with PSMILES.

2.6.2 Polymer Chain Bandgap (E_{gc}) Random Split Scores

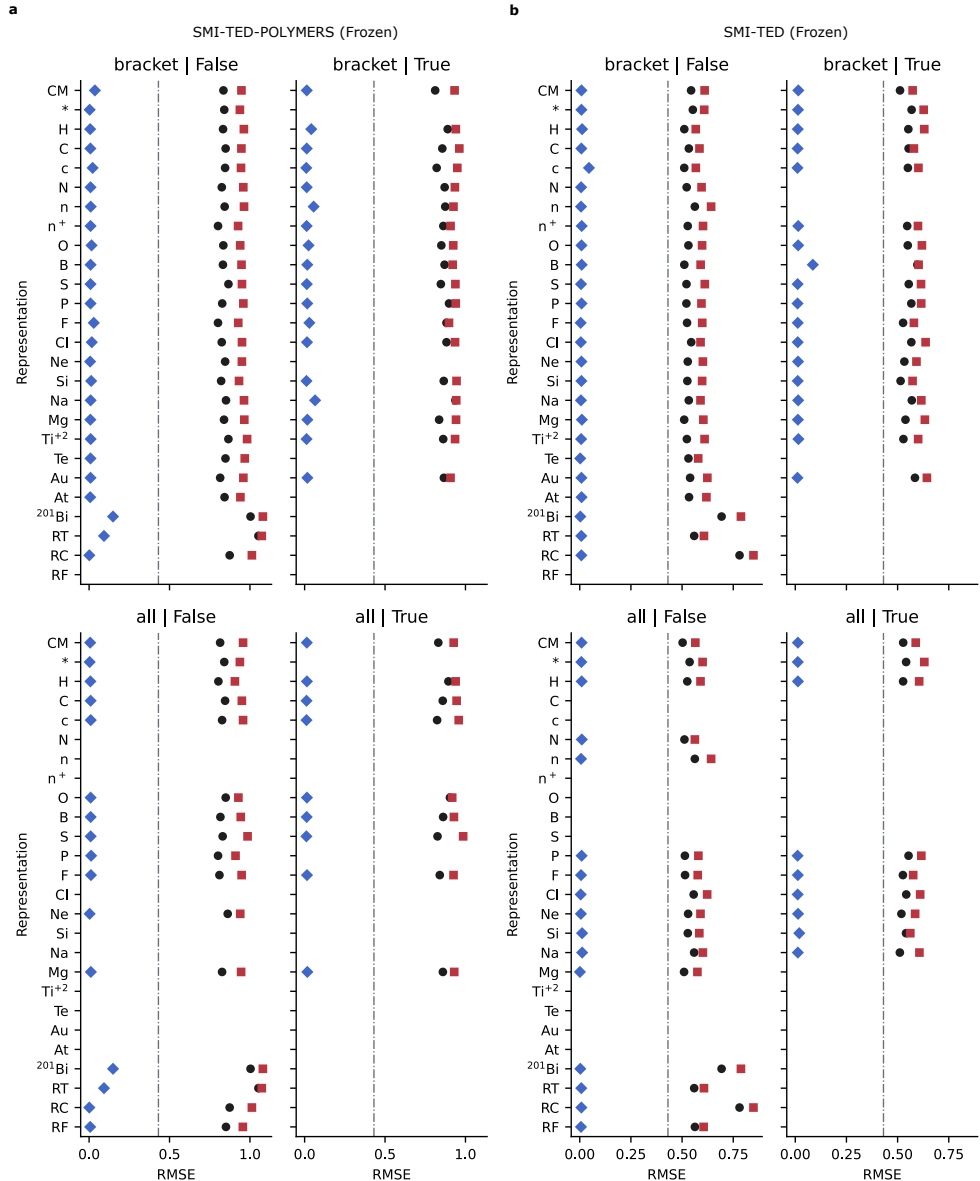


Fig. 41 Point plots for E_{gc} benchmark experiments of RMSE using the base random train, valid, and test splits for SMI-TED-POLYMER (a) and SMI-TED (b) models with frozen weights.

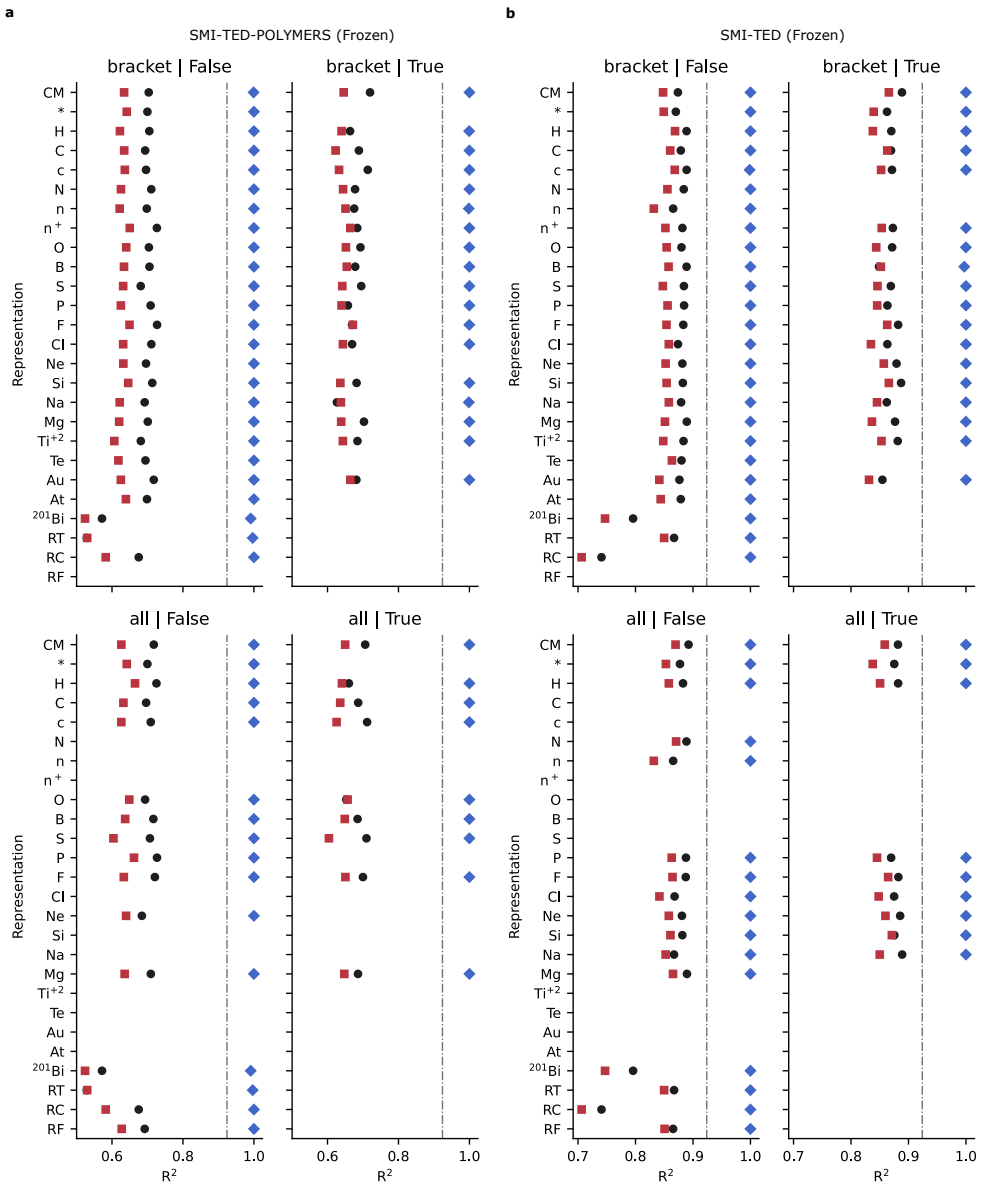


Fig. 42 Point plots for E_{gc} benchmark experiments of R^2 using the base random train, valid, and test splits for SMI-TED-POLYMER **(a)** and SMI-TED **(b)** models with frozen weights.

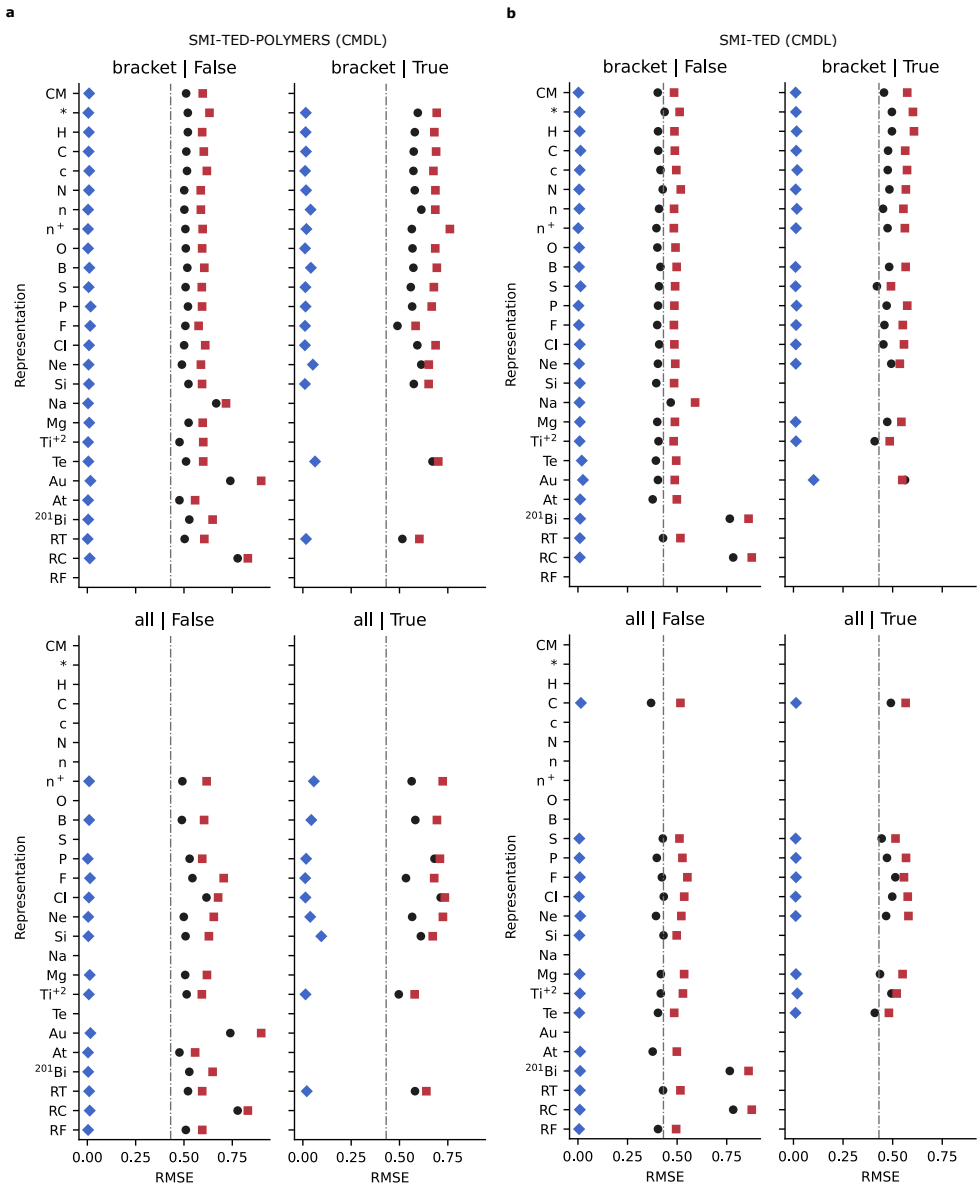


Fig. 43 Point plots for E_{gc} benchmark experiments of RMSE using the base random train, valid, and test splits for SMI-TED-POLYMER (a) and SMI-TED (b) models fine-tuned using the CPG representation.

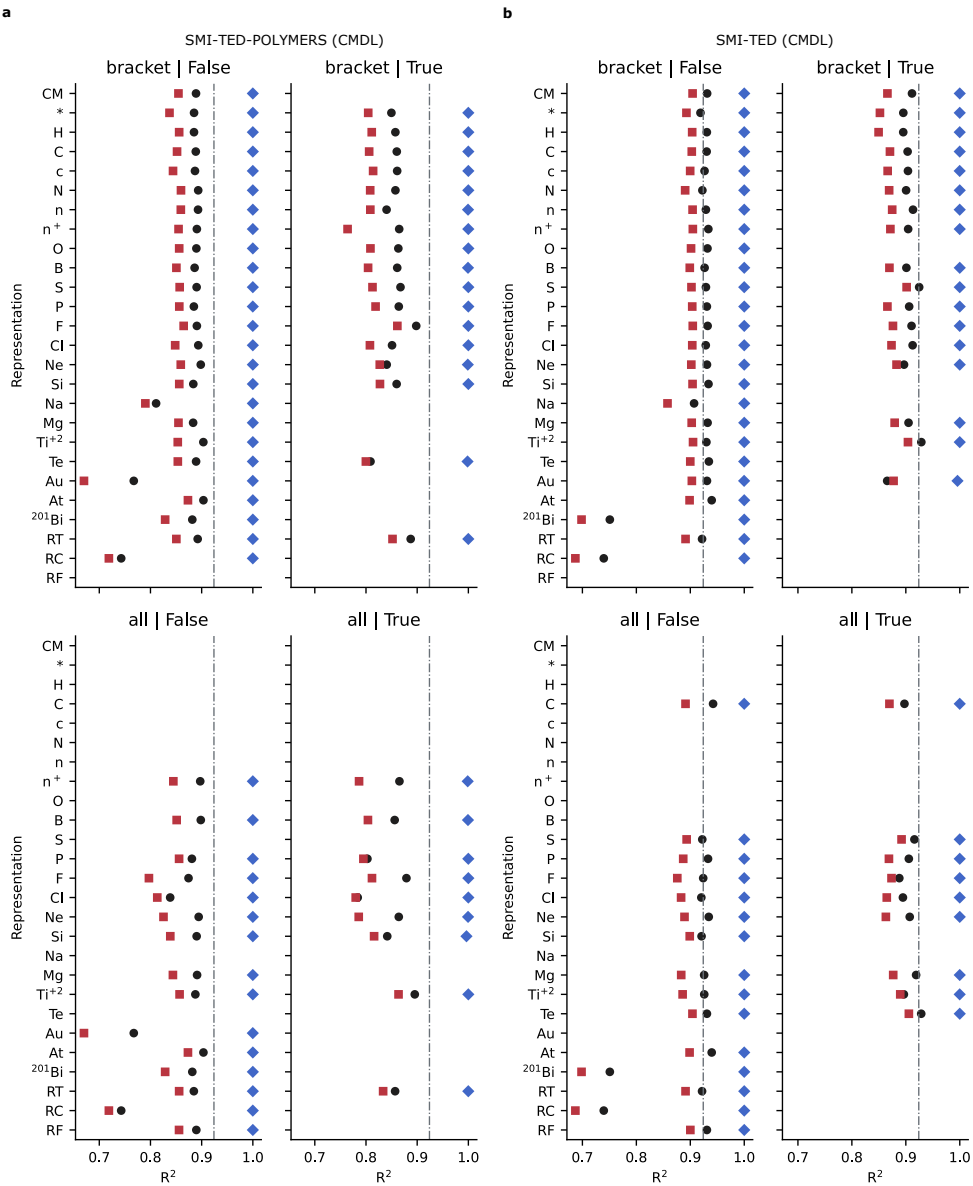


Fig. 44 Point plots for E_{gc} benchmark experiments of R^2 using the base random train, valid, and test splits for SMI-TED-POLYMER (a) and SMI-TED (b) models fine-tuned using the CPG representation.

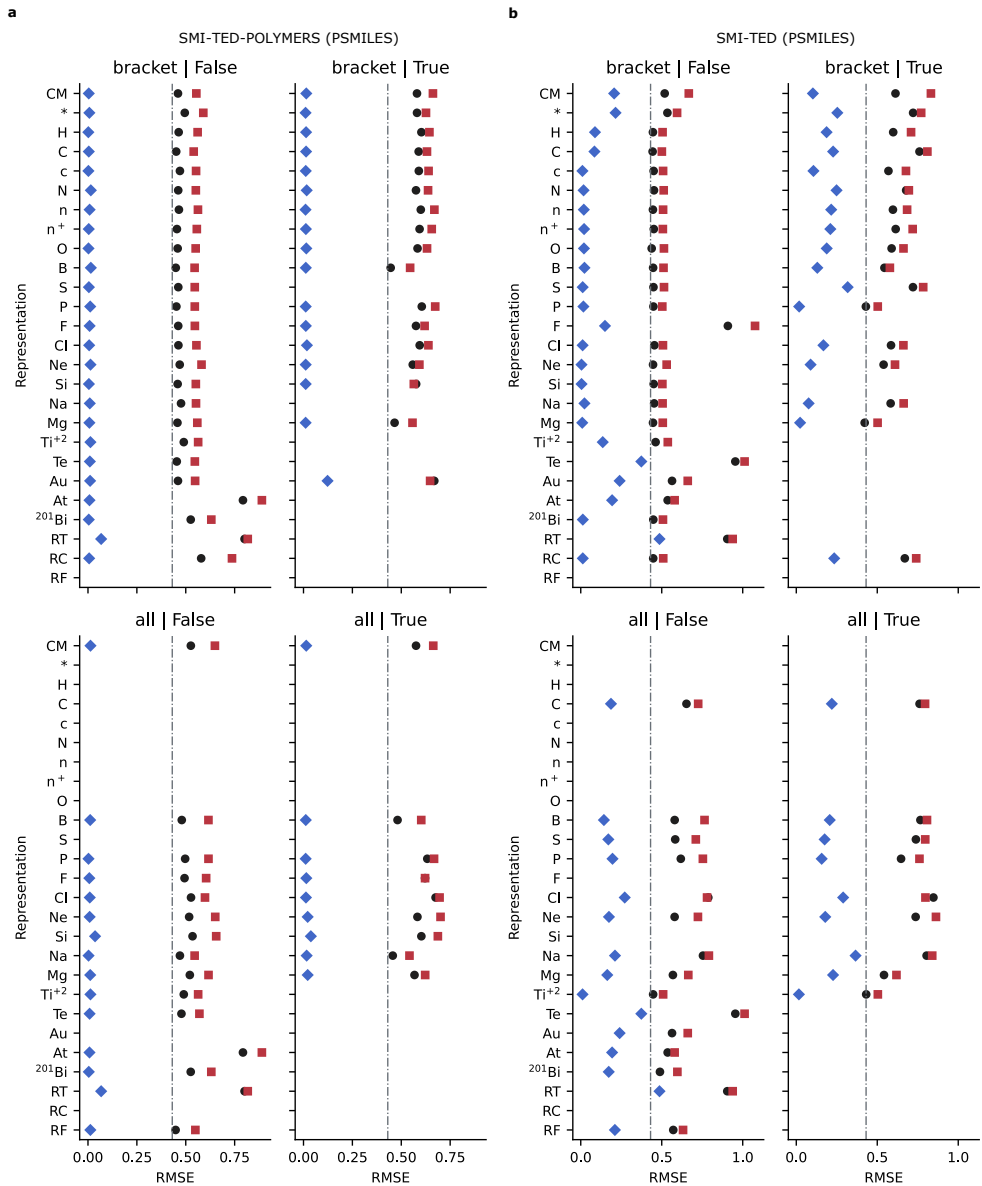


Fig. 45 Point plots for E_{gc} benchmark experiments of RMSE using the base random train, valid, and test splits for SMI-TED-POLYMERS (a) and SMI-TED (b) models fine-tuned using PSMILES.

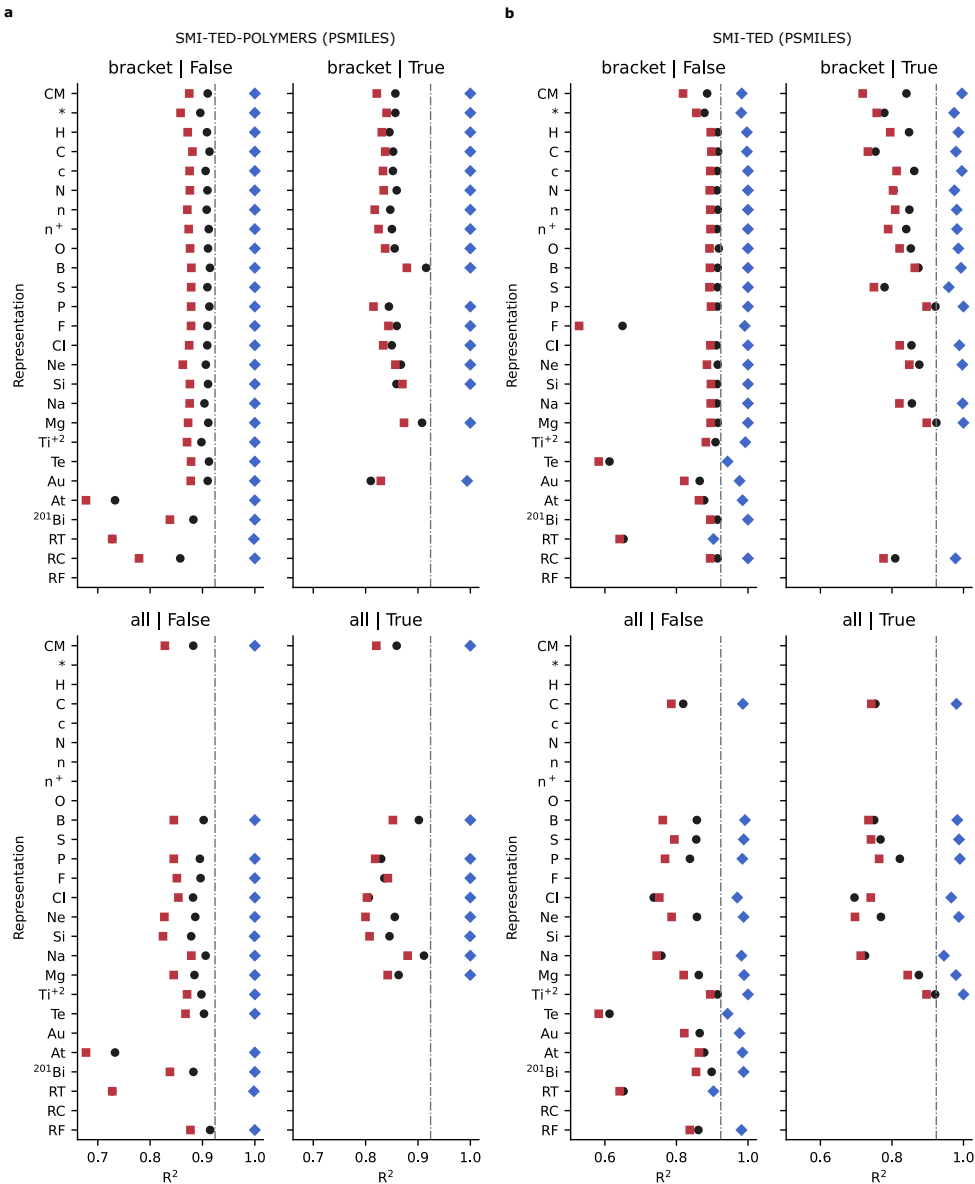


Fig. 46 Point plots for E_{gc} benchmark experiments of R^2 using the base random train, valid, and test splits for SMI-TED-POLYMERS (a) and SMI-TED (b) models fine-tuned using PSMILES.

2.6.3 Polymer Bulk Bandgap (E_{gb}) CV Scores

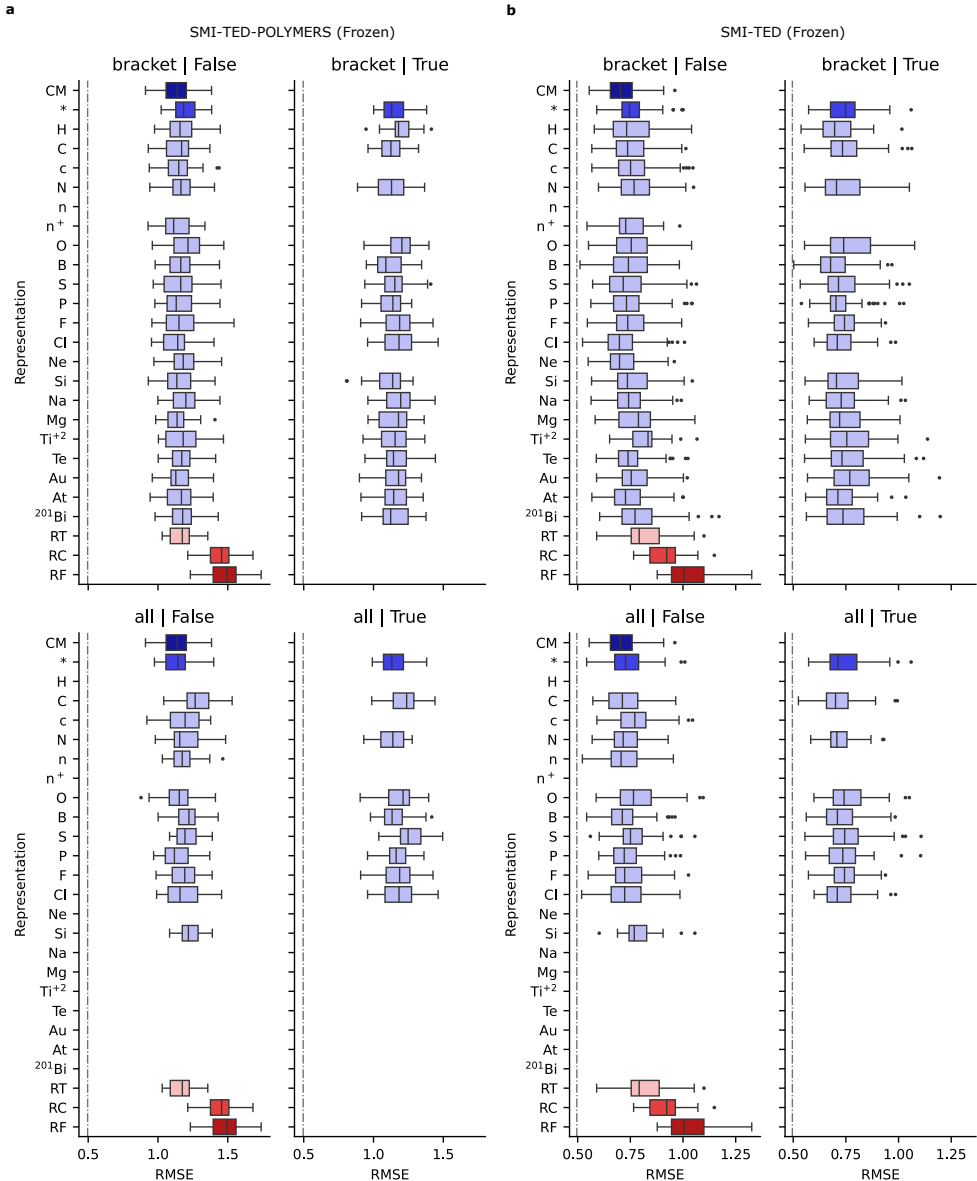


Fig. 47 Box plots for E_{gb} repeated cross-validation experiments for SMI-TED-POLYMER (a) and SMI-TED (b) models with frozen weights.

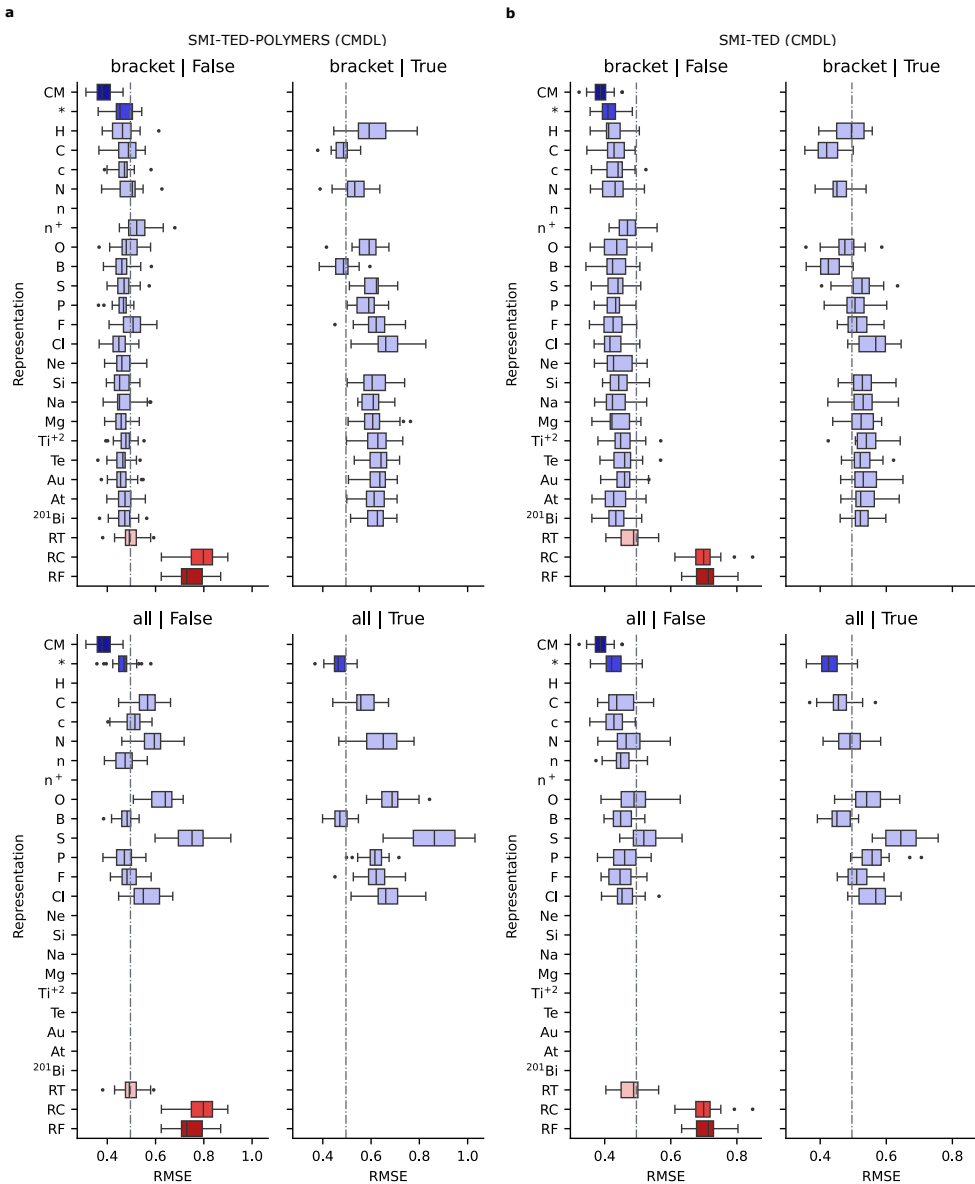


Fig. 48 Box plots for E_{gb} repeated cross-validation experiments for SMI-TED-POLYMER **(a)** and SMI-TED **(b)** models fine-tuned with the CPG polymer graphs.

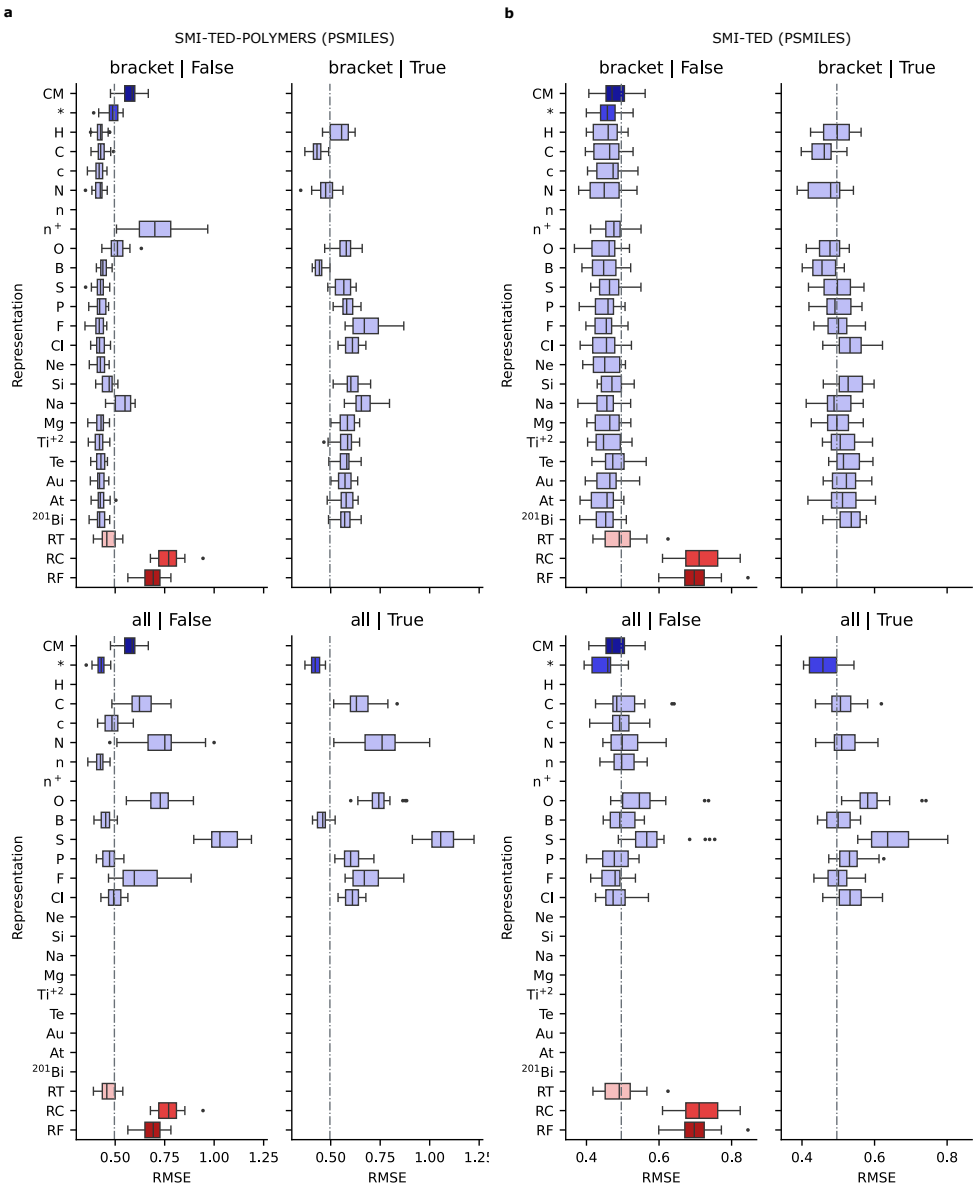


Fig. 49 Box plots for E_{gb} repeated cross-validation experiments for SMI-TED-POLYMER (a) and SMI-TED (b) models fine-tuned with PSMILES.

2.6.4 Polymer Bulk Bandgap (E_{gb}) Random Split Scores

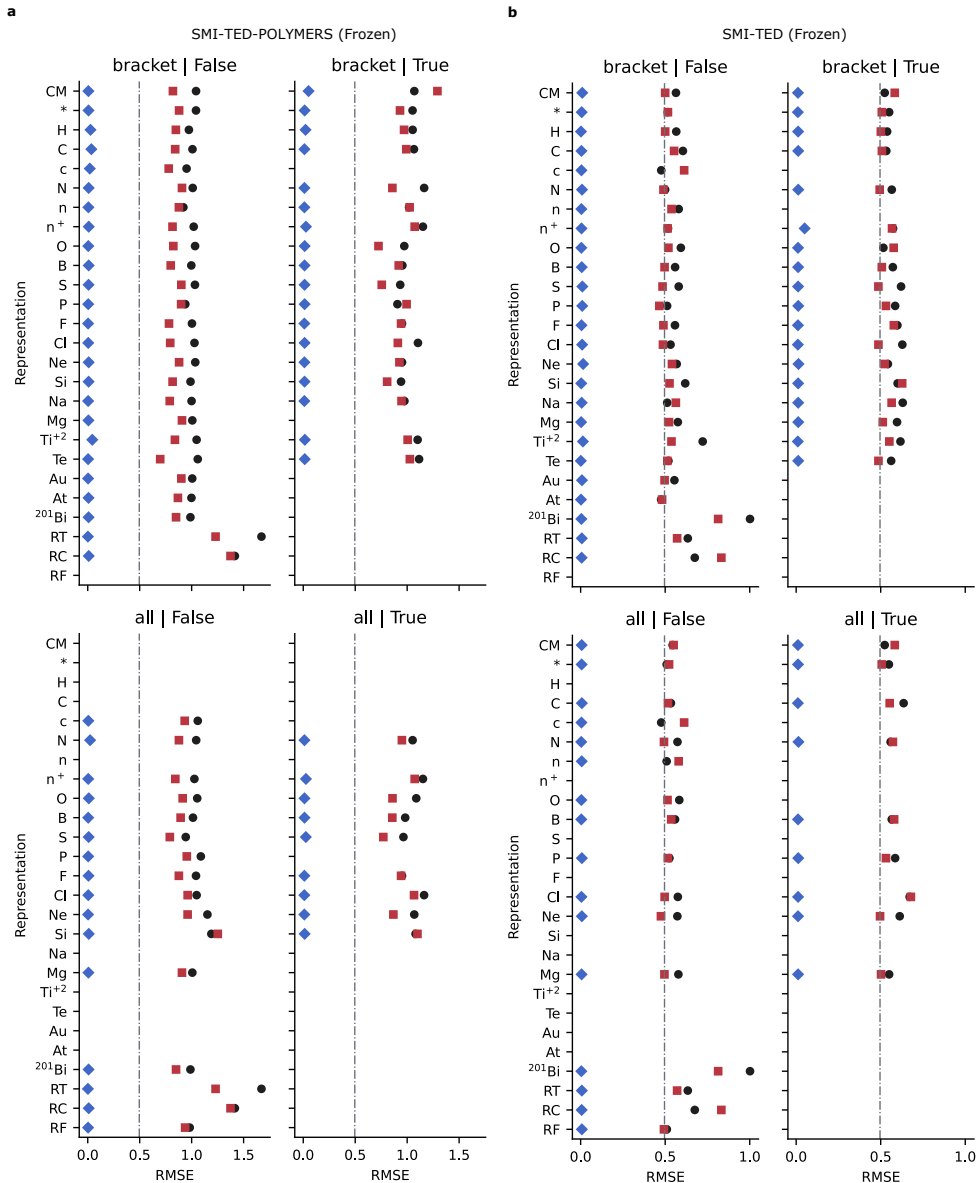


Fig. 50 Point plots for E_{gb} benchmark experiments of RMSE using the base random train, valid, and test splits for SMI-TED-POLYMER (a) and SMI-TED (b) models with frozen weights.

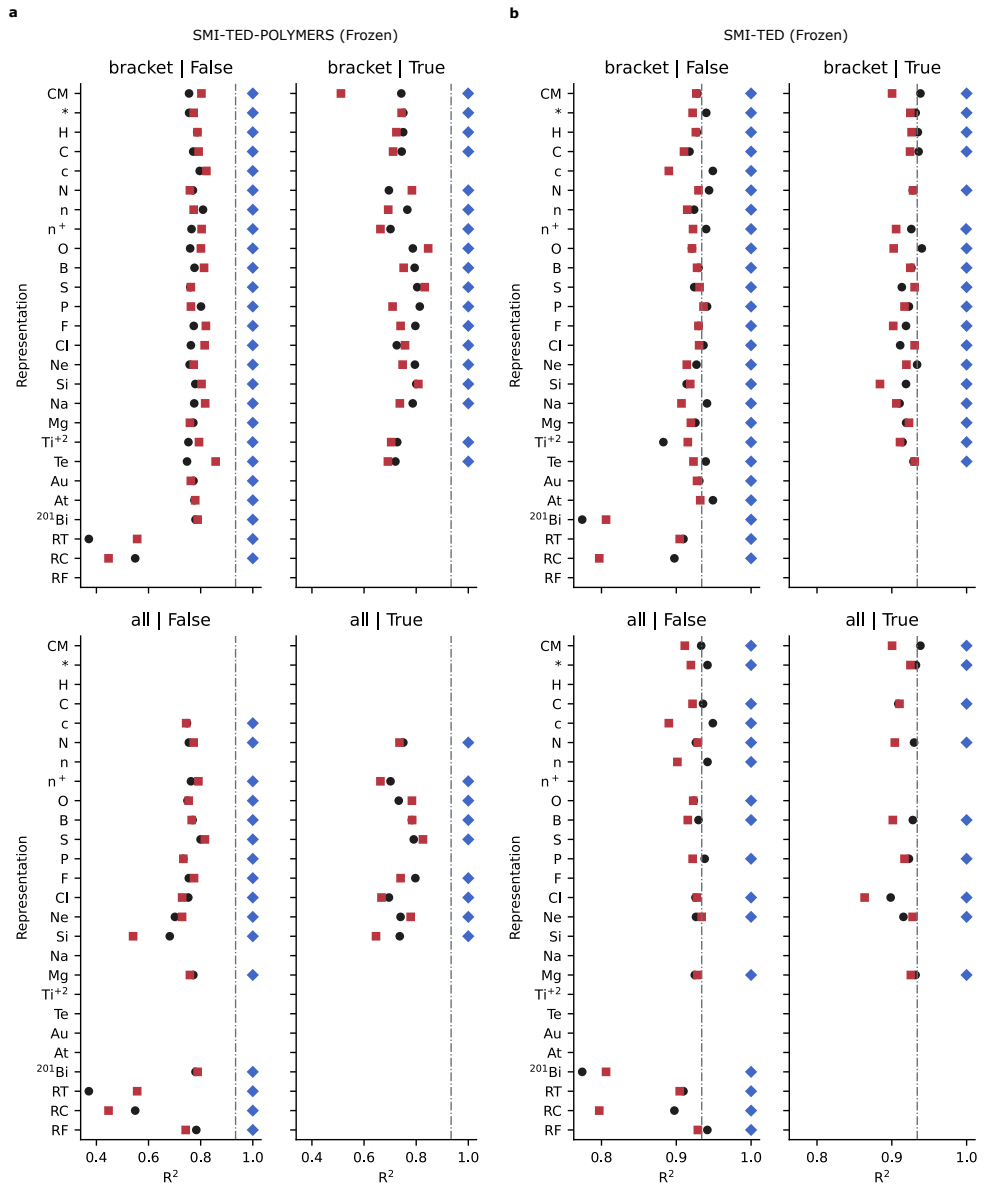


Fig. 51 Point plots for E_{gb} benchmark experiments of R^2 using the base random train, valid, and test splits for SMI-TED-POLYMER (a) and SMI-TED (b) models with frozen weights.

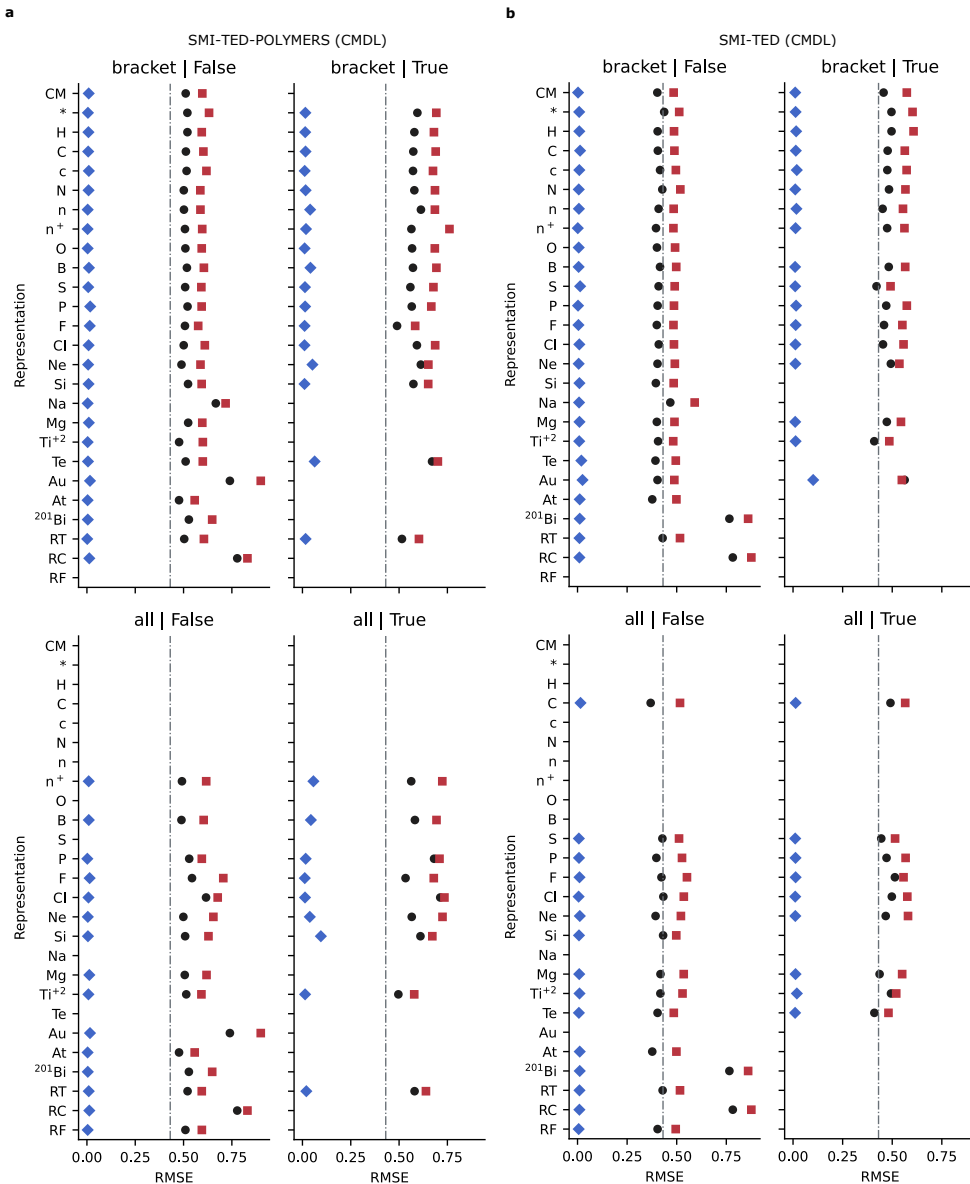


Fig. 52 Point plots for E_{gb} benchmark experiments of RMSE using the base random train, valid, and test splits for SMI-TED-POLYMER (a) and SMI-TED (b) models fine-tuned using the CPG representation.

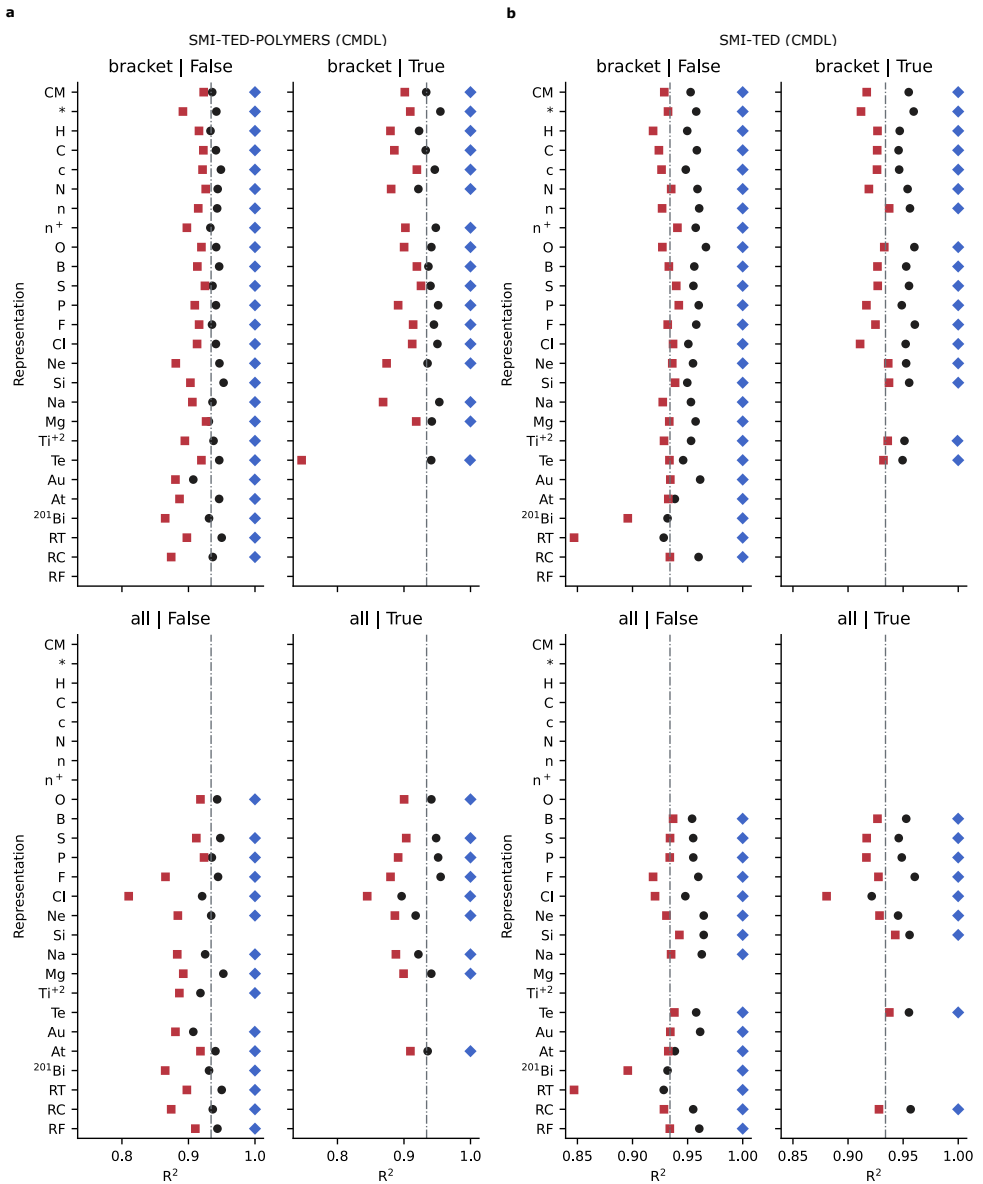


Fig. 53 Point plots for E_{gb} benchmark experiments of R^2 using the base random train, valid, and test splits for SMI-TED-POLYMER (a) and SMI-TED (b) models fine-tuned using the CPG representation.

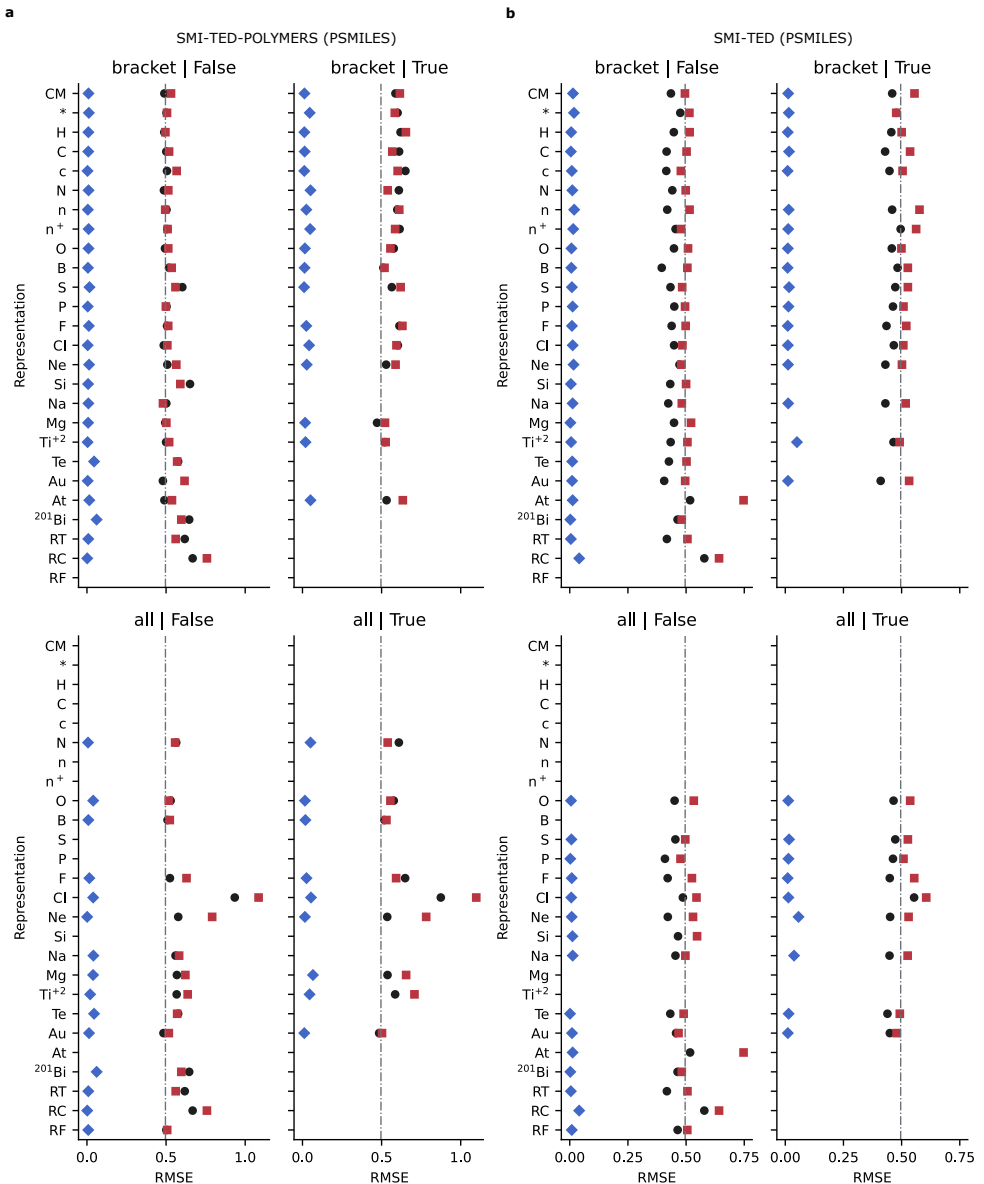


Fig. 54 Point plots for E_{gb} benchmark experiments of RMSE using the base random train, valid, and test splits for SMI-TED-POLYMER (a) and SMI-TED (b) models fine-tuned using PSMILES.

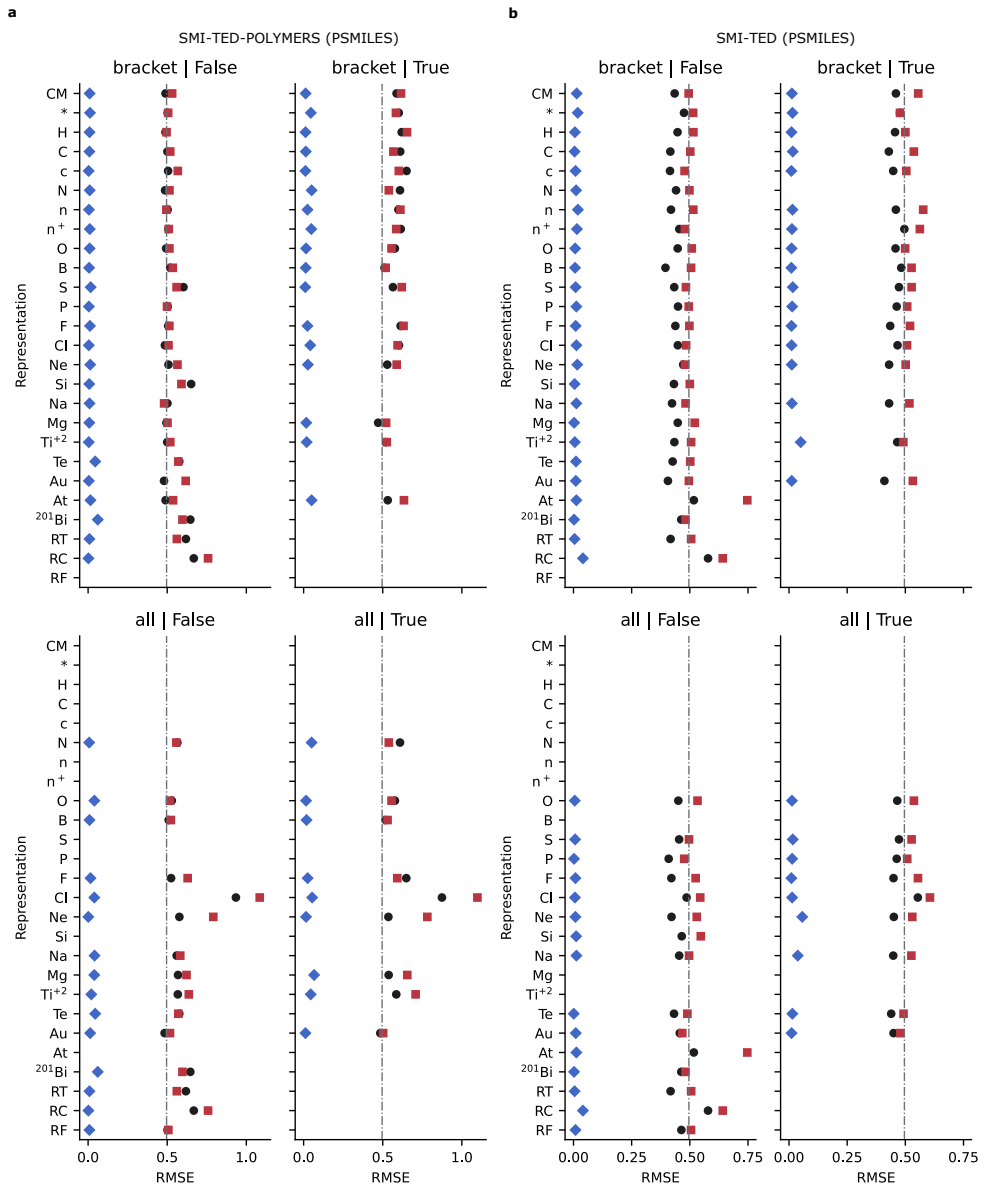


Fig. 55 Point plots for E_{gb} benchmark experiments of R^2 using the base random train, valid, and test splits for SMI-TED-POLYMER (a) and SMI-TED (b) models fine-tuned using PSMILES.

2.6.5 Polymer Ionization Energy (E_i) CV Scores

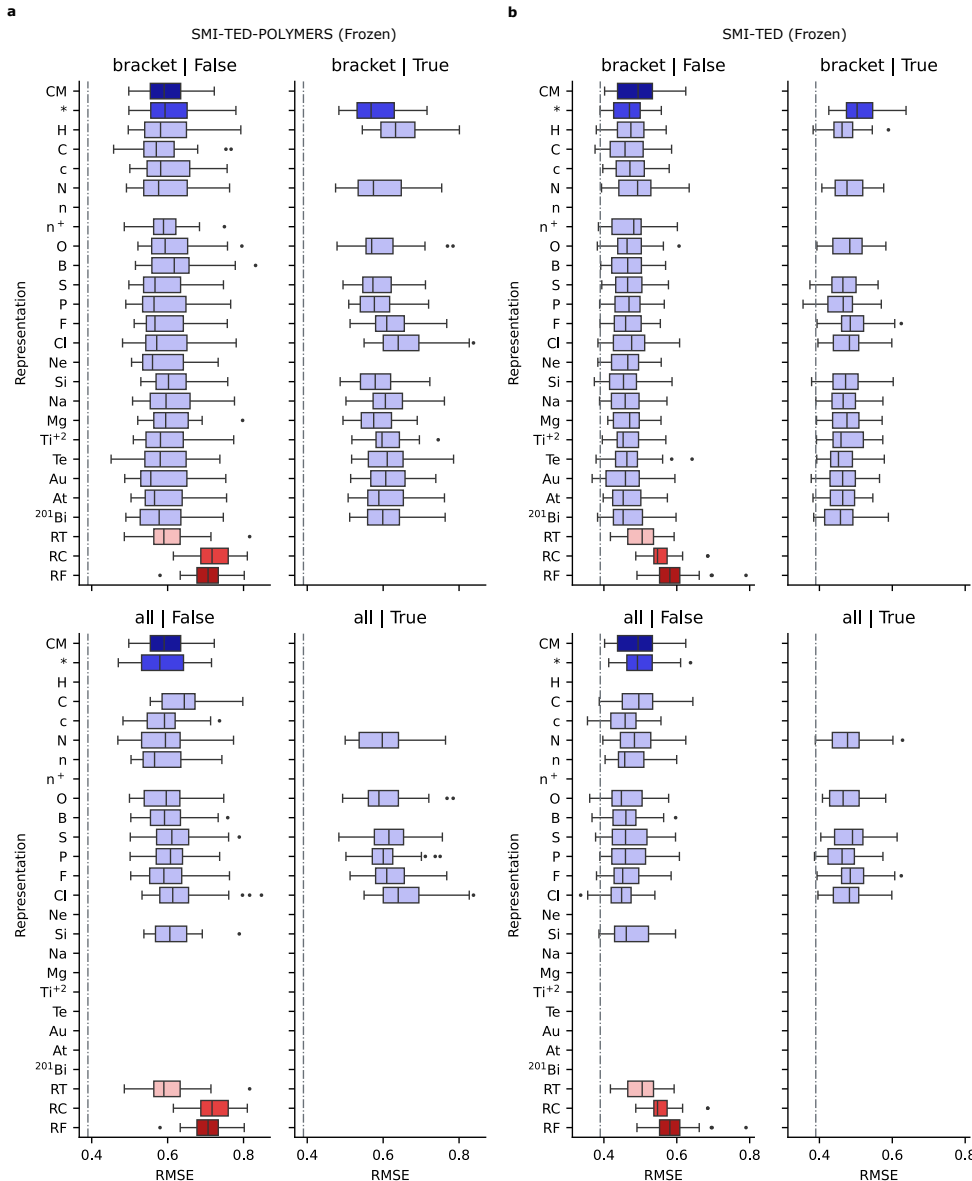


Fig. 56 Box plots for E_i repeated cross-validation experiments for SMI-TED-POLYMER (a) and SMI-TED (b) models with frozen weights.

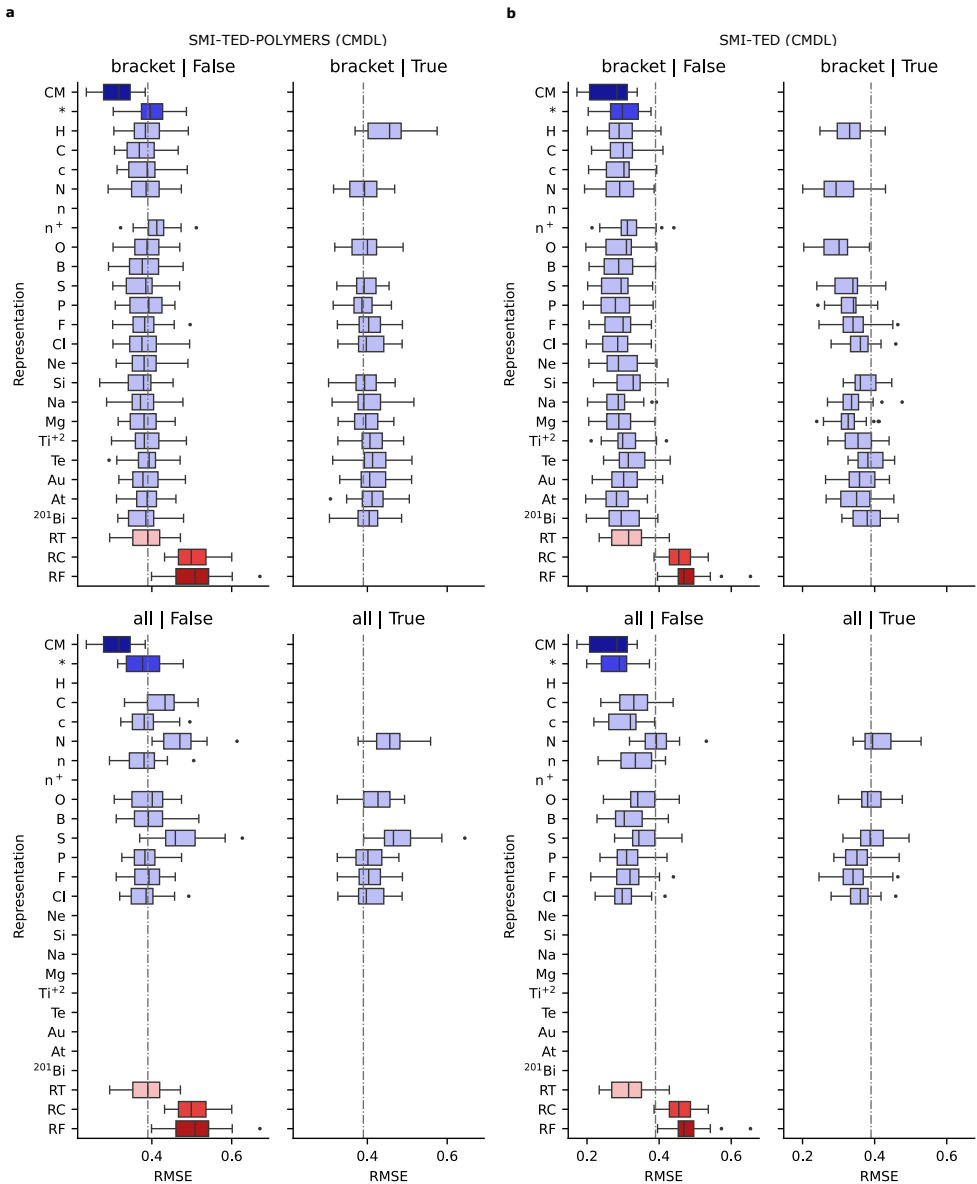


Fig. 57 Box plots for E_i repeated cross-validation experiments for SMI-TED-POLYMER (a) and SMI-TED (b) models fine-tuned with the CPG polymer graphs.

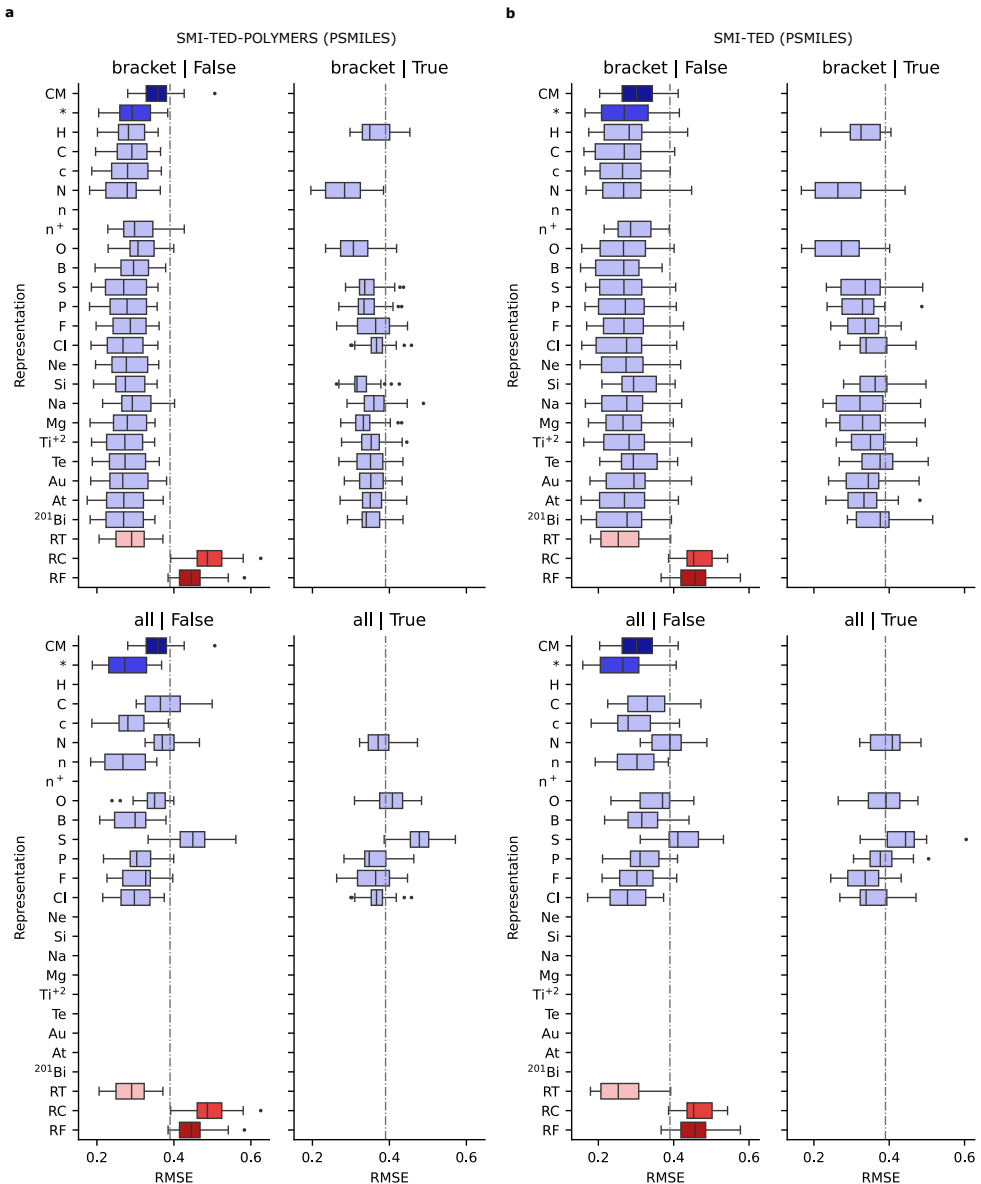


Fig. 58 Box plots for E_i repeated cross-validation experiments for SMI-TED-POLYMER **(a)** and SMI-TED **(b)** models fine-tuned with PSMILES.

2.6.6 Polymer Ionization Energy (E_i) Random Split Scores

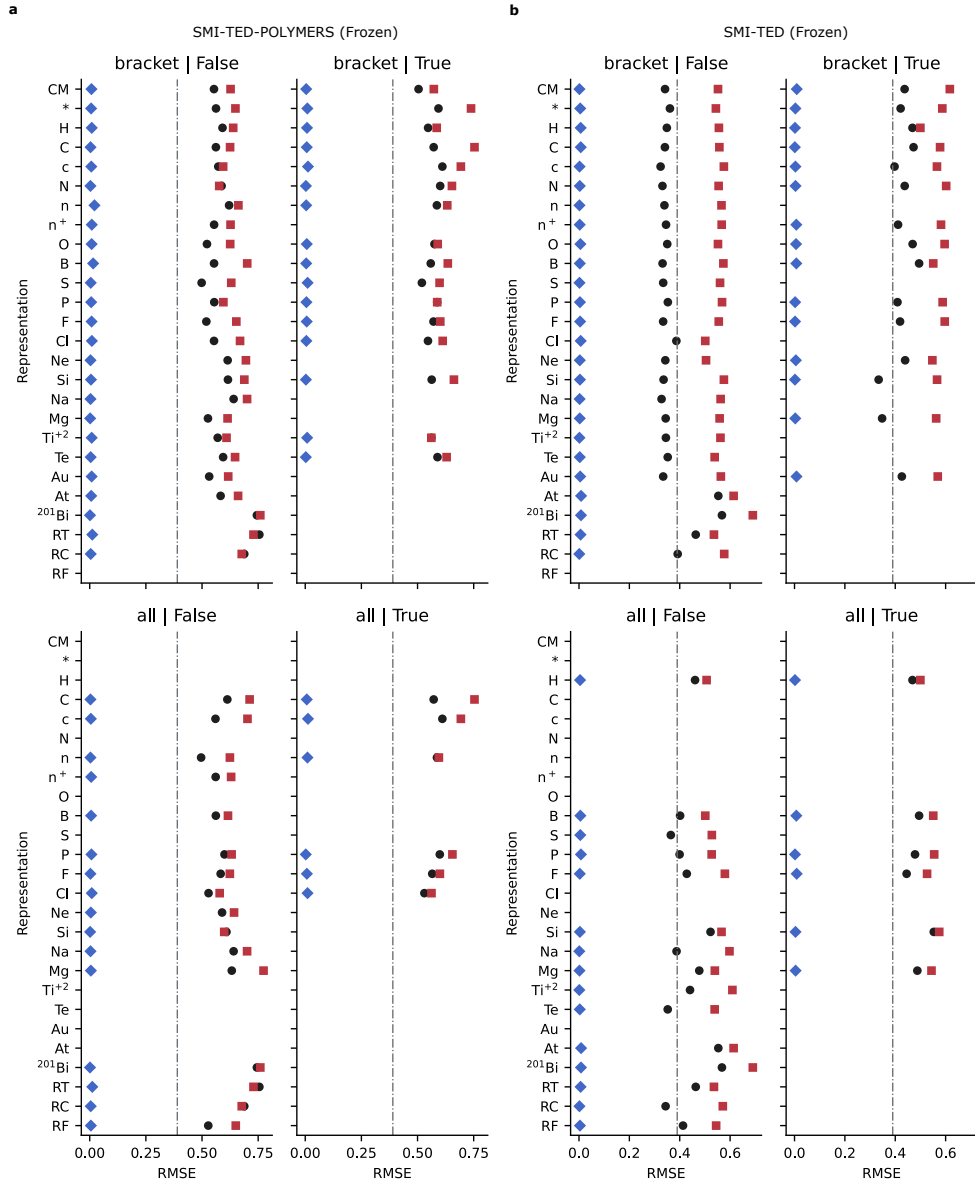


Fig. 59 Point plots for E_i benchmark experiments of RMSE using the base random train, valid, and test splits for SMI-TED-POLYMER (a) and SMI-TED (b) models with frozen weights.

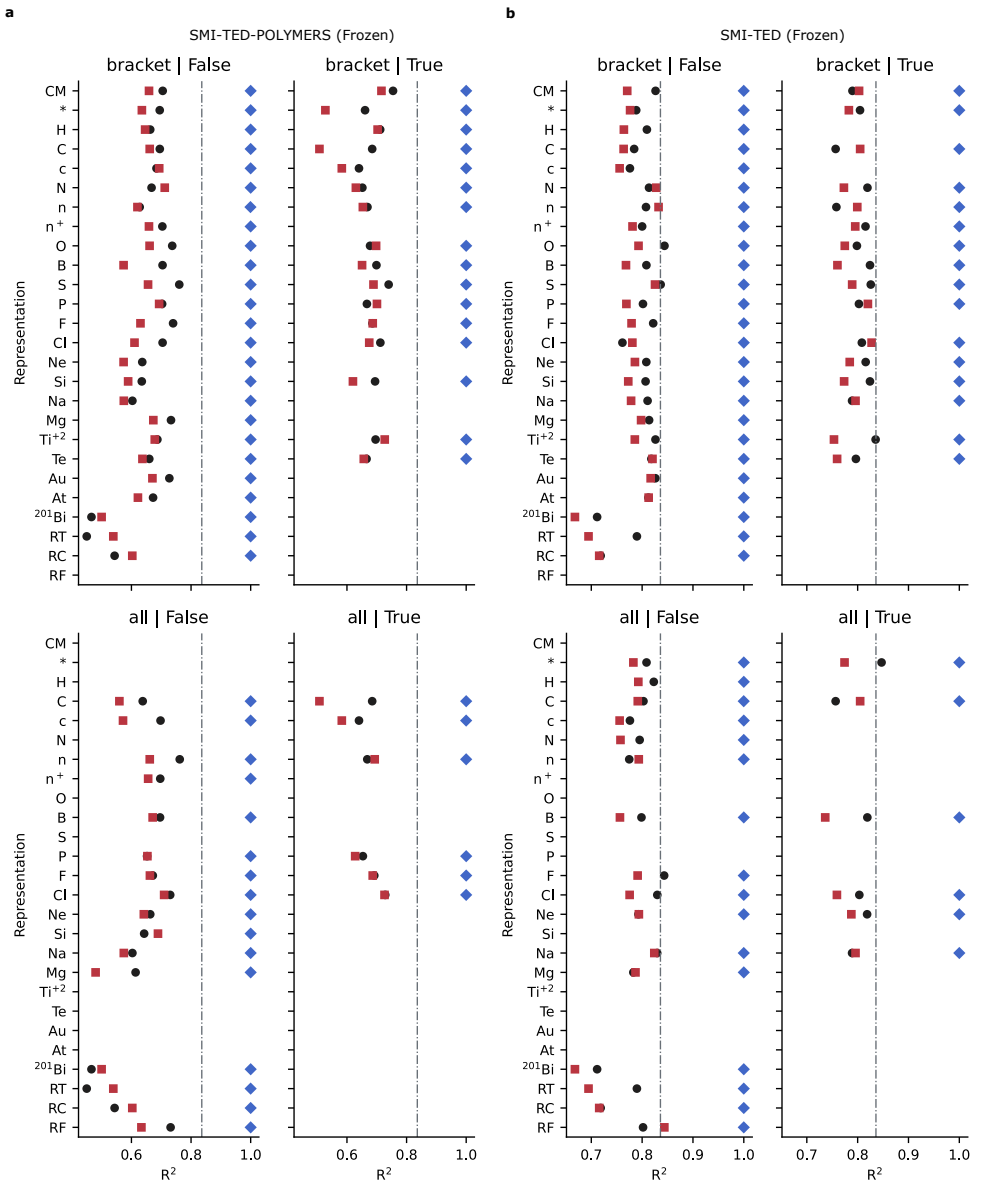


Fig. 60 Point plots for E_i benchmark experiments of R^2 using the base random train, valid, and test splits for SMI-TED-POLYMER **(a)** and SMI-TED **(b)** models with frozen weights.

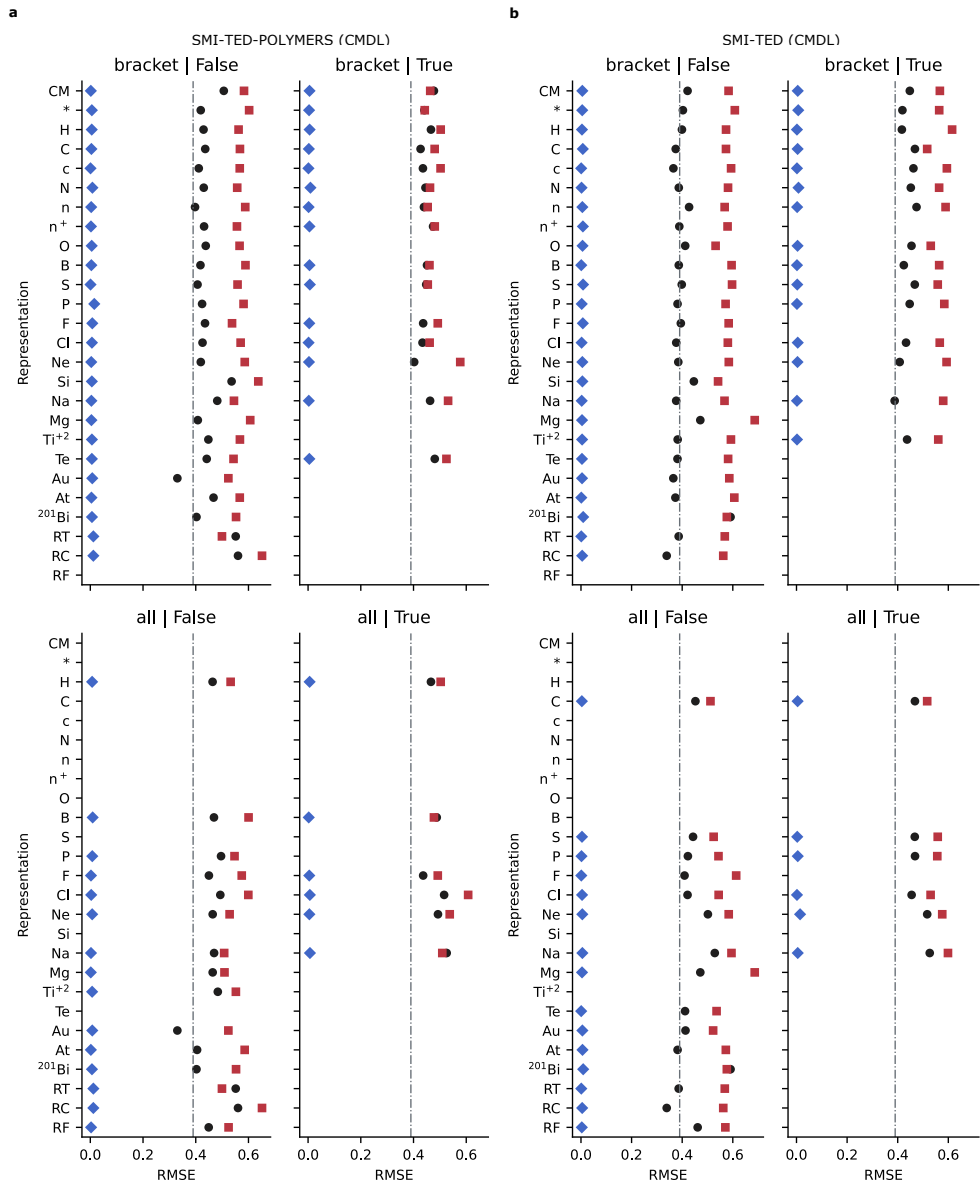


Fig. 61 Point plots for E_i benchmark experiments of RMSE using the base random train, valid, and test splits for SMI-TED-POLYMER (a) and SMI-TED (b) models fine-tuned using the CPG representation.

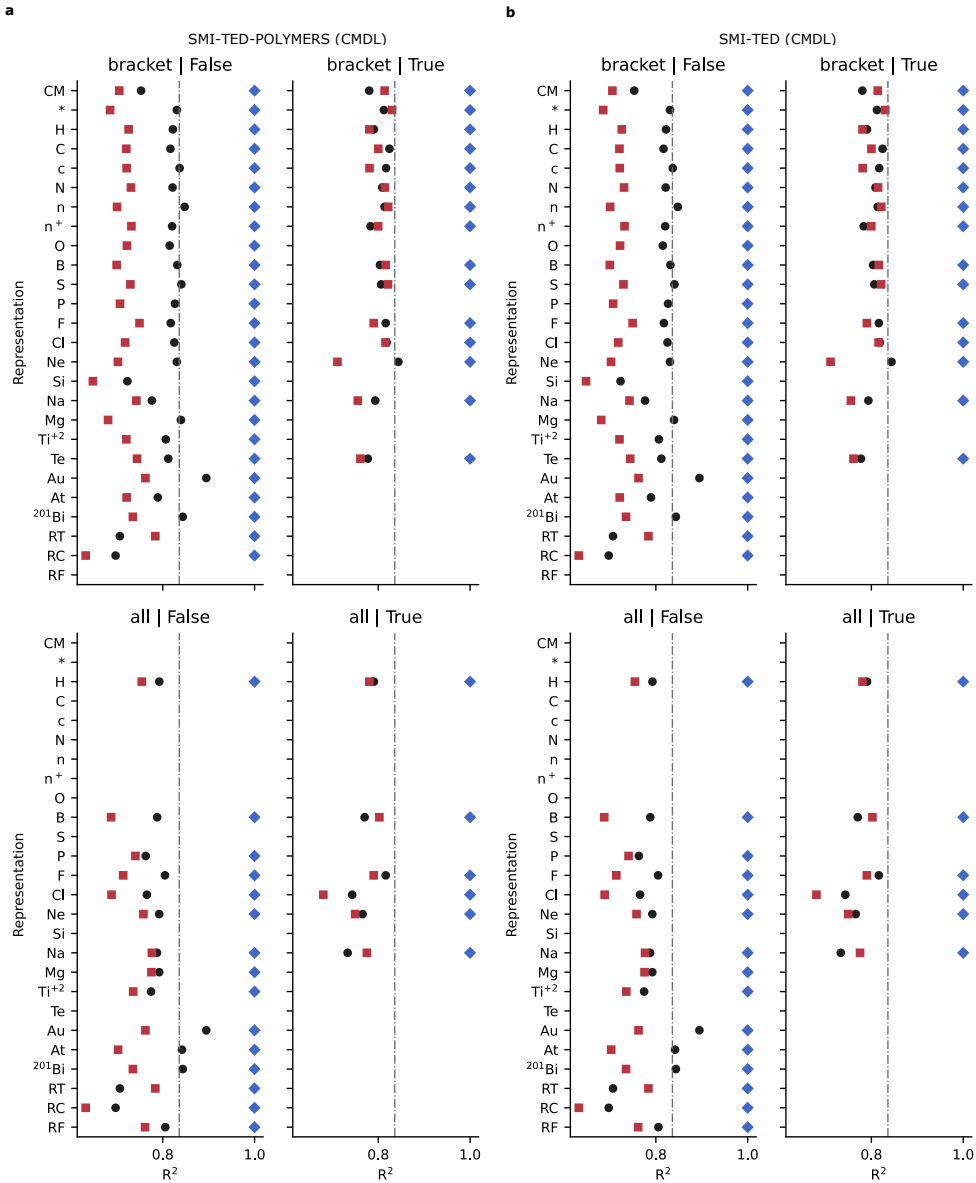


Fig. 62 Point plots for E_i benchmark experiments of R^2 using the base random train, valid, and test splits for SMI-TED-POLYMER (a) and SMI-TED (b) models fine-tuned using the CPG representation.

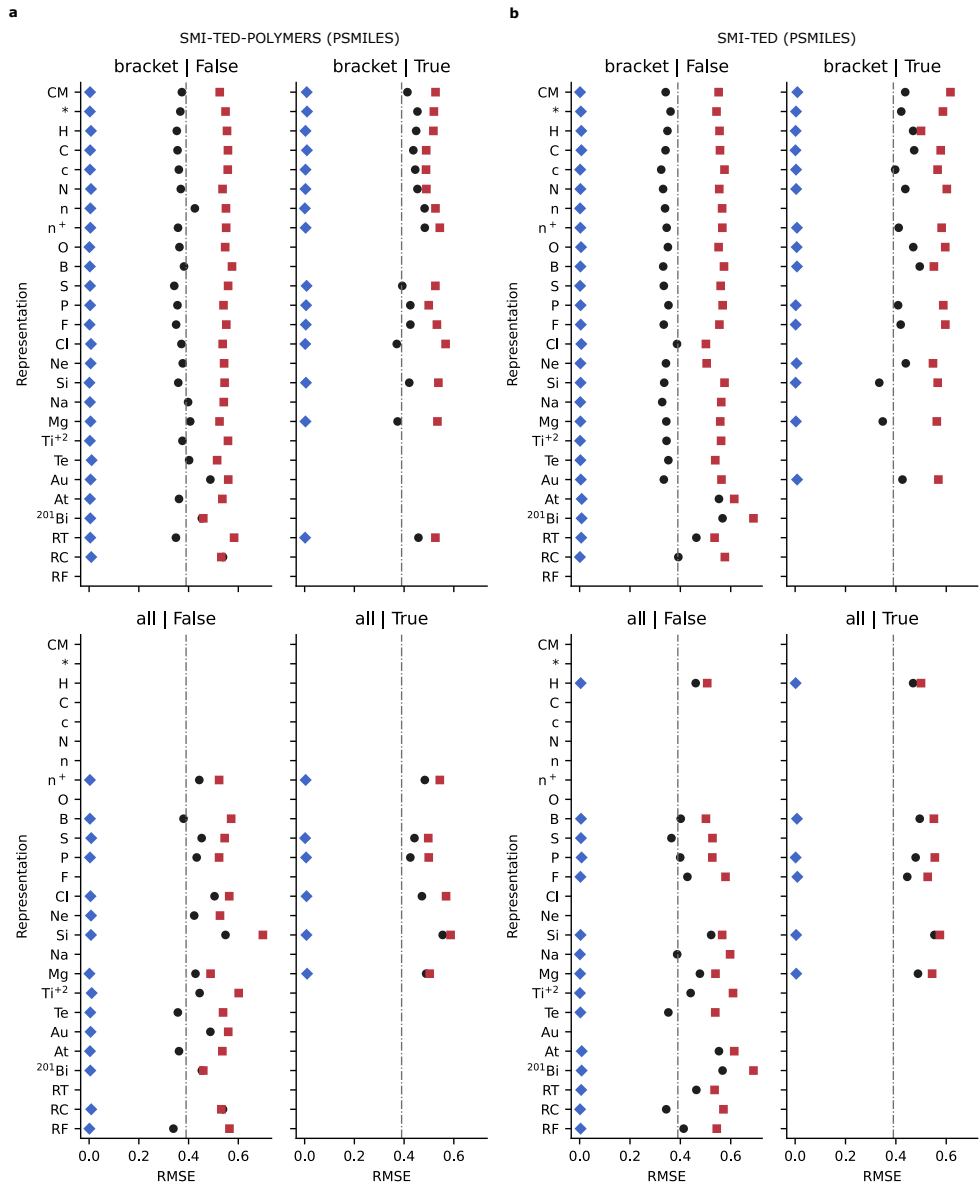


Fig. 63 Point plots for E_i benchmark experiments of RMSE using the base random train, valid, and test splits for SMI-TED-POLYMER (a) and SMI-TED (b) models fine-tuned using PSMILES.

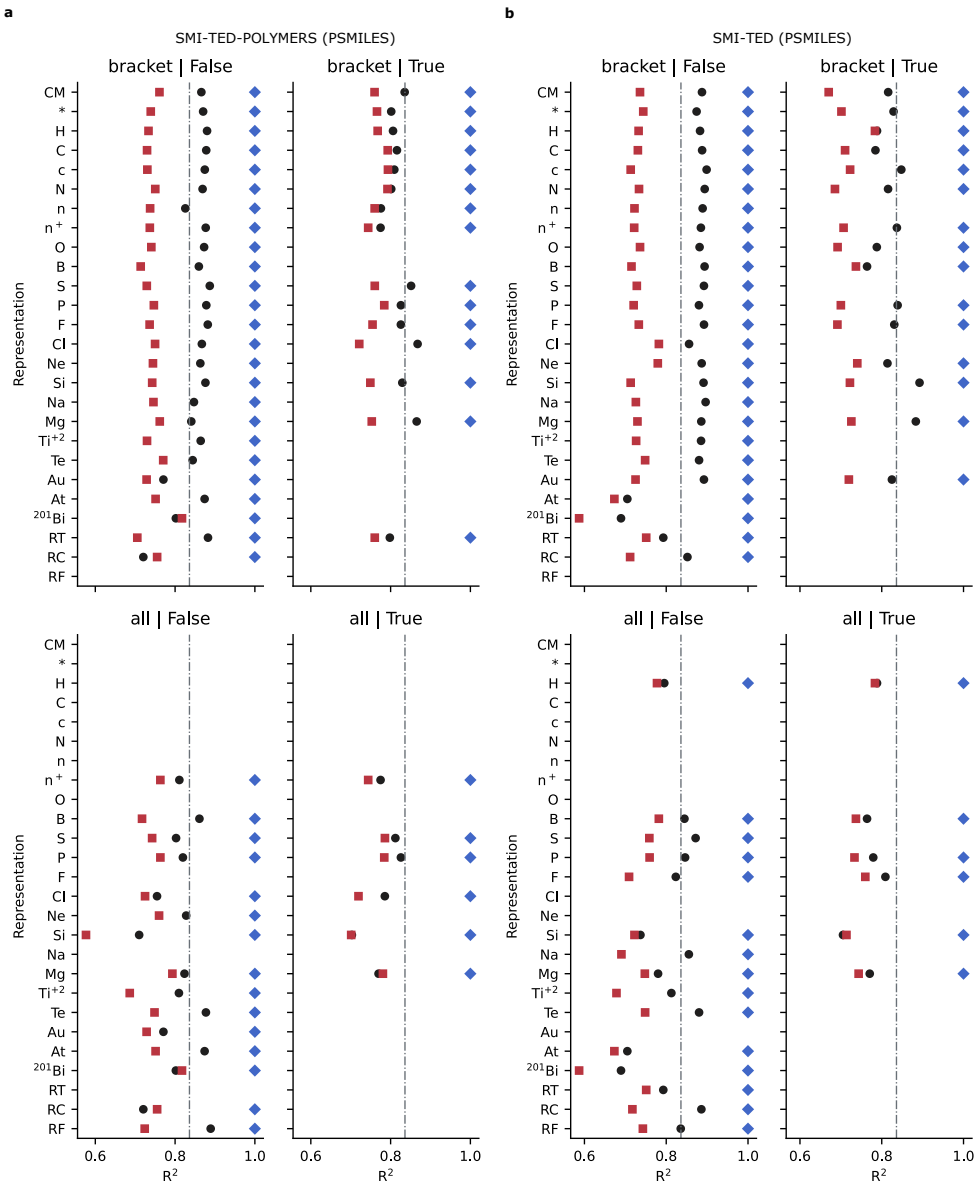


Fig. 64 Point plots for E_i benchmark experiments of R^2 using the base random train, valid, and test splits for SMI-TED-POLYMER (a) and SMI-TED (b) models fine-tuned using PSMILES.

2.6.7 Polymer Dielectric Constant (EPS) CV Scores

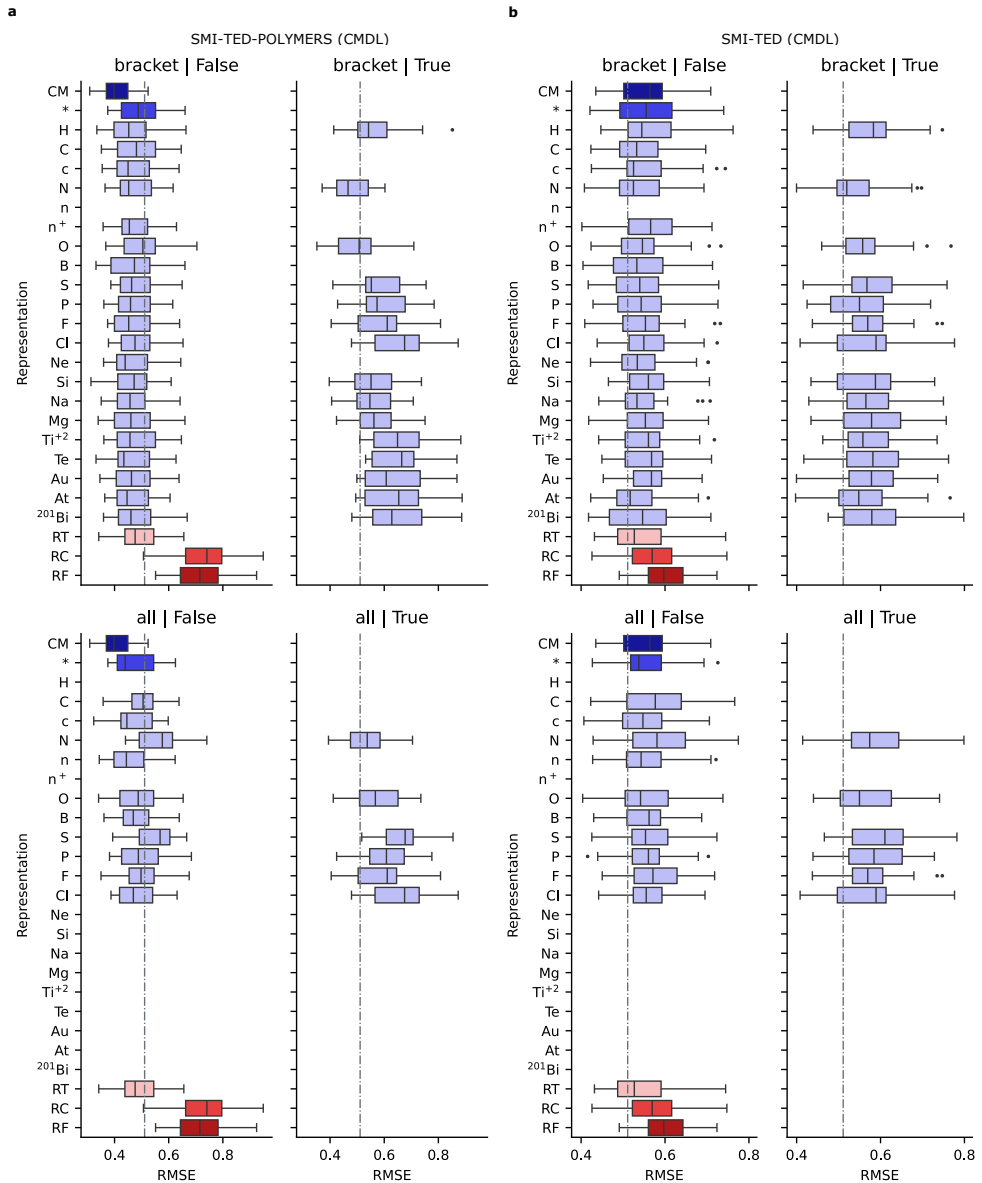


Fig. 65 Box plots for EPS repeated cross-validation experiments for SMI-TED-POLYMER (a) and SMI-TED (b) models fine-tuned with the CPG polymer graphs.

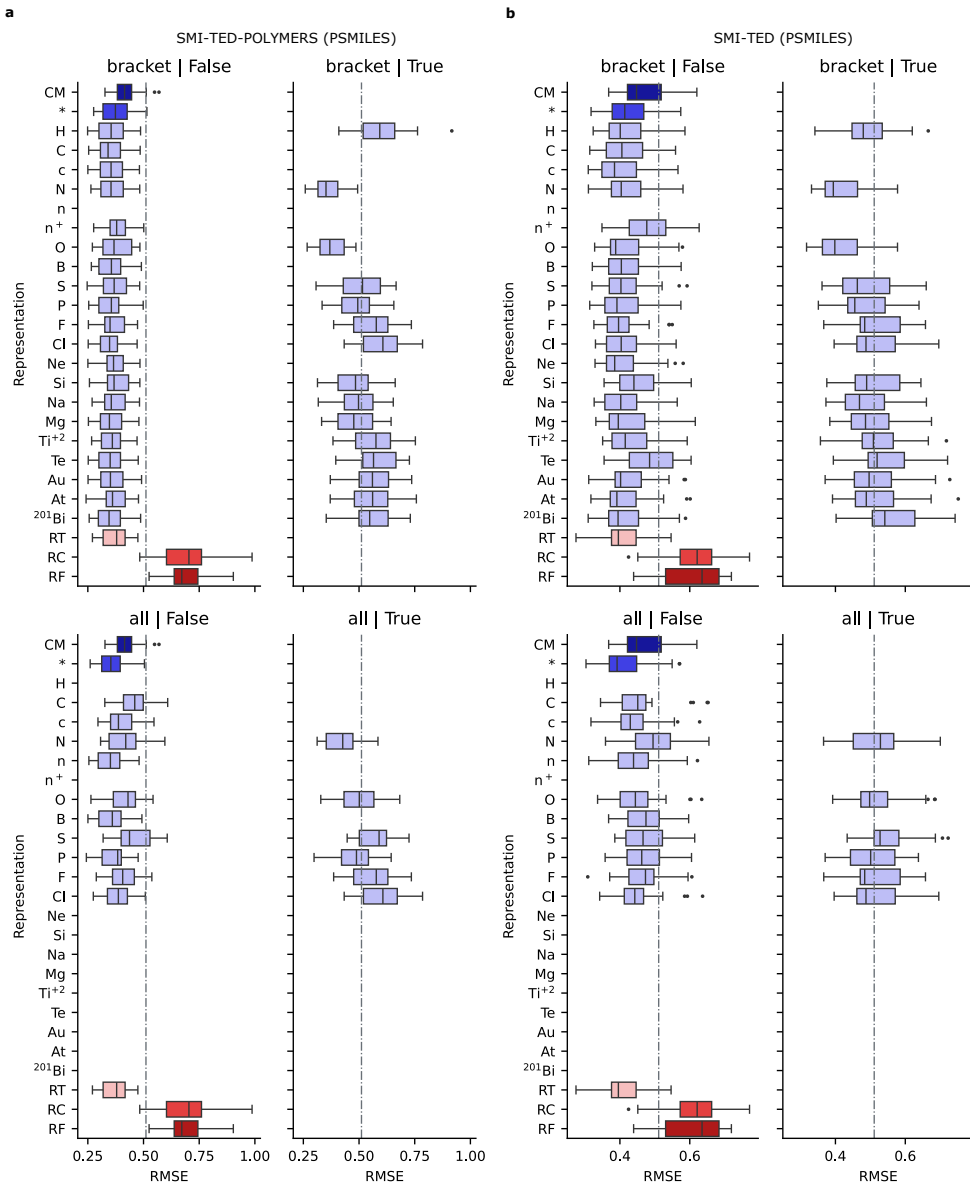


Fig. 66 Box plots for EPS repeated cross-validation experiments for SMI-TED-POLYMER **(a)** and SMI-TED **(b)** models fine-tuned with PSMILES.

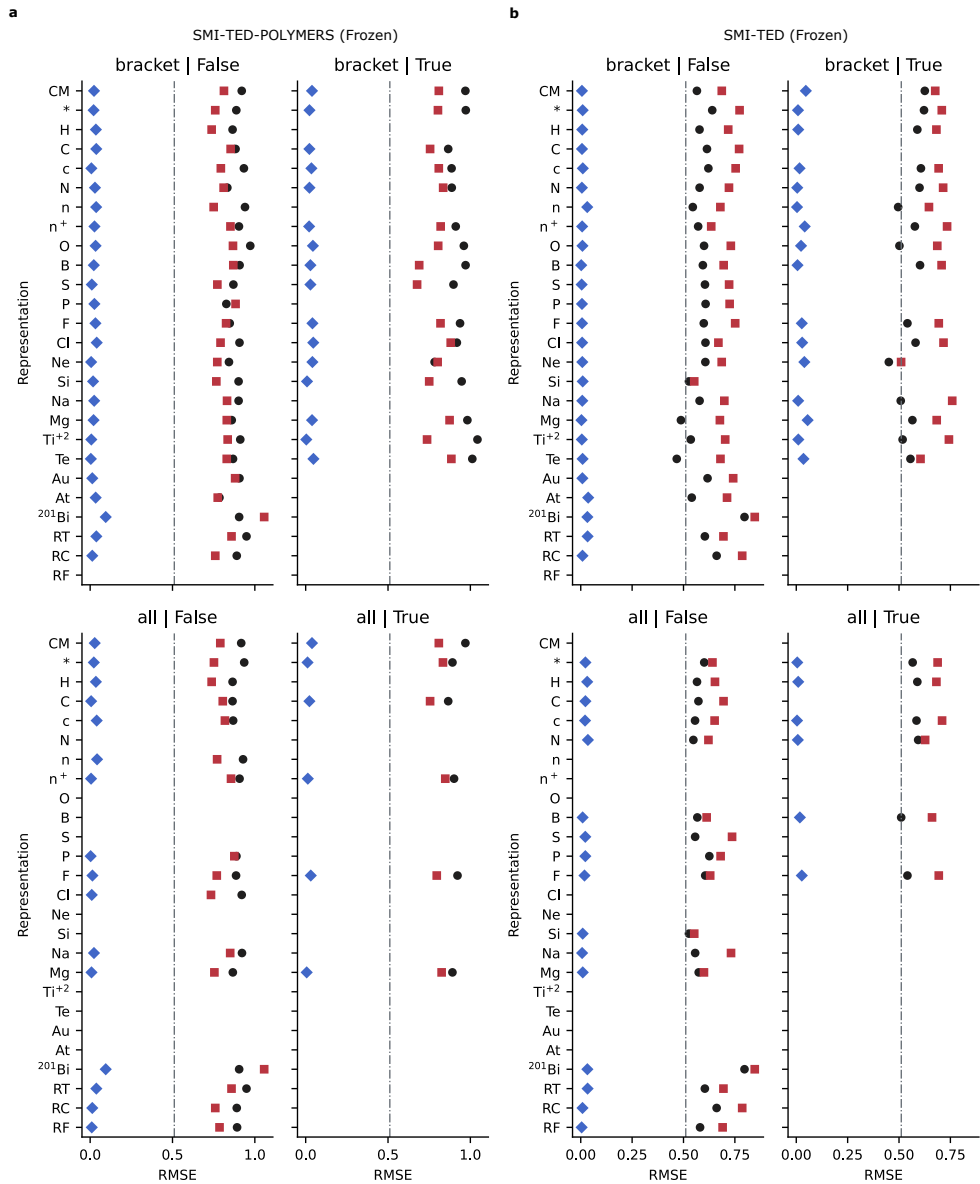


Fig. 67 Point plots for EPS benchmark experiments of RMSE using the base random train, valid, and test splits for SMI-TED-POLYMER **(a)** and SMI-TED **(b)** models with frozen weights.

2.6.8 Polymer Dielectric Constant (EPS) Random Split Scores

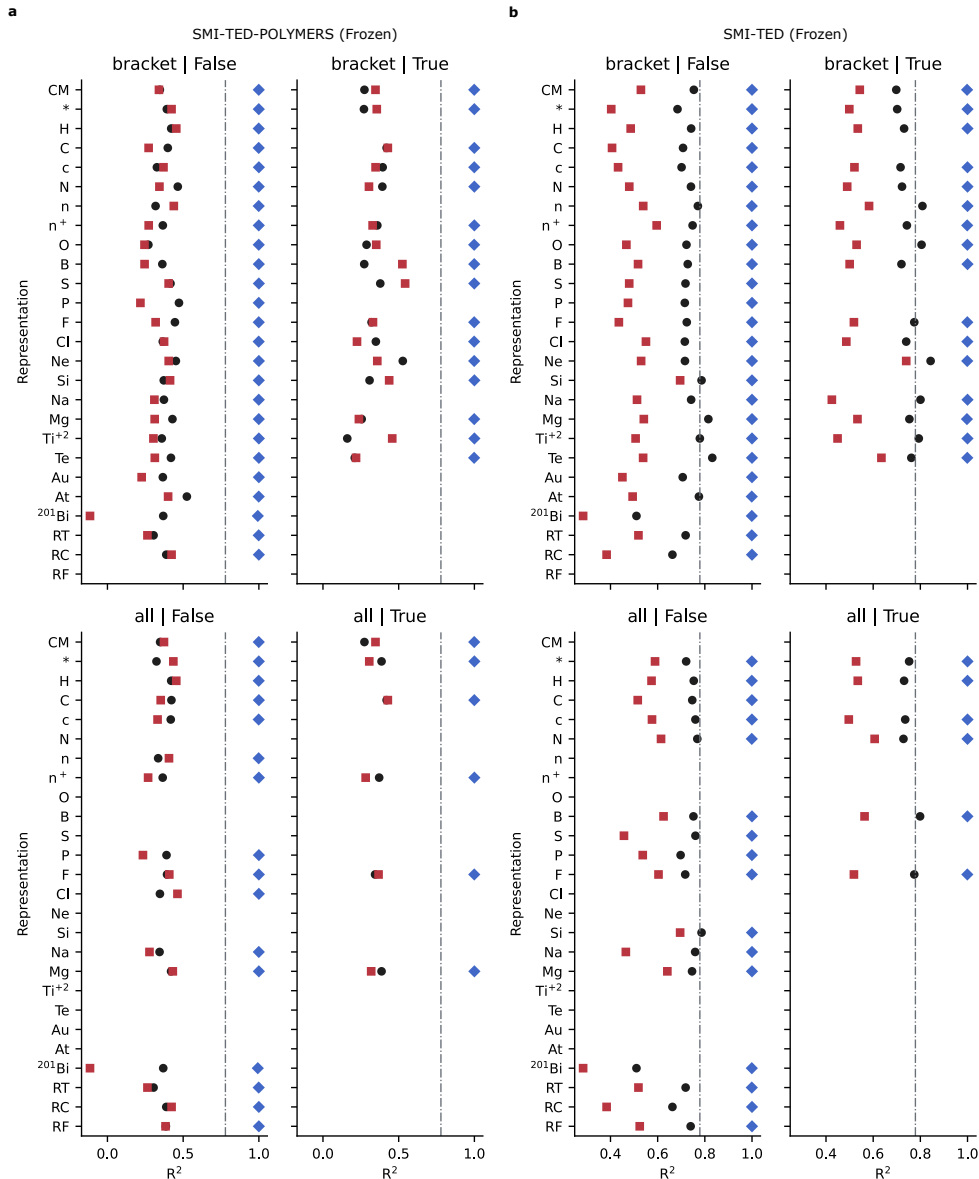


Fig. 68 Point plots for EPS benchmark experiments of R^2 using the base random train, valid, and test splits for SMI-TED-POLYMER (a) and SMI-TED (b) models with frozen weights.

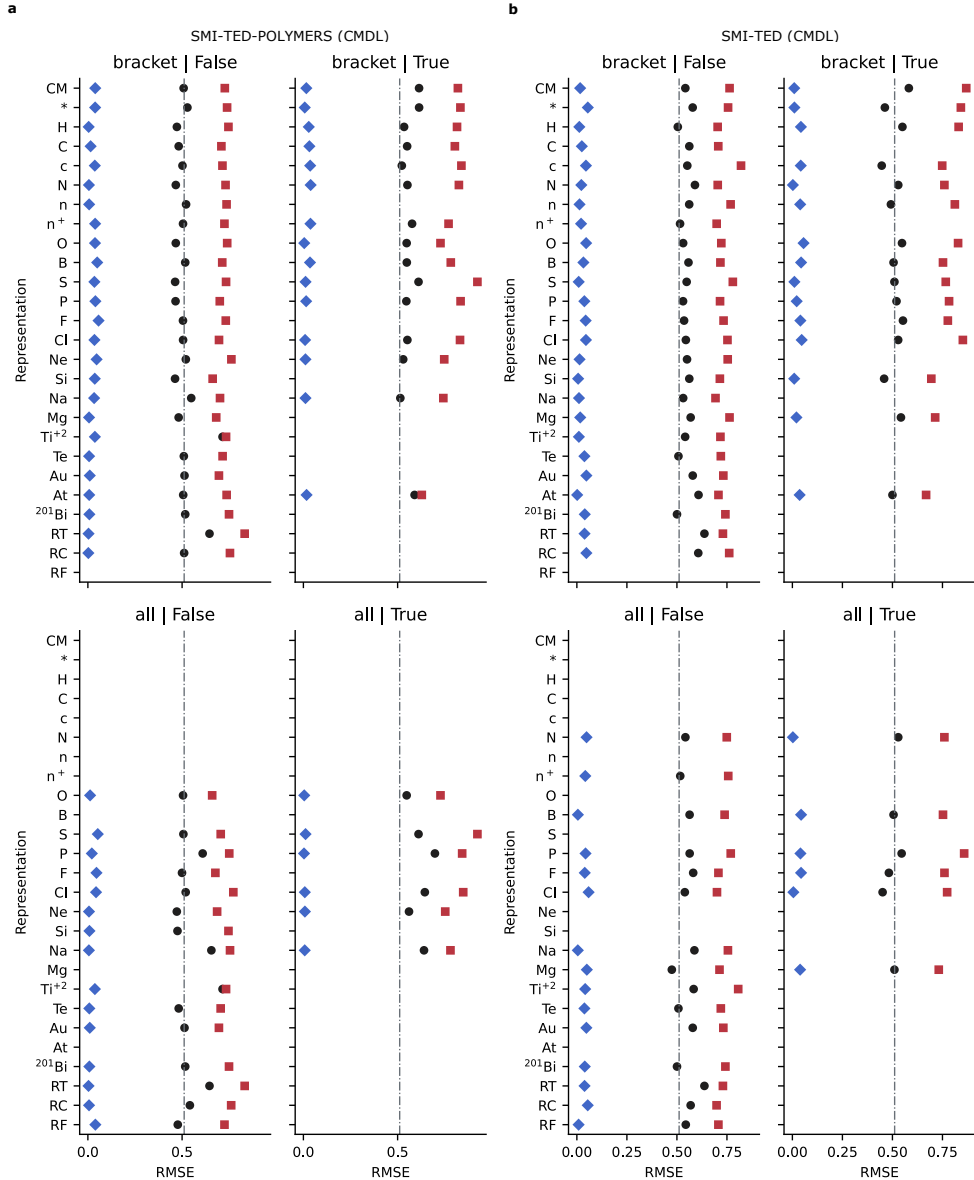


Fig. 69 Point plots for EPS benchmark experiments of RMSE using the base random train, valid, and test splits for SMI-TED-POLYMER (a) and SMI-TED (b) models fine-tuned using the CPG representation.

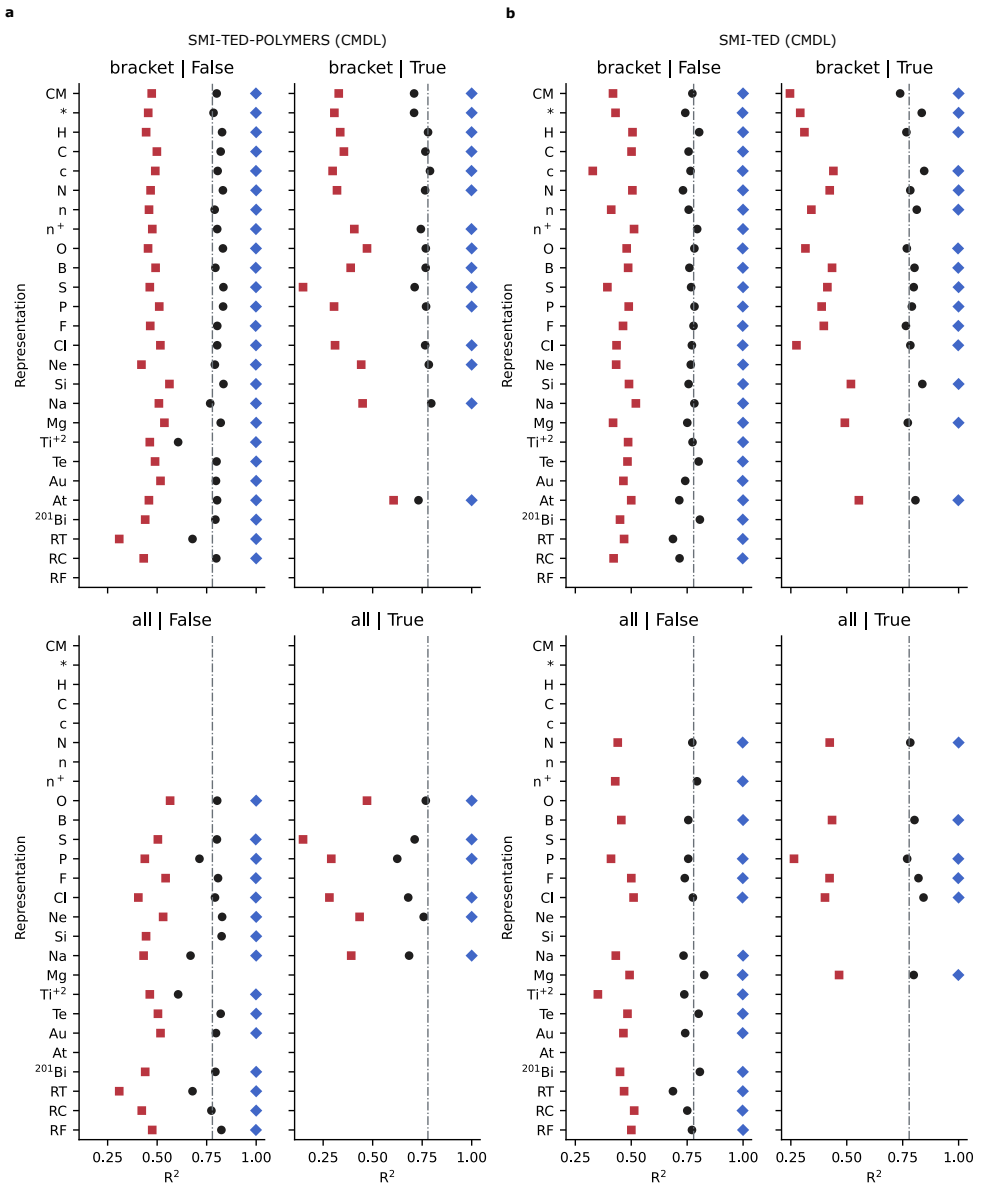


Fig. 70 Point plots for EPS benchmark experiments of R^2 using the base random train, valid, and test splits for SMI-TED-POLYMER (a) and SMI-TED (b) models fine-tuned using the CPG representation.

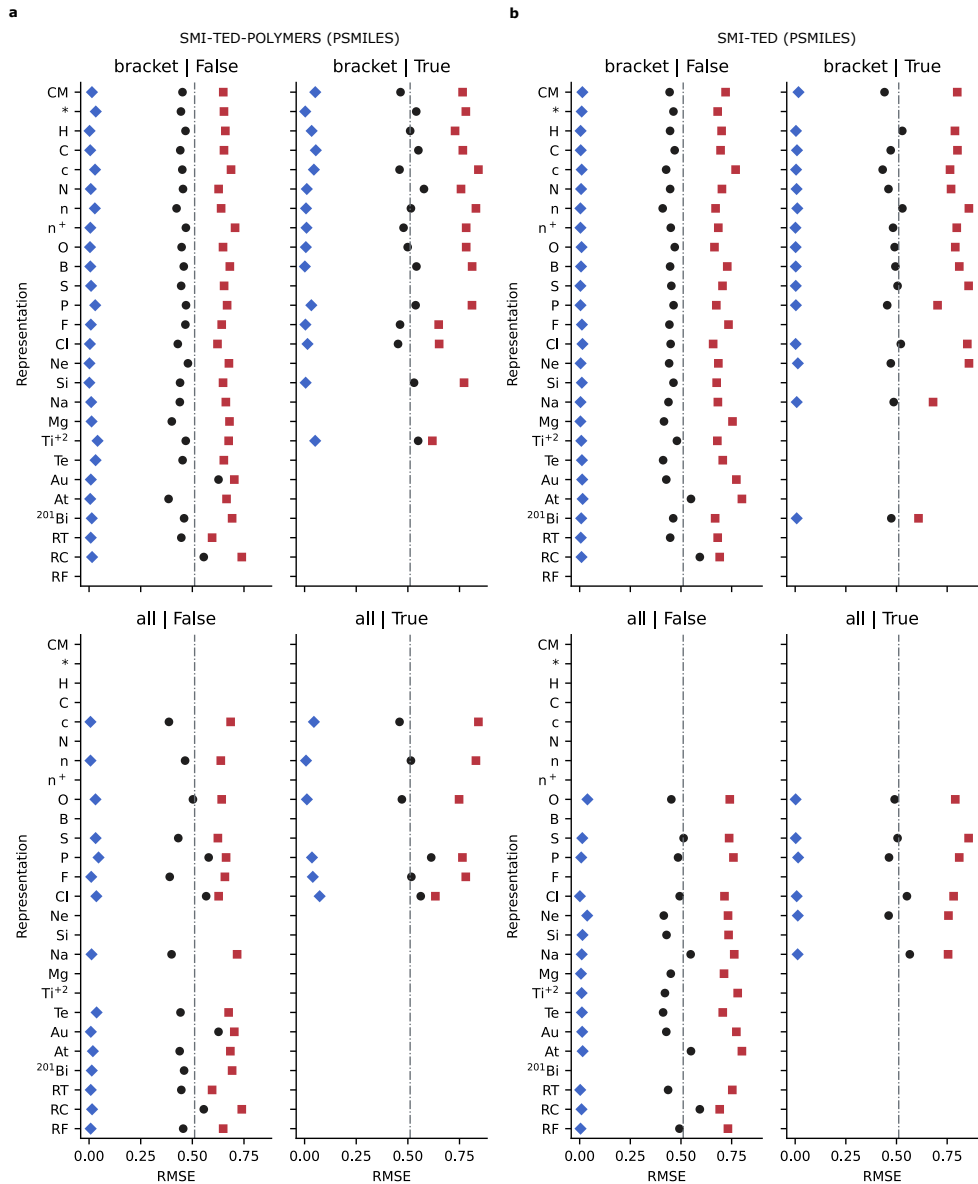


Fig. 71 Point plots for EPS benchmark experiments of RMSE using the base random train, valid, and test splits for SMI-TED-POLYMER **(a)** and SMI-TED **(b)** models fine-tuned using PSMILES.

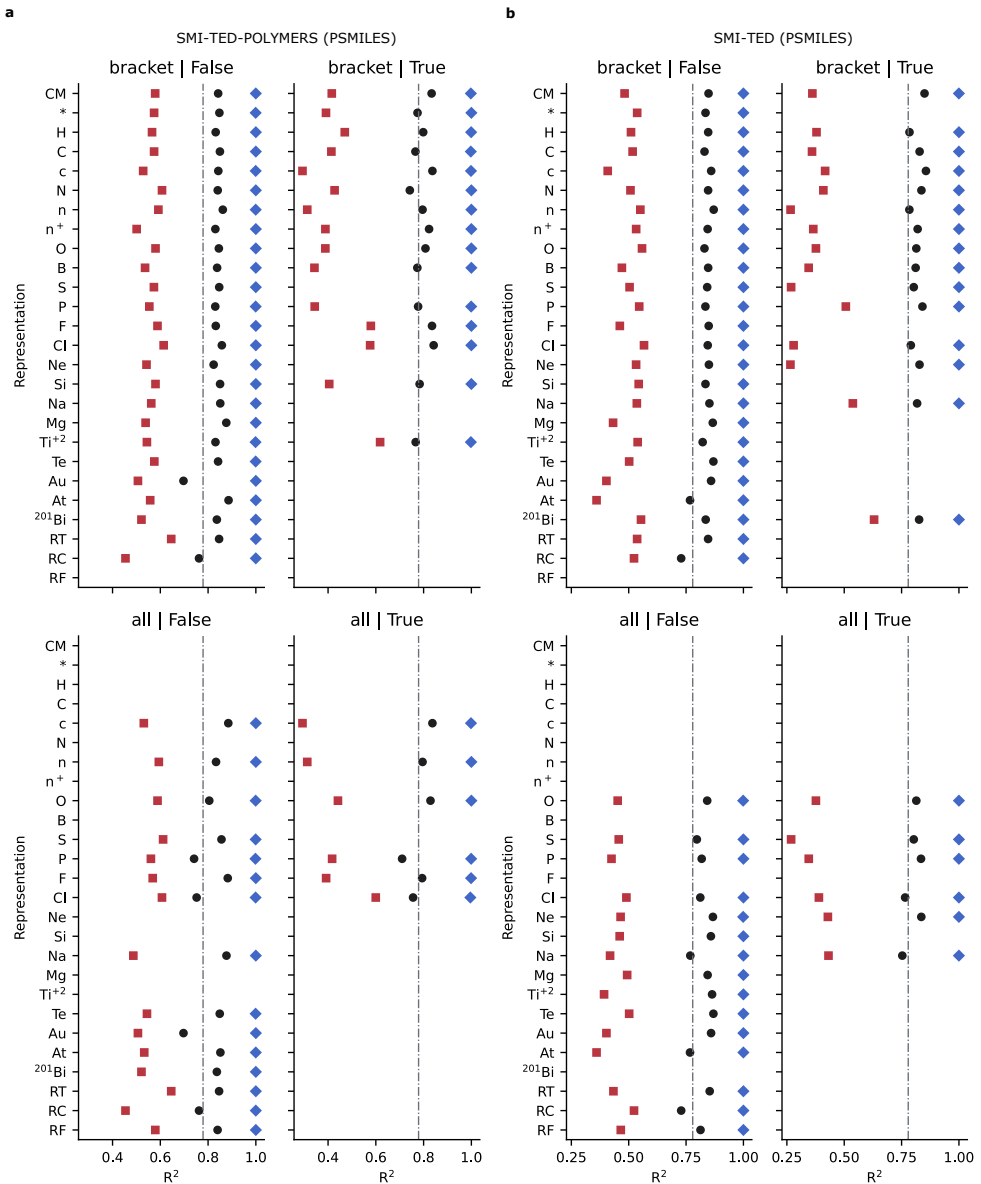


Fig. 72 Point plots for EPS benchmark experiments of R^2 using the base random train, valid, and test splits for SMI-TED-POLYMER (a) and SMI-TED (b) models fine-tuned using PSMILES.

2.6.9 Polymer Electron Affinity (E_{ea}) CV Scores

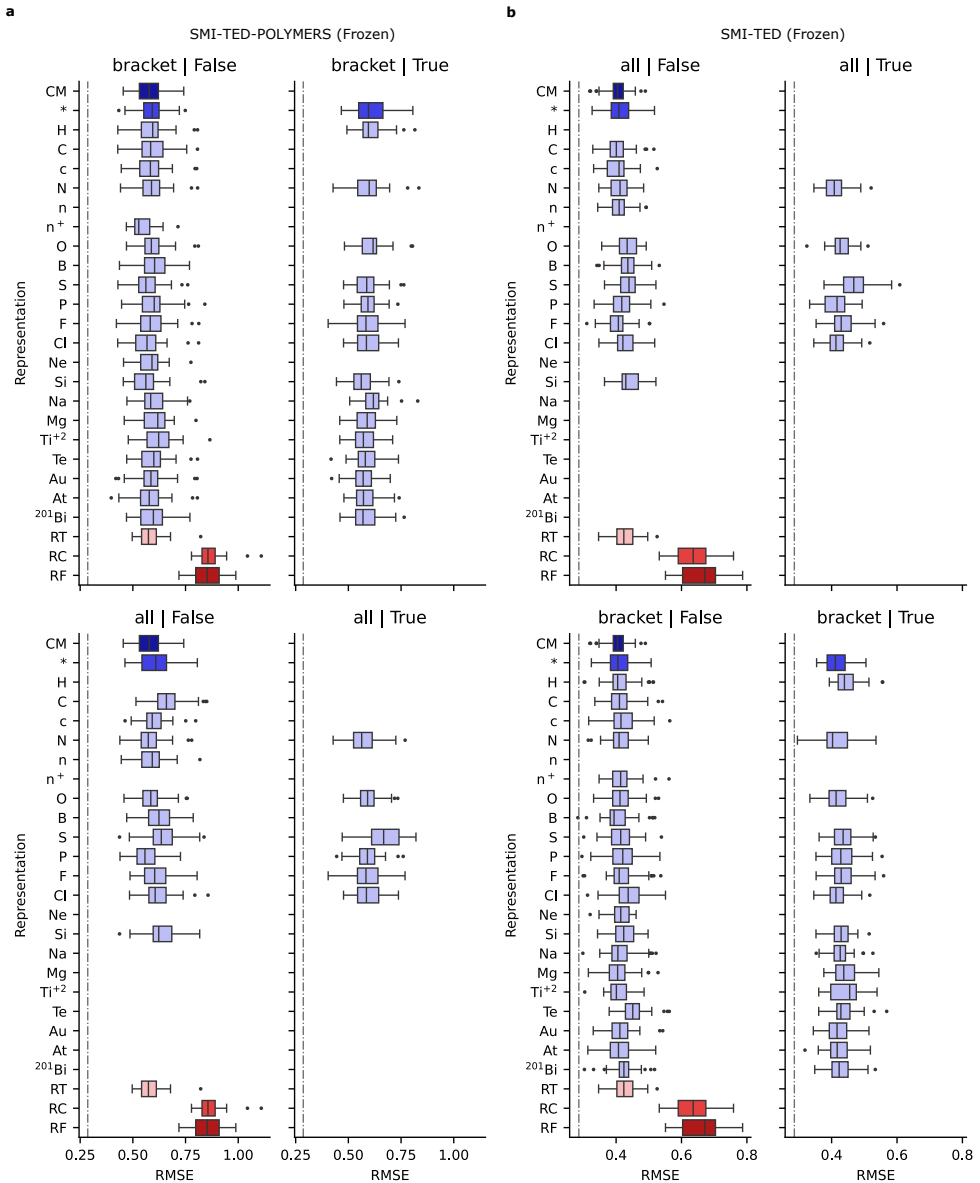


Fig. 73 Box plots for E_{ea} repeated cross-validation experiments for SMI-TED-POLYMER (a) and SMI-TED (b) models with frozen weights.

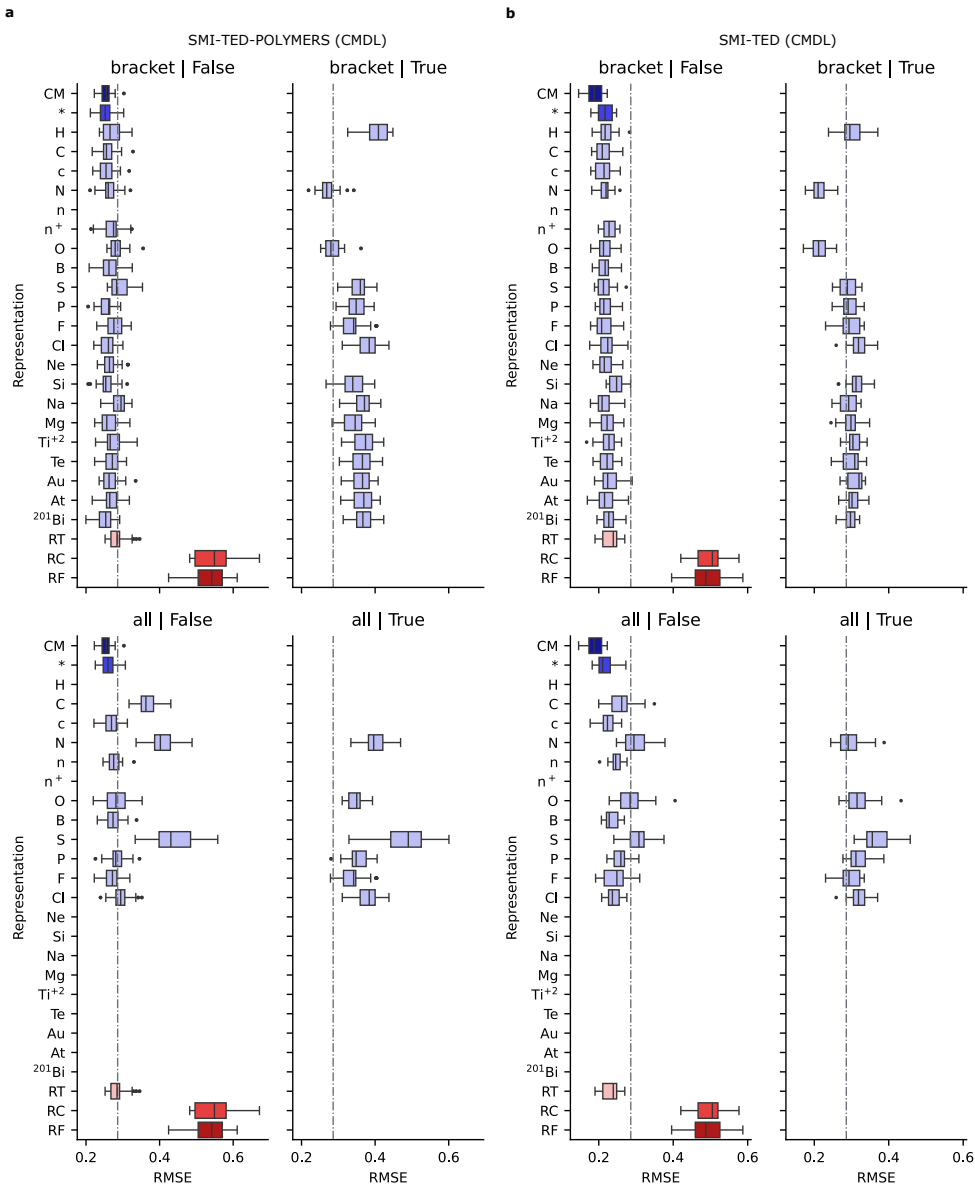


Fig. 74 Box plots for E_{ea} repeated cross-validation experiments for SMI-TED-POLYMER **(a)** and SMI-TED **(b)** models fine-tuned with the CPG polymer graphs.

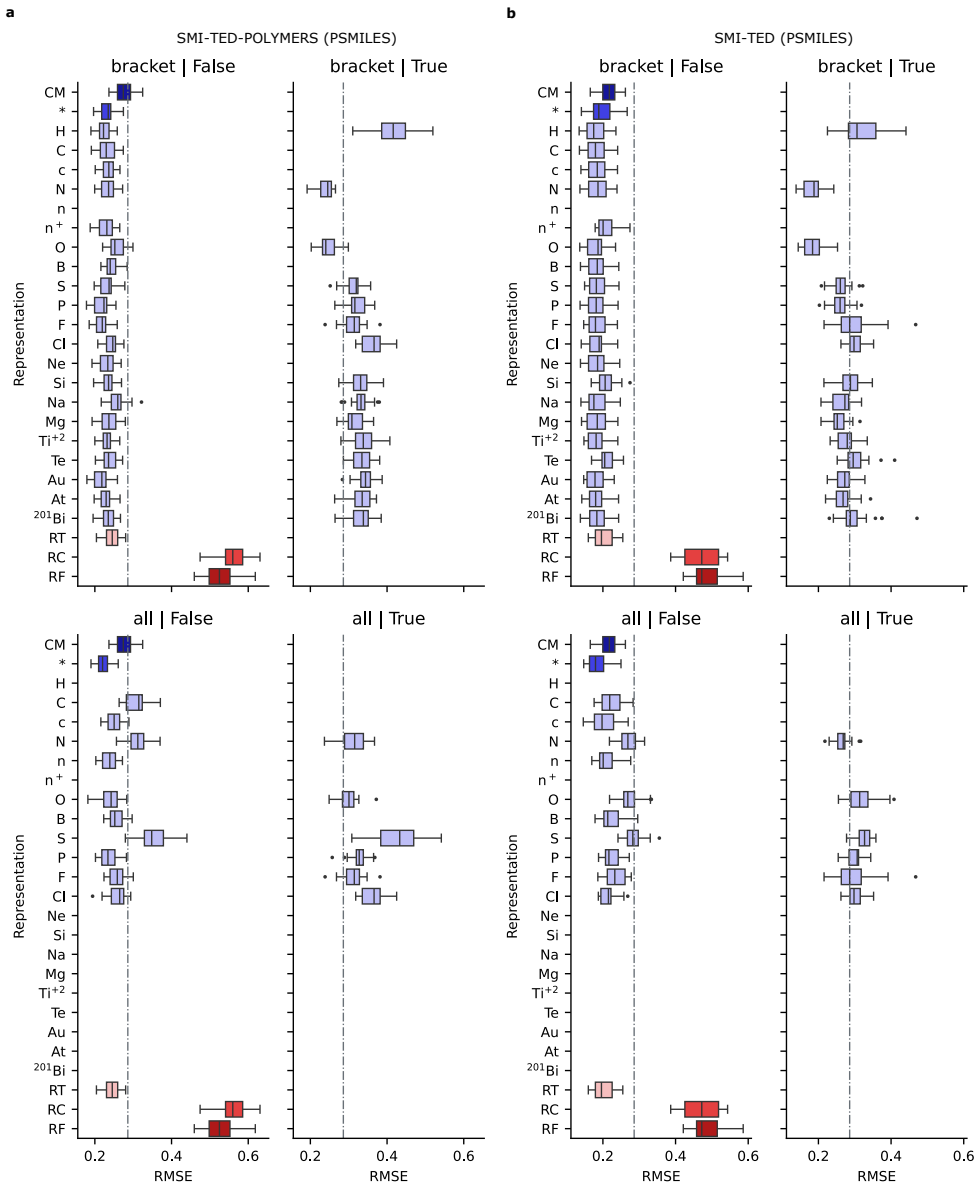


Fig. 75 Box plots for E_{ea} repeated cross-validation experiments for SMI-TED-POLYMER (a) and SMI-TED (b) models fine-tuned with PSMILES.

2.6.10 Polymer Electron Affinity (E_{ea}) Random Split Scores

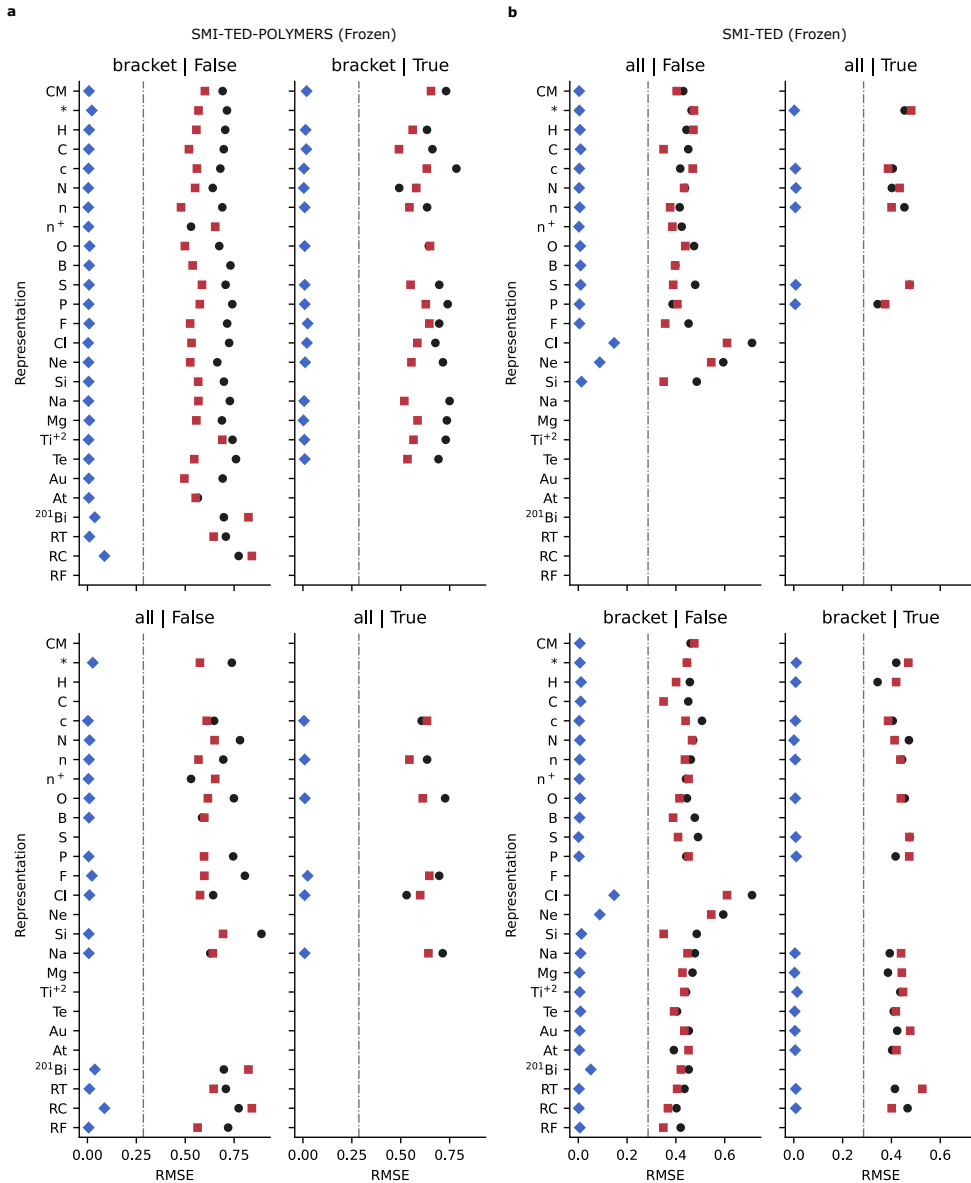


Fig. 76 Point plots for E_{ea} benchmark experiments of RMSE using the base random train, valid, and test splits for SMI-TED-POLYMER (a) and SMI-TED (b) models with frozen weights.

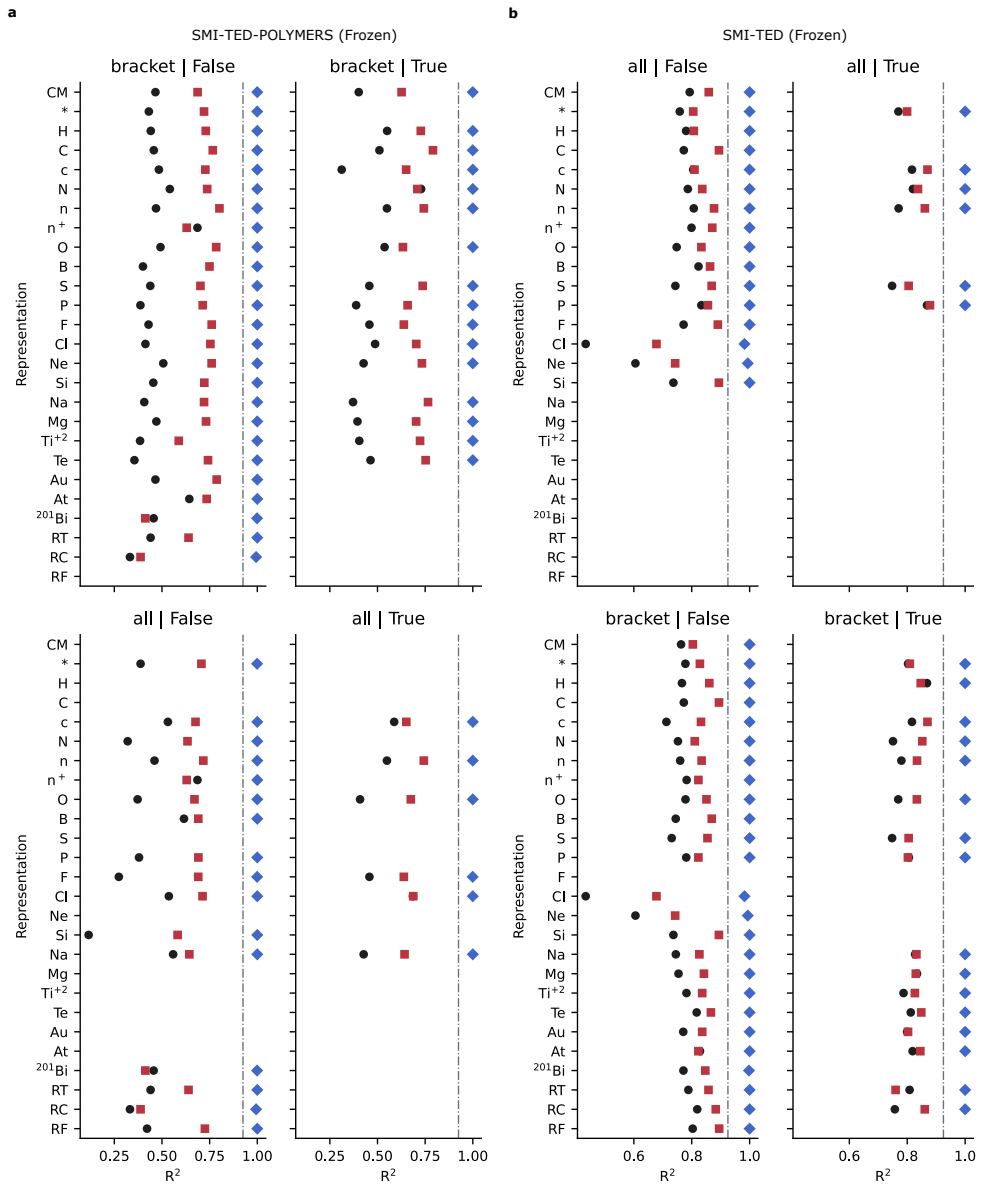


Fig. 77 Point plots for E_{ea} benchmark experiments of R^2 using the base random train, valid, and test splits for SMI-TED-POLYMER (a) and SMI-TED (b) models with frozen weights.

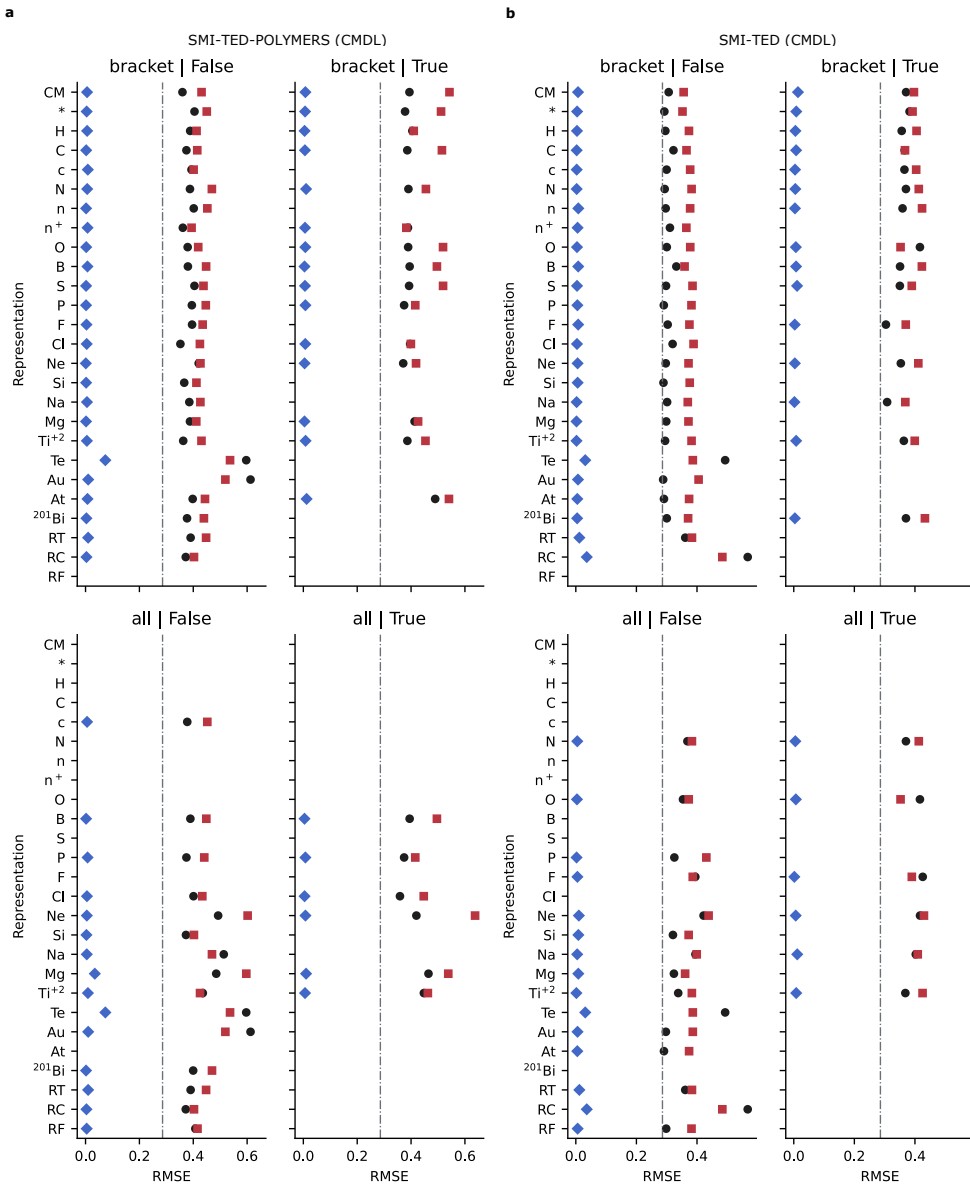


Fig. 78 Point plots for E_{ea} benchmark experiments of RMSE using the base random train, valid, and test splits for SMI-TED-POLYMER (a) and SMI-TED (b) models fine-tuned using the CPG representation.

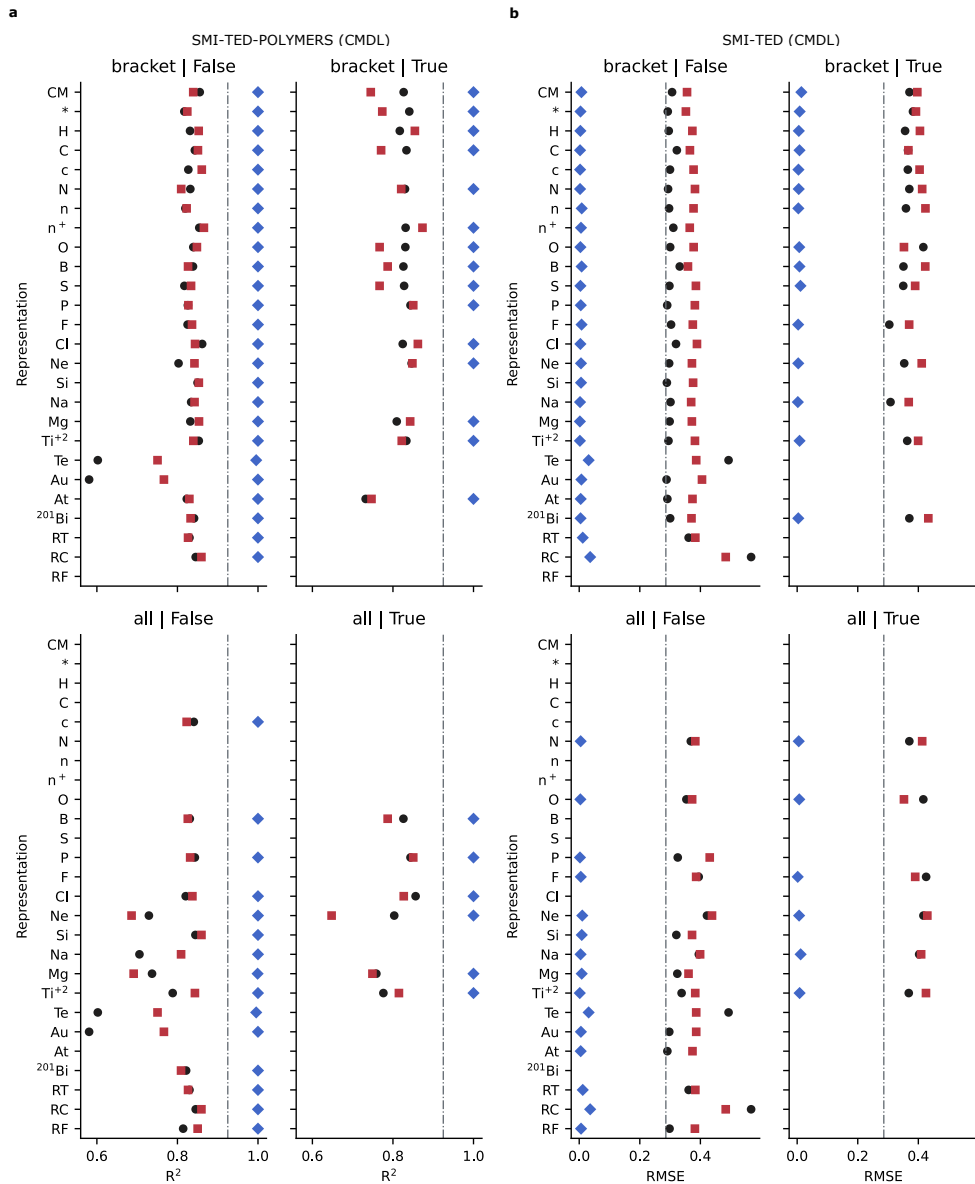


Fig. 79 Point plots for E_{ea} benchmark experiments of R^2 using the base random train, valid, and test splits for SMI-TED-POLYMER (a) and SMI-TED (b) models fine-tuned using the CPG representation.

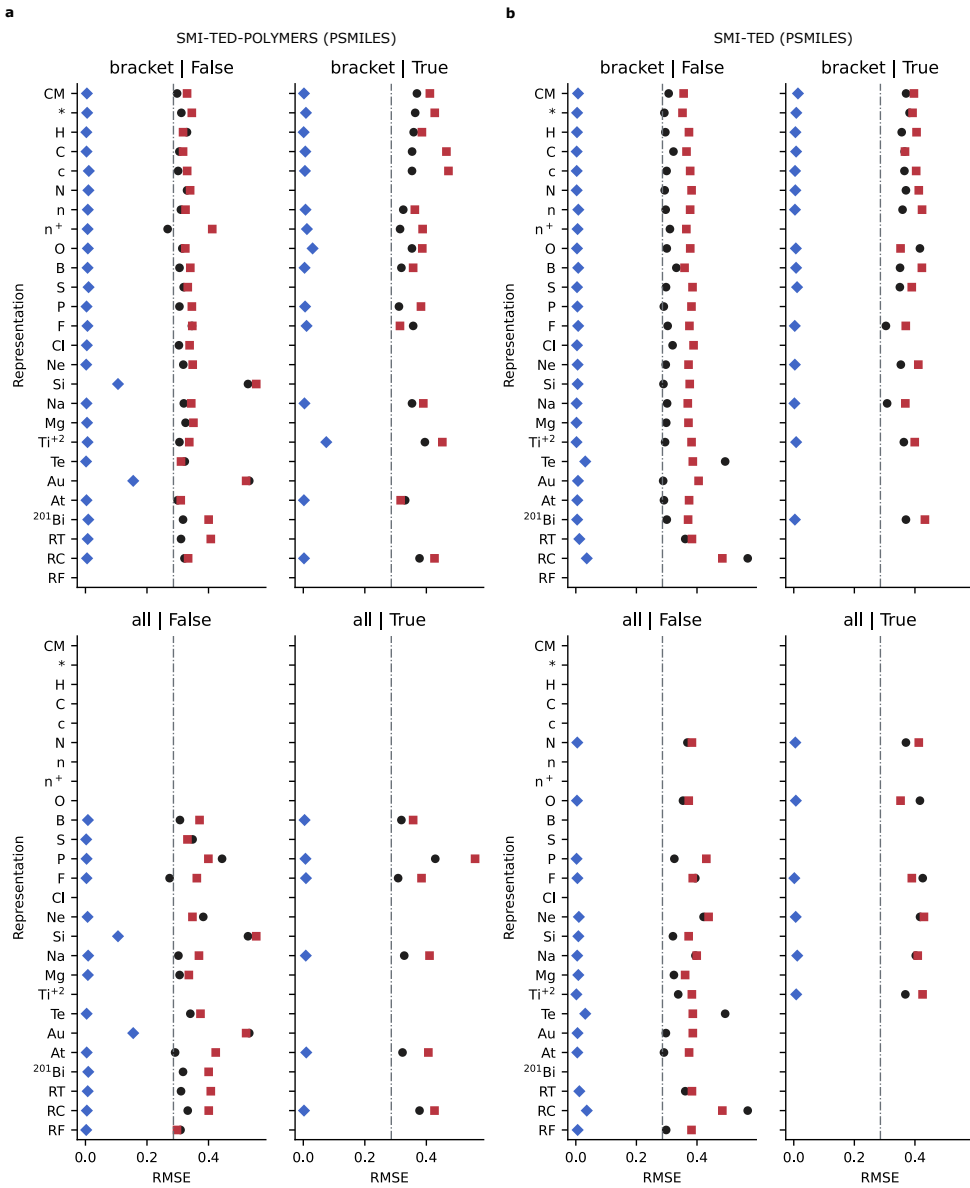


Fig. 80 Point plots for E_{ea} benchmark experiments of RMSE using the base random train, valid, and test splits for SMI-TED-POLYMER (a) and SMI-TED (b) models fine-tuned using PSMILES.

2.6.11 Polymer Atomization Energy (E_{at}) CV Scores

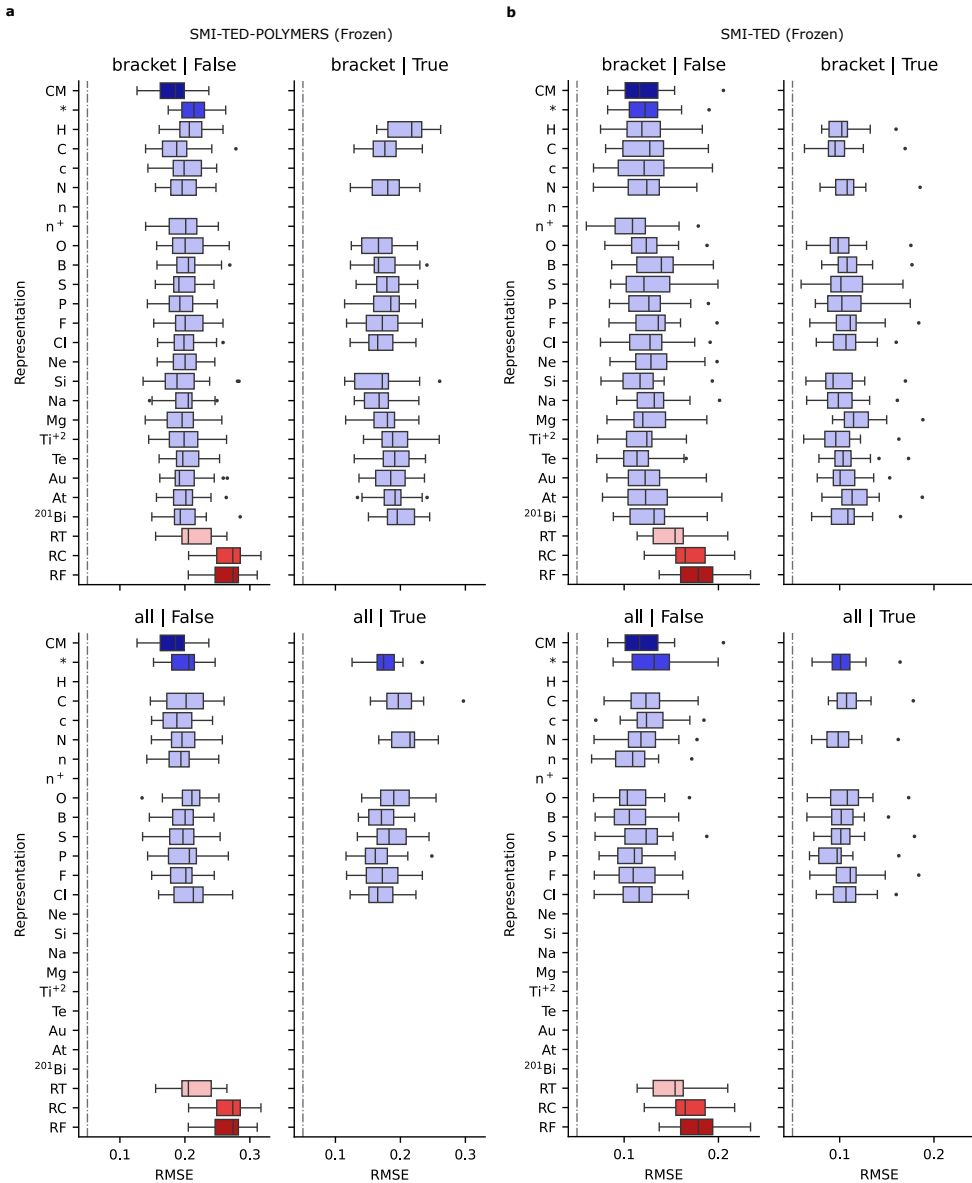


Fig. 82 Box plots for E_{at} repeated cross-validation experiments for SMI-TED-POLYMER **(a)** and SMI-TED **(b)** models with frozen weights.

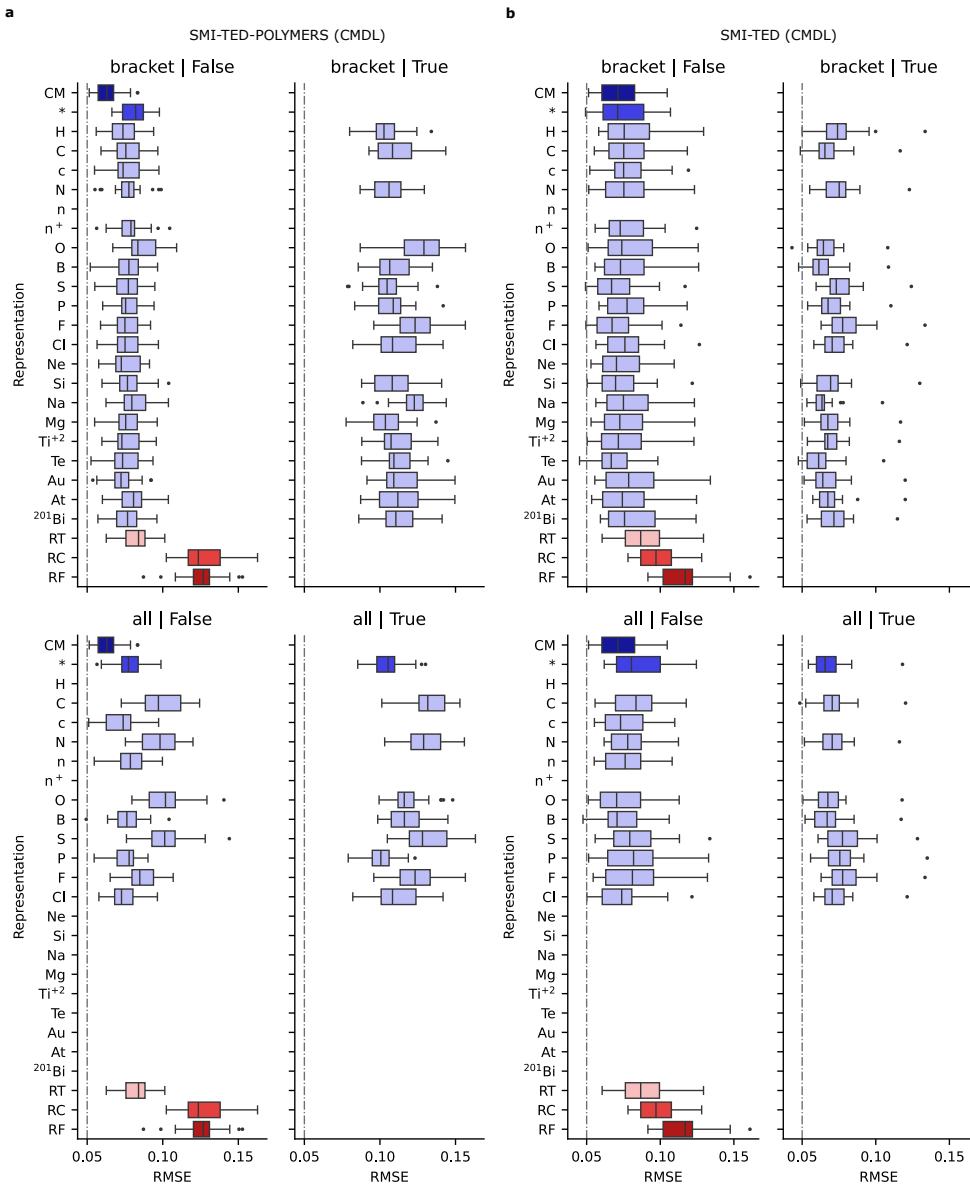


Fig. 83 Box plots for E_{at} repeated cross-validation experiments for SMI-TED-POLYMER **(a)** and SMI-TED **(b)** models fine-tuned with the CPG polymer graphs.

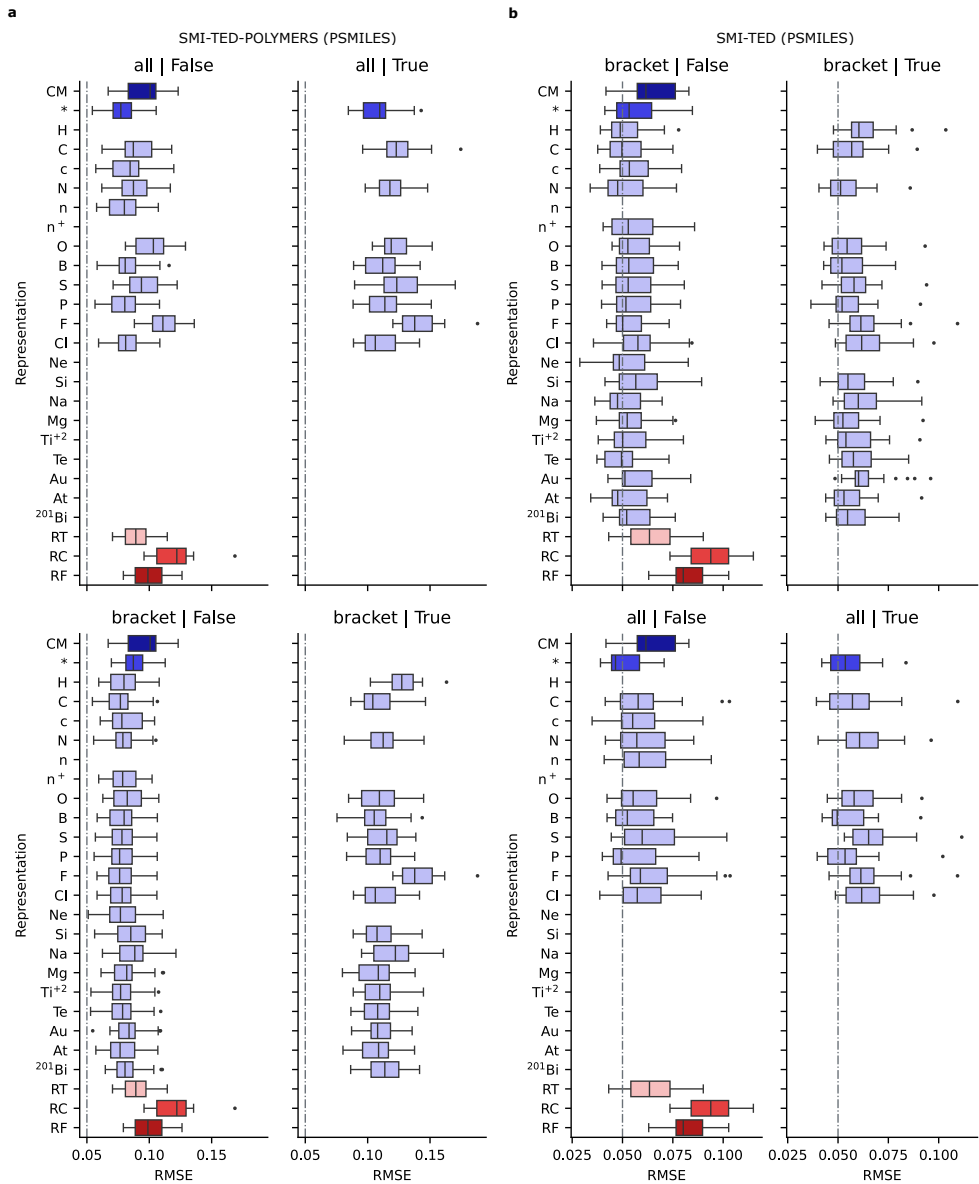


Fig. 84 Box plots for E_{at} repeated cross-validation experiments for SMI-TED-POLYMER (a) and SMI-TED (b) models fine-tuned with PSMILES.

2.6.12 Polymer Atomization Energy (E_{at}) Random Split Scores

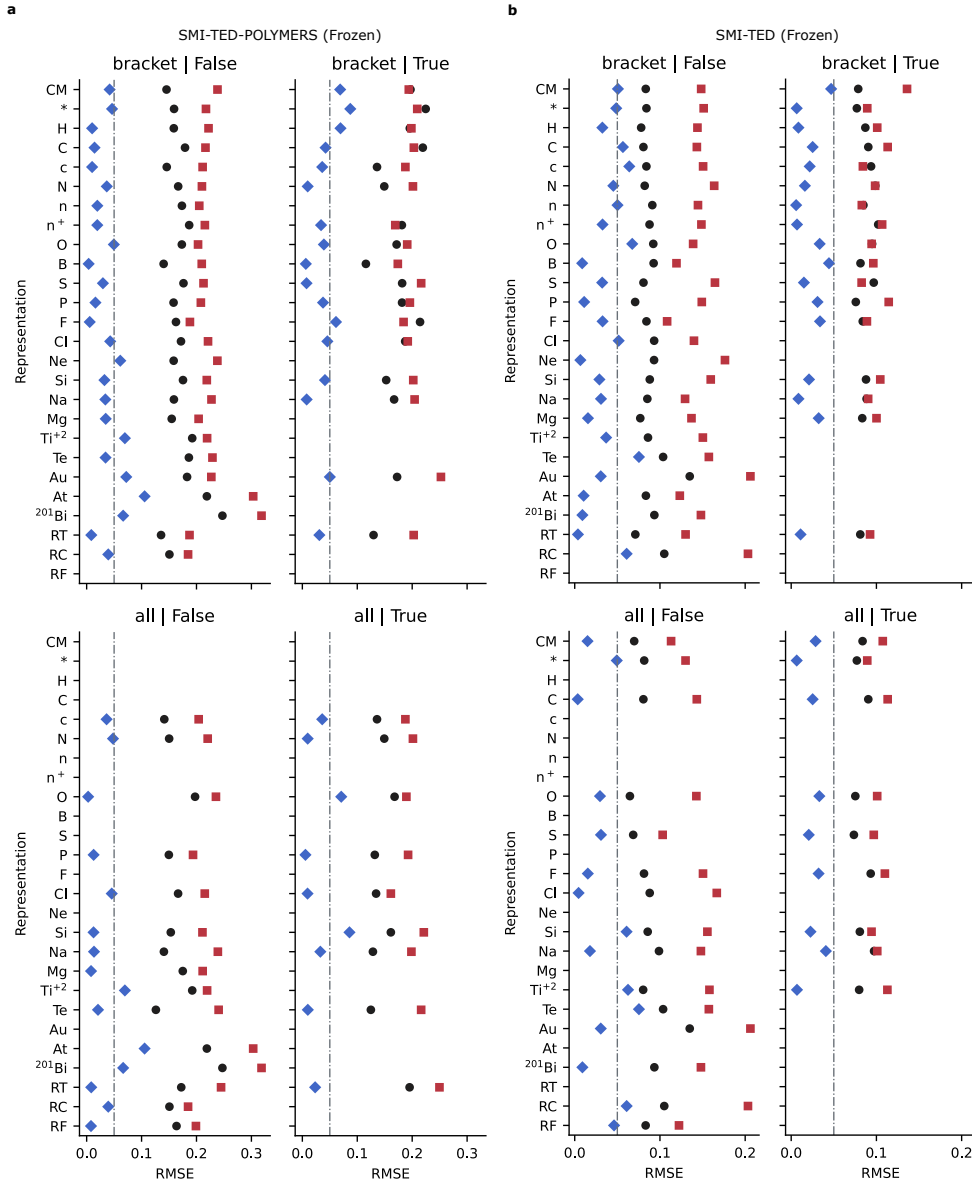


Fig. 85 Point plots for E_{at} benchmark experiments of RMSE using the base random train, valid, and test splits for SMI-TED-POLYMER (a) and SMI-TED (b) models with frozen weights.

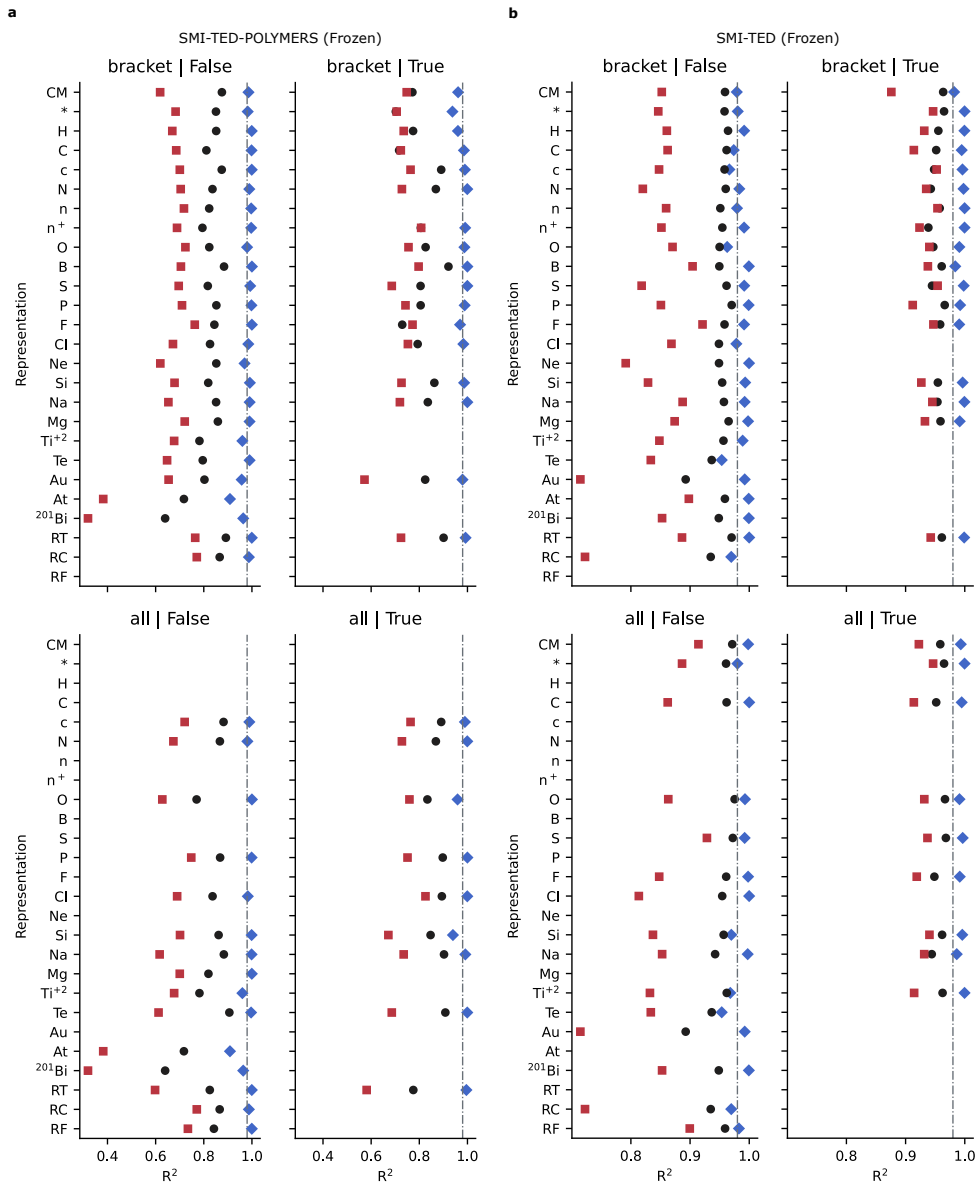


Fig. 86 Point plots for E_{at} benchmark experiments of R^2 using the base random train, valid, and test splits for SMI-TED-POLYMER (a) and SMI-TED (b) models with frozen weights.

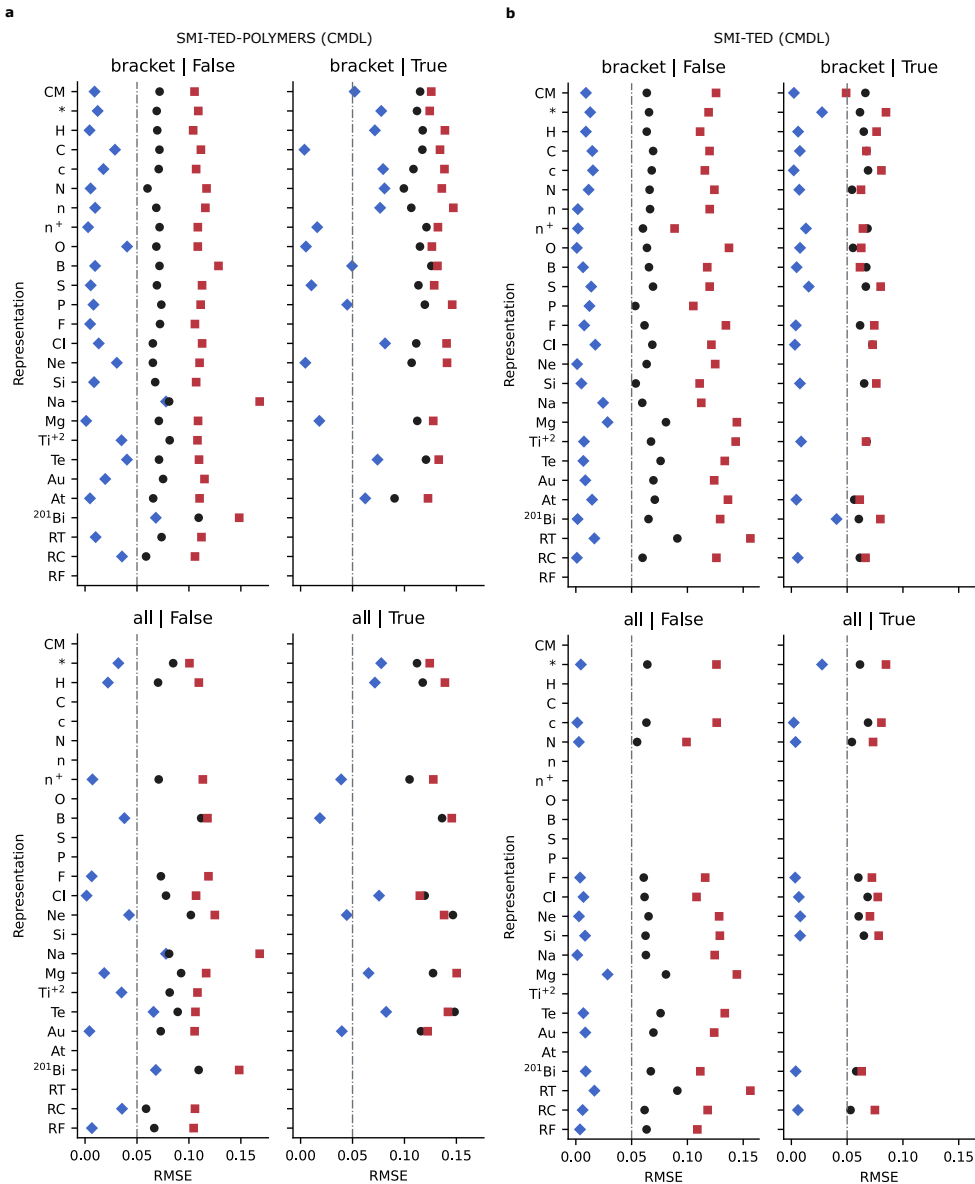


Fig. 87 Point plots for E_{at} benchmark experiments of RMSE using the base random train, valid, and test splits for SMI-TED-POLYMER (a) and SMI-TED (b) models fine-tuned using the CPG representation.

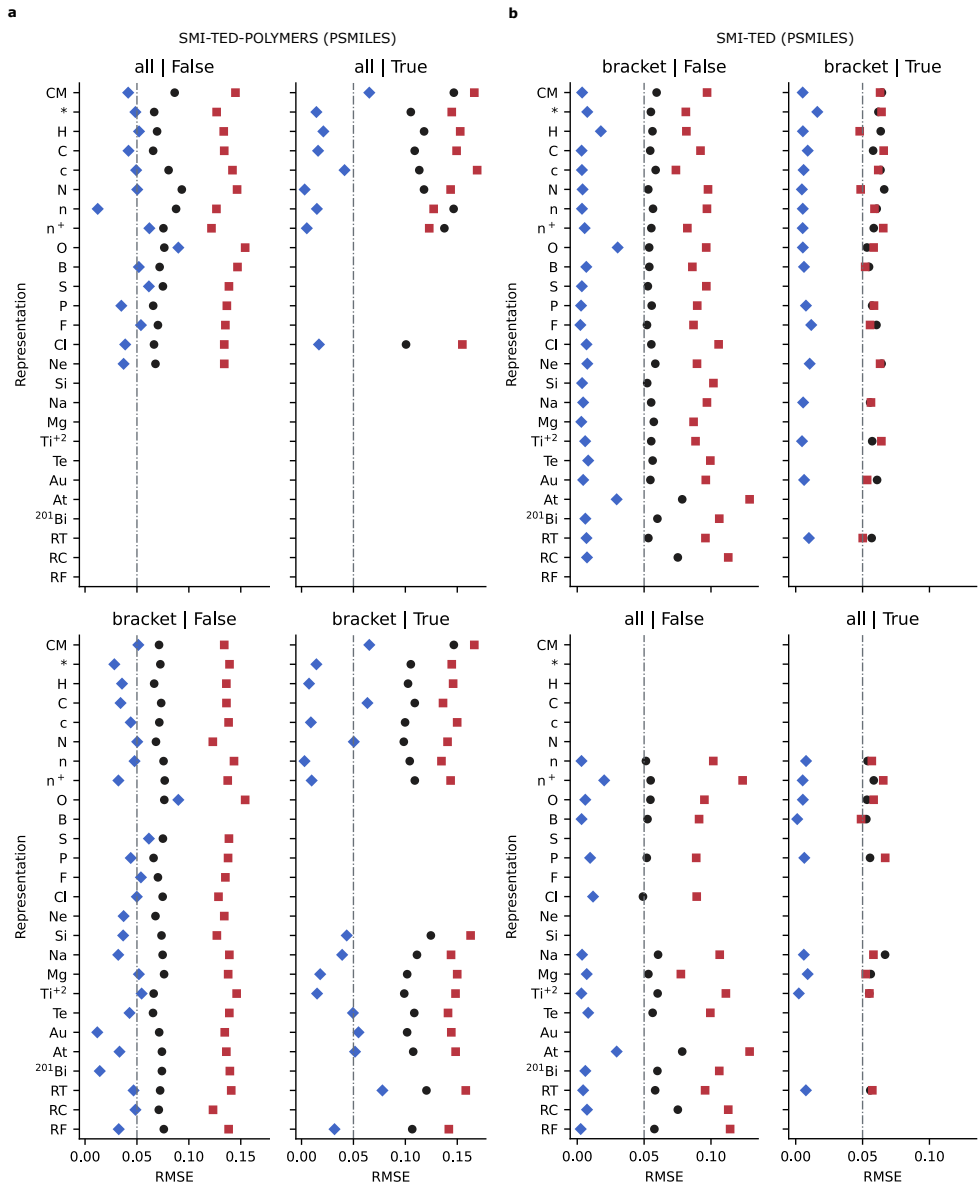


Fig. 89 Point plots for E_{at} benchmark experiments of RMSE using the base random train, valid, and test splits for SMI-TED-POLYMER (a) and SMI-TED (b) models fine-tuned using PSMILES.

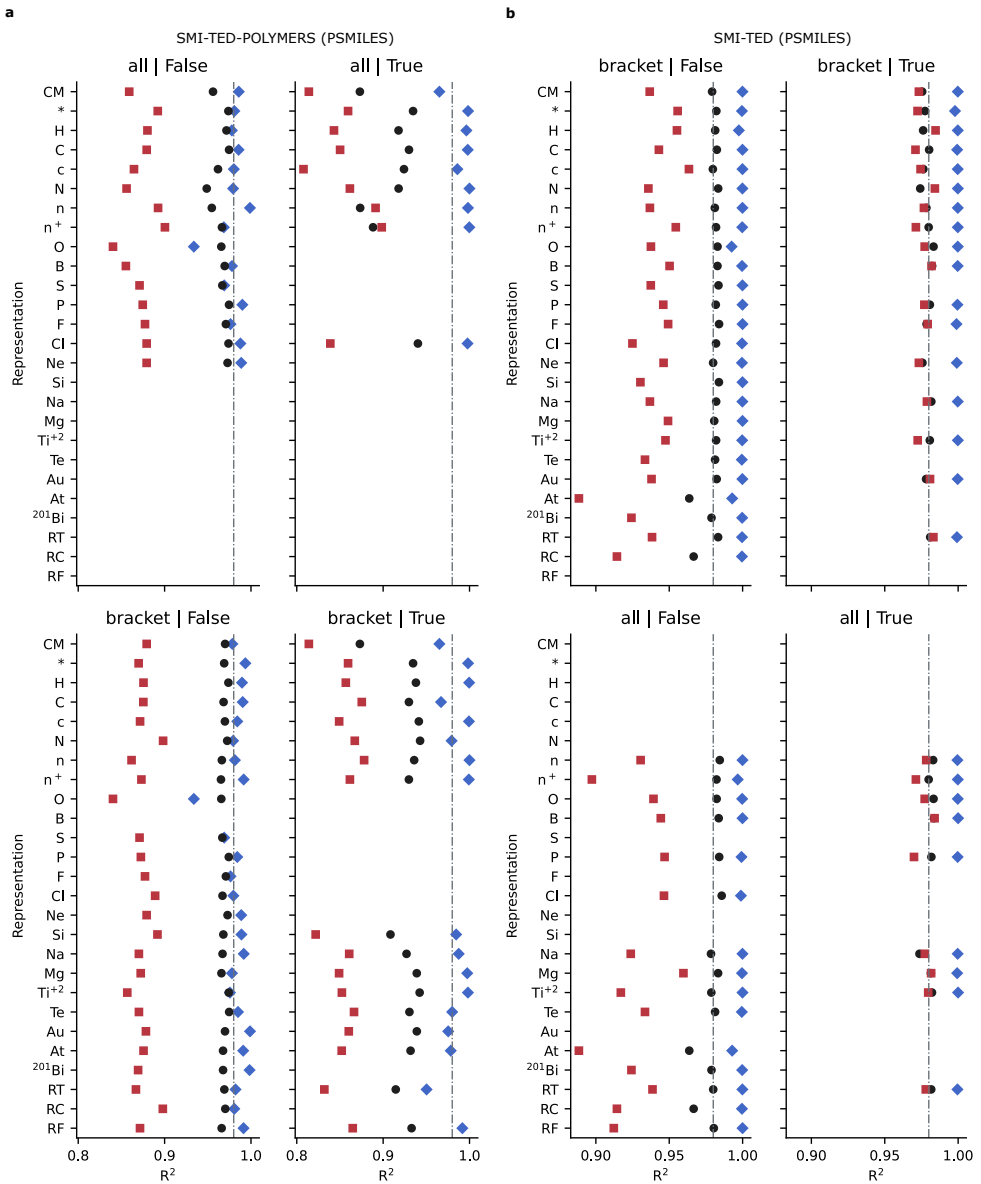


Fig. 90 Point plots for E_i benchmark experiments of R^2 using the base random train, valid, and test splits for SMI-TED-POLYMER (a) and SMI-TED (b) models fine-tuned using PSMILES.

2.6.13 Refractivity Index (N_c) CV Scores

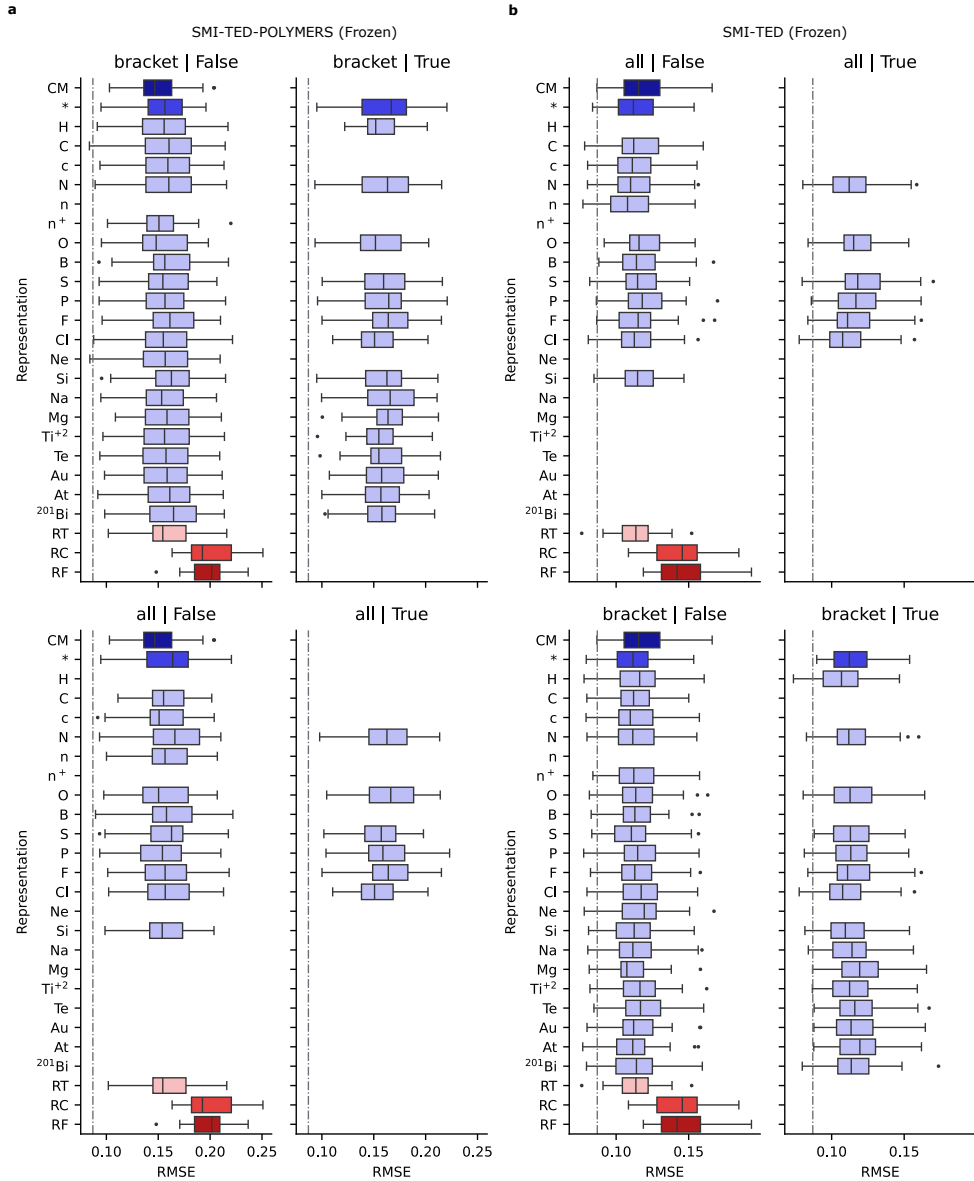


Fig. 91 Box plots for N_c repeated cross-validation experiments for SMI-TED-POLYMER (a) and SMI-TED (b) models with frozen weights.

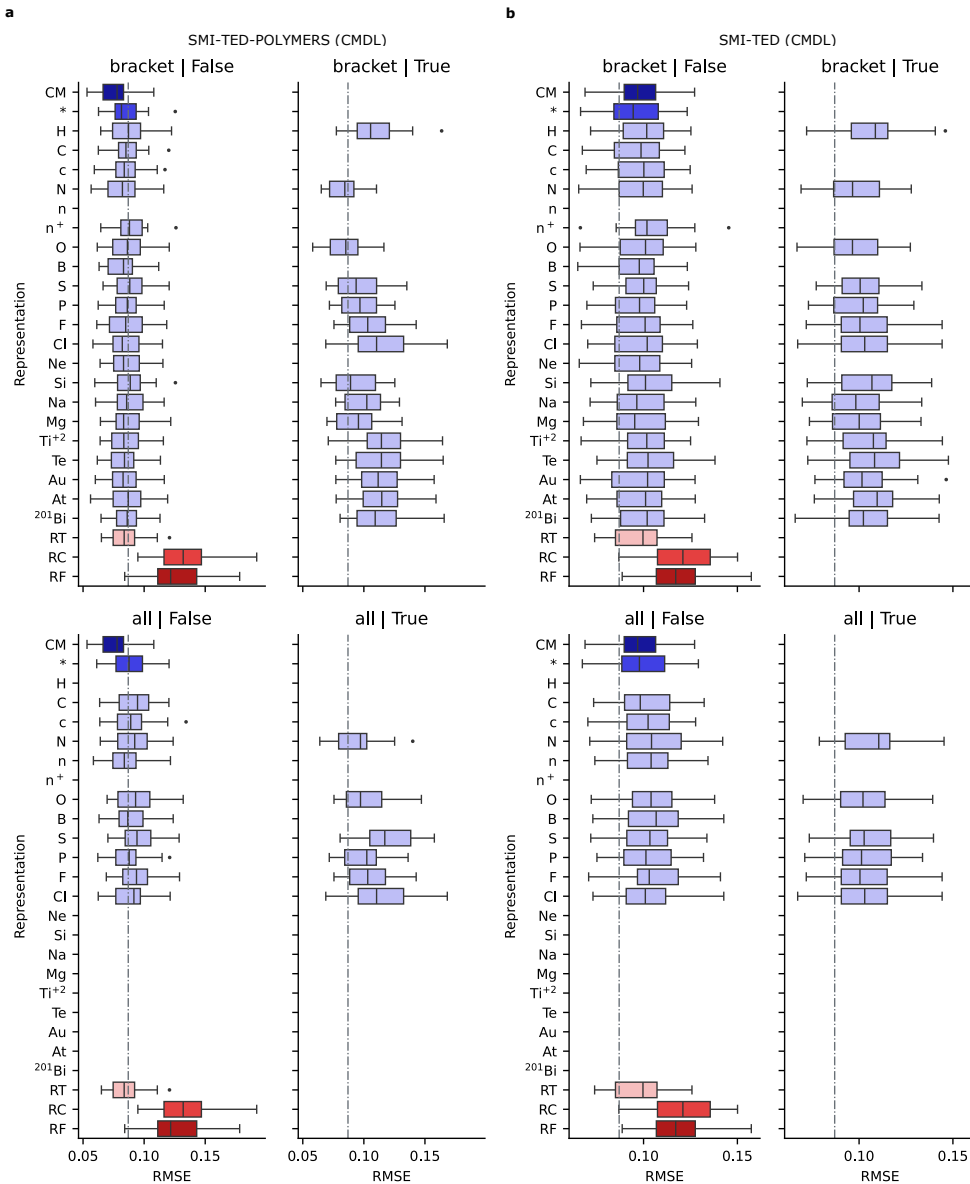


Fig. 92 Box plots for N_c repeated cross-validation experiments for SMI-TED-POLYMER **(a)** and SMI-TED **(b)** models fine-tuned with the CPG polymer graphs.

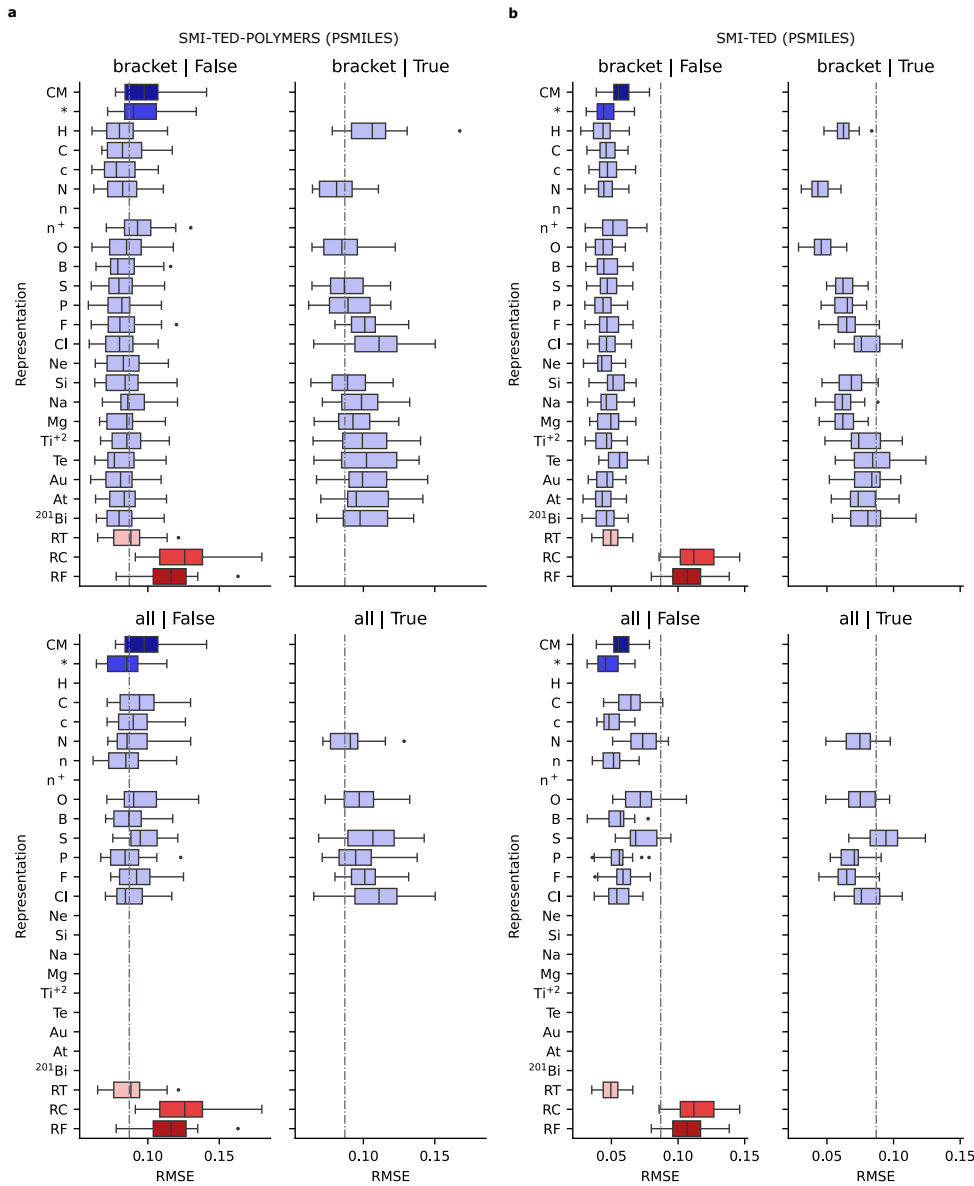


Fig. 93 Box plots for N_c repeated cross-validation experiments for SMI-TED-POLYMER (a) and SMI-TED (b) models fine-tuned with PSMILES.

2.6.14 Refractivity Index (N_c) Random Split Scores

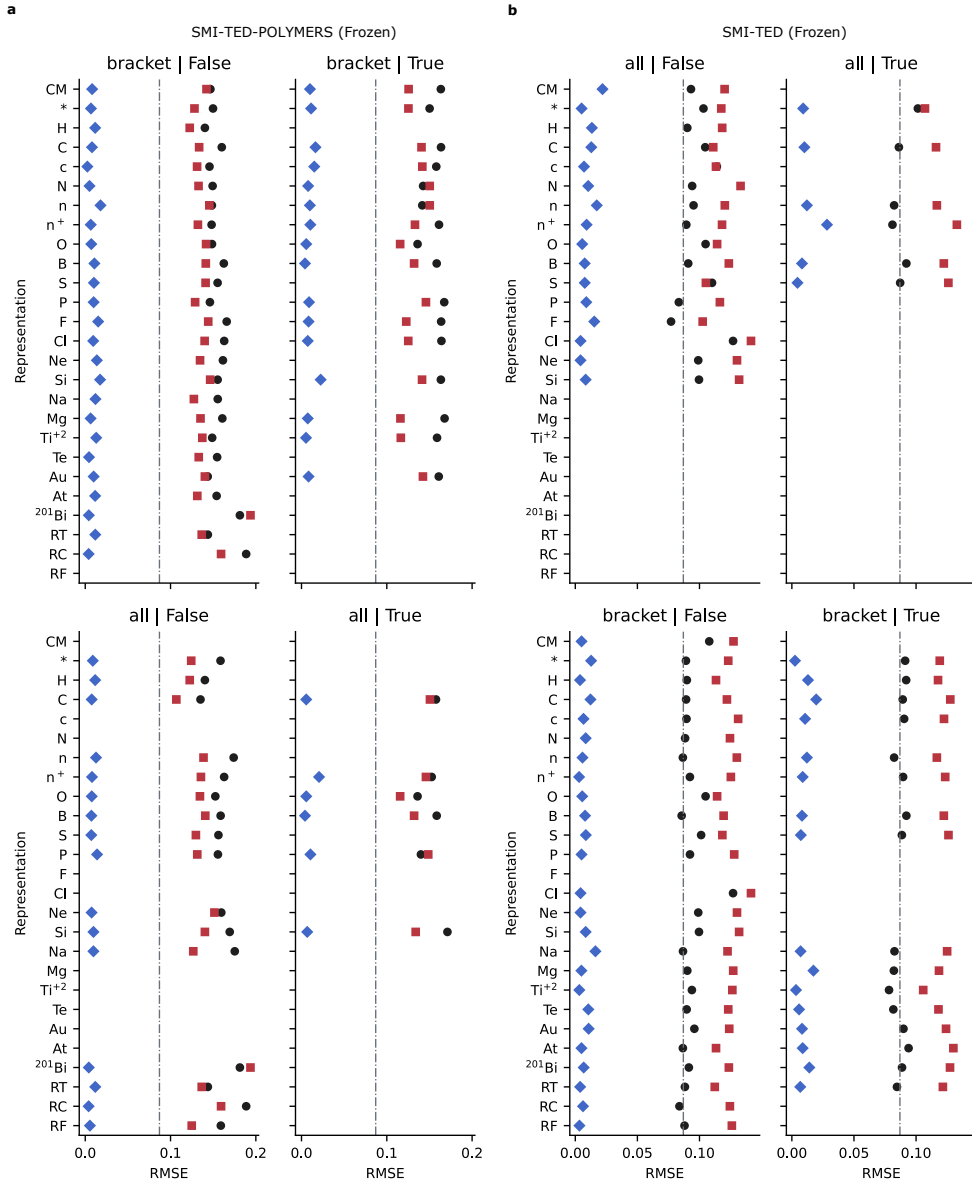


Fig. 94 Point plots for N_c benchmark experiments of RMSE using the base random train, valid, and test splits for SMI-TED-POLYMER (a) and SMI-TED (b) models with frozen weights.

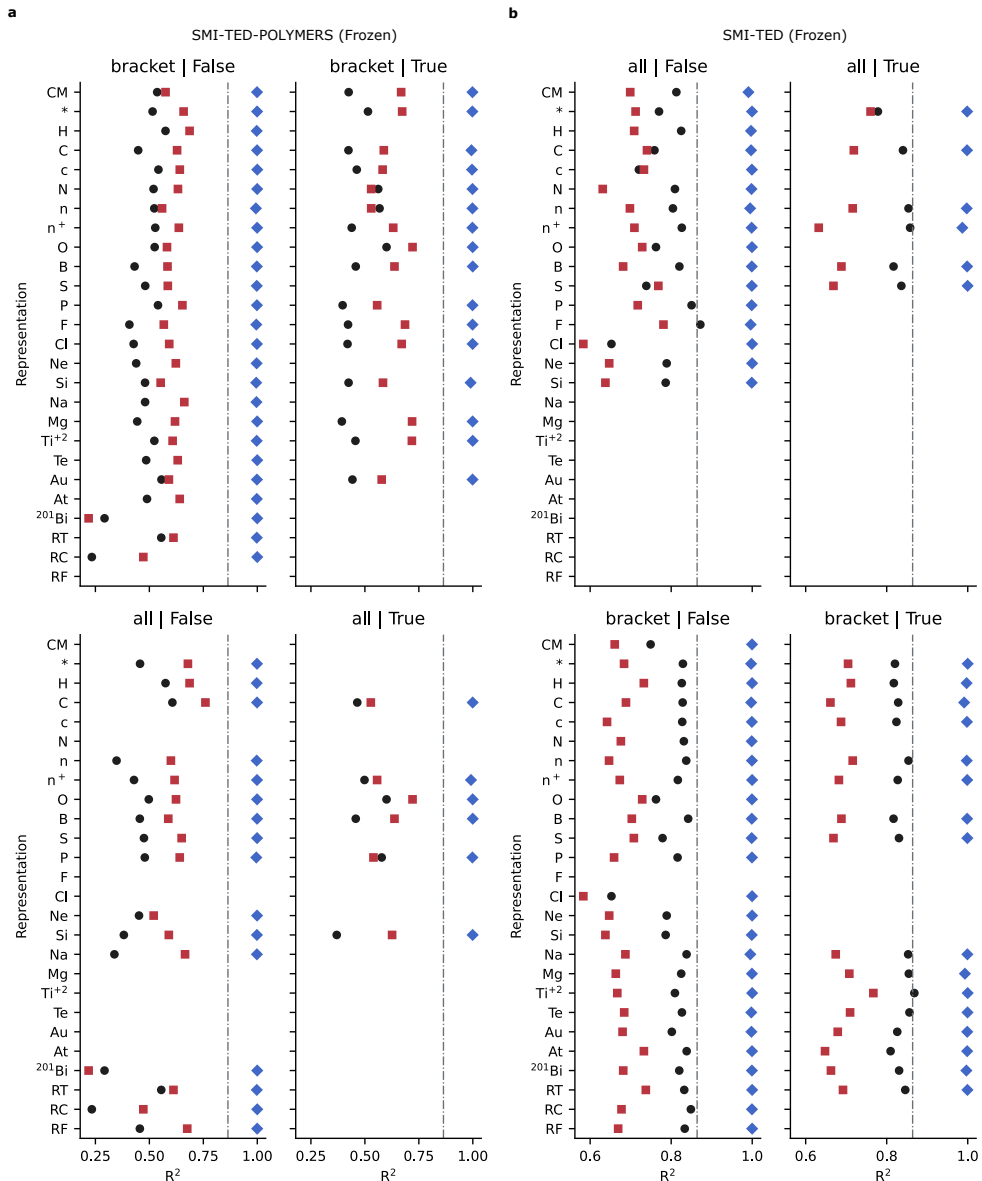


Fig. 95 Point plots for N_c benchmark experiments of R^2 using the base random train, valid, and test splits for SMI-TED-POLYMER (a) and SMI-TED (b) models with frozen weights.

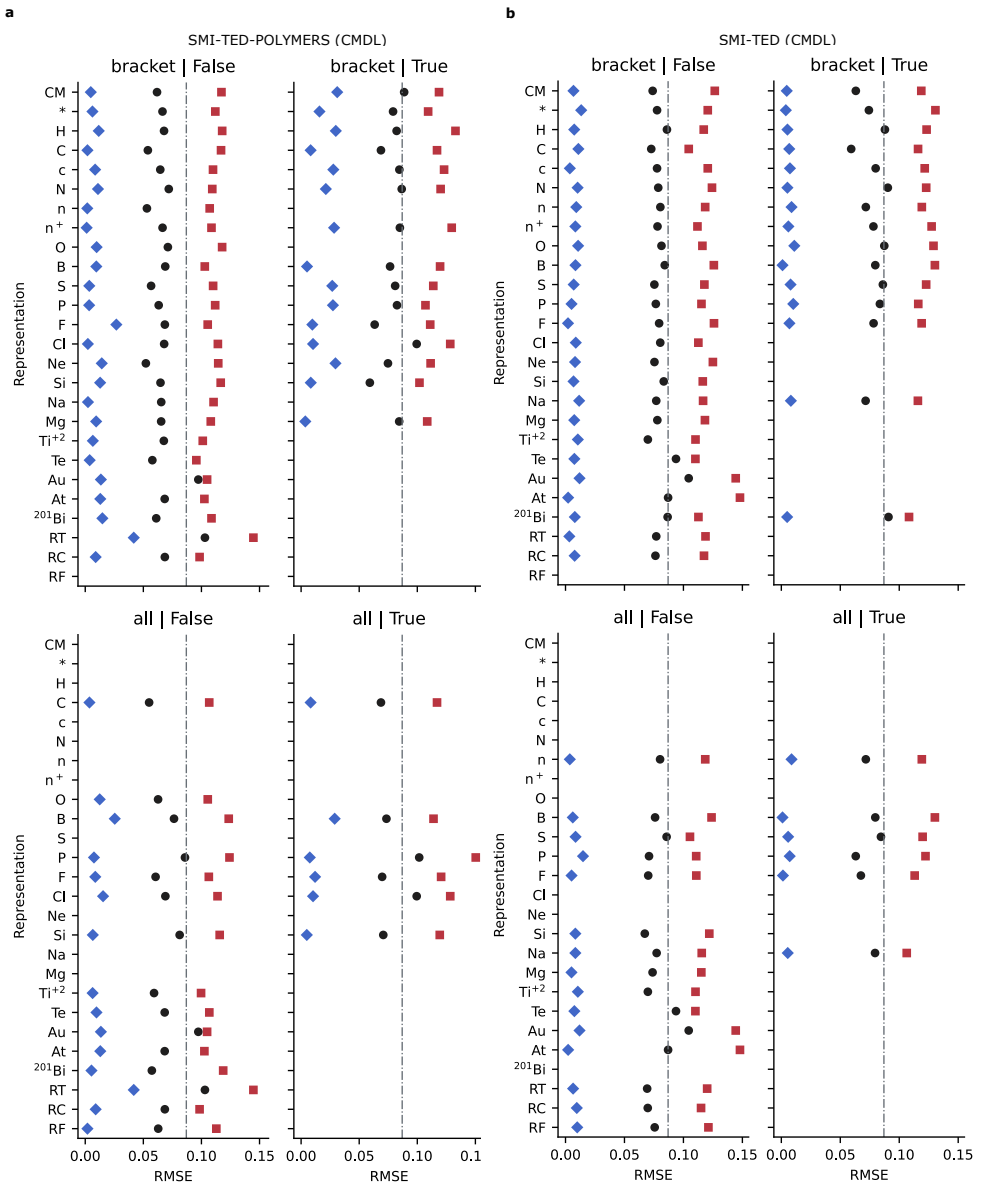


Fig. 96 Point plots for N_c benchmark experiments of RMSE using the base random train, valid, and test splits for SMI-TED-POLYMER (a) and SMI-TED (b) models fine-tuned with CPG.

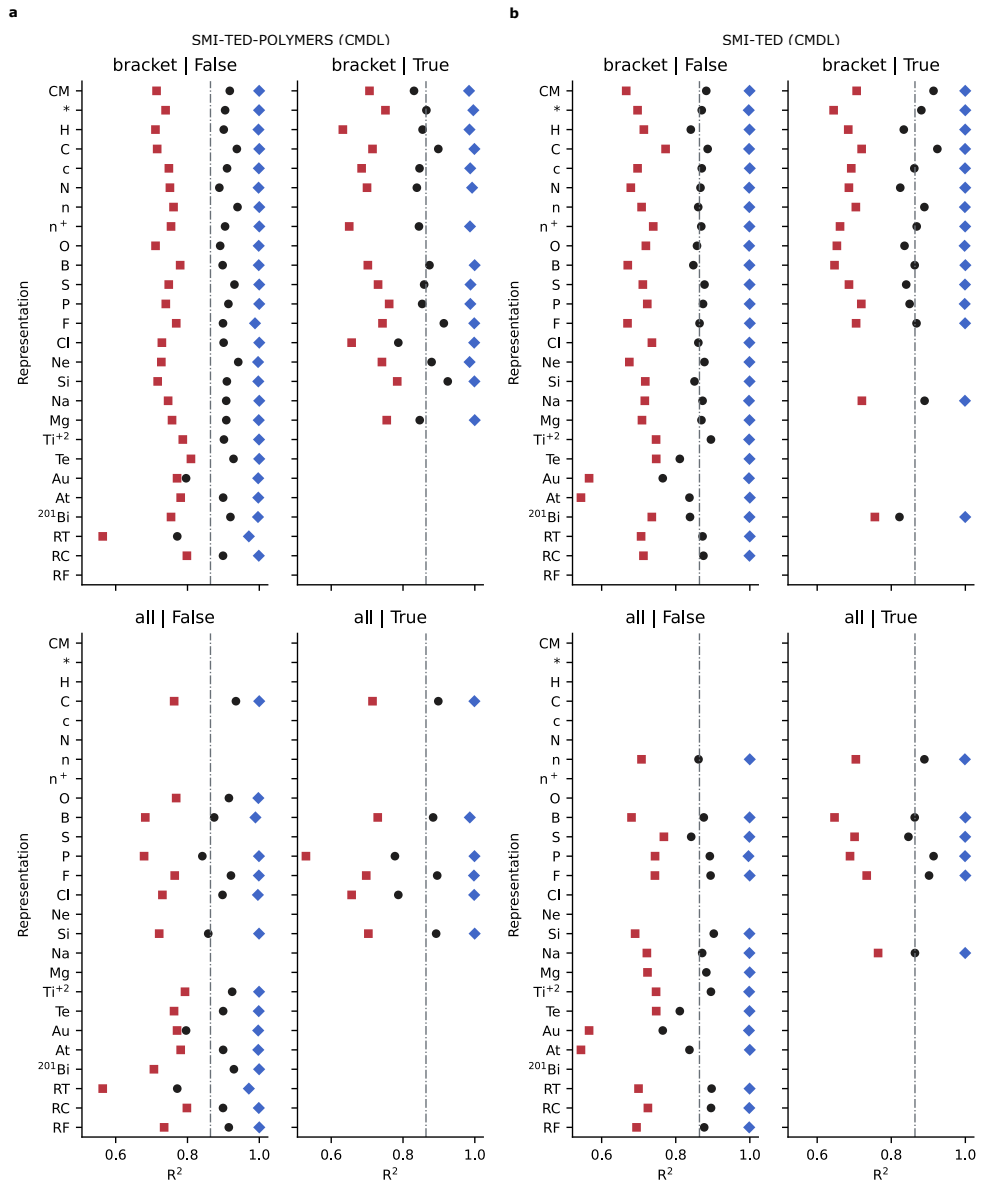


Fig. 97 Point plots for N_c benchmark experiments of R^2 using the base random train, valid, and test splits for SMI-TED-POLYMER (a) and SMI-TED (b) models fine-tuned with CPG.

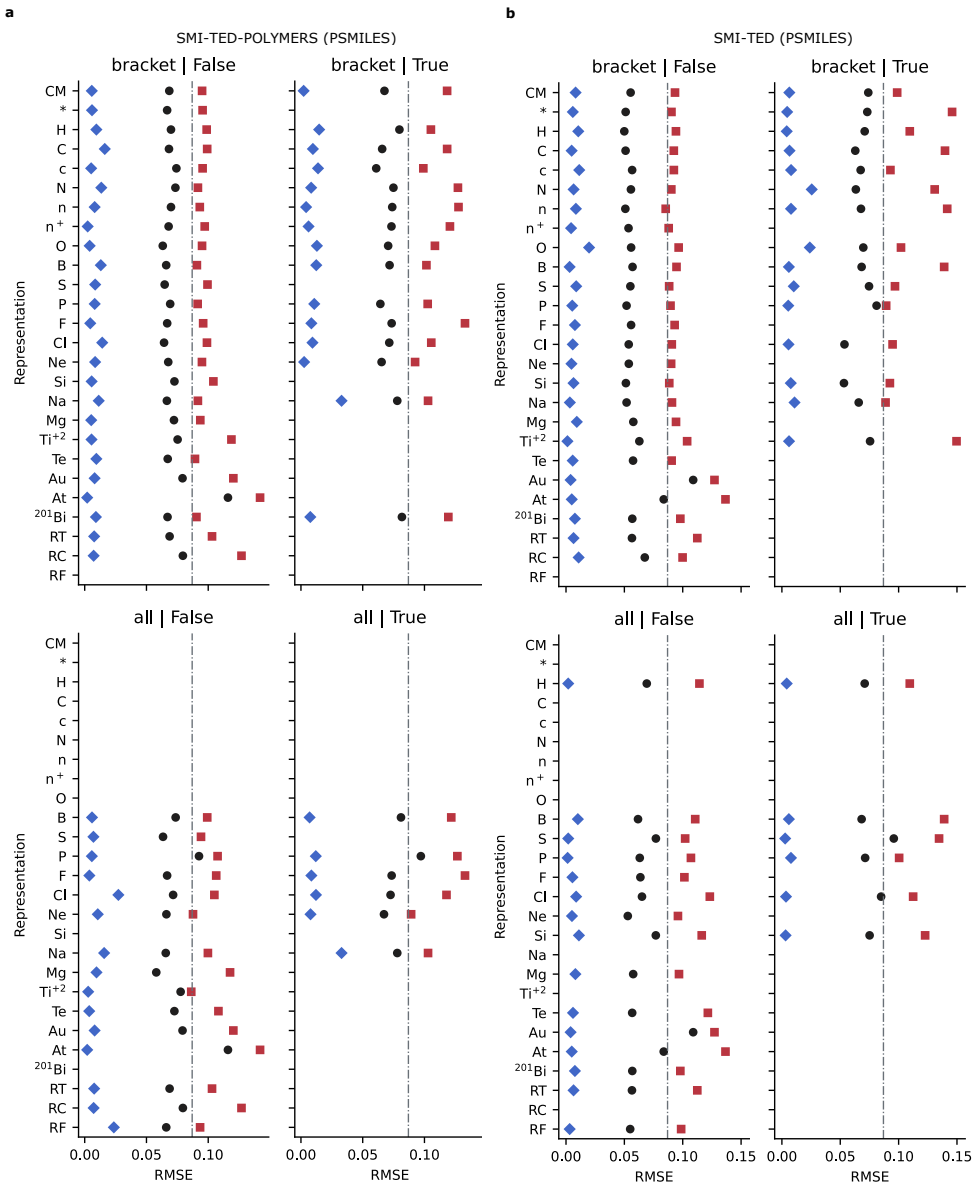


Fig. 98 Point plots for N_c benchmark experiments of RMSE using the base random train, valid, and test splits for SMI-TED-POLYMER (a) and SMI-TED (b) models fine-tuned with PSMILES.

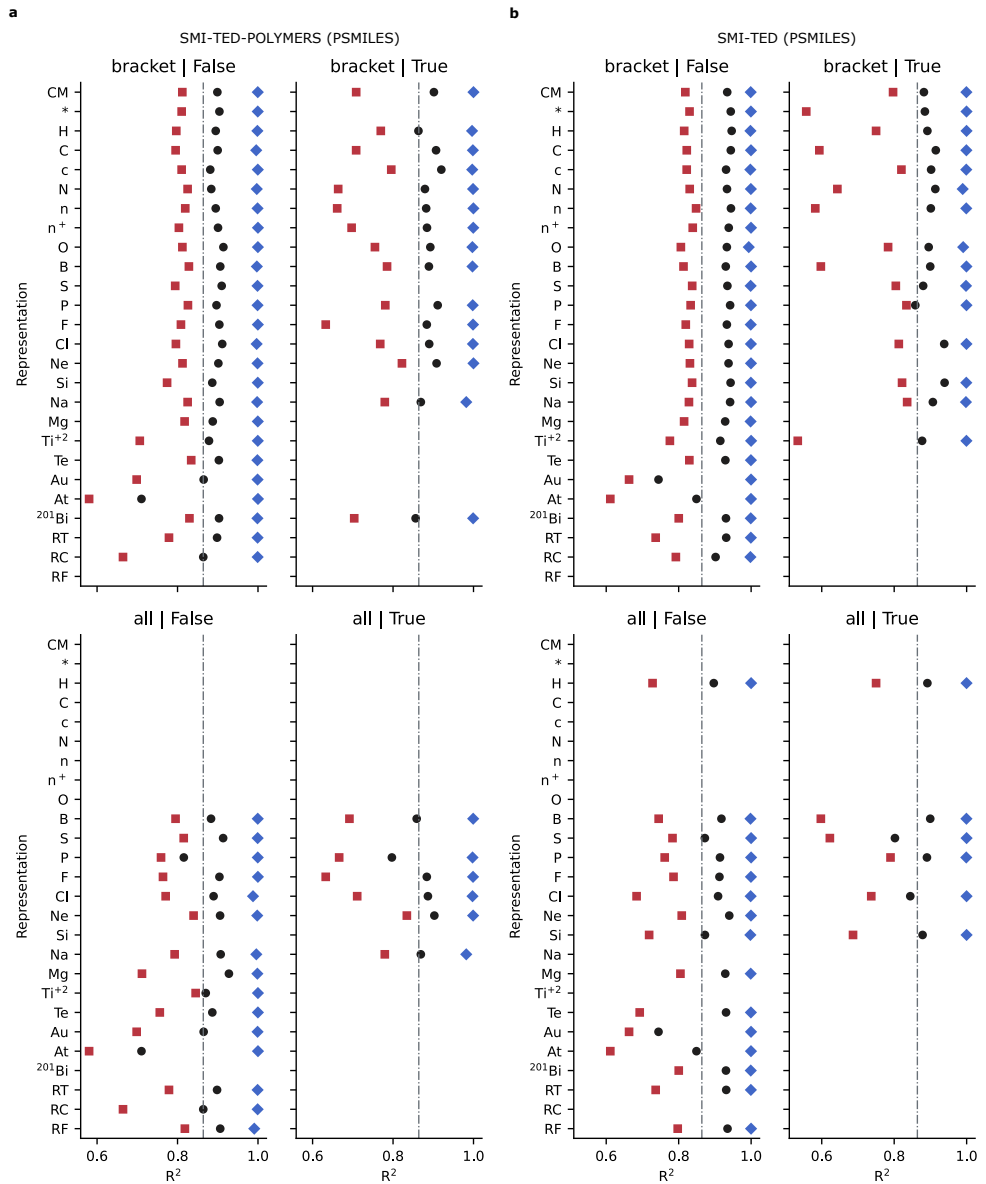


Fig. 99 Point plots for N_c benchmark experiments of R^2 using the base random train, valid, and test splits for SMI-TED-POLYMER (a) and SMI-TED (b) models fine-tuned with PSMILES.

2.6.15 Crystallization Tendency (X_c) CV Scores

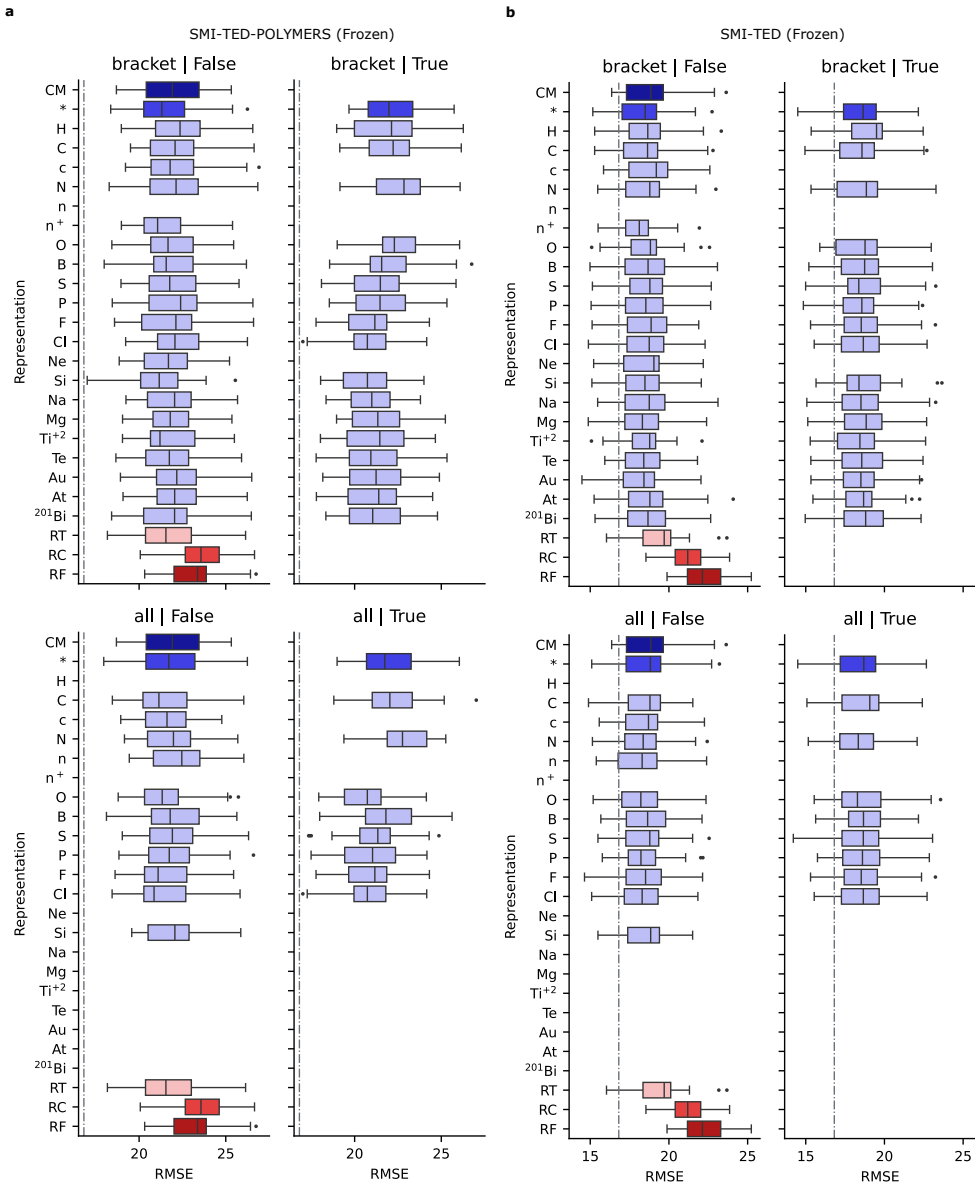


Fig. 100 Box plots for X_c repeated cross-validation experiments for SMI-TED-POLYMER **(a)** and SMI-TED **(b)** models with frozen weights.

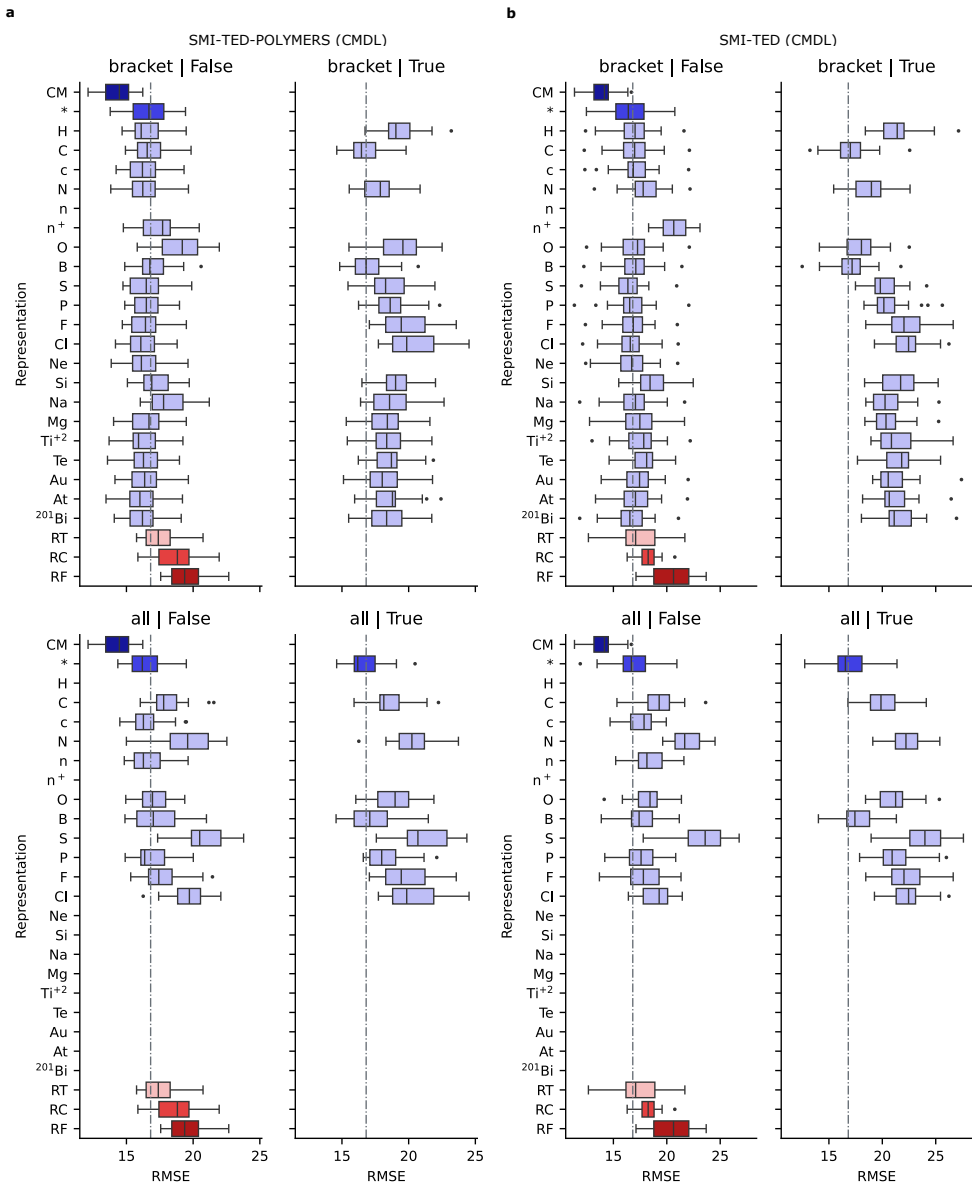


Fig. 101 Box plots for X_c repeated cross-validation experiments for SMI-TED-POLYMER (a) and SMI-TED (b) models fine-tuned with the CPG polymer graphs.

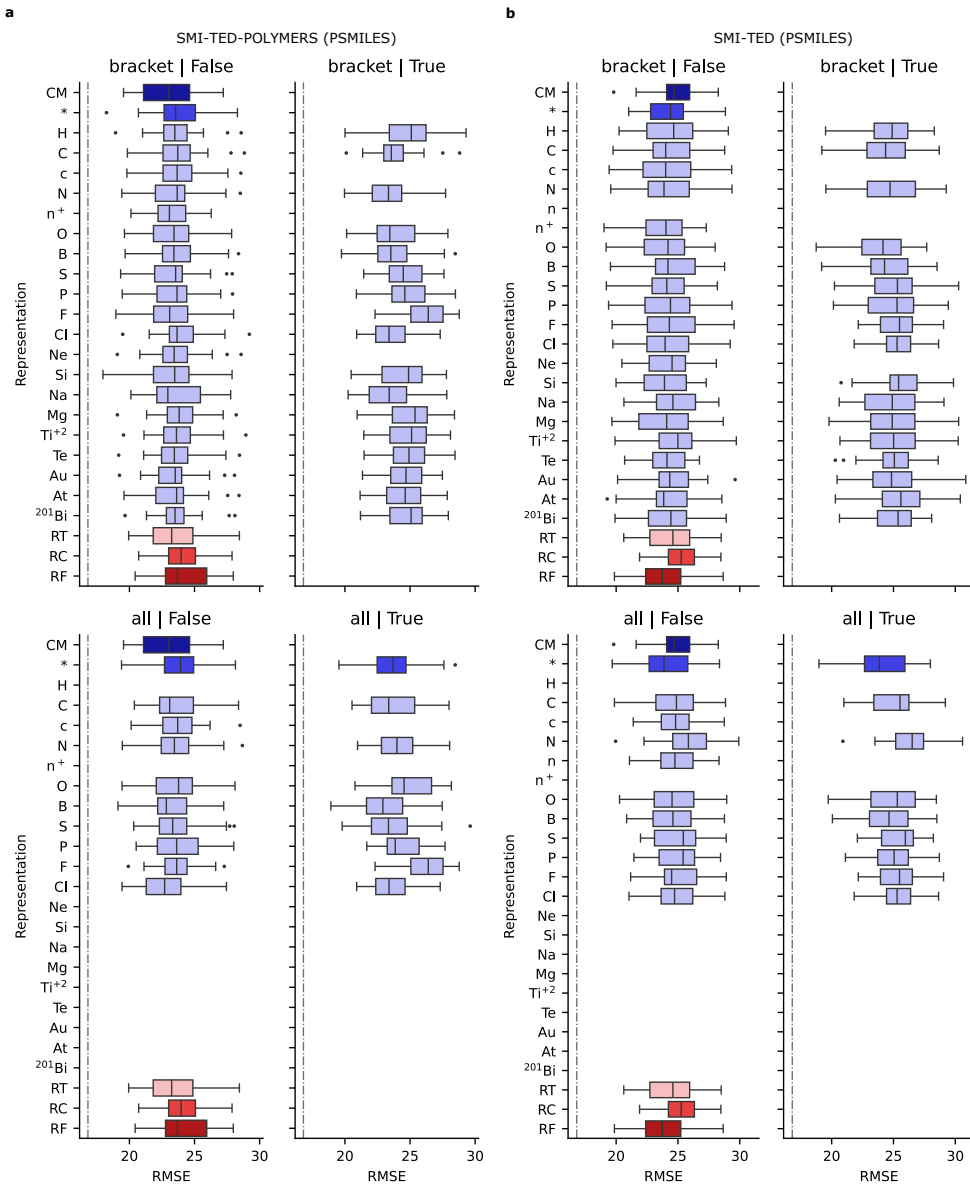


Fig. 102 Box plots for X_c repeated cross-validation experiments for SMI-TED-POLYMER **(a)** and SMI-TED **(b)** models fine-tuned with PSMILES.

2.6.16 Crystallization Tendency (X_c) Random Split Scores

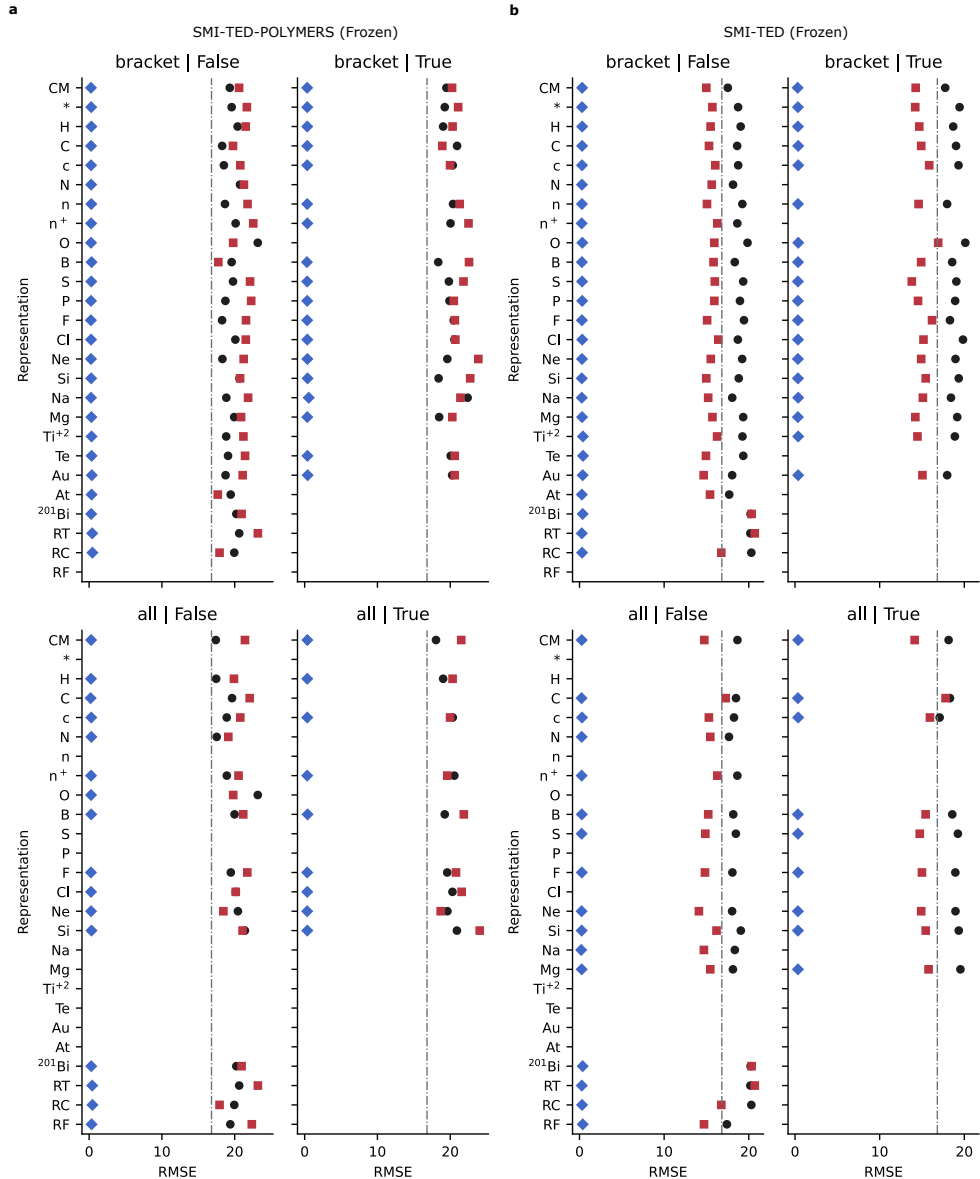


Fig. 103 Point plots for X_c benchmark experiments of RMSE using the base random train, valid, and test splits for SMI-TED-POLYMER (a) and SMI-TED (b) models with frozen weights.

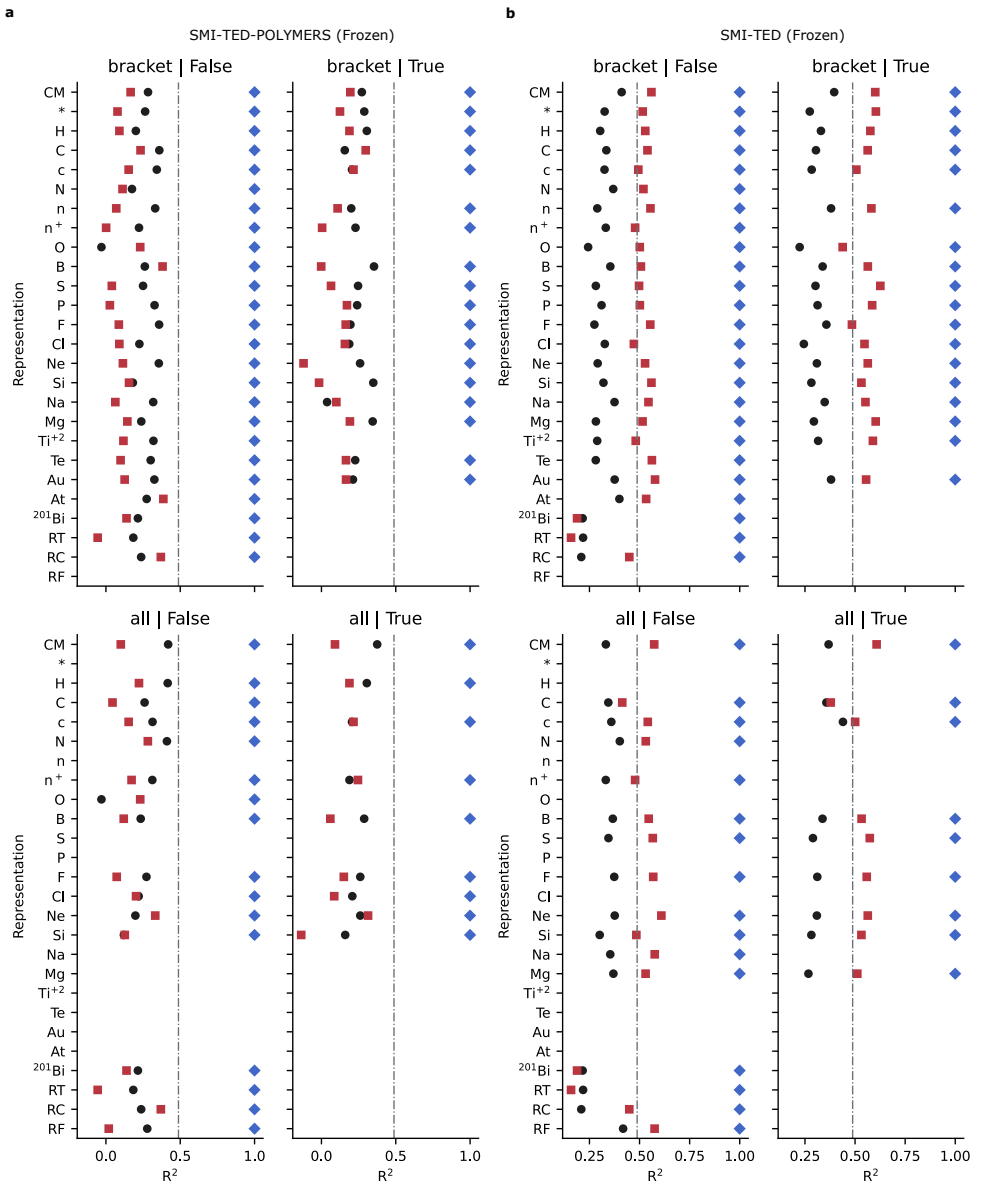


Fig. 104 Point plots for X_c benchmark experiments of R^2 using the base random train, valid, and test splits for SMI-TED-POLYMER (a) and SMI-TED (b) models with frozen weights.

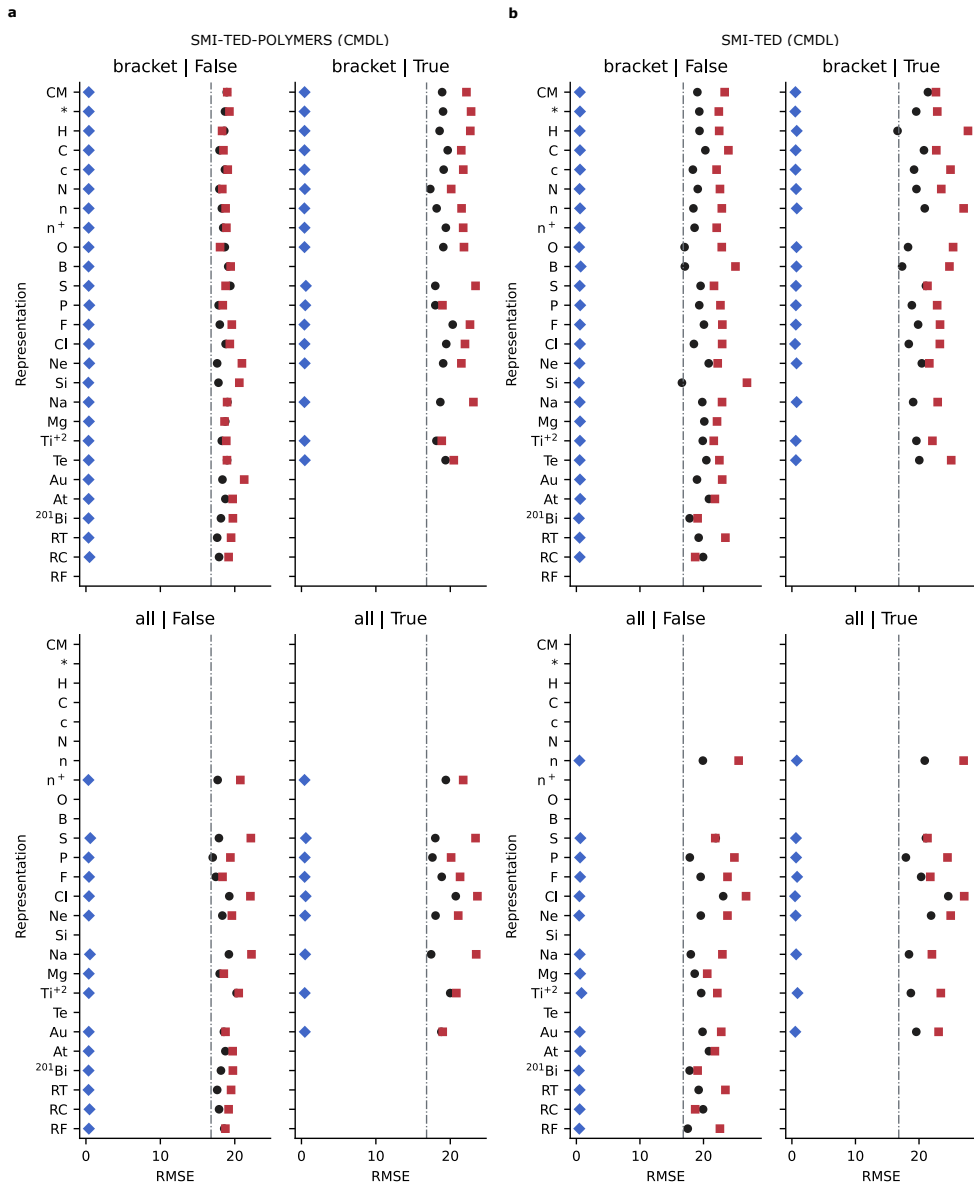


Fig. 105 Point plots for X_c benchmark experiments of RMSE using the base random train, valid, and test splits for SMI-TED-POLYMER (a) and SMI-TED (b) models fine-tuned with CPG.

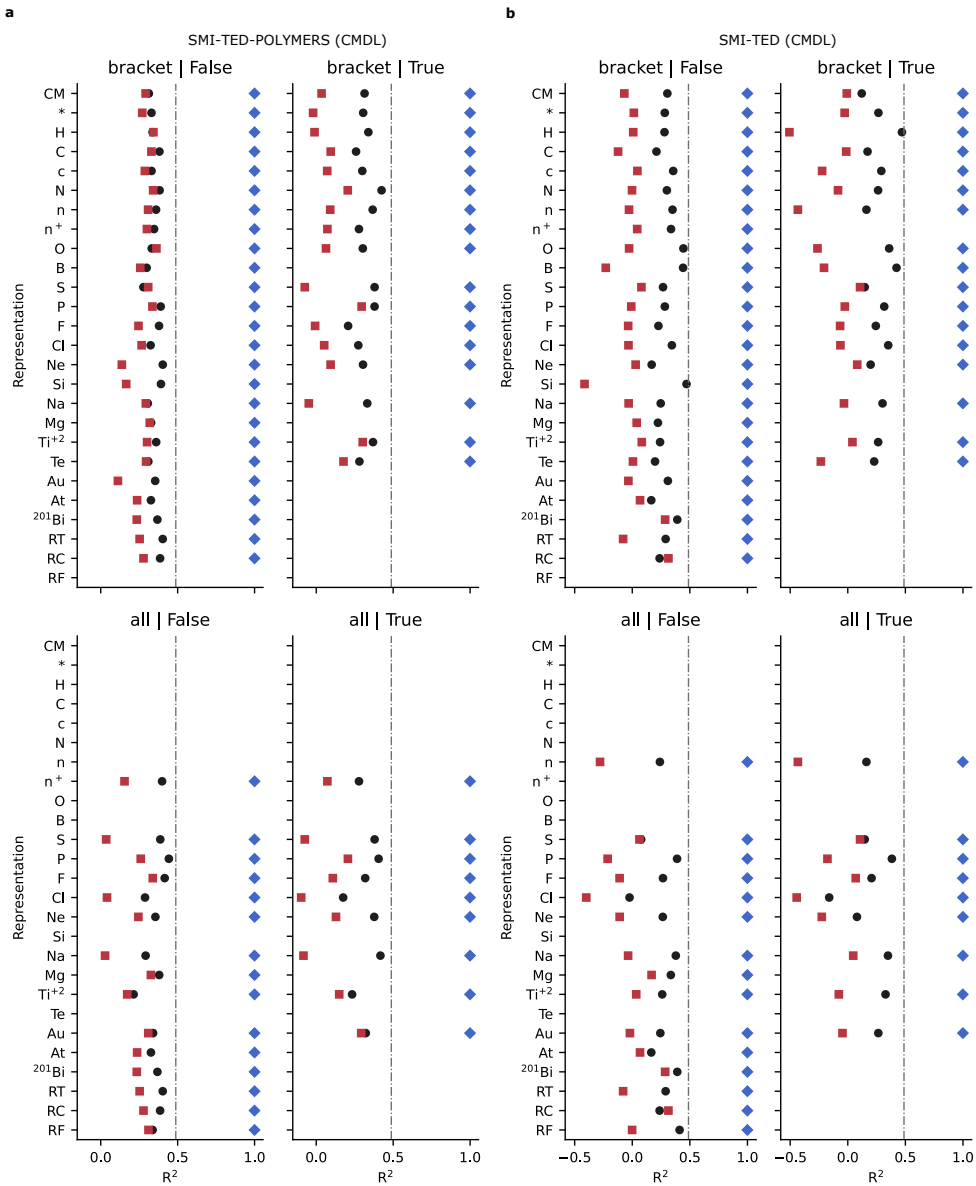


Fig. 106 Point plots for X_c benchmark experiments of R^2 using the base random train, valid, and test splits for SMI-TED-POLYMER (a) and SMI-TED (b) models fine-tuned with CPG.

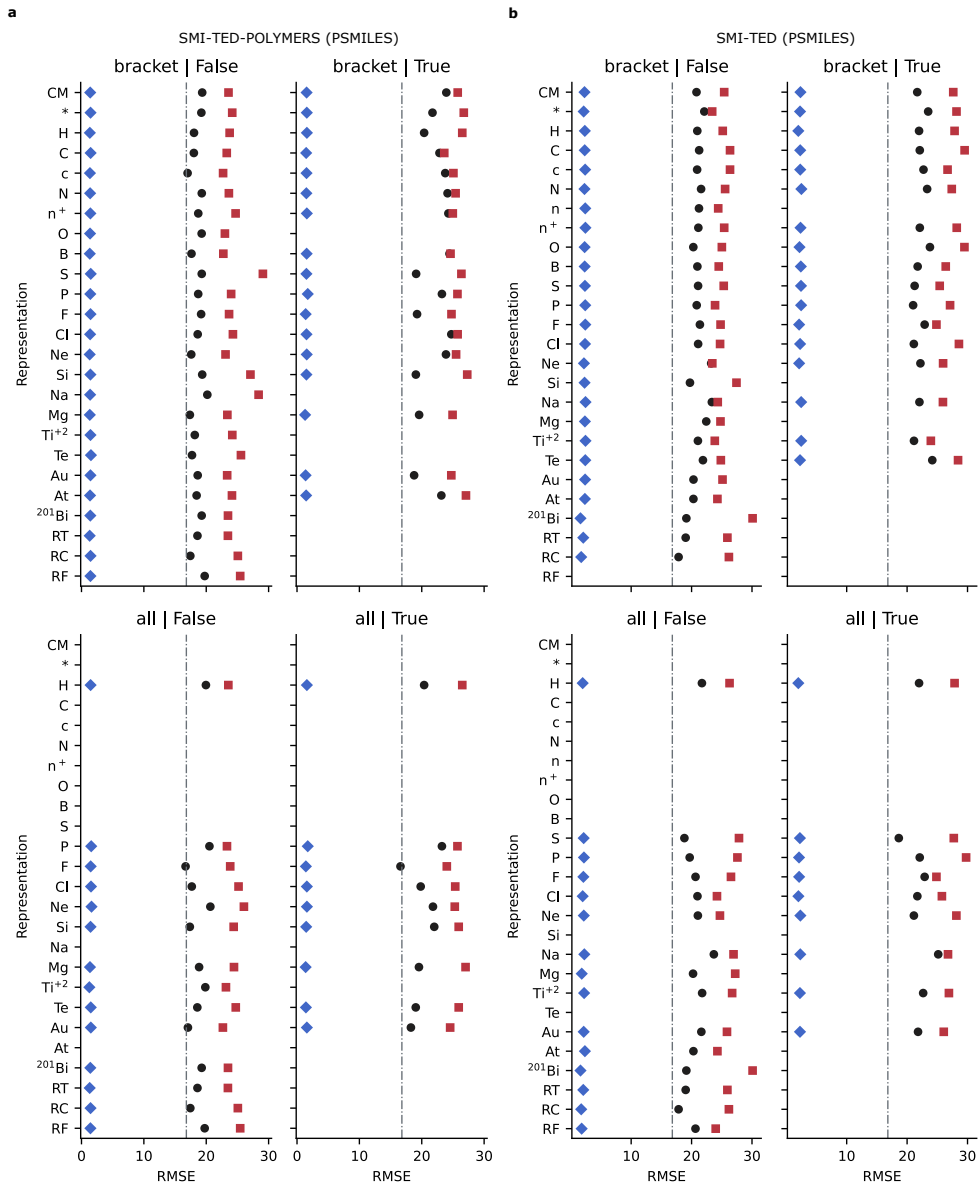


Fig. 107 Point plots for X_c benchmark experiments of RMSE using the base random train, valid, and test splits for SMI-TED-POLYMER (a) and SMI-TED (b) models fine-tuned with PSMILES.

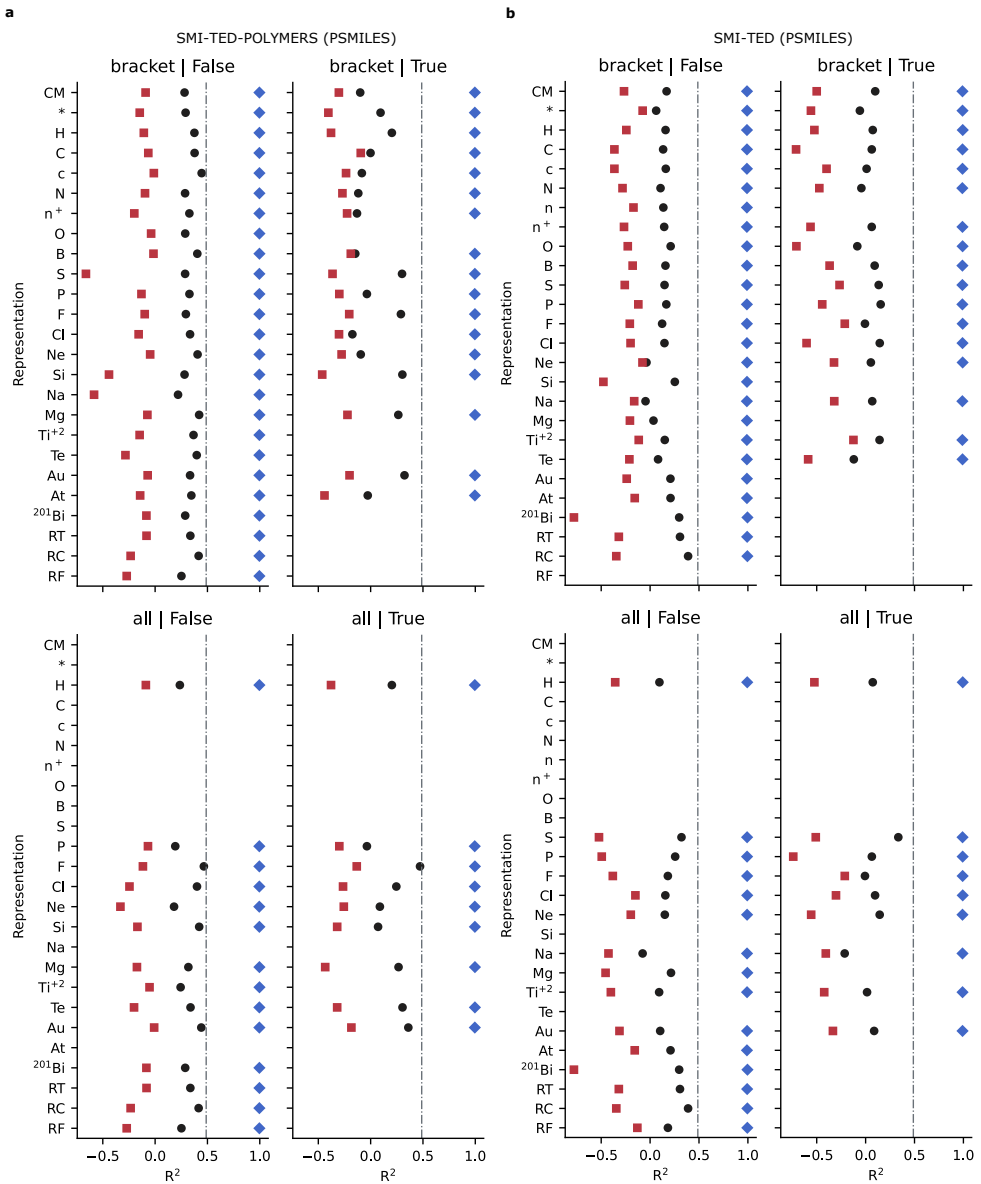


Fig. 108 Point plots for X_c benchmark experiments of R^2 using the base random train, valid, and test splits for SMI-TED-POLYMER (a) and SMI-TED (b) models fine-tuned with PSMILES.

2.6.17 Glass Transition Temperature (T_g -II) CV Scores

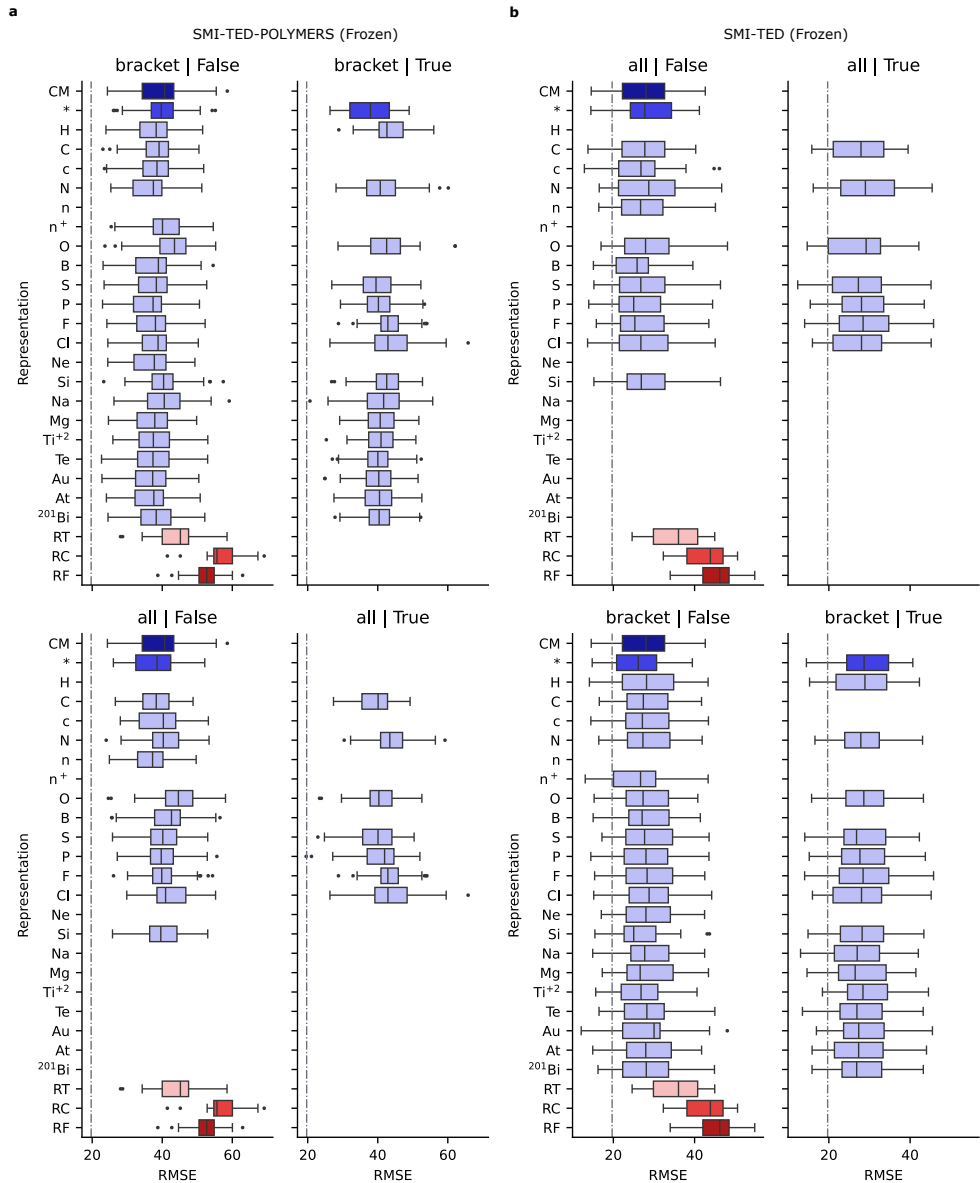


Fig. 109 Box plots for T_g -II repeated cross-validation experiments for SMI-TED-POLYMER (a) and SMI-TED (b) models with frozen weights.

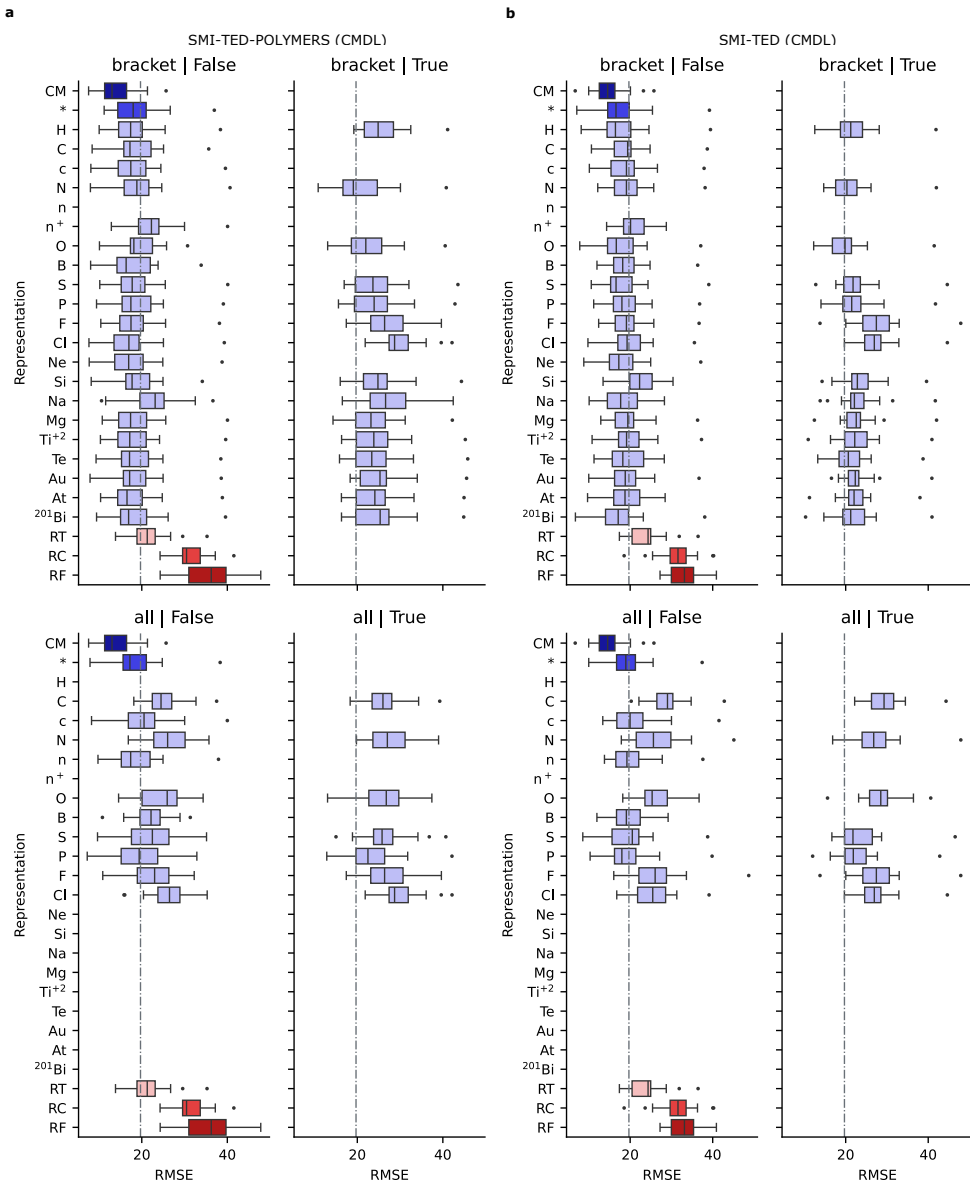


Fig. 110 Box plots for T_g -II repeated cross-validation experiments for SMI-TED-POLYMER (**a**) and SMI-TED (**b**) models fine-tuned with the CPG polymer graphs.

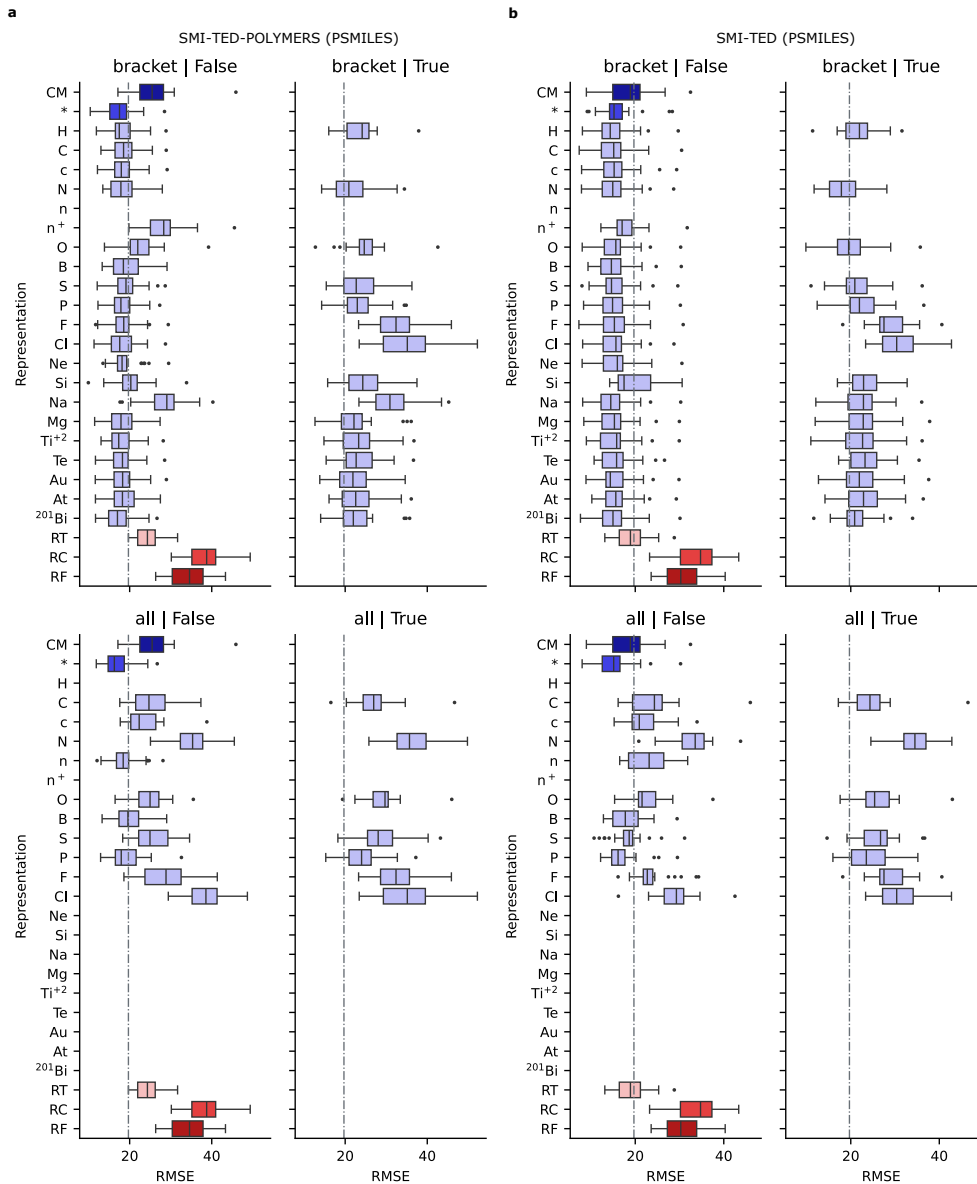


Fig. 111 Box plots for T_g -II repeated cross-validation experiments for SMI-TED-POLYMER **(a)** and SMI-TED **(b)** models fine-tuned with PSMILES.

2.6.18 Glass Transition Temperature (T_g -II) Random Split Scores

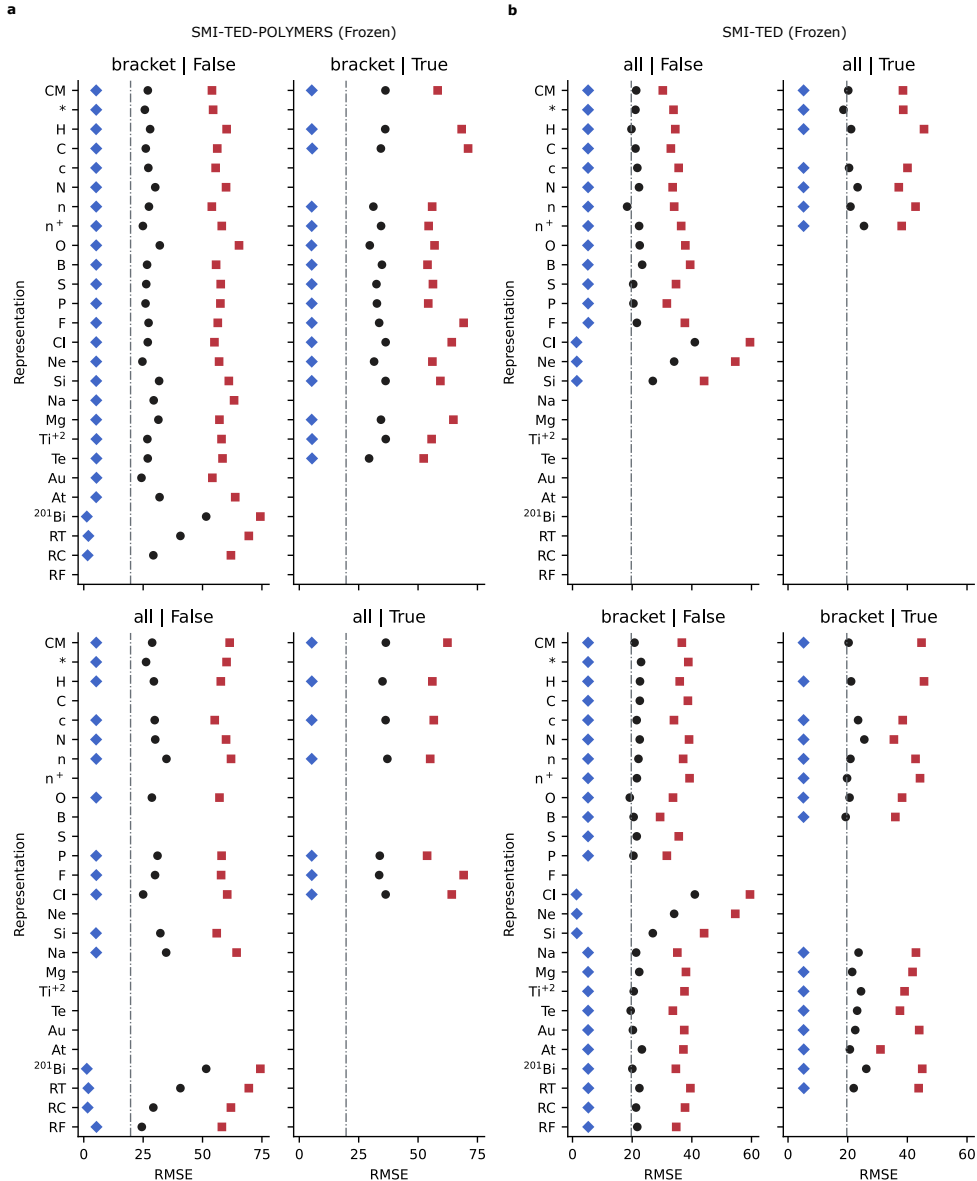


Fig. 112 Point plots for T_g -II benchmark experiments of RMSE using the base random train, valid, and test splits for SMI-TED-POLYMER (a) and SMI-TED (b) models with frozen weights.

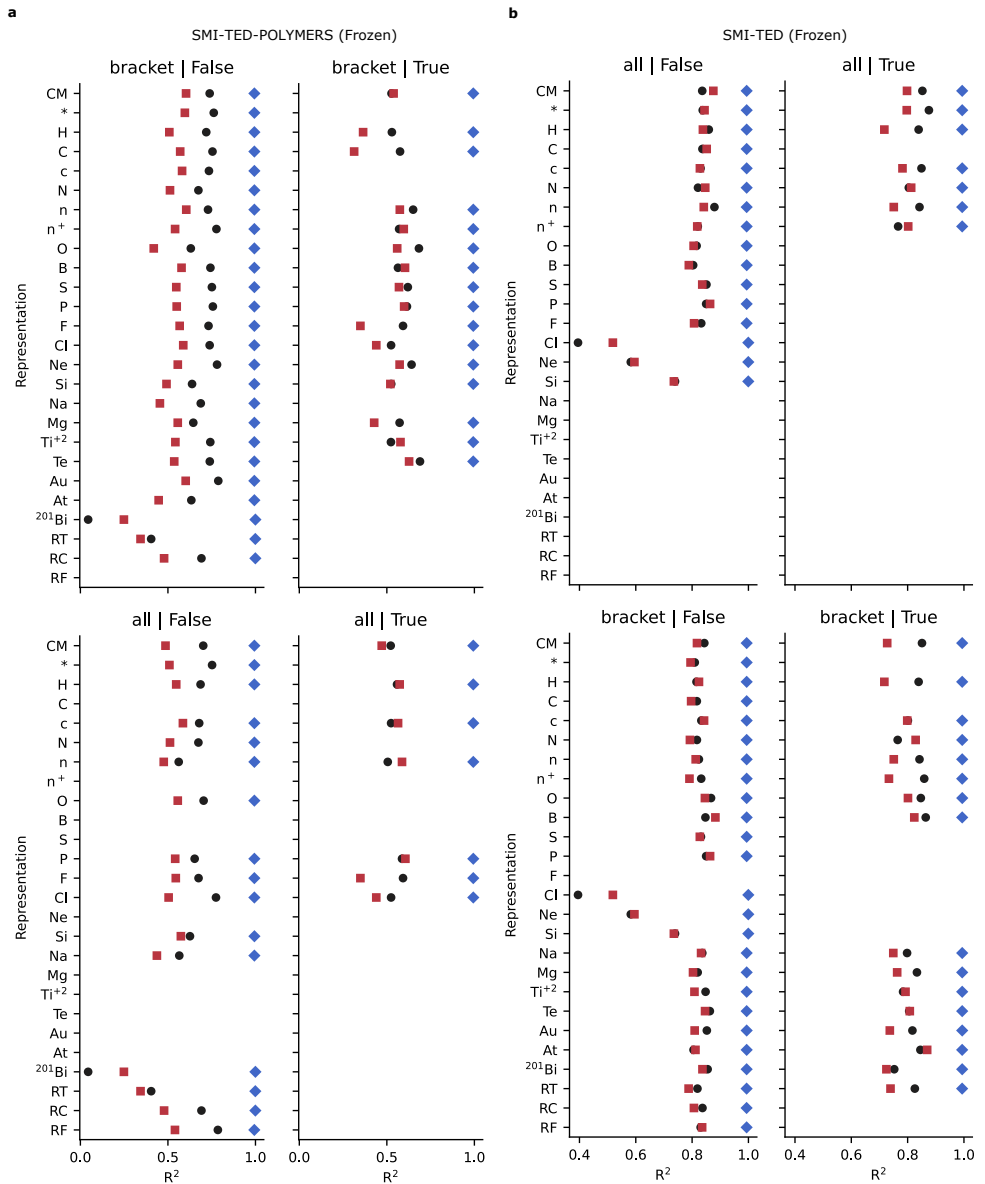


Fig. 113 Point plots for T_g-II benchmark experiments of R² using the base random train, valid, and test splits for SMI-TED-POLYMER **(a)** and SMI-TED **(b)** models with frozen weights.

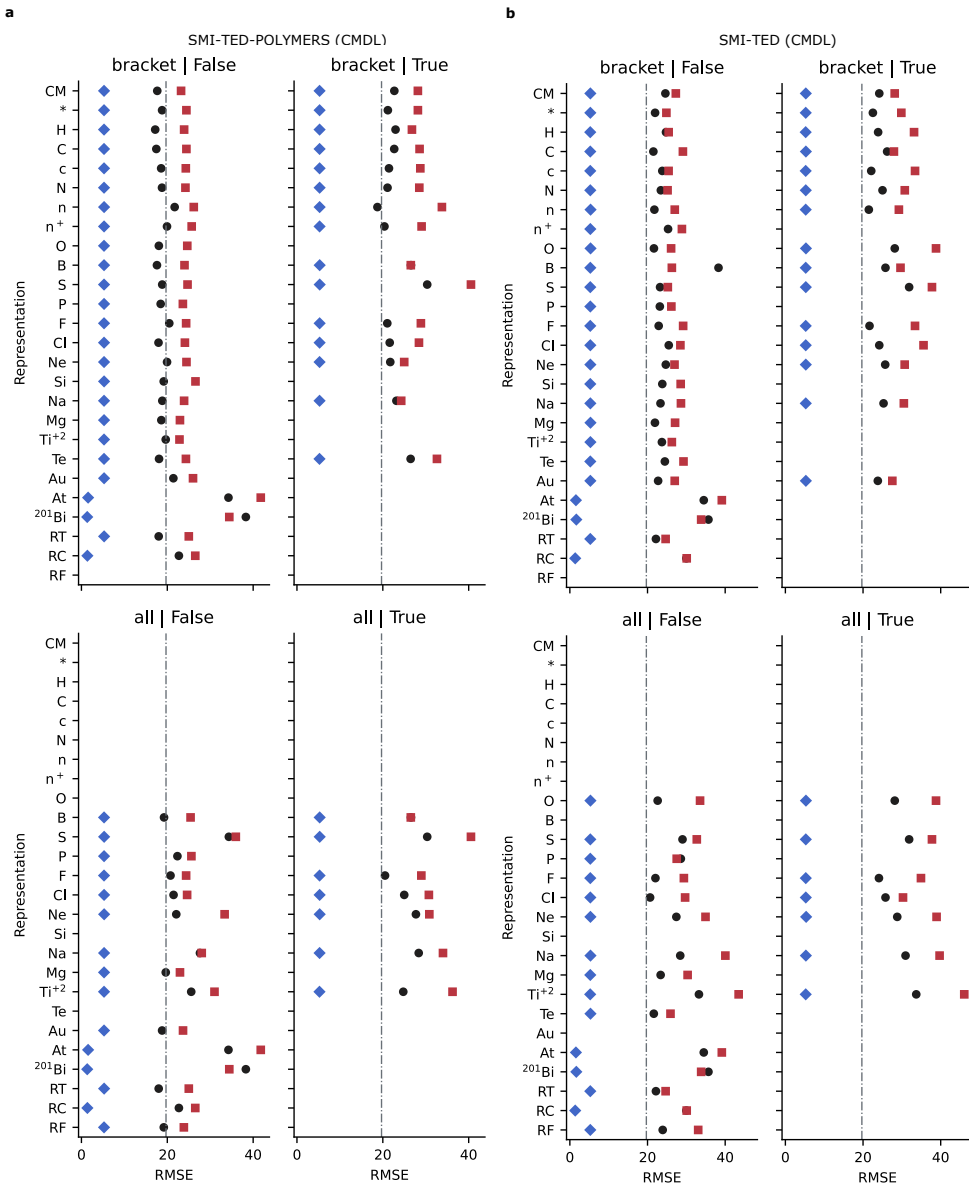


Fig. 114 Point plots for T_g -II benchmark experiments of RMSE using the base random train, valid, and test splits for SMI-TED-POLYMER (a) and SMI-TED (b) models fine-tuned with CPG.

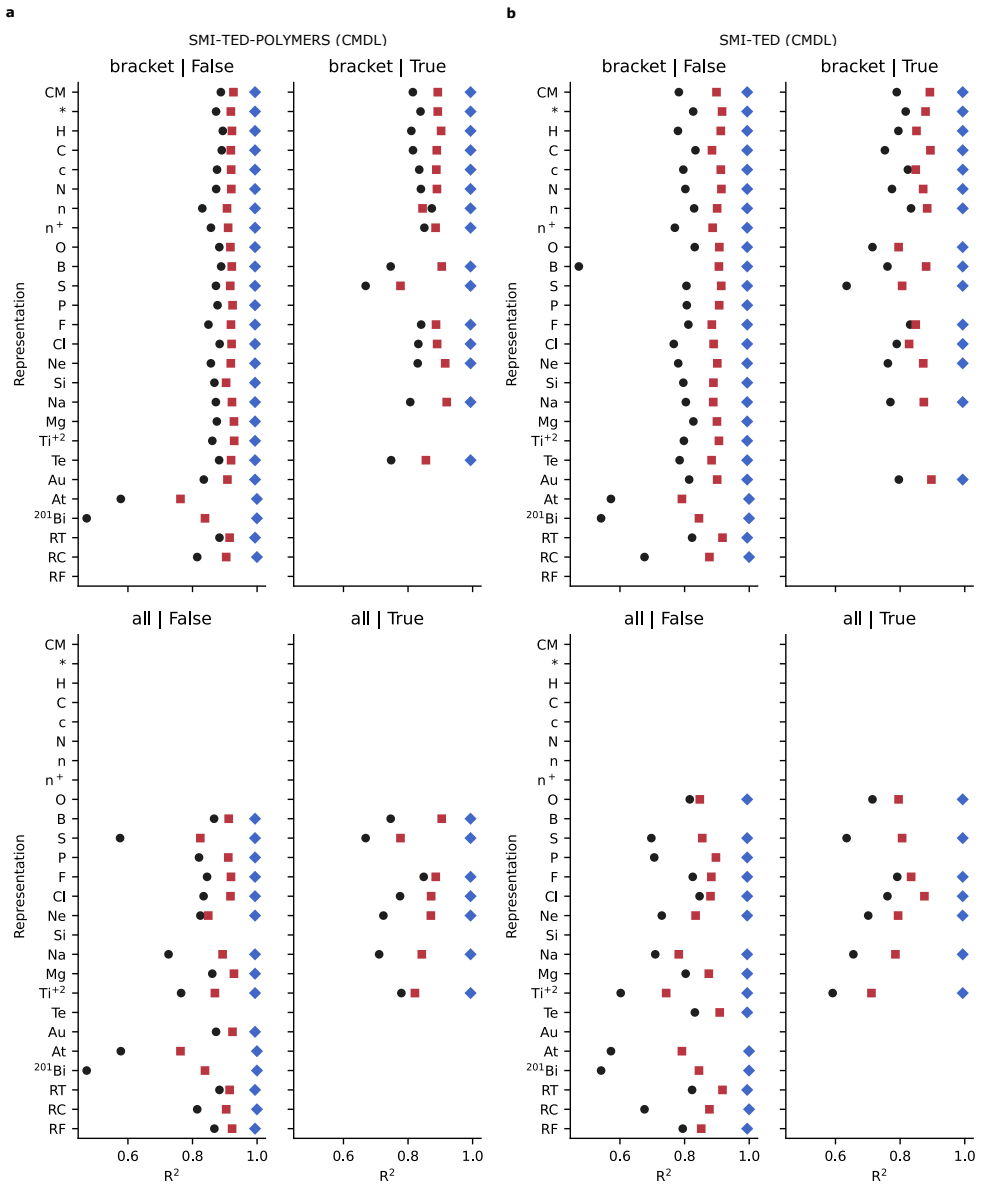


Fig. 115 Point plots for T_g-II benchmark experiments of R² using the base random train, valid, and test splits for SMI-TED-POLYMER **(a)** and SMI-TED **(b)** models fine-tuned with CPG.

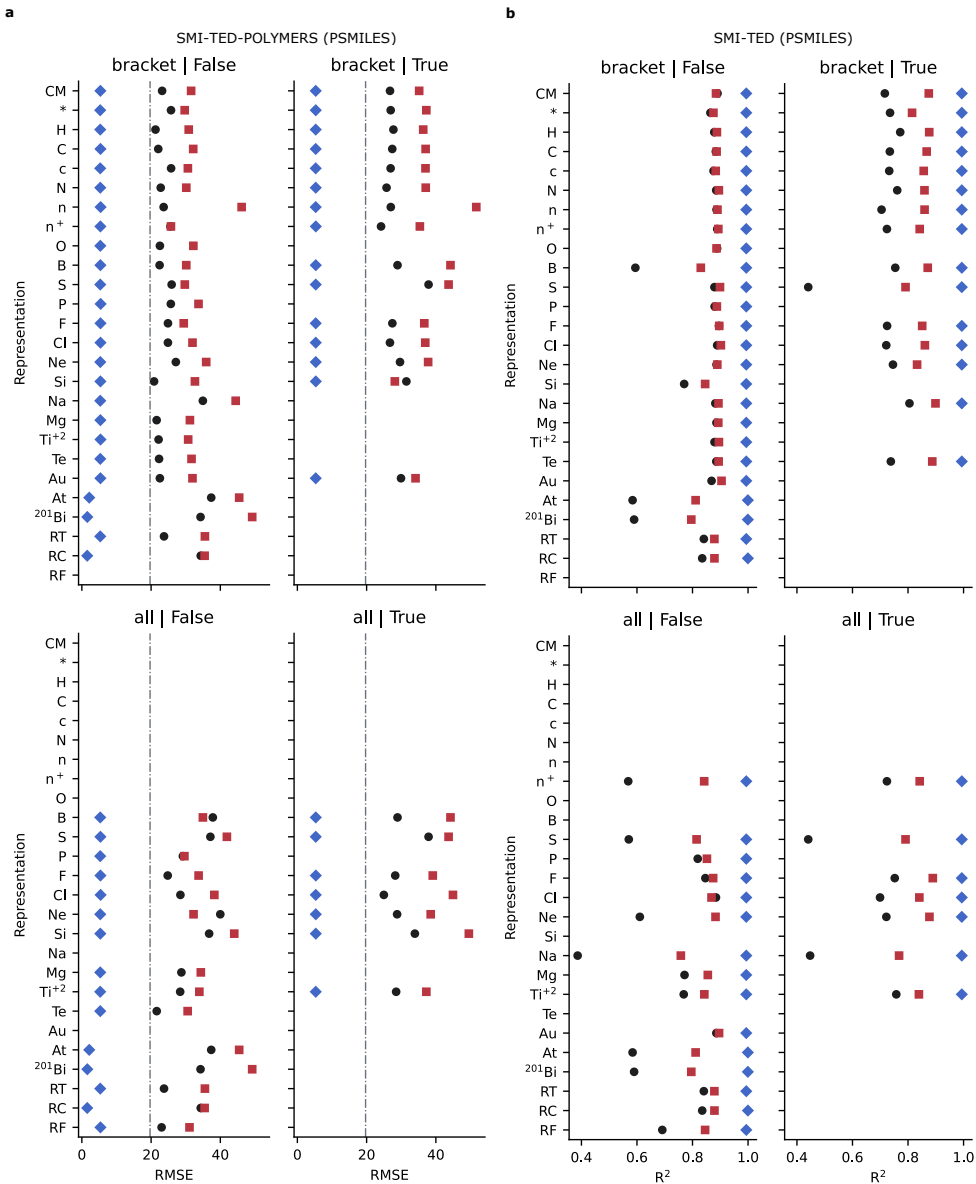


Fig. 116 Point plots for T_g -II benchmark experiments of RMSE using the base random train, valid, and test splits for SMI-TED-POLYMER (a) and SMI-TED (b) models fine-tuned with PSMILES.

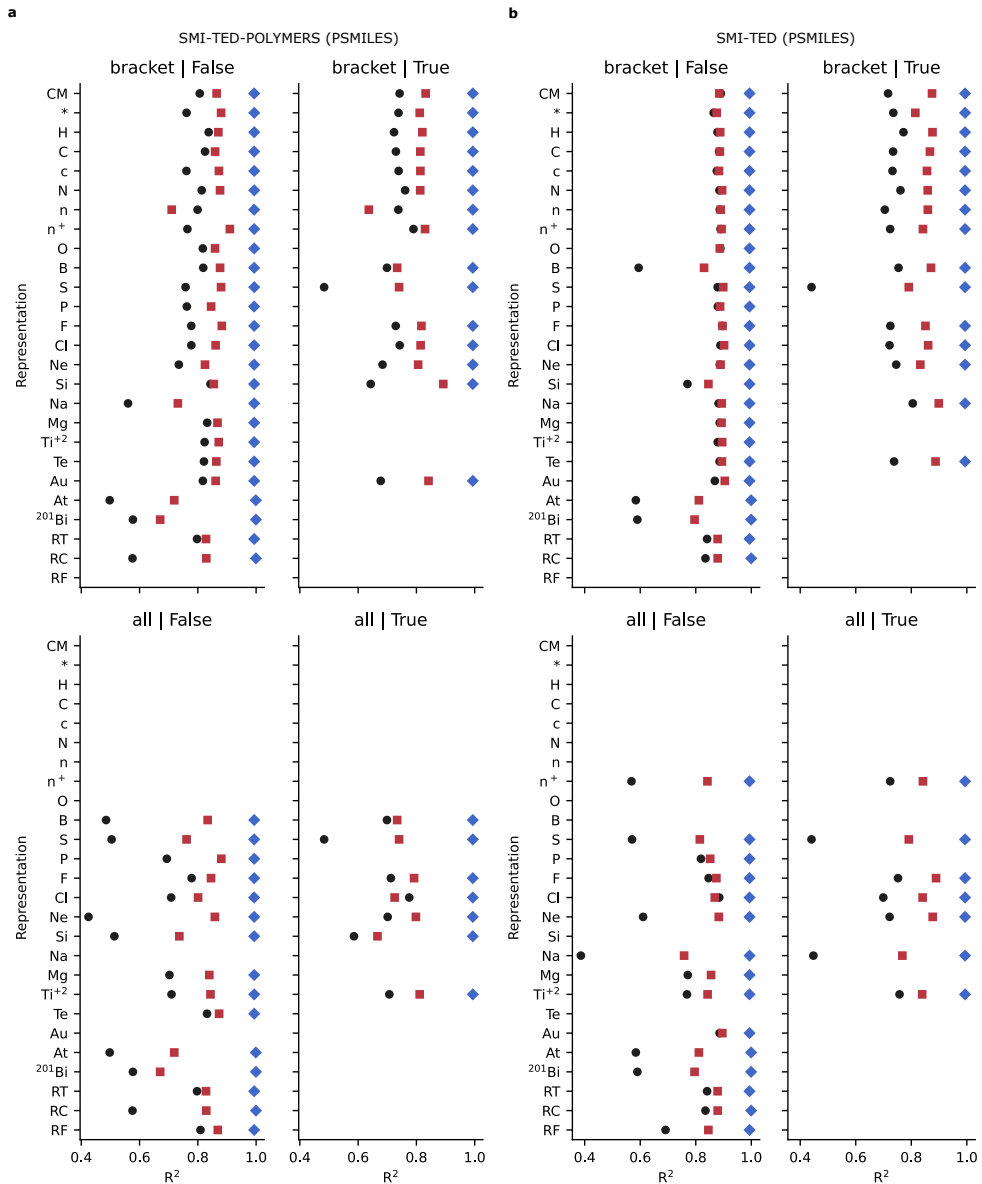
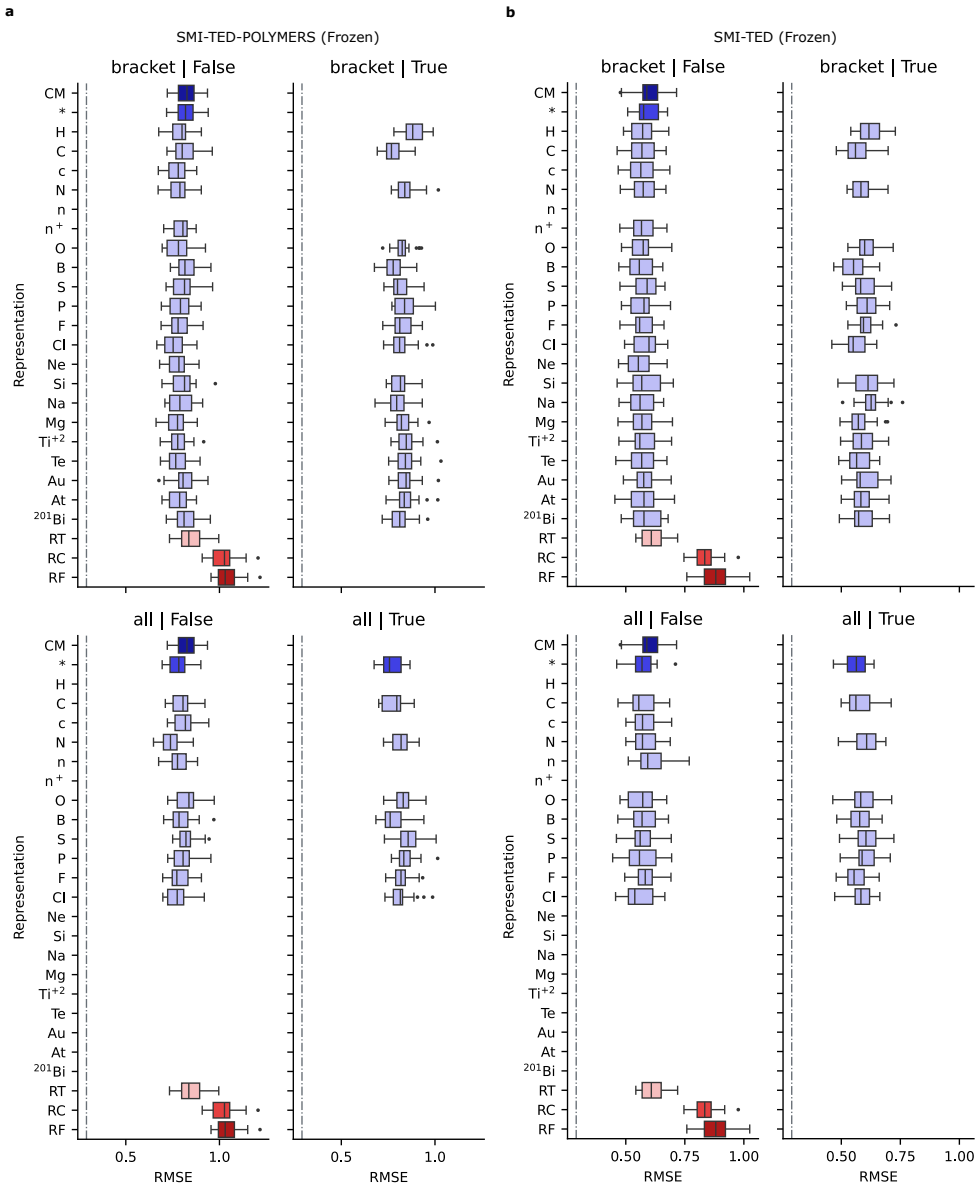


Fig. 117 Point plots for T_g -II benchmark experiments of R^2 using the base random train, valid, and test splits for SMI-TED-POLYMER (a) and SMI-TED (b) models fine-tuned with PSMILES.

2.6.19 CO₂ Gas Permeability CV Scores



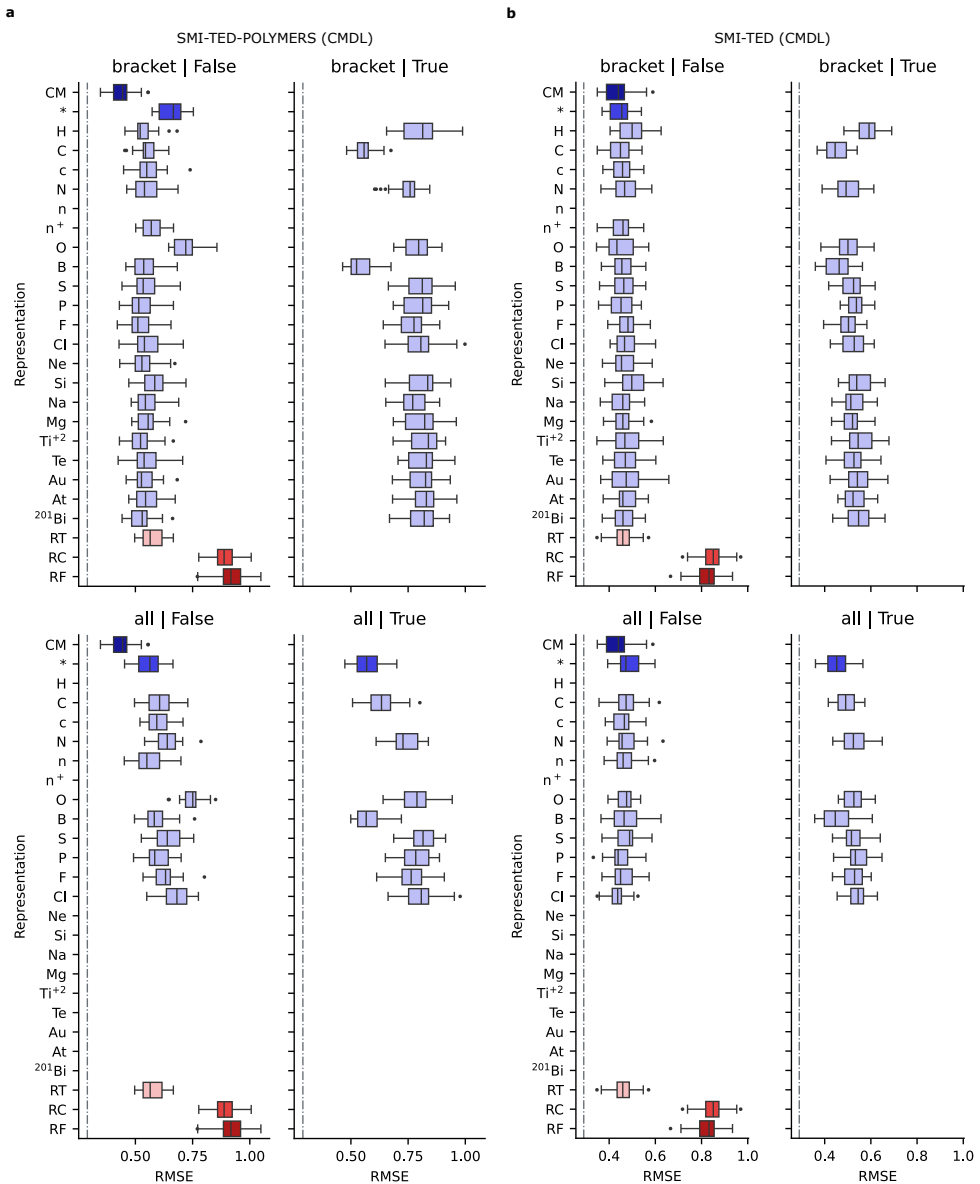


Fig. 119 Box plots for CO_2 gas permeability repeated cross-validation experiments for SMI-TED-POLYMER (a) and SMI-TED (b) models fine-tuned with the CPG polymer graphs.

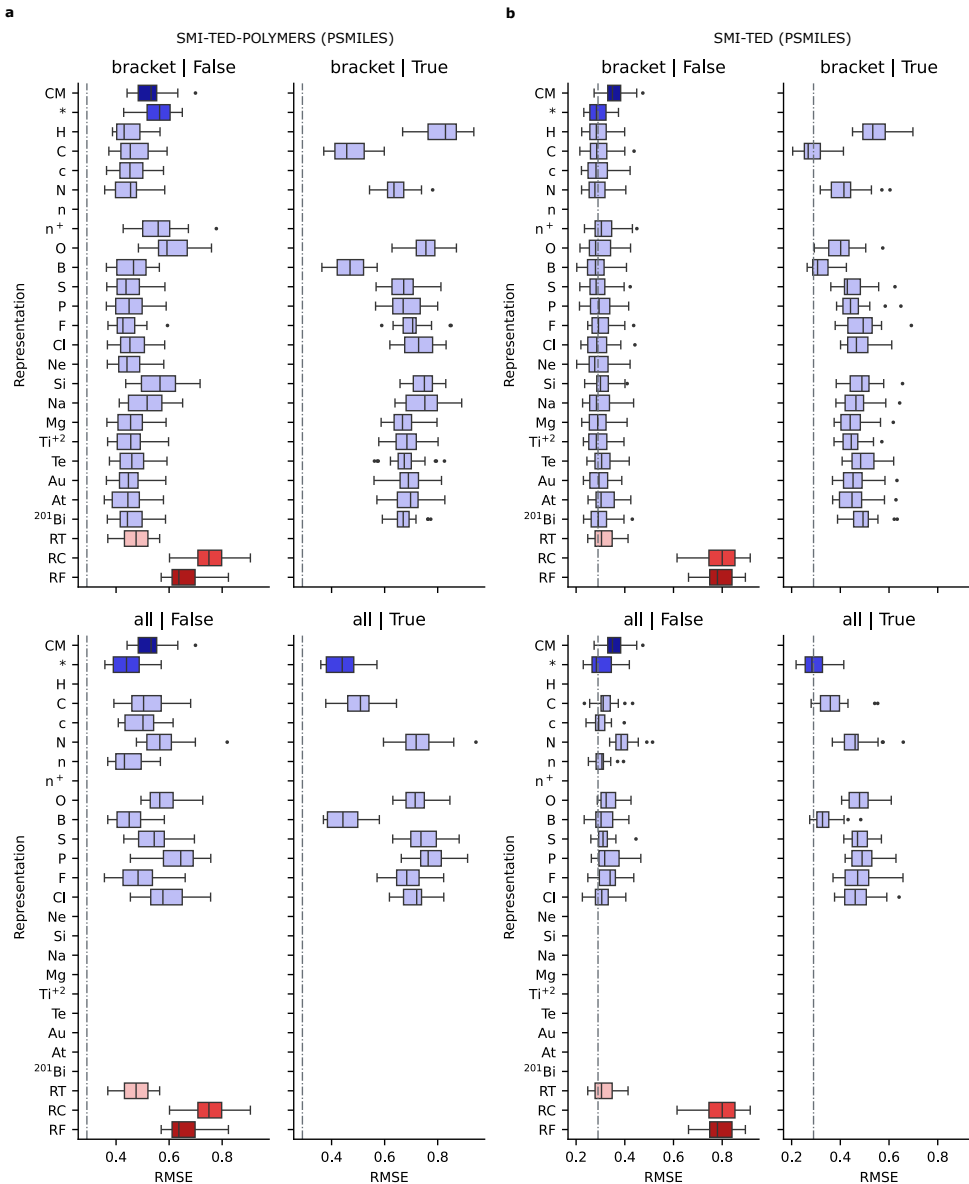


Fig. 120 Box plots for CO_2 gas permeability repeated cross-validation experiments for SMI-TED-POLYMER (**a**) and SMI-TED (**b**) models fine-tuned with PSMILES.

2.6.20 CO₂ Gas Permeability Random Split Scores

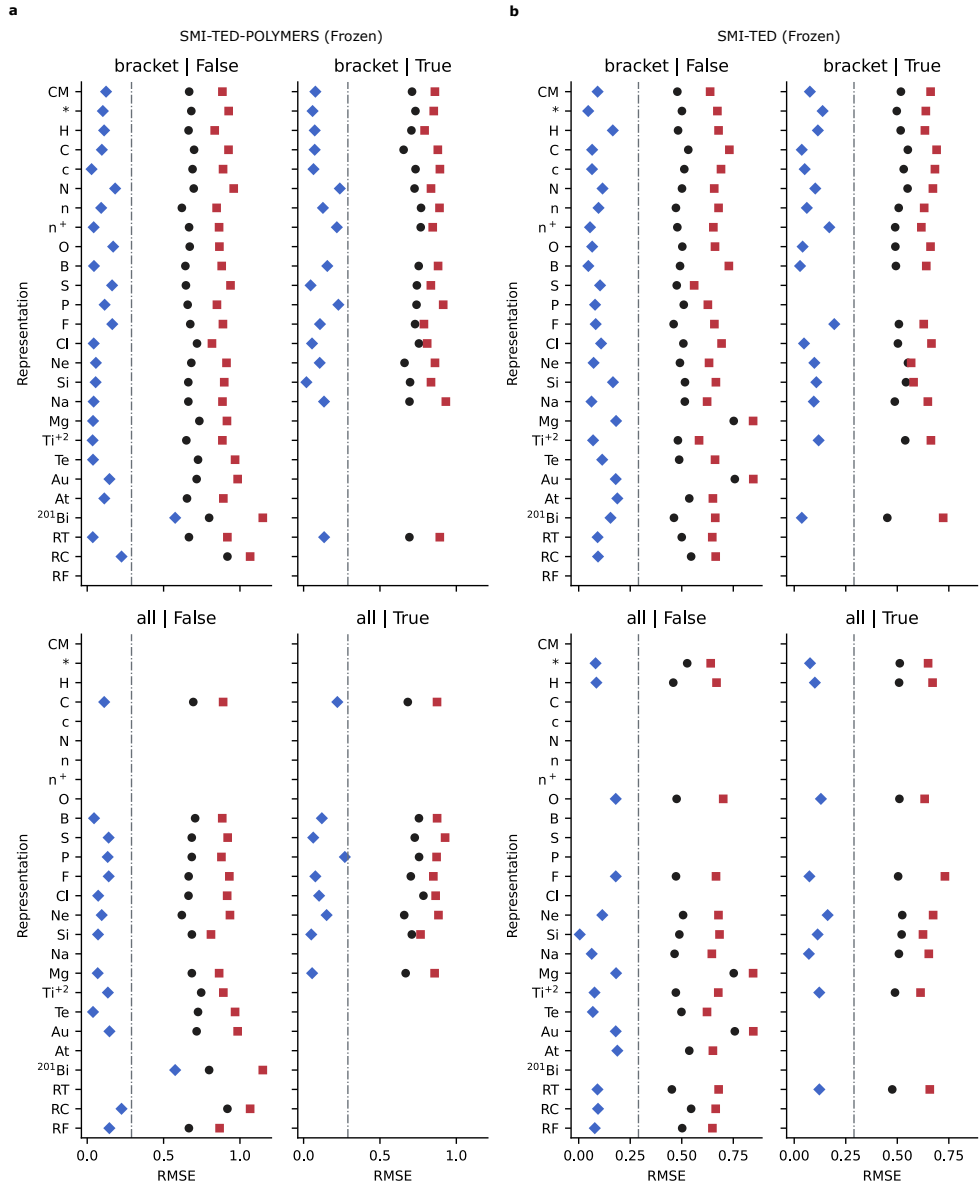


Fig. 121 Point plots for CO₂ gas permeability benchmark experiments of RMSE using the base random train, valid, and test splits for SMI-TED-POLYMER (a) and SMI-TED (b) models with frozen weights.

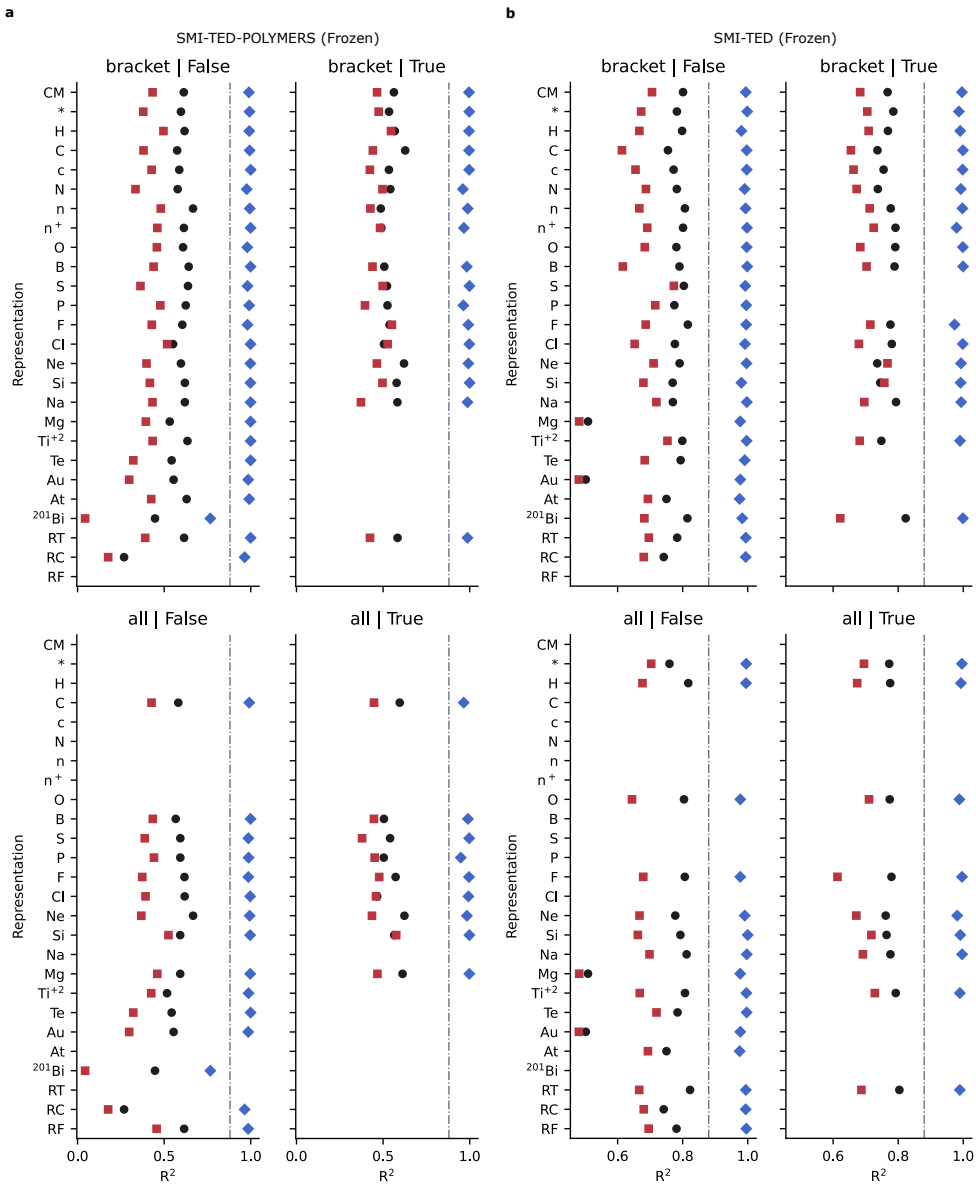


Fig. 122 Point plots for CO_2 gas permeability benchmark experiments of R^2 using the base random train, valid, and test splits for SMI-TED-POLYMER (a) and SMI-TED (b) models with frozen weights.

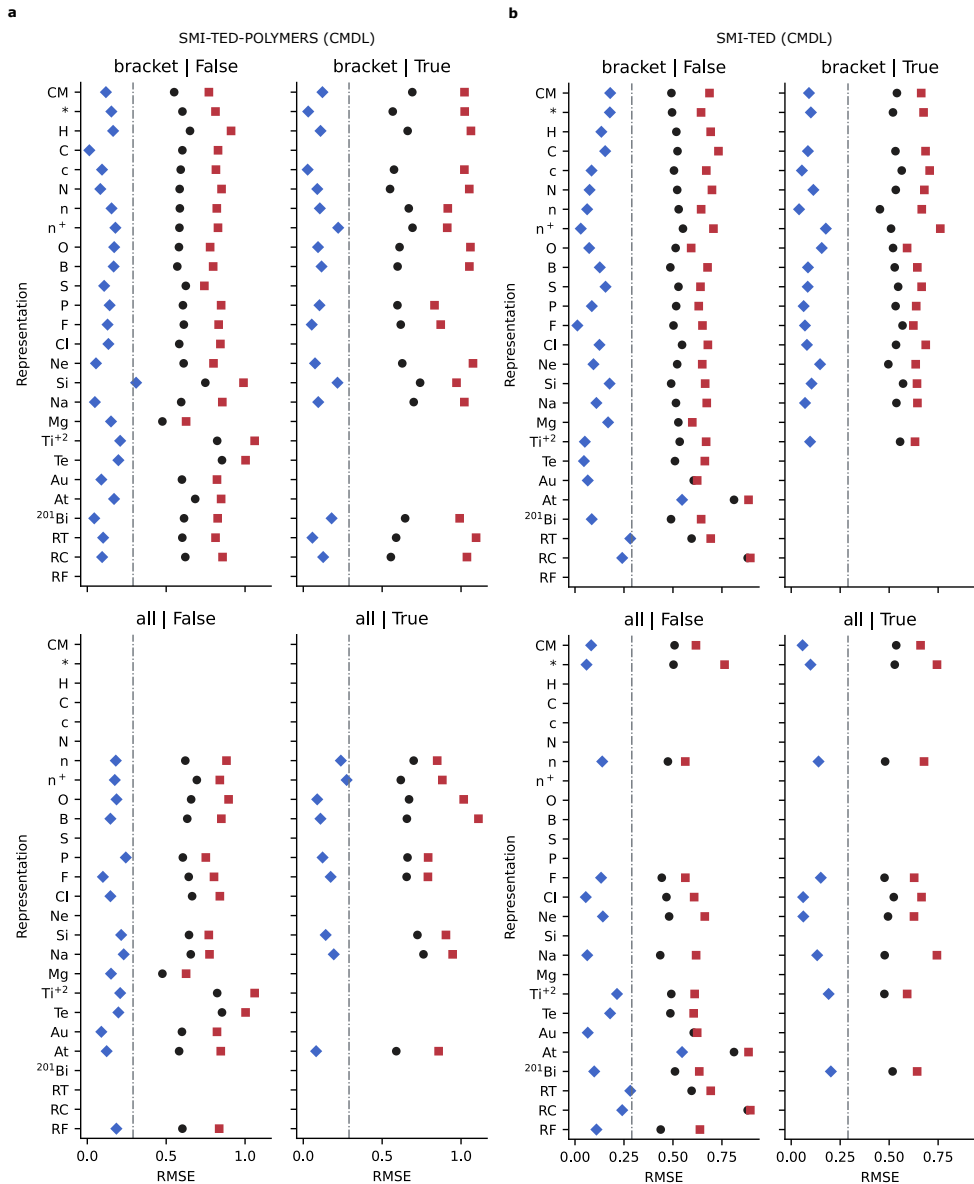


Fig. 123 Point plots for CO_2 gas permeability benchmark experiments of RMSE using the base random train, valid, and test splits for SMI-TED-POLYMER (a) and SMI-TED (b) models fine-tuned using the CPG representation.

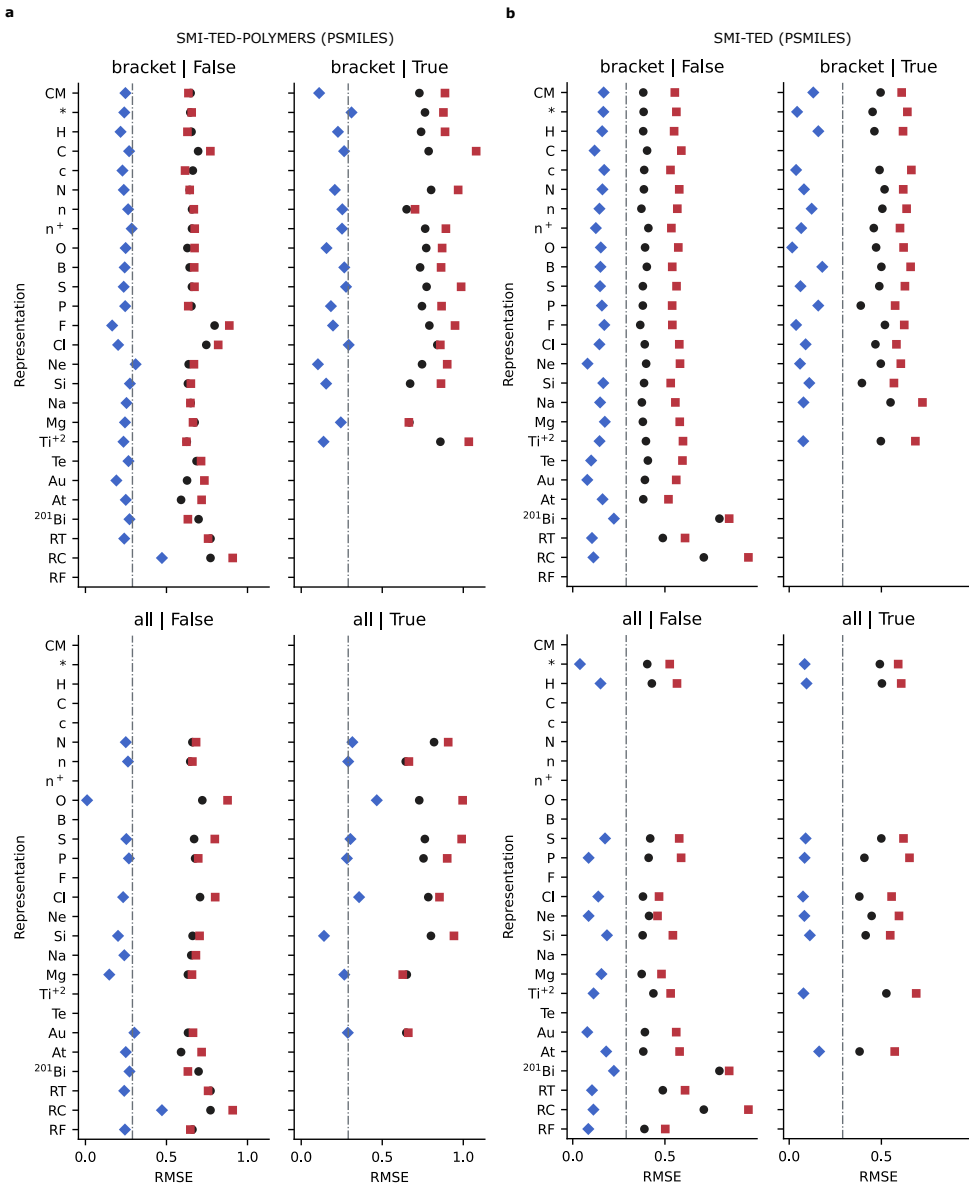


Fig. 125 Point plots for CO_2 gas permeability benchmark experiments of RMSE using the base random train, valid, and test splits for SMI-TED-POLYMER (a) and SMI-TED (b) models fine-tuned using PSMILES.

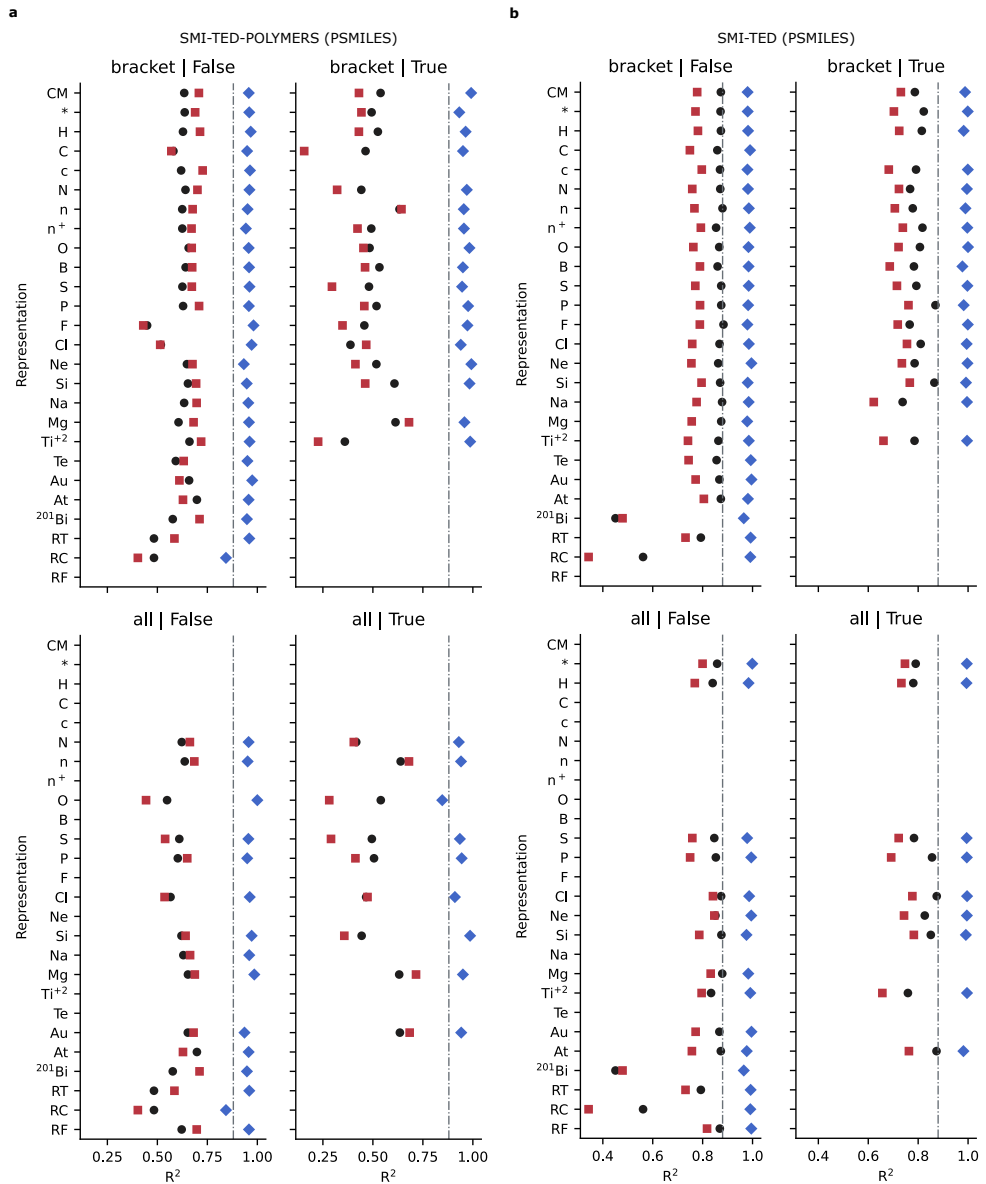


Fig. 126 Point plots for CO_2 gas permeability benchmark experiments of R^2 using the base random train, valid, and test splits for SMI-TED-POLYMER (a) and SMI-TED (b) models fine-tuned using PSMILES.

2.6.21 N₂ Gas Permeability CV Scores

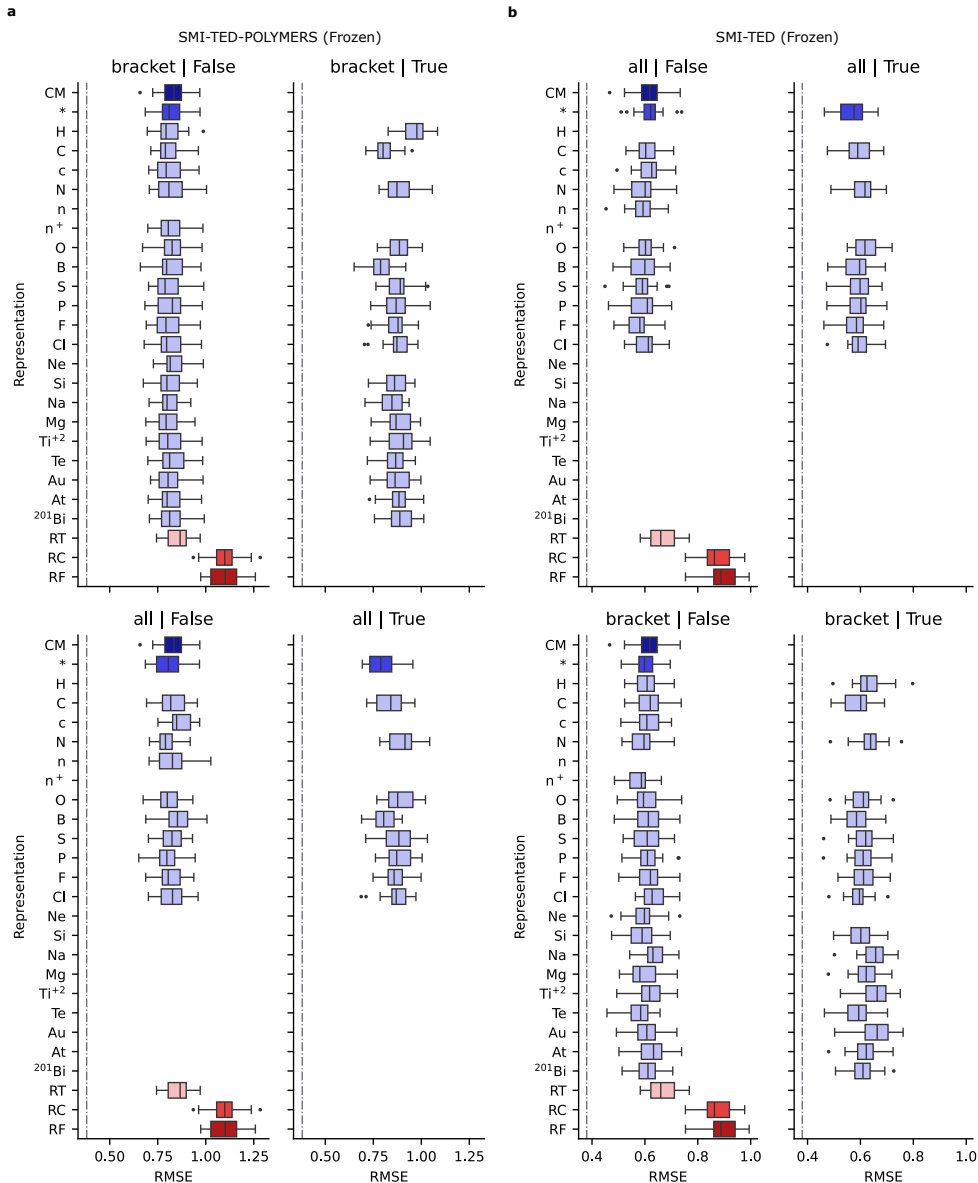


Fig. 127 Box plots for N₂ gas permeability repeated cross-validation experiments for SMI-TED-POLYMER (a) and SMI-TED (b) models with frozen weights.

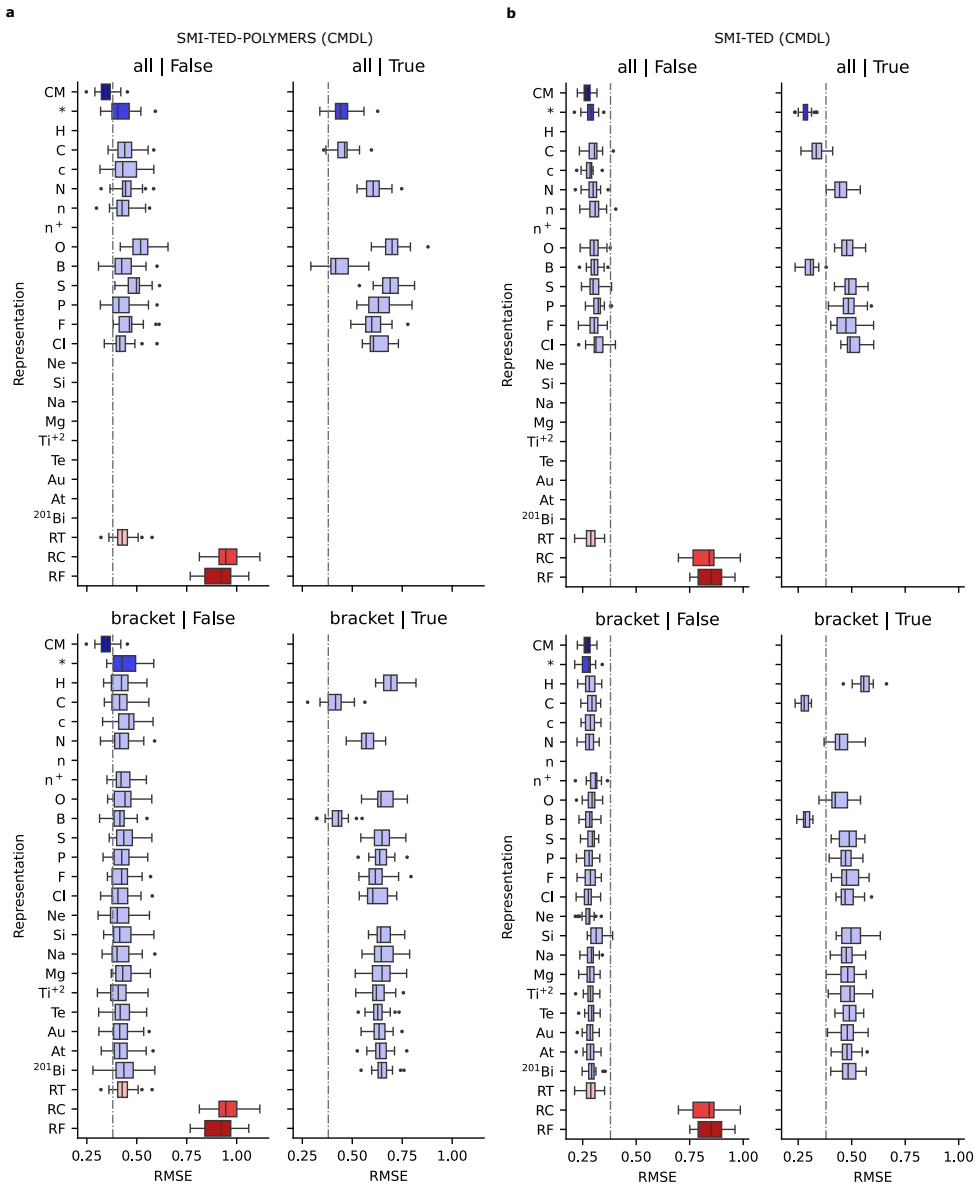


Fig. 128 Box plots for N_2 gas permeability repeated cross-validation experiments for SMI-TED-POLYMER (a) and SMI-TED (b) models fine-tuned with the CPG polymer graphs.

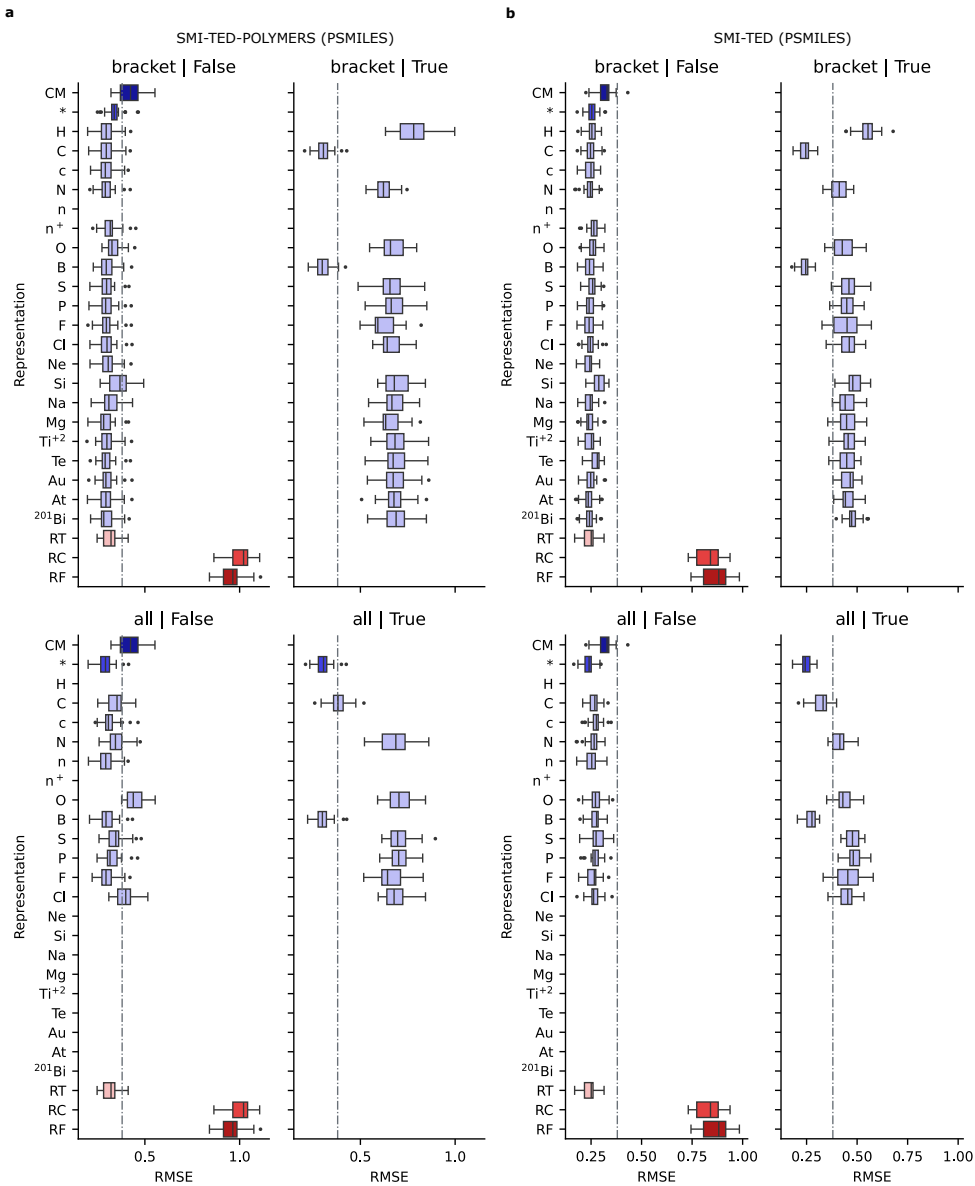


Fig. 129 Box plots for N_2 gas permeability repeated cross-validation experiments for SMI-TED-POLYMER (a) and SMI-TED (b) models fine-tuned with PSMILES.

2.6.22 N₂ Gas Permeability Random Split Scores

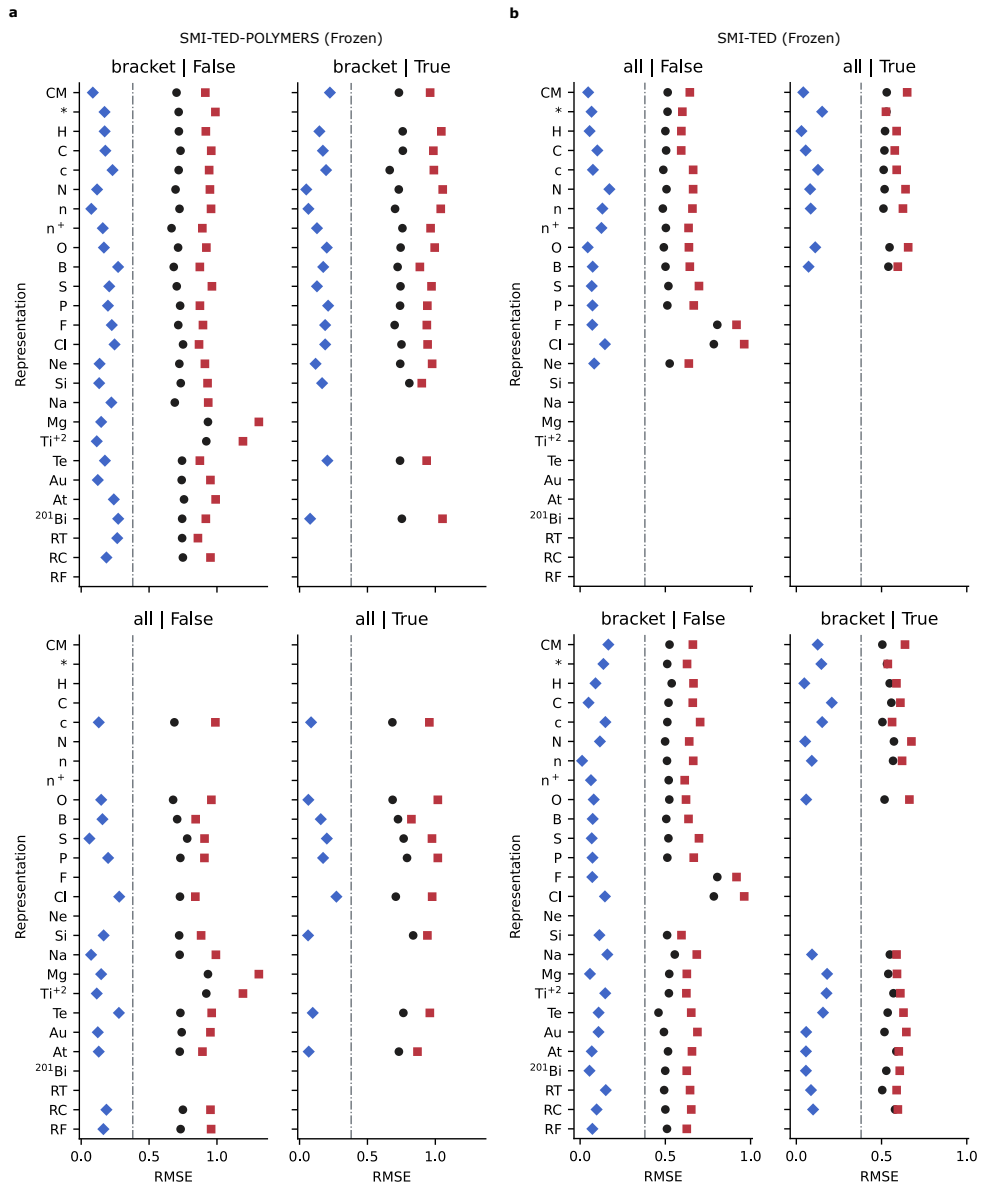


Fig. 130 Point plots for N₂ gas permeability benchmark experiments of RMSE using the base random train, valid, and test splits for SMI-TED-POLYMER (a) and SMI-TED (b) models with frozen weights.

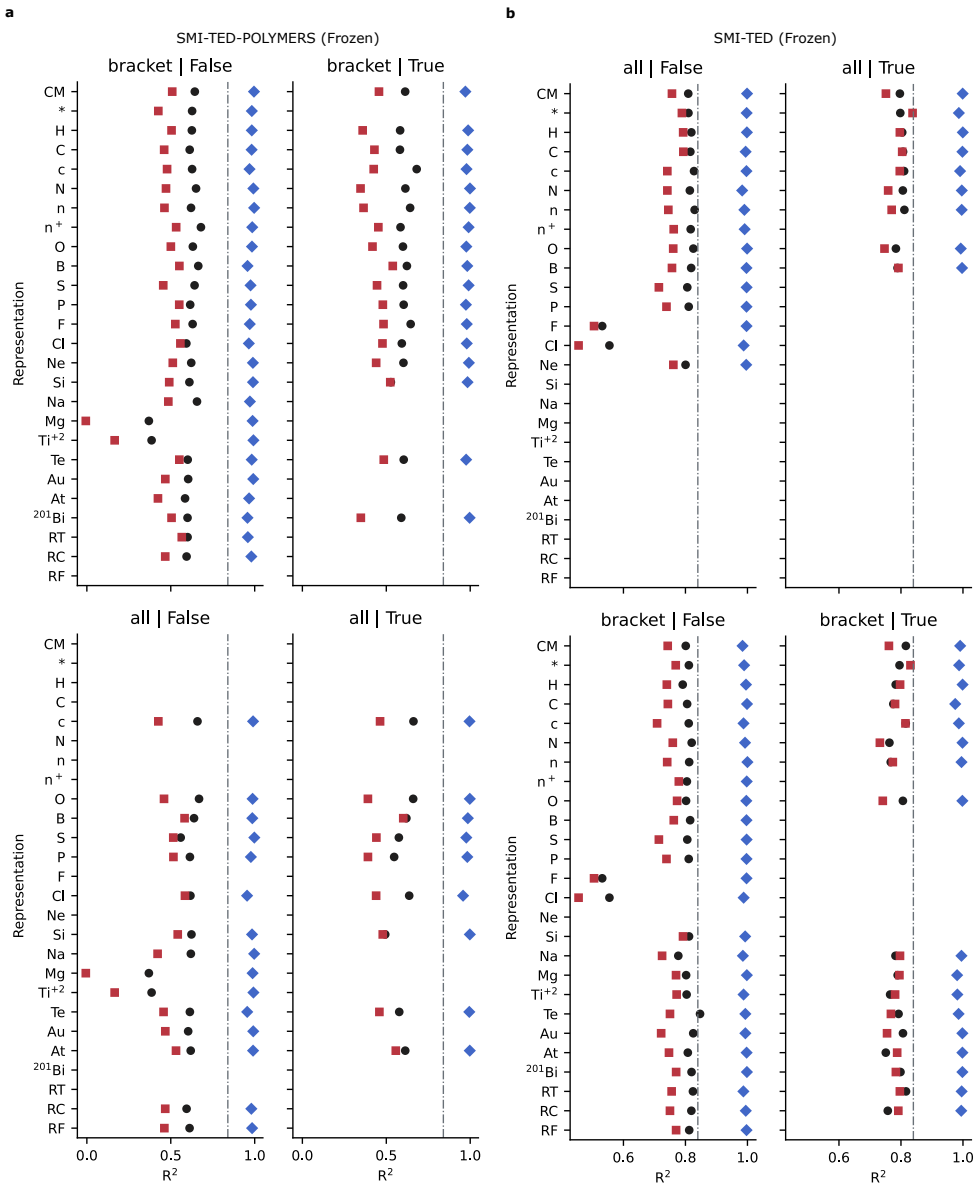


Fig. 131 Point plots for N_2 gas permeability benchmark experiments of R^2 using the base random train, valid, and test splits for SMI-TED-POLYMER (a) and SMI-TED (b) models with frozen weights.

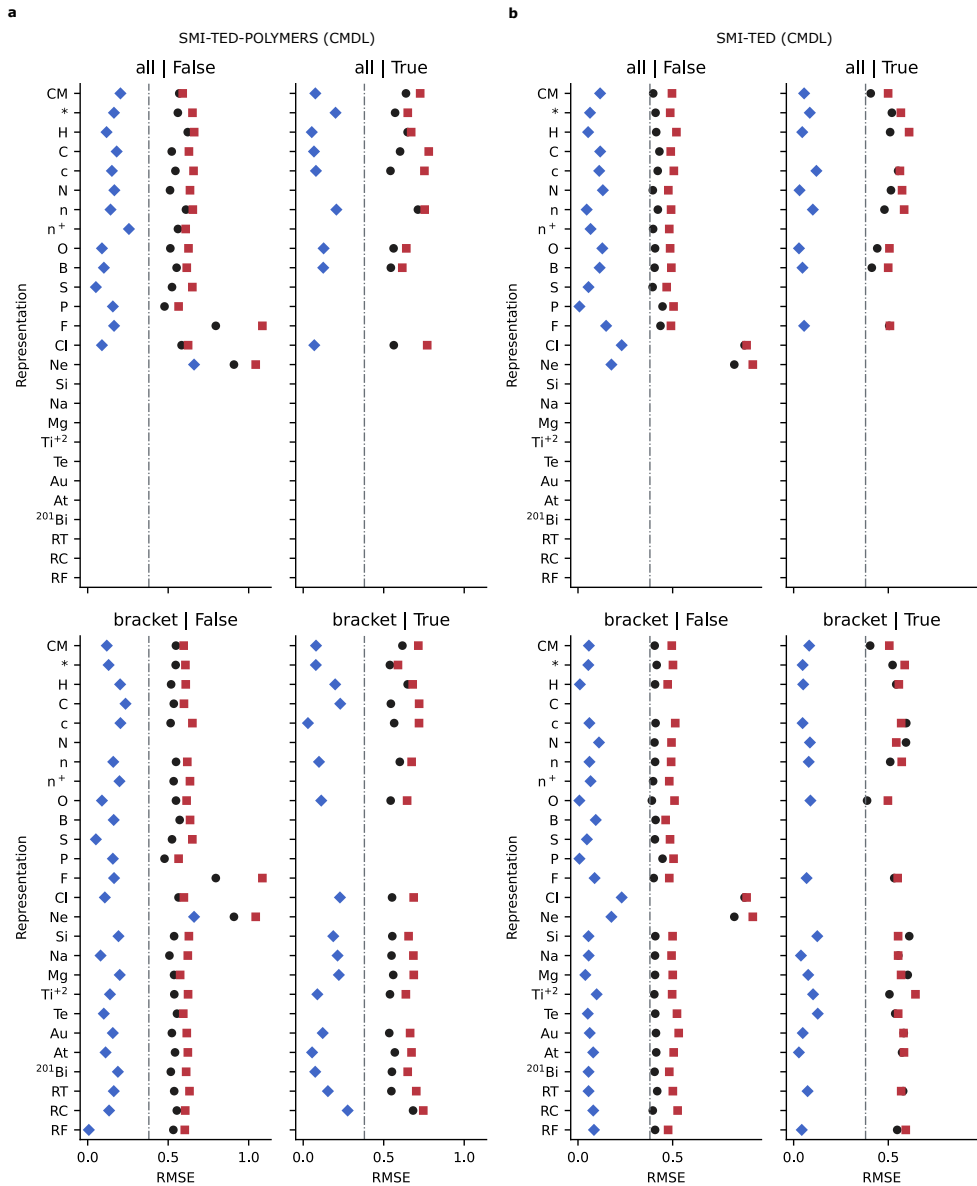


Fig. 132 Point plots for N_2 gas permeability benchmark experiments of RMSE using the base random train, valid, and test splits for SMI-TED-POLYMER (a) and SMI-TED (b) models fine-tuned using the CPG representation.

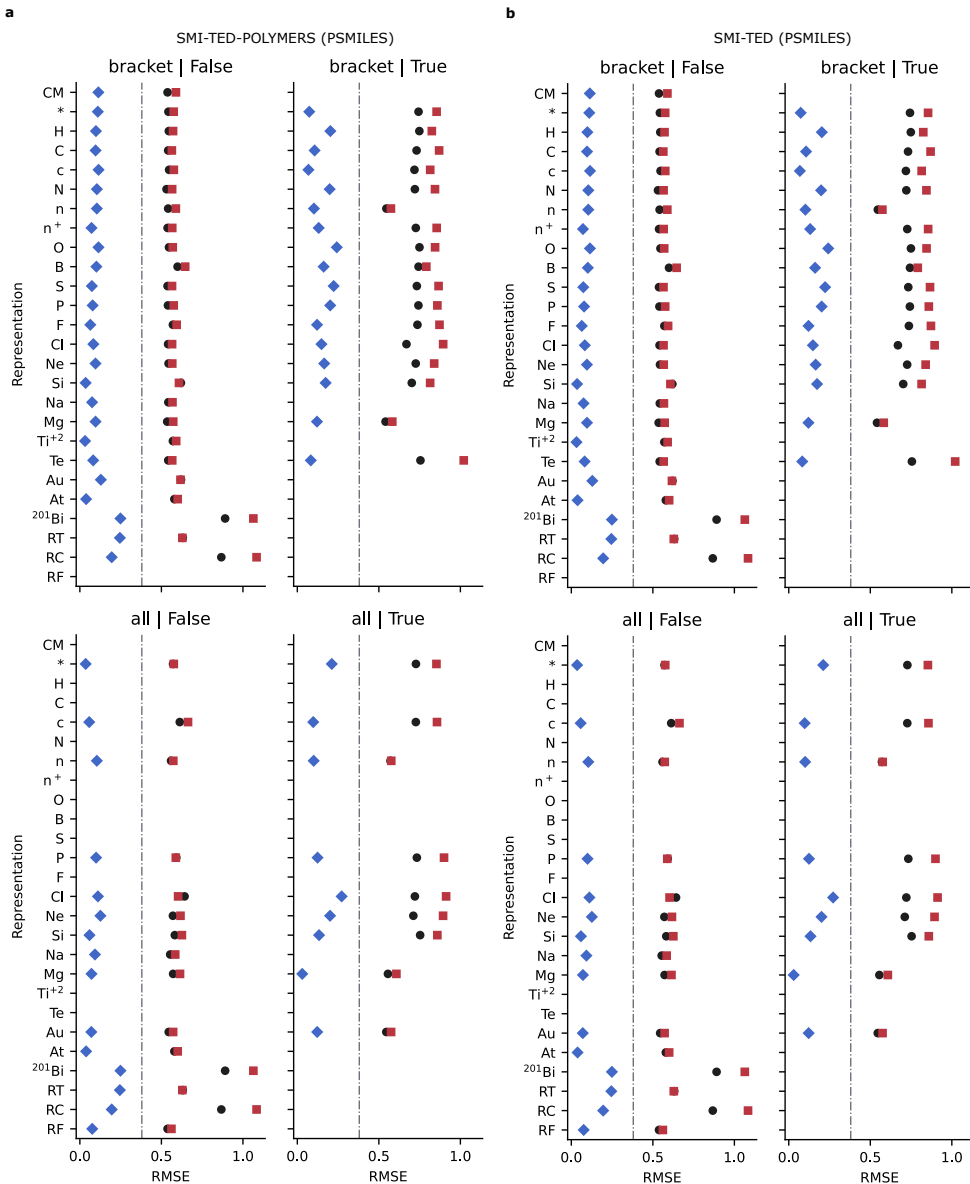


Fig. 134 Point plots for N₂ gas permeability benchmark experiments of RMSE using the base random train, valid, and test splits for SMI-TED-POLYMER (a) and SMI-TED (b) models fine-tuned using PSMILES.

2.6.23 CH₄ Gas Permeability CV Scores

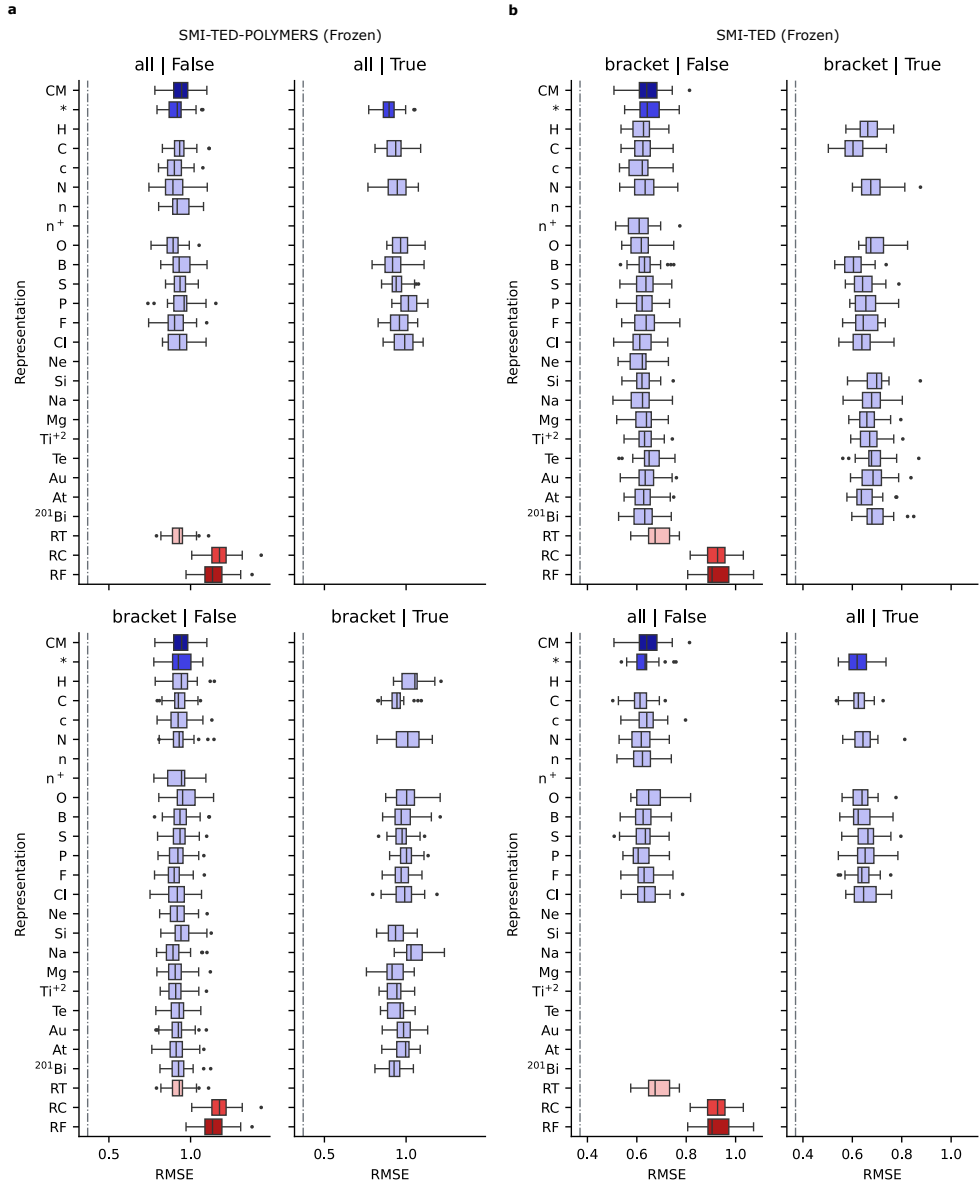


Fig. 135 Box plots for CH₄ gas permeability repeated cross-validation experiments for SMI-TED-POLYMERS (a) and SMI-TED (b) models with frozen weights.

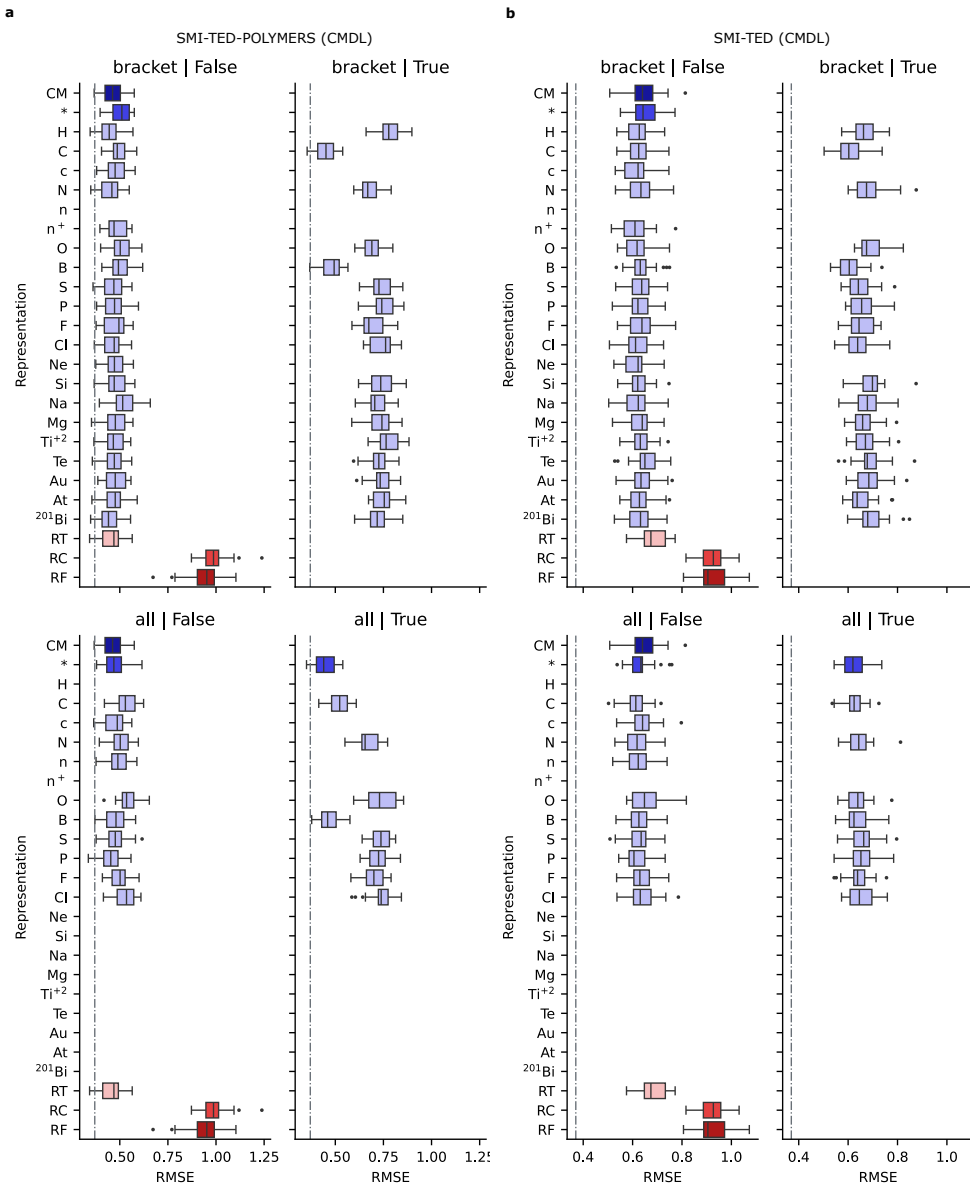


Fig. 136 Box plots for CH_4 gas permeability repeated cross-validation experiments for SMI-TED-POLYMER (**a**) and SMI-TED (**b**) models fine-tuned with the CPG polymer graphs.

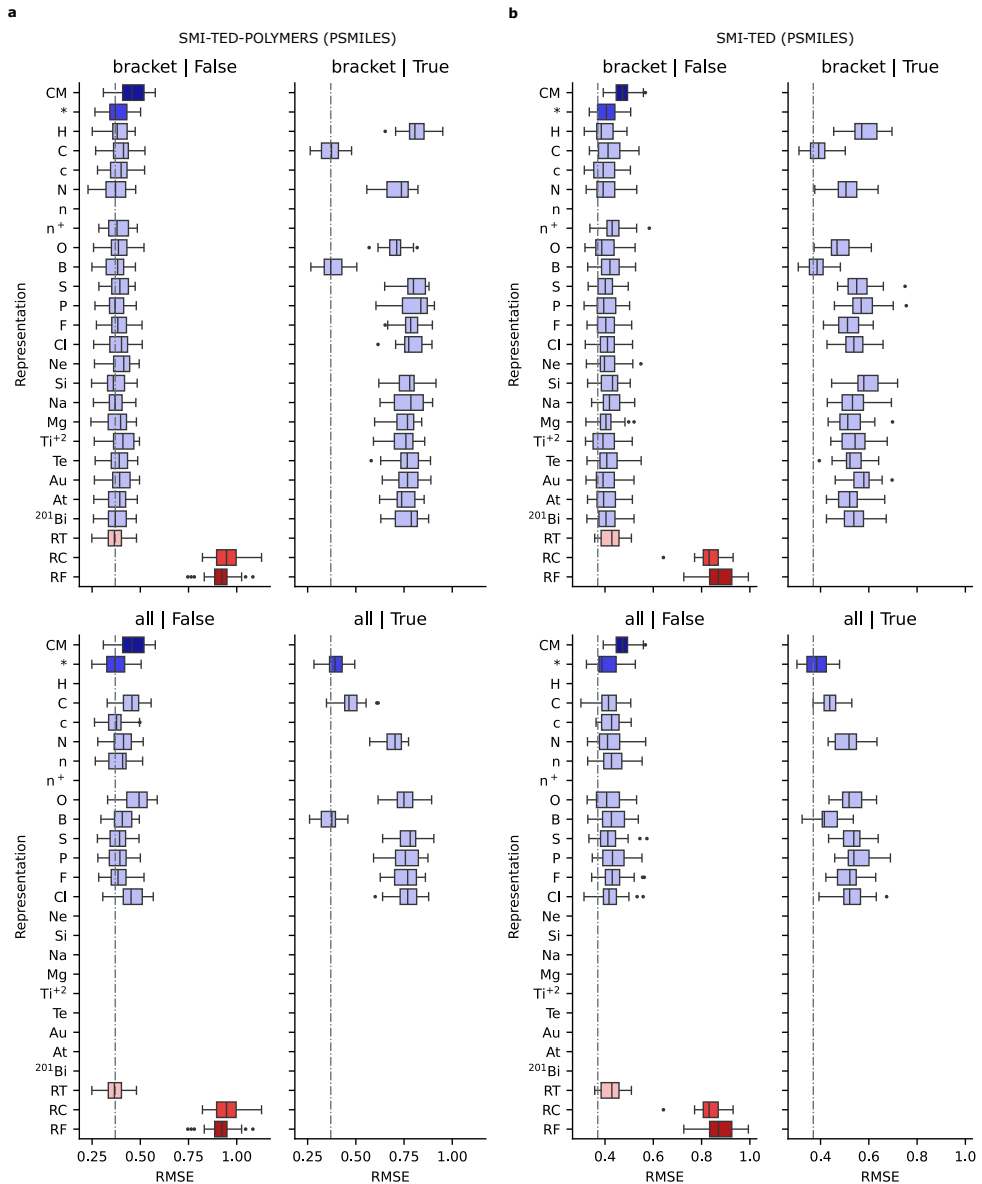


Fig. 137 Box plots for CH_4 gas permeability repeated cross-validation experiments for SMI-TED-POLYMER (a) and SMI-TED (b) models fine-tuned with PSMILES.

2.6.24 CH₄ Gas Permeability Random Split Scores

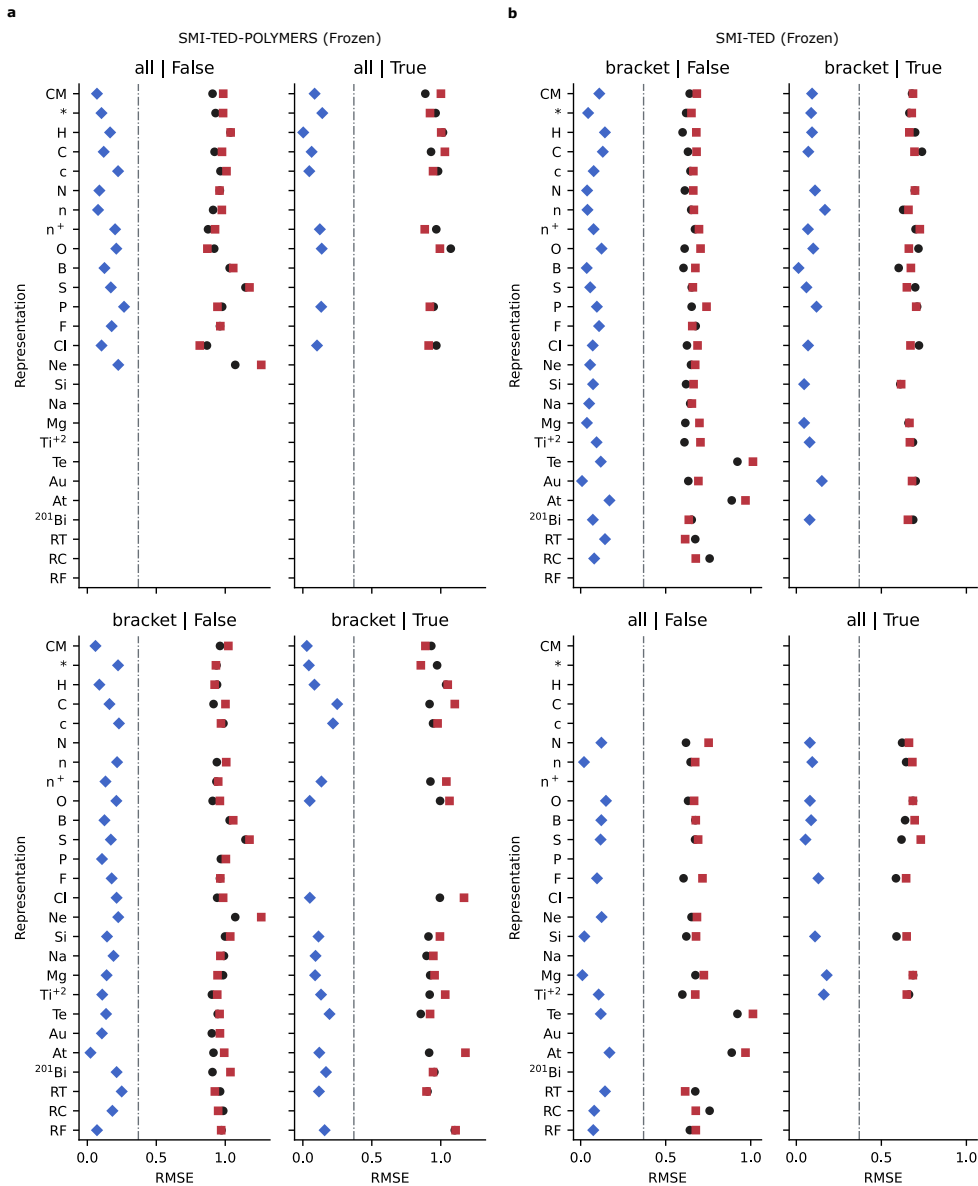


Fig. 138 Point plots for CH₄ gas permeability benchmark experiments of RMSE using the base random train, valid, and test splits for SMI-TED-POLYMER (a) and SMI-TED (b) models with frozen weights.

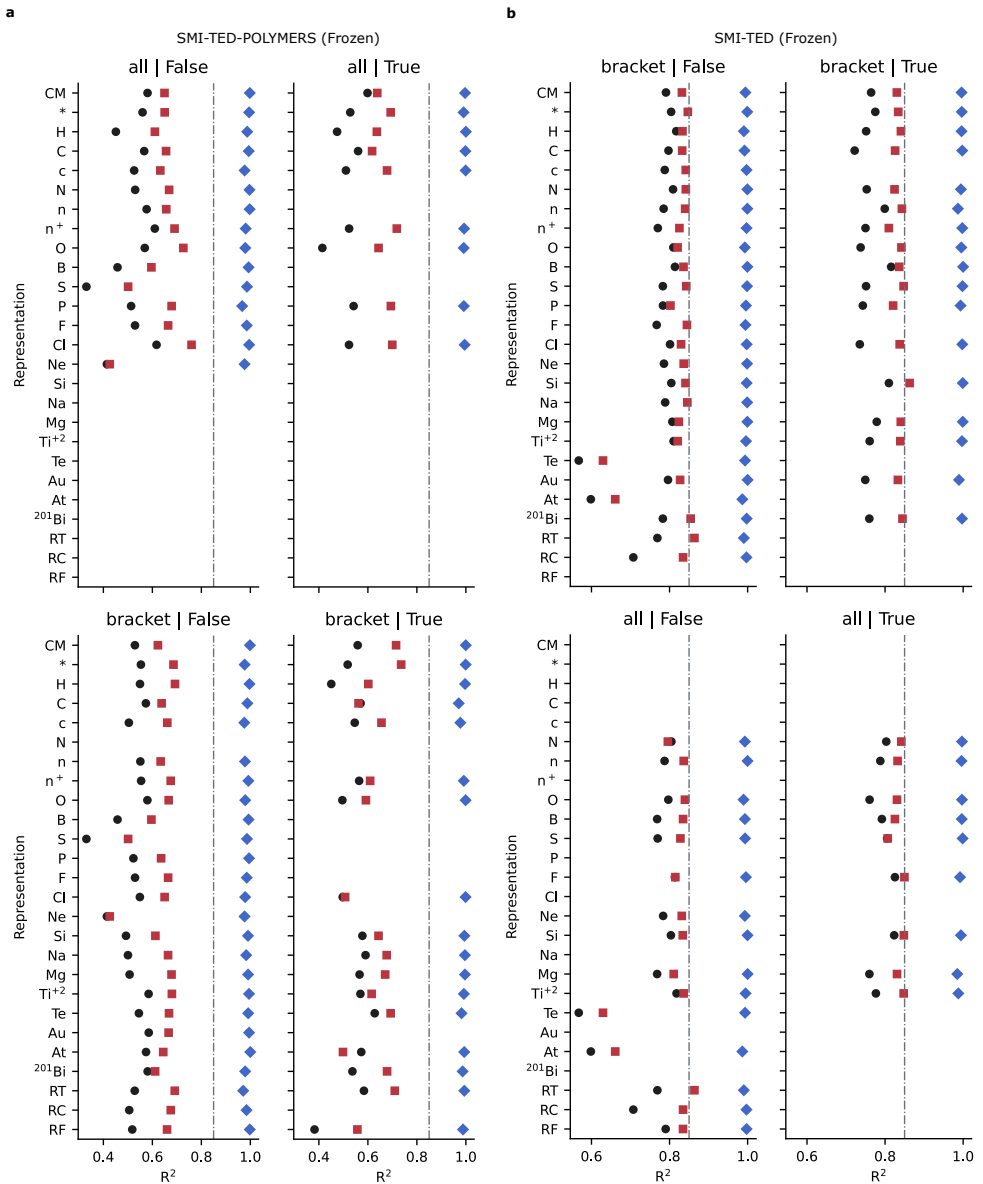


Fig. 139 Point plots for CH_4 gas permeability benchmark experiments of R^2 using the base random train, valid, and test splits for SMI-TED-POLYMER (a) and SMI-TED (b) models with frozen weights.

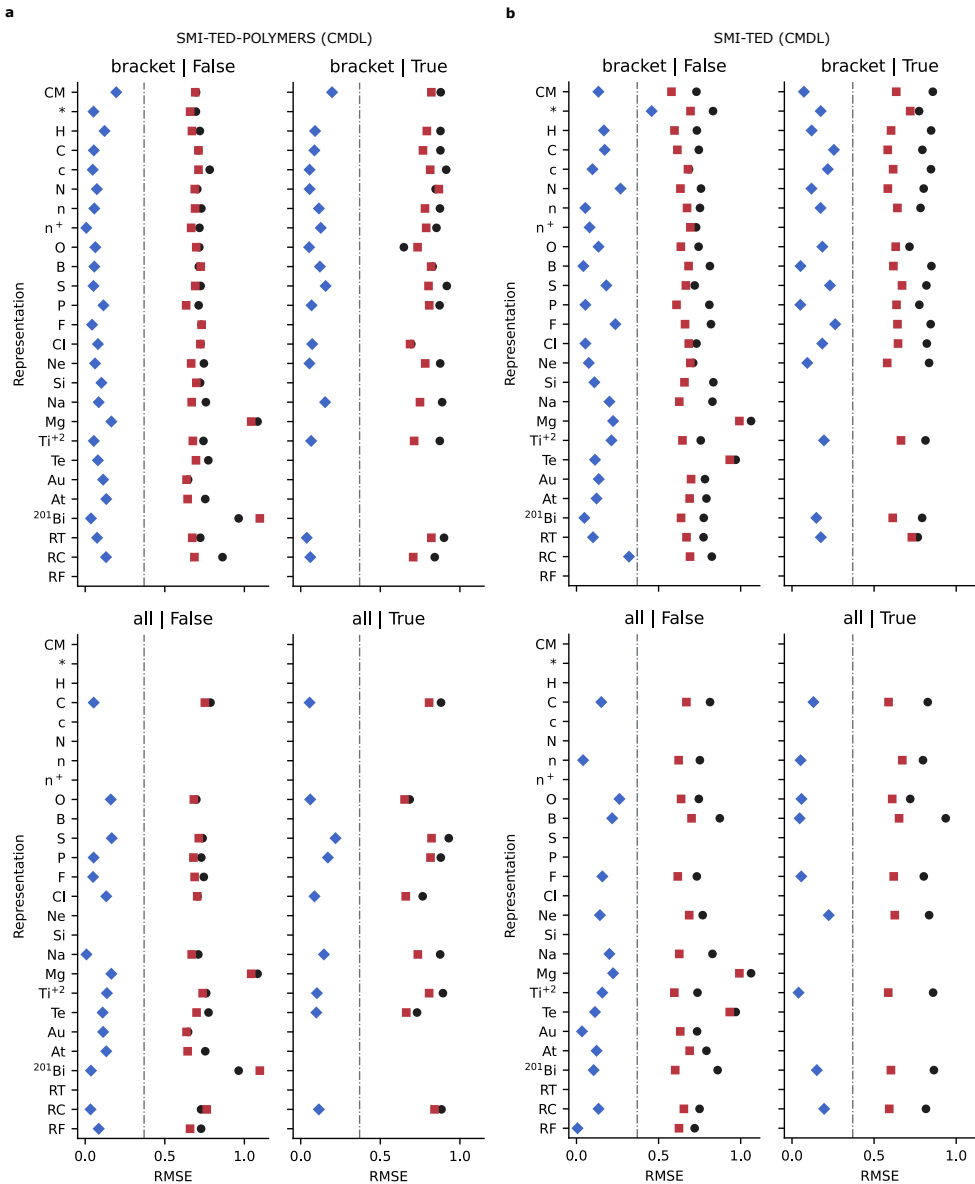


Fig. 140 Point plots for CH_4 gas permeability benchmark experiments of RMSE using the base random train, valid, and test splits for SMI-TED-POLYMER (a) and SMI-TED (b) models fine-tuned using the CPG representation.

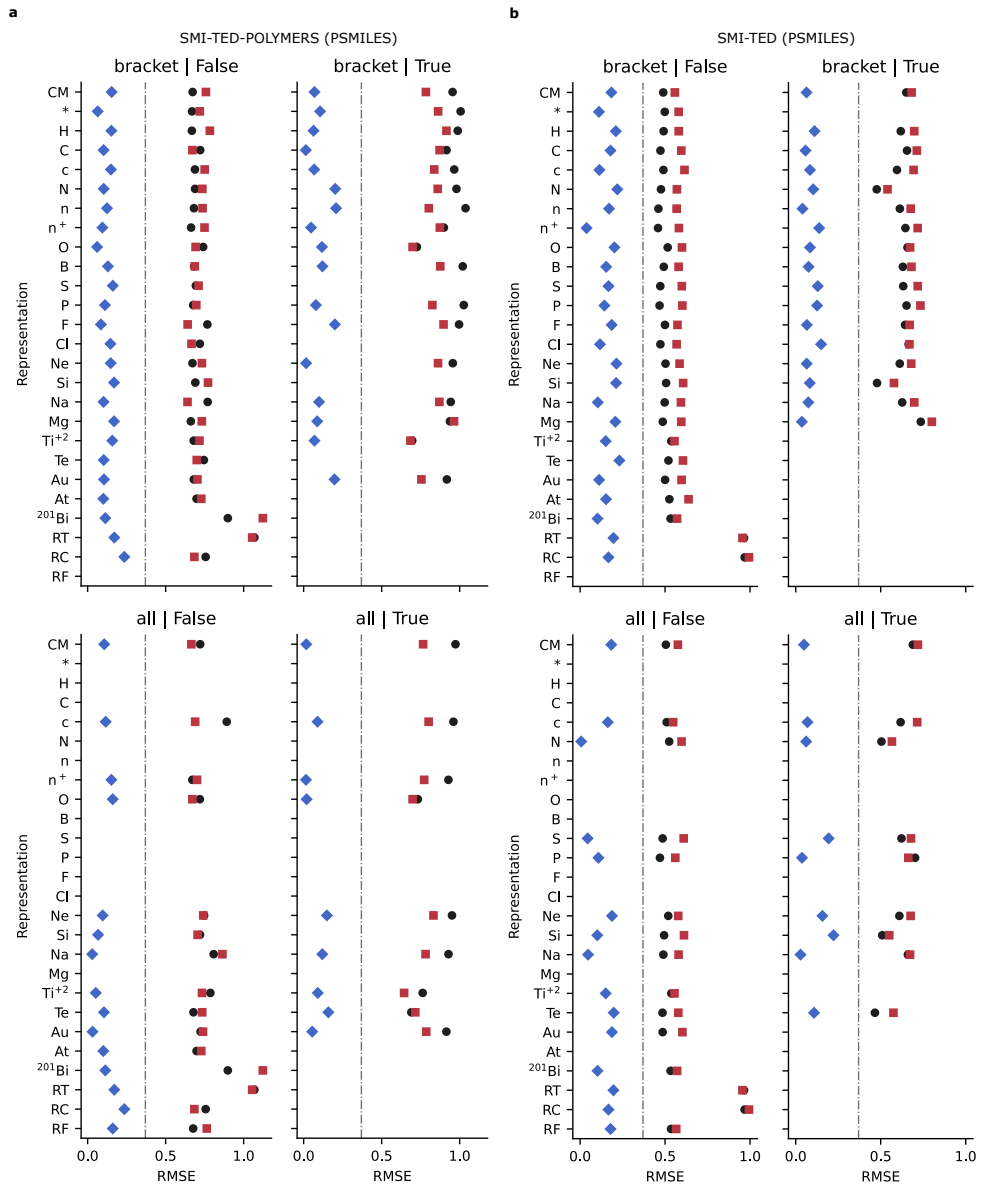


Fig. 142 Point plots for CH_4 gas permeability benchmark experiments of RMSE using the base random train, valid, and test splits for SMI-TED-POLYMER (a) and SMI-TED (b) models fine-tuned using PSMILES.

2.6.25 CO₂:CH₄ Gas Selectivity CV Scores

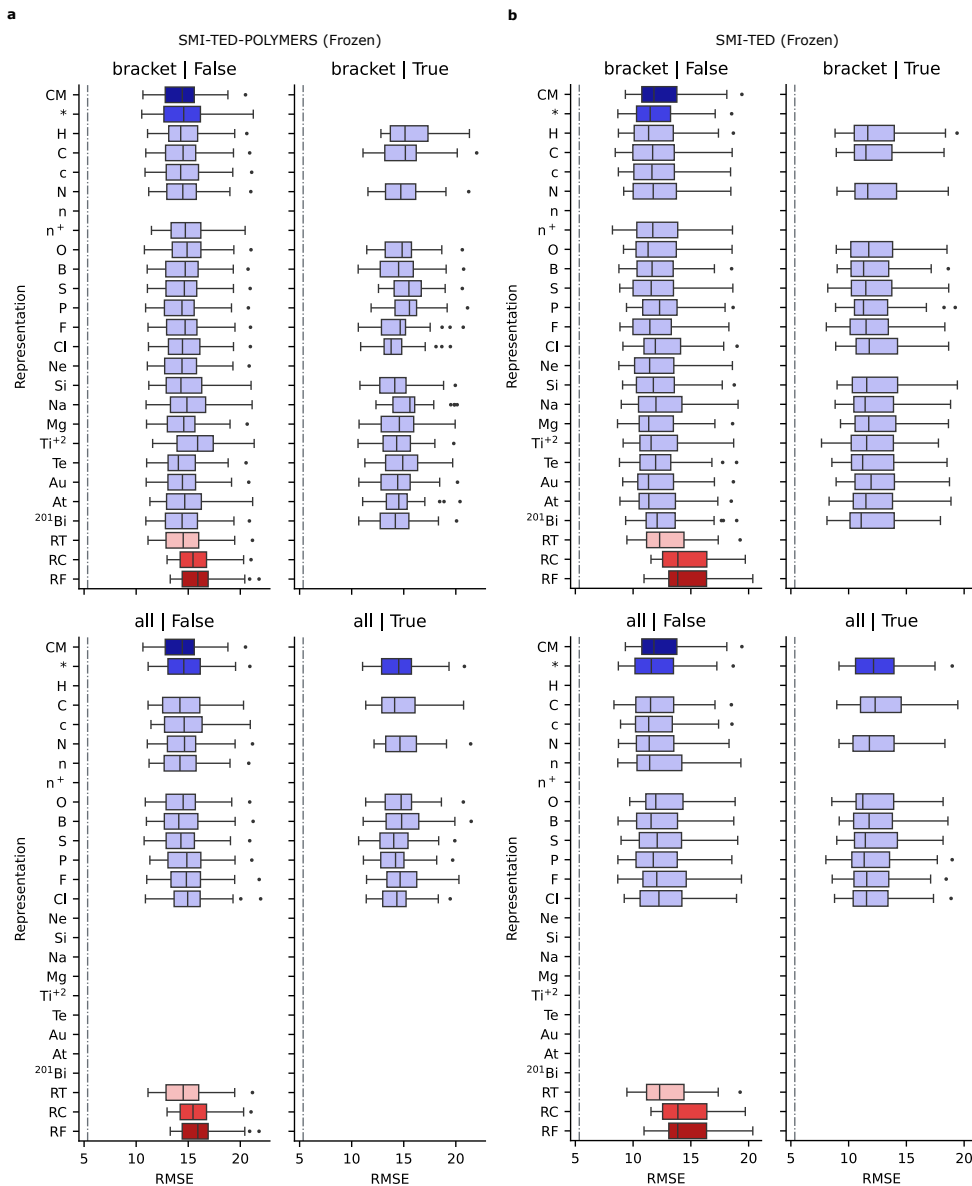


Fig. 143 Box plots for CO₂:CH₄ gas selectivity repeated cross-validation experiments for SMI-TED-POLYMER (a) and SMI-TED (b) models with frozen weights.

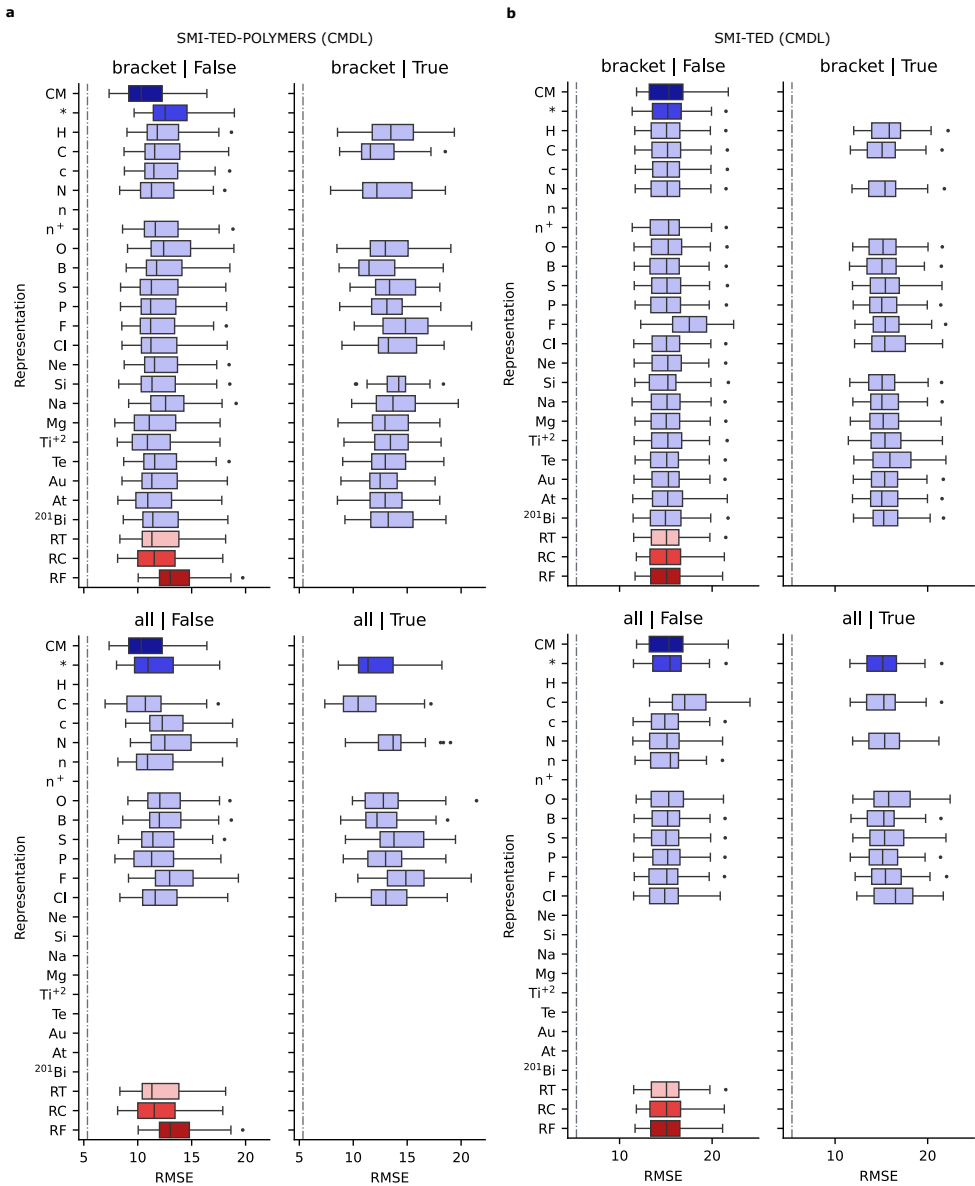


Fig. 144 Box plots for $\text{CO}_2:\text{CH}_4$ gas selectivity repeated cross-validation experiments for SMI-TED-POLYMER (a) and SMI-TED (b) models fine-tuned with the CPG polymer graphs.

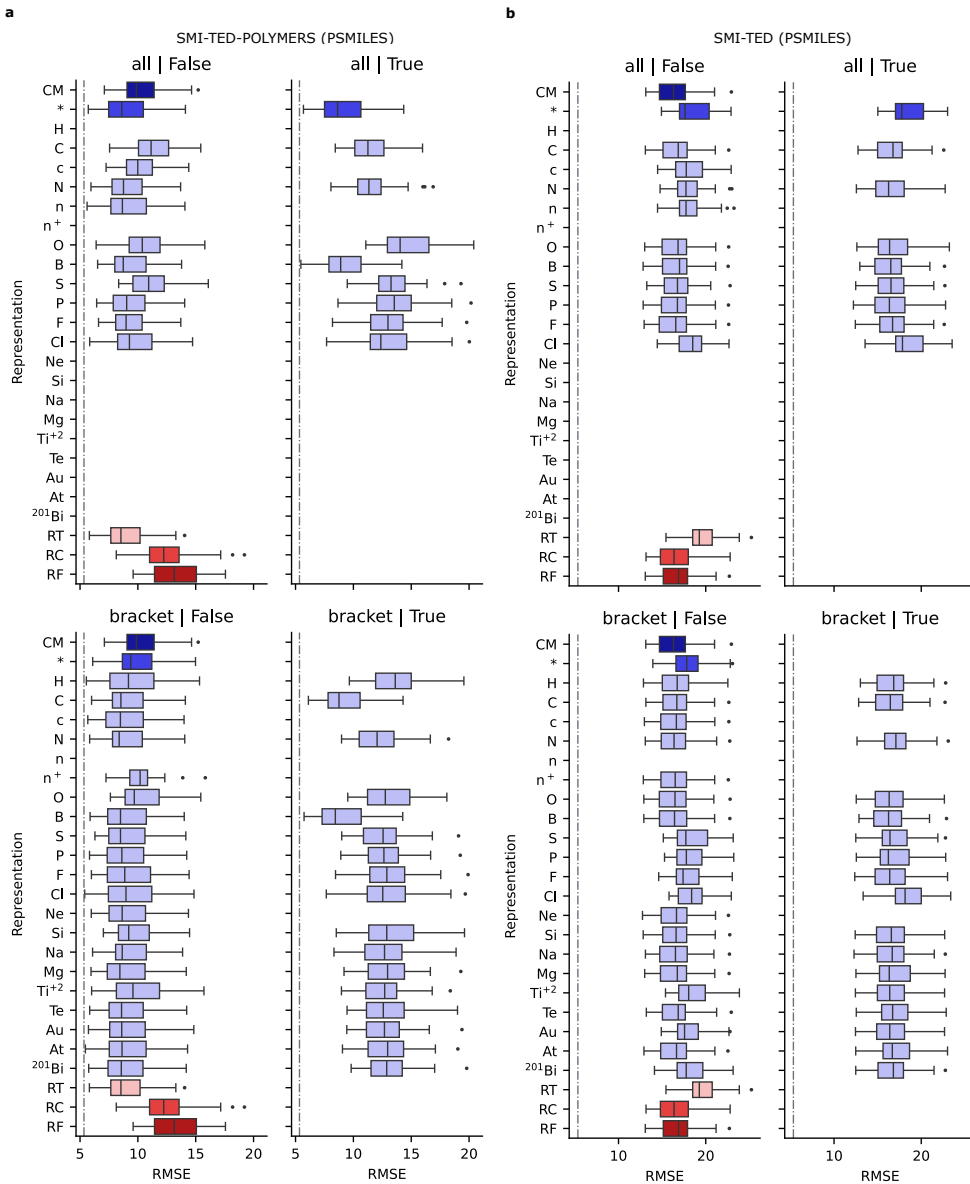


Fig. 145 Box plots for $\text{CO}_2:\text{CH}_4$ gas selectivity repeated cross-validation experiments for SMI-TED-POLYMER (a) and SMI-TED (b) models fine-tuned with PSMILES.

2.6.26 CO₂:CH₄ Gas Selectivity Random Split Scores

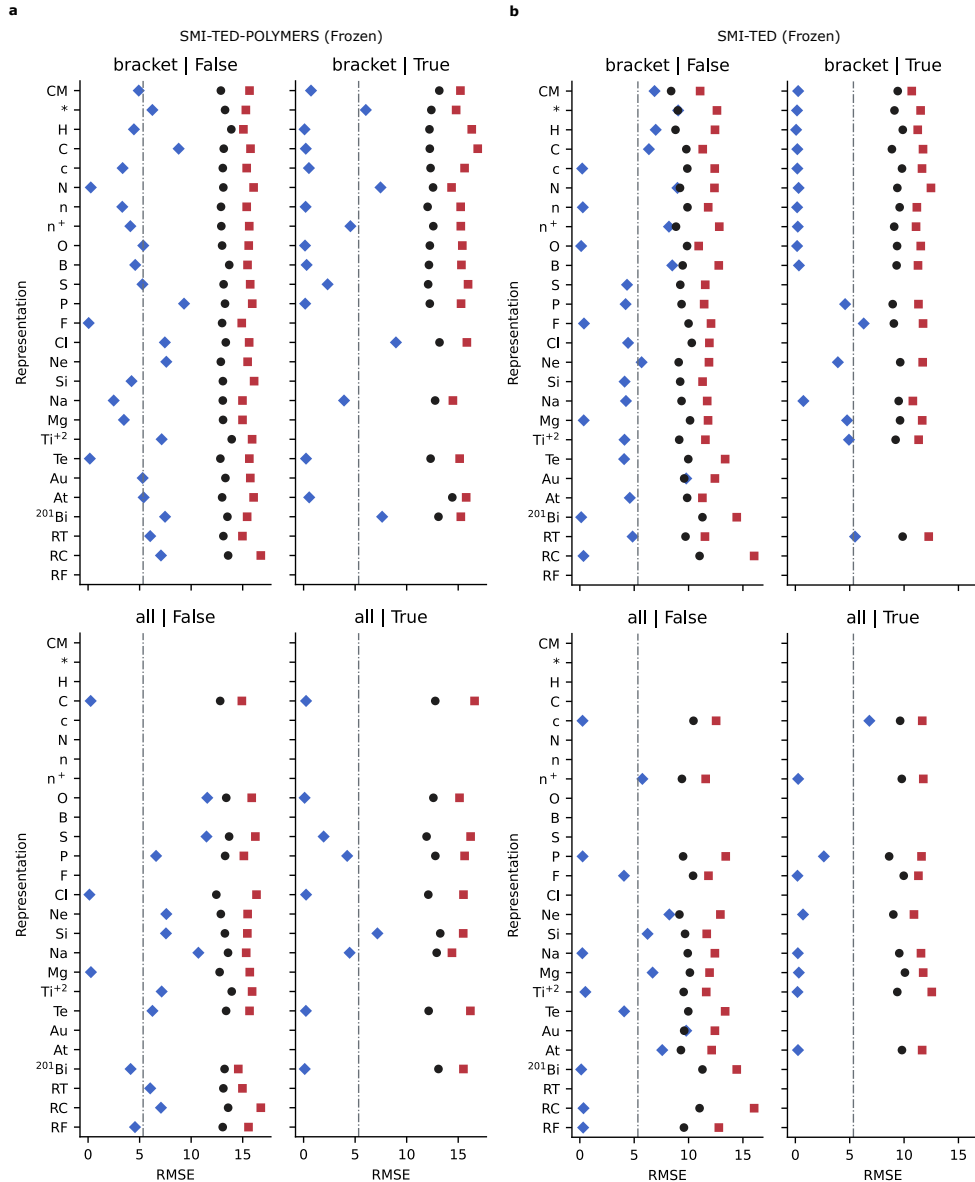


Fig. 146 Point plots for CO₂:CH₄ gas selectivity benchmark experiments of RMSE using the base random train, valid, and test splits for SMI-TED-POLYMER (a) and SMI-TED (b) models with frozen weights.

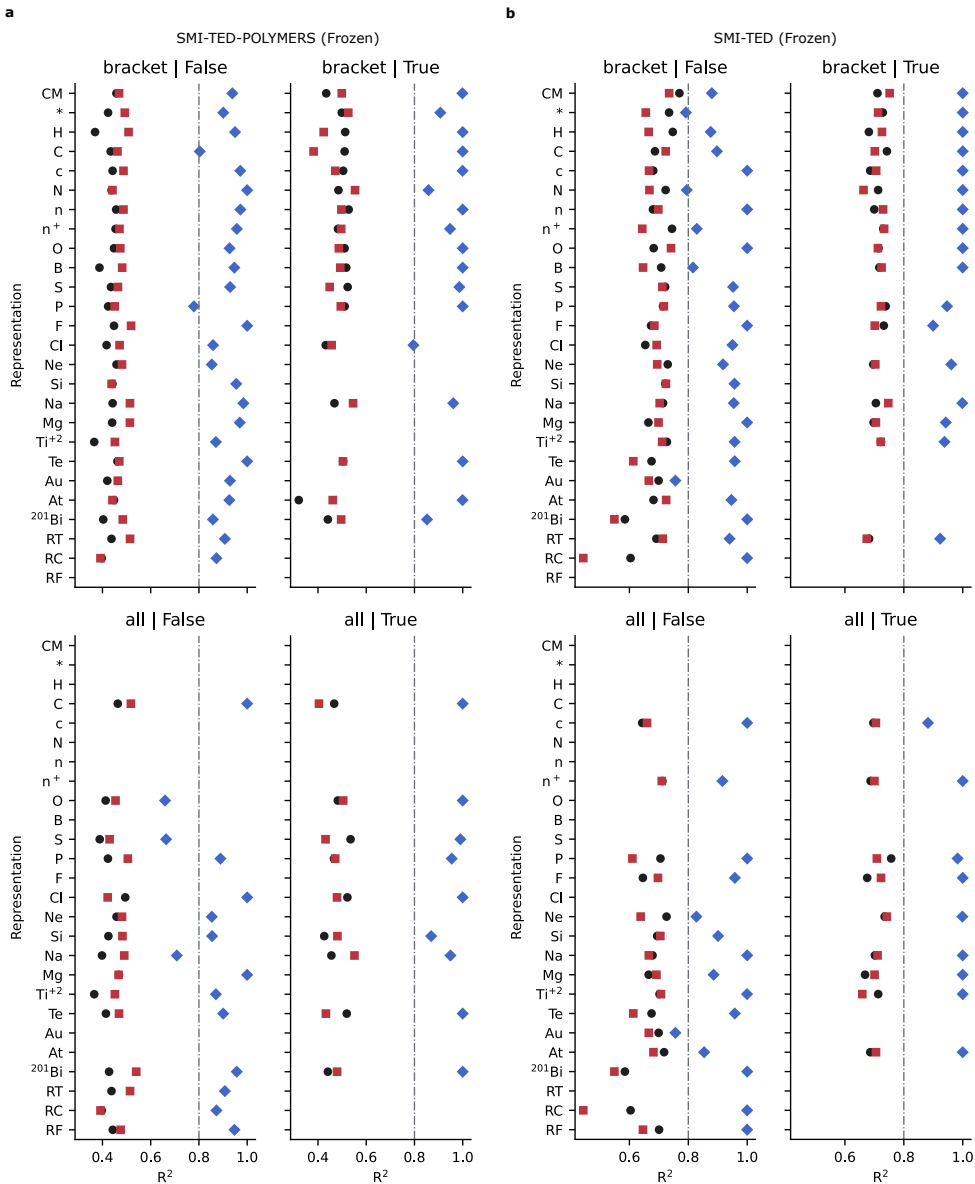


Fig. 147 Point plots for $\text{CO}_2:\text{CH}_4$ gas selectivity benchmark experiments of R^2 using the base random train, valid, and test splits for SMI-TED-POLYMER (a) and SMI-TED (b) models with frozen weights.

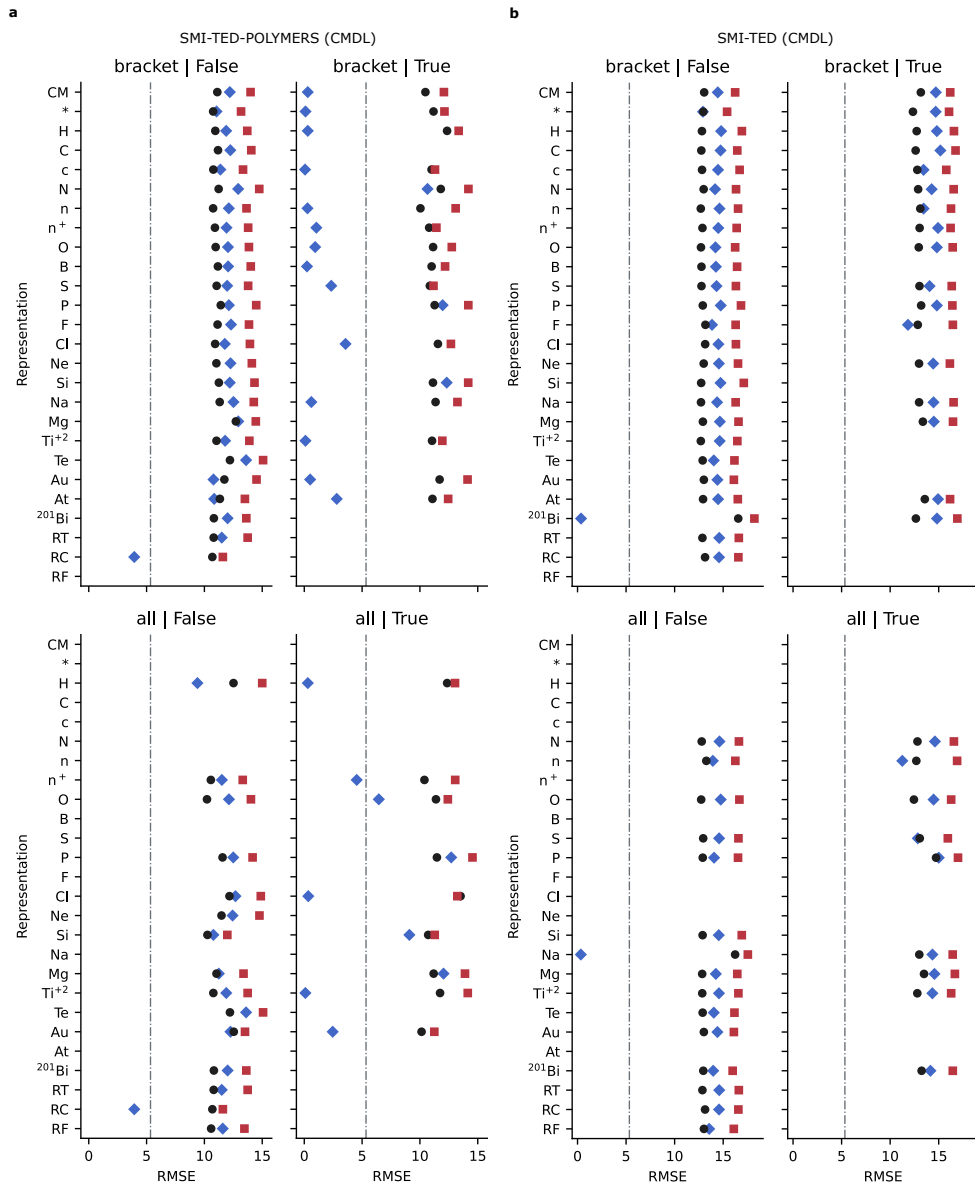


Fig. 148 Point plots for $\text{CO}_2:\text{CH}_4$ gas selectivity benchmark experiments of RMSE using the base random train, valid, and test splits for SMI-TED-POLYMER (a) and SMI-TED (b) models fine-tuned using the CPG representation.

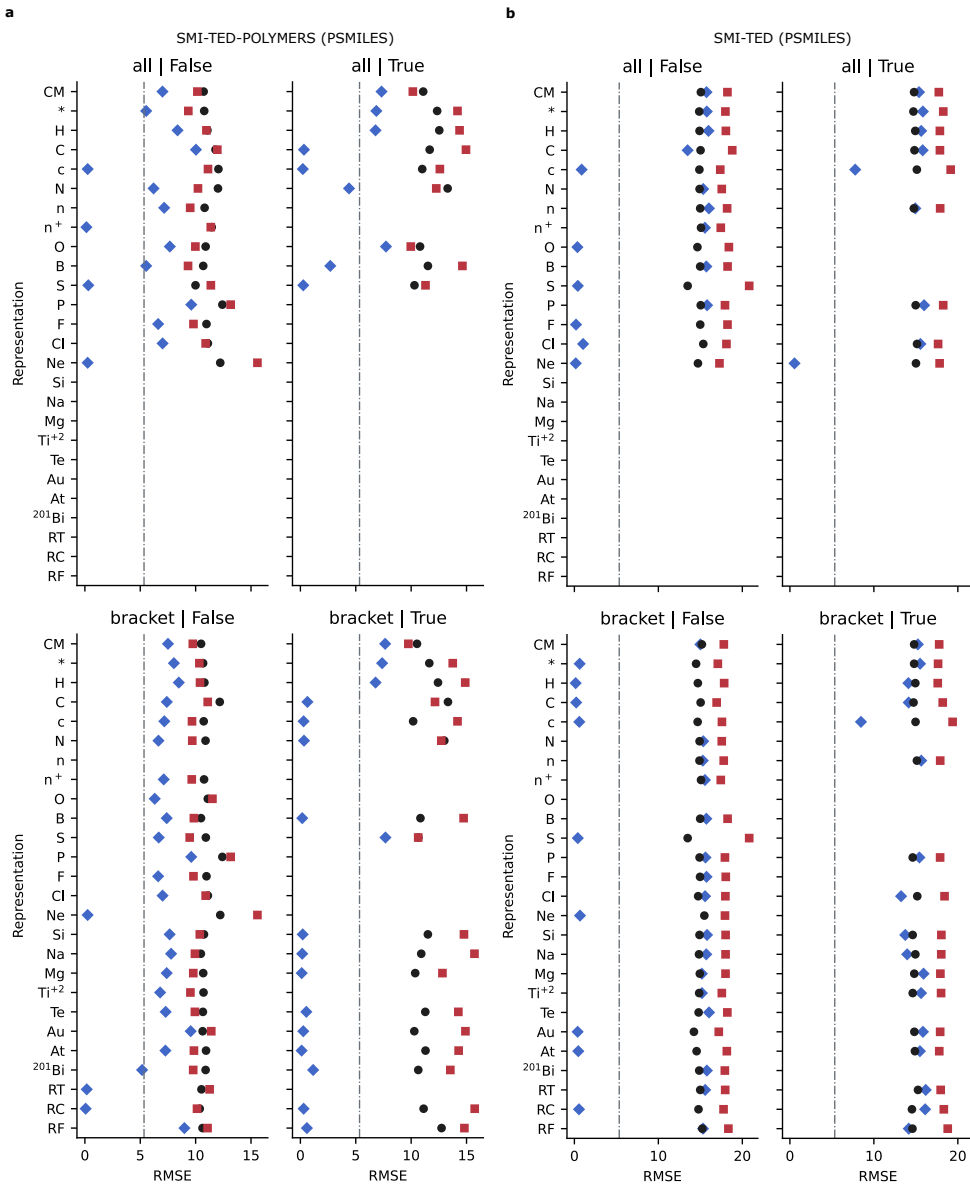


Fig. 150 Point plots for $\text{CO}_2:\text{CH}_4$ gas selectivity benchmark experiments of RMSE using the base random train, valid, and test splits for SMI-TED-POLYMER (a) and SMI-TED (b) models fine-tuned using PSMILES.

2.6.27 CO₂:N₂ Gas Selectivity CV Scores

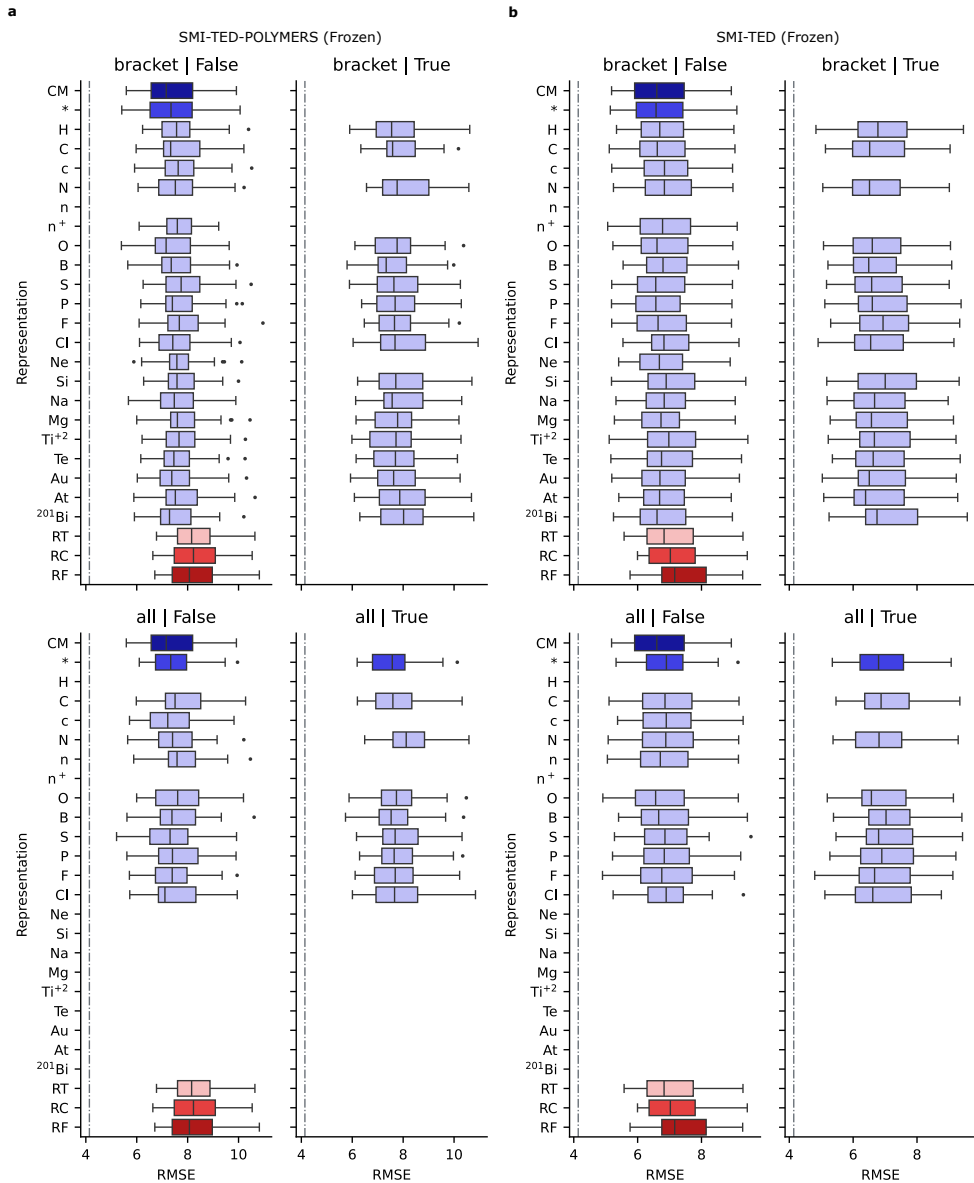


Fig. 151 Box plots for CO₂:N₂ gas selectivity repeated cross-validation experiments for SMI-TED-POLYMERS (a) and SMI-TED (b) models with frozen weights.

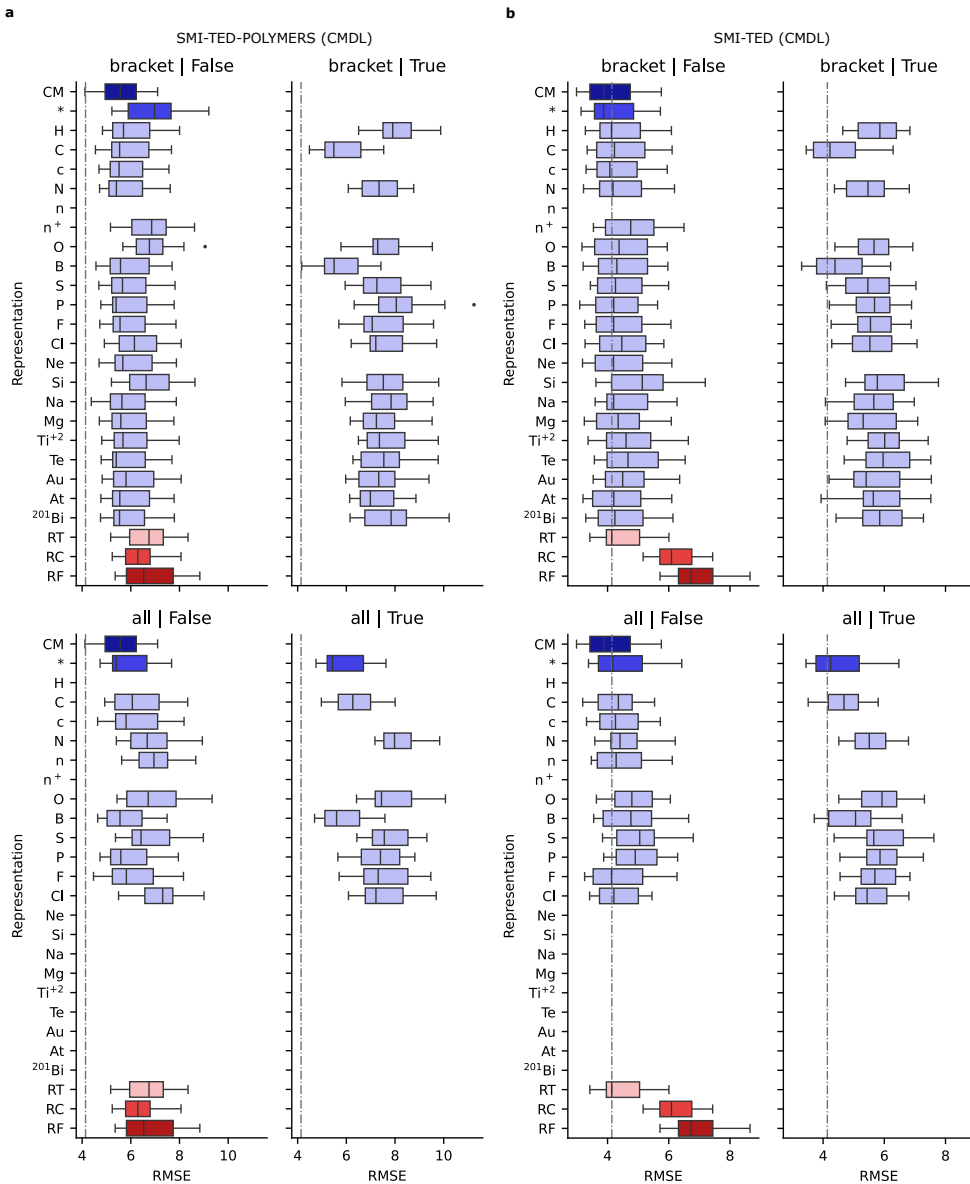


Fig. 152 Box plots for $\text{CO}_2:\text{N}_2$ gas selectivity repeated cross-validation experiments for SMI-TED-POLYMER (**a**) and SMI-TED (**b**) models fine-tuned with the CPG polymer graphs.

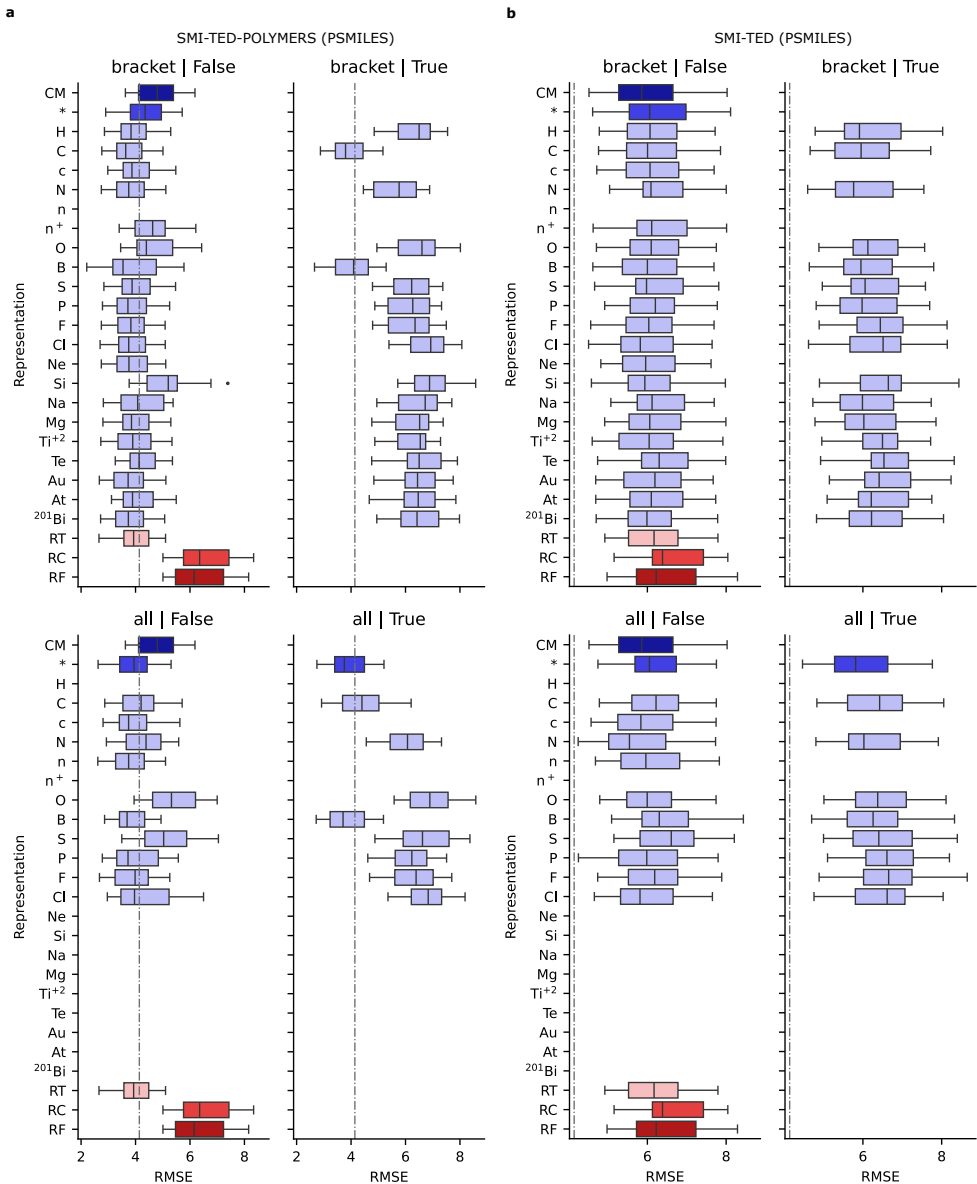


Fig. 153 Box plots for $\text{CO}_2:\text{N}_2$ gas selectivity repeated cross-validation experiments for SMI-TED-POLYMER (a) and SMI-TED (b) models fine-tuned with PSMILES.

2.6.28 CO₂:N₂ Gas Selectivity Random Split Scores

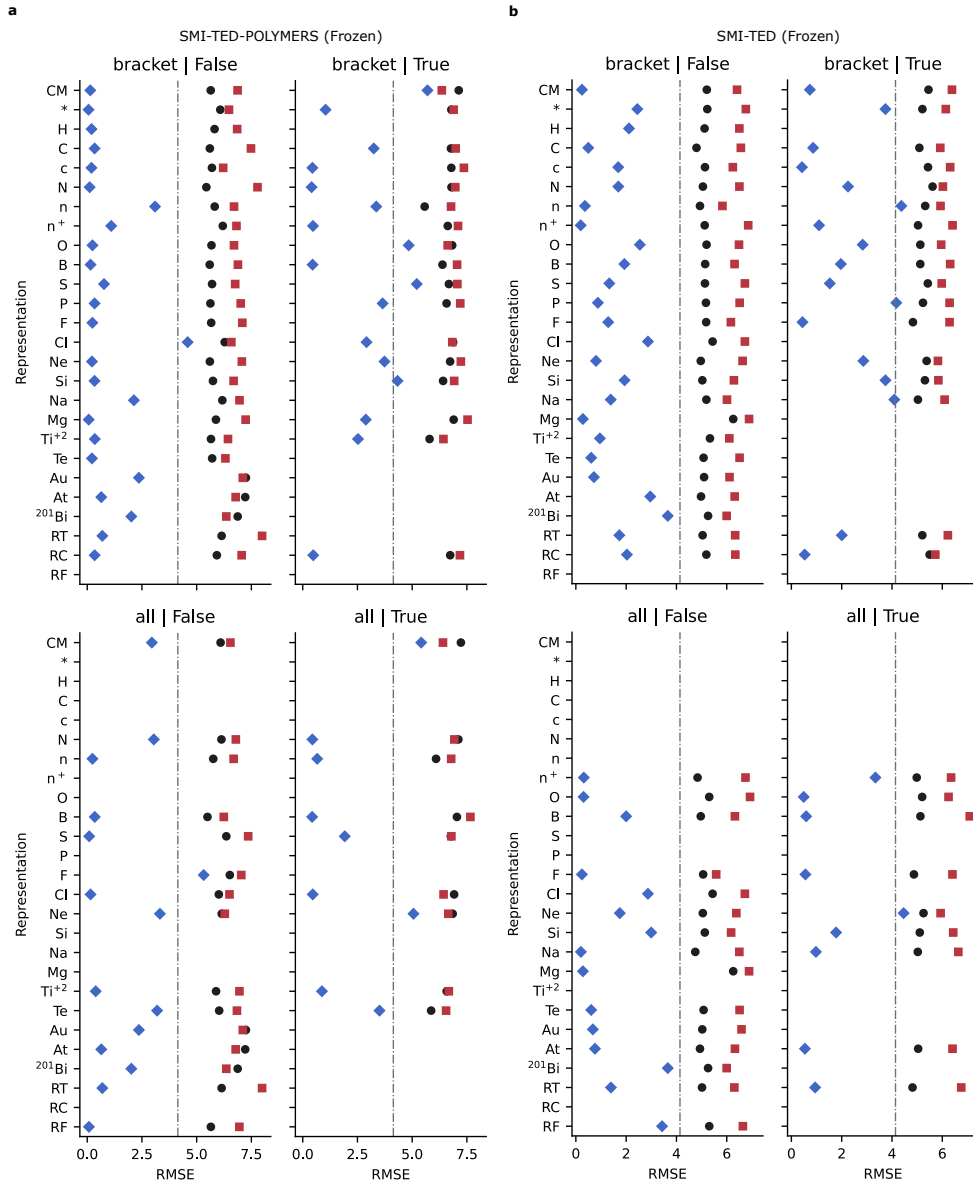


Fig. 154 Point plots for CO₂:N₂ gas selectivity benchmark experiments of RMSE using the base random train, valid, and test splits for SMI-TED-POLYMER (a) and SMI-TED (b) models with frozen weights.

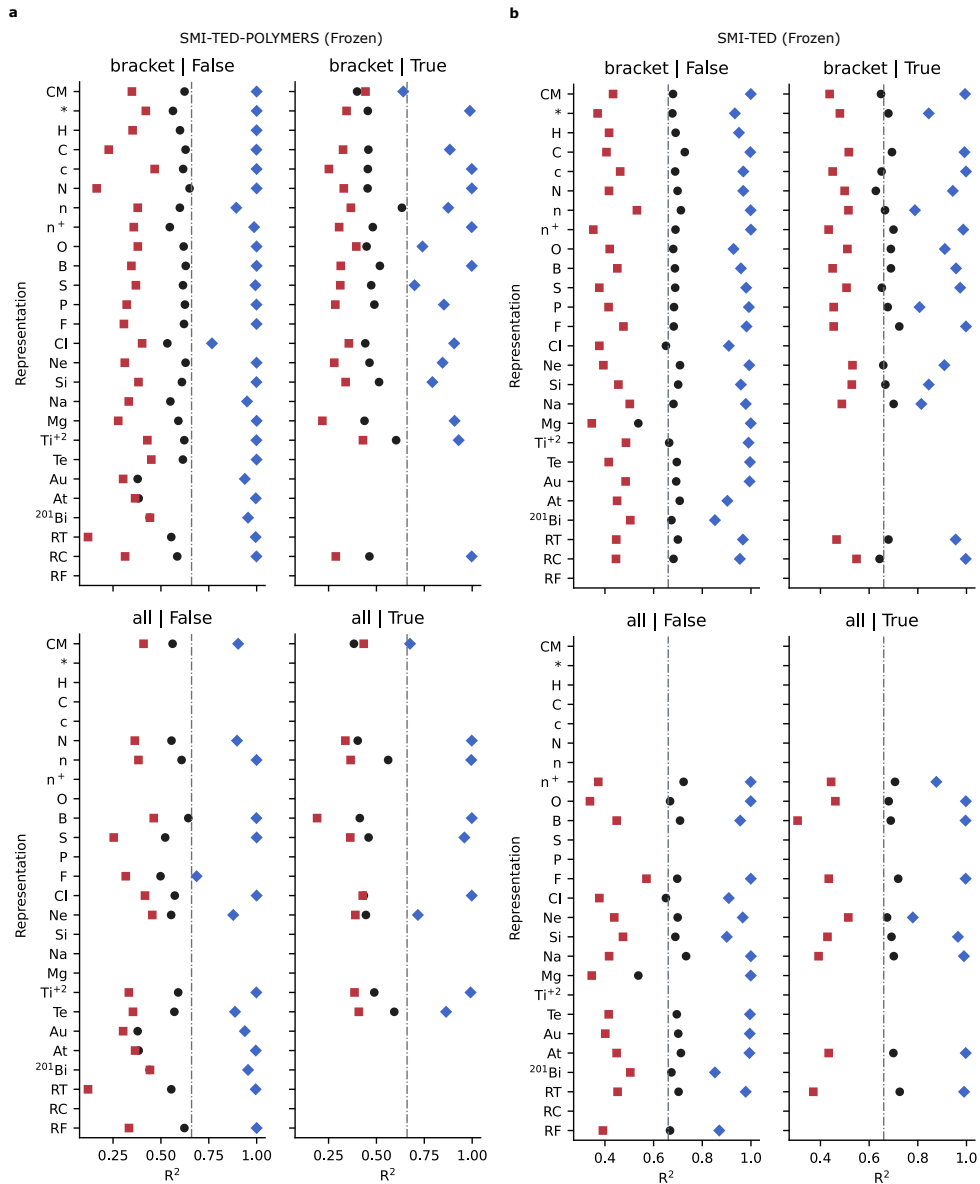


Fig. 155 Point plots for $\text{CO}_2:\text{N}_2$ gas selectivity benchmark experiments of R^2 using the base random train, valid, and test splits for SMI-TED-POLYMER (a) and SMI-TED (b) models with frozen weights.

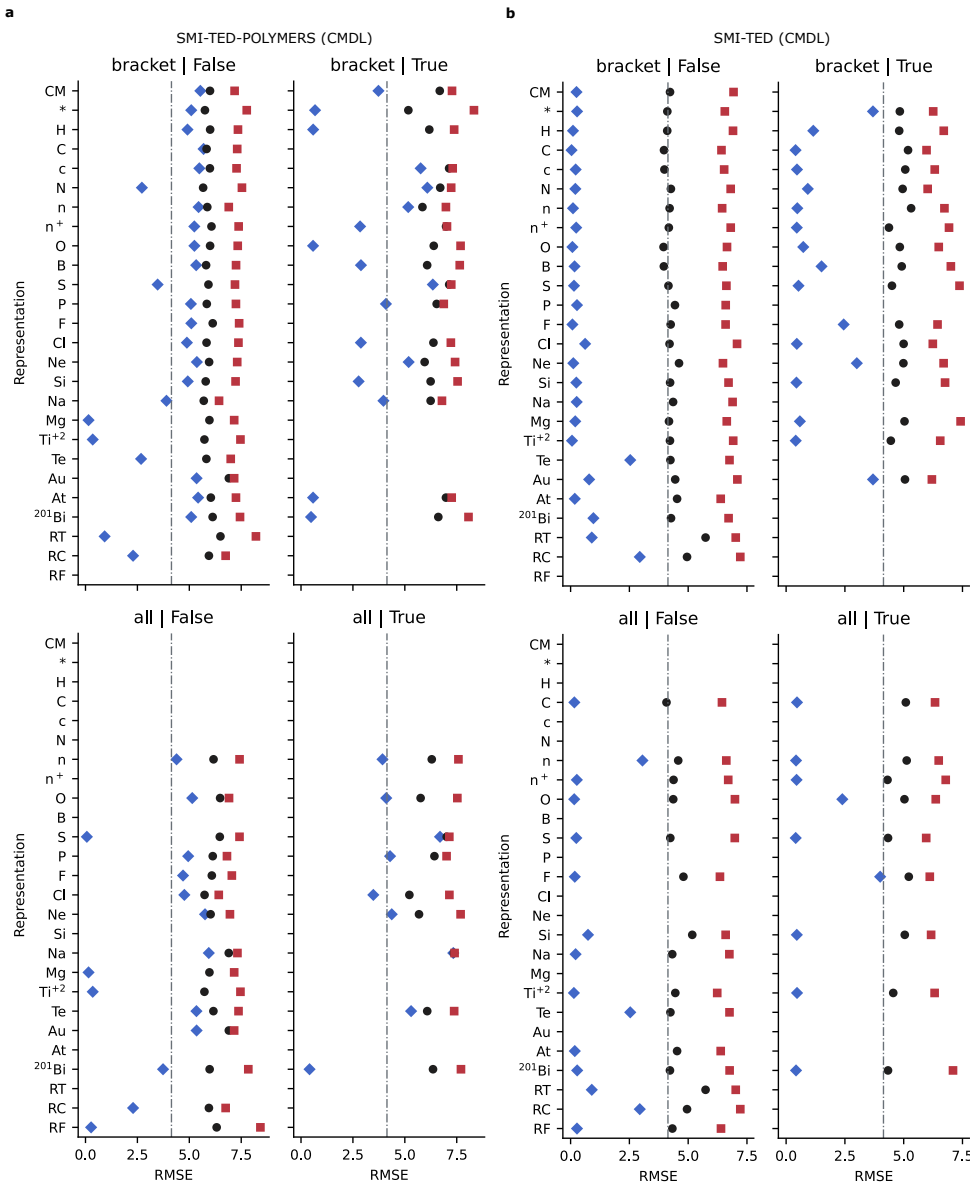


Fig. 156 Point plots for $\text{CO}_2:\text{N}_2$ gas selectivity benchmark experiments of RMSE using the base random train, valid, and test splits for SMI-TED-POLYMER (a) and SMI-TED (b) models fine-tuned using the CPG representation.

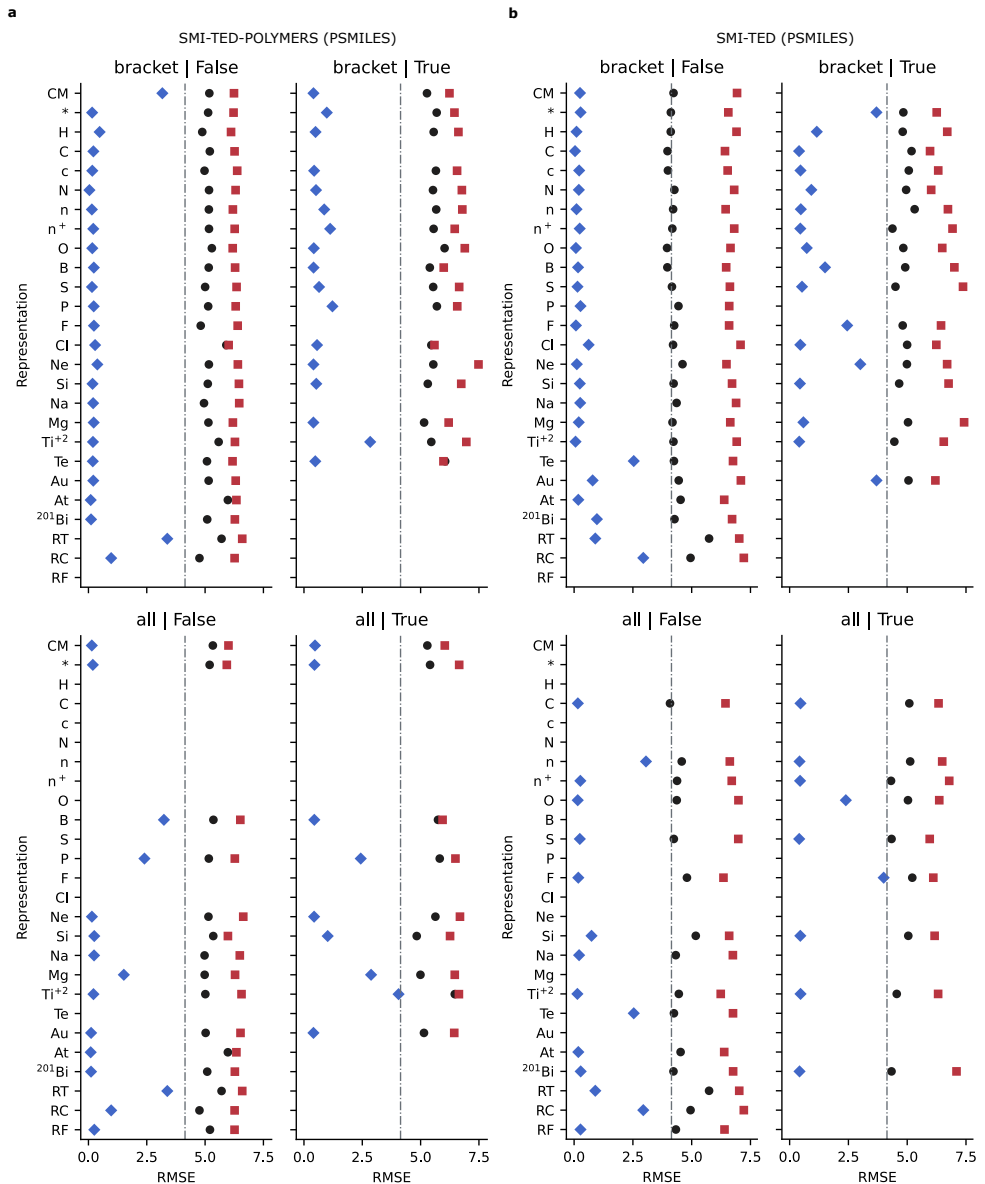


Fig. 158 Point plots for $\text{CO}_2:\text{N}_2$ gas selectivity benchmark experiments of RMSE using the base random train, valid, and test splits for SMI-TED-POLYMER (a) and SMI-TED (b) models fine-tuned using PSMILES.

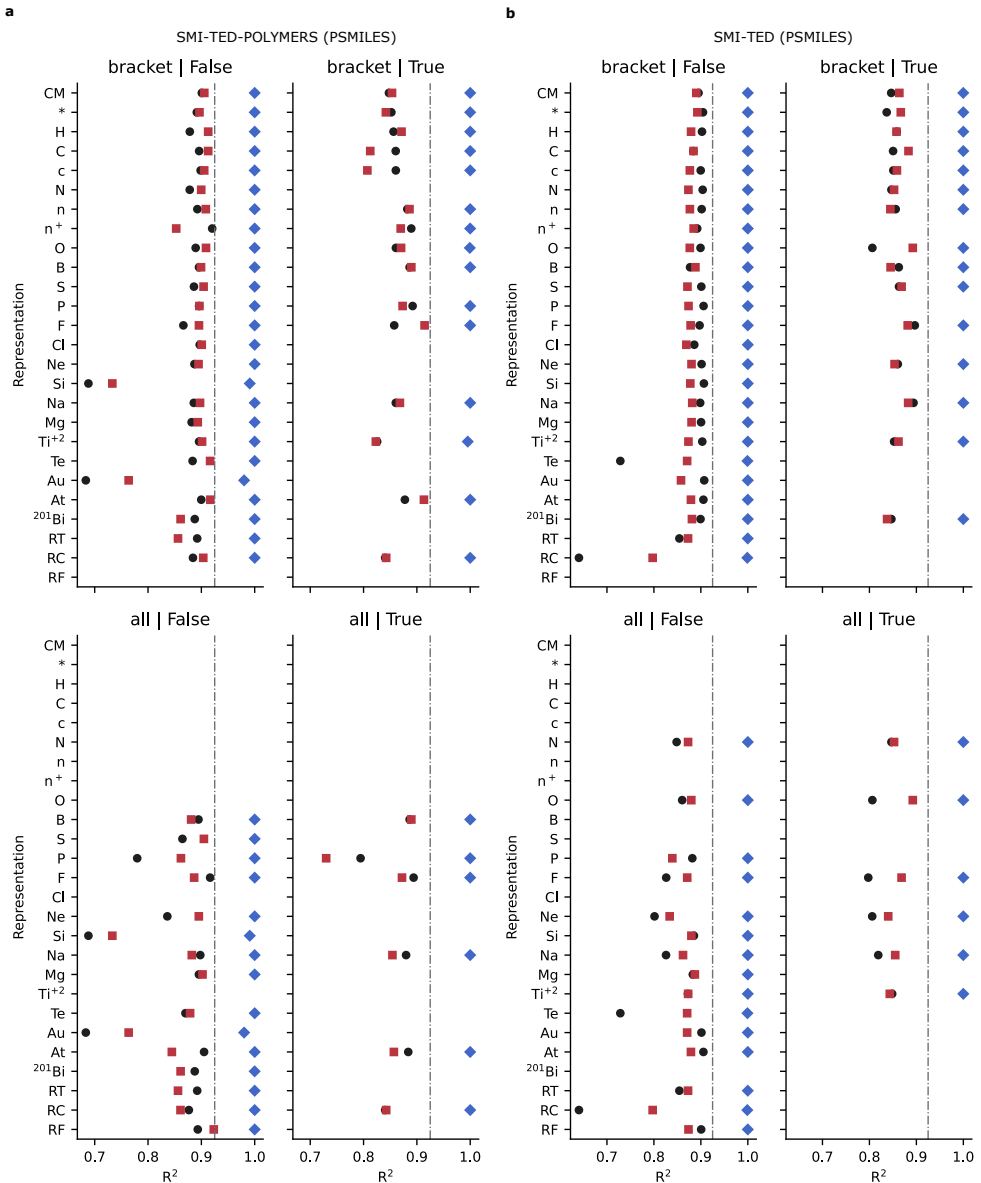


Fig. 81 Point plots for E_{ea} benchmark experiments of R^2 using the base random train, valid, and test splits for SMI-TED-POLYMER (a) and SMI-TED (b) models fine-tuned using PSMILES.

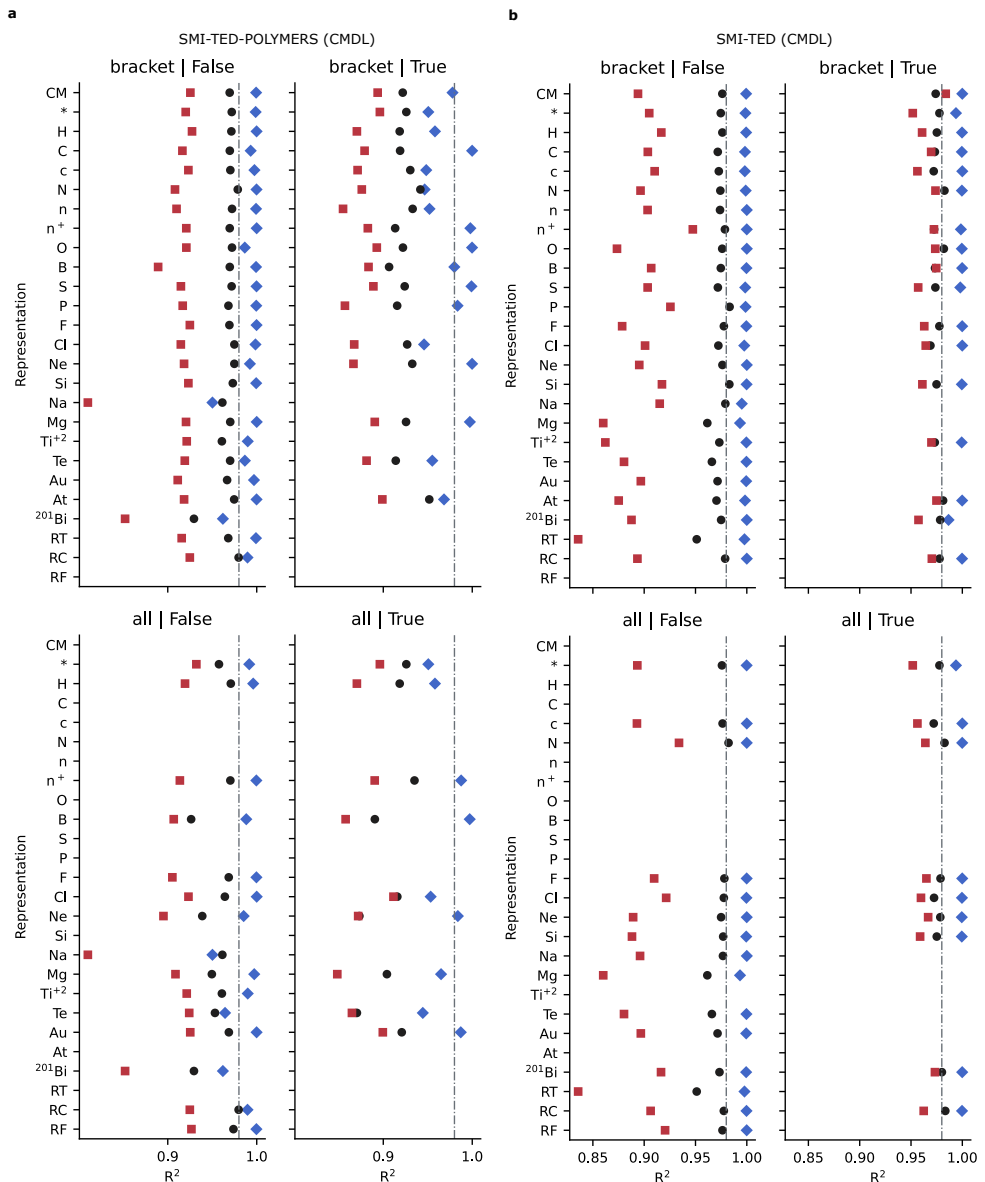


Fig. 88 Point plots for E_{at} benchmark experiments of R^2 using the base random train, valid, and test splits for SMI-TED-POLYMER (a) and SMI-TED (b) models fine-tuned using the CPG representation.

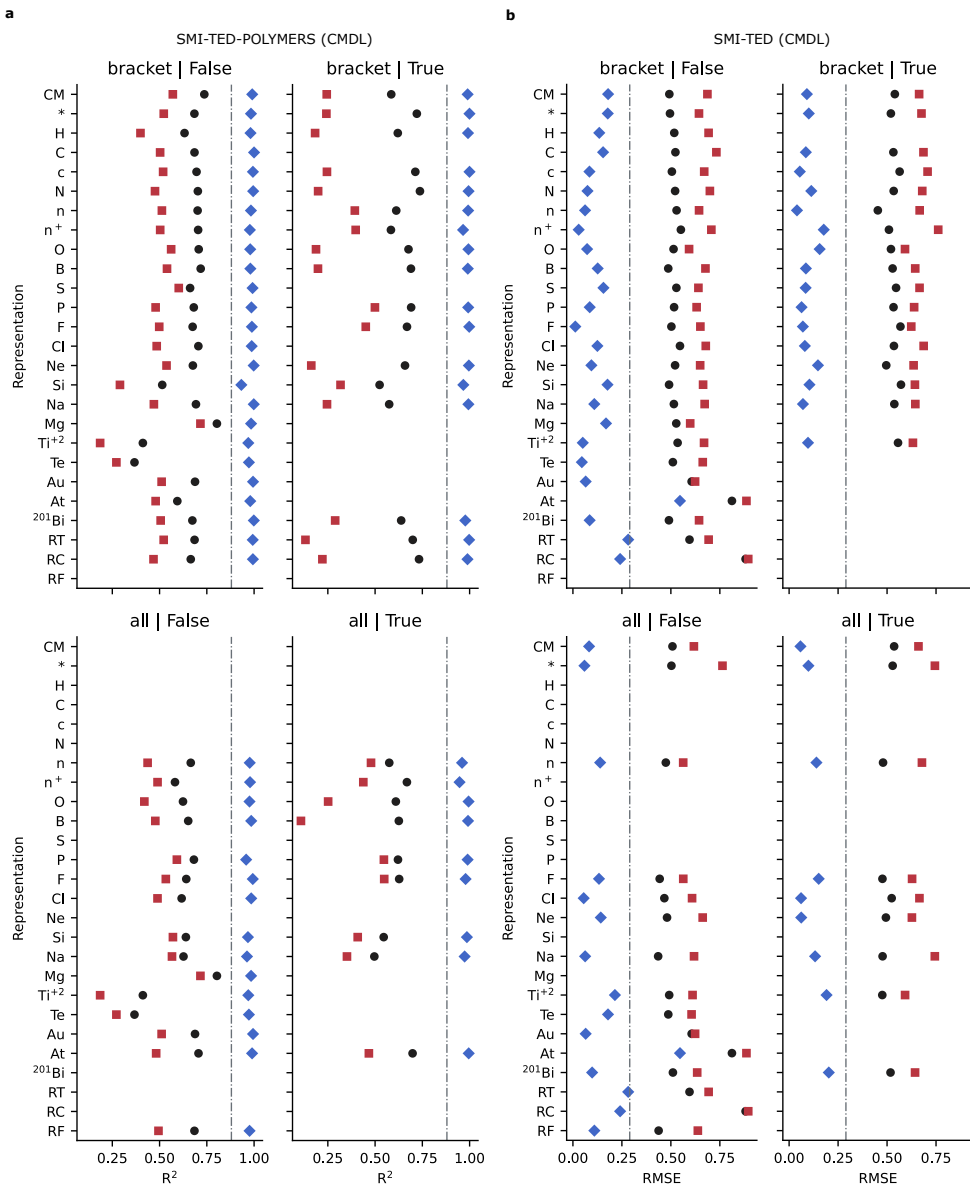


Fig. 124 Point plots for CO_2 gas permeability benchmark experiments of R^2 using the base random train, valid, and test splits for SMI-TED-POLYMER (a) and SMI-TED (b) models fine-tuned using the CPG representation.

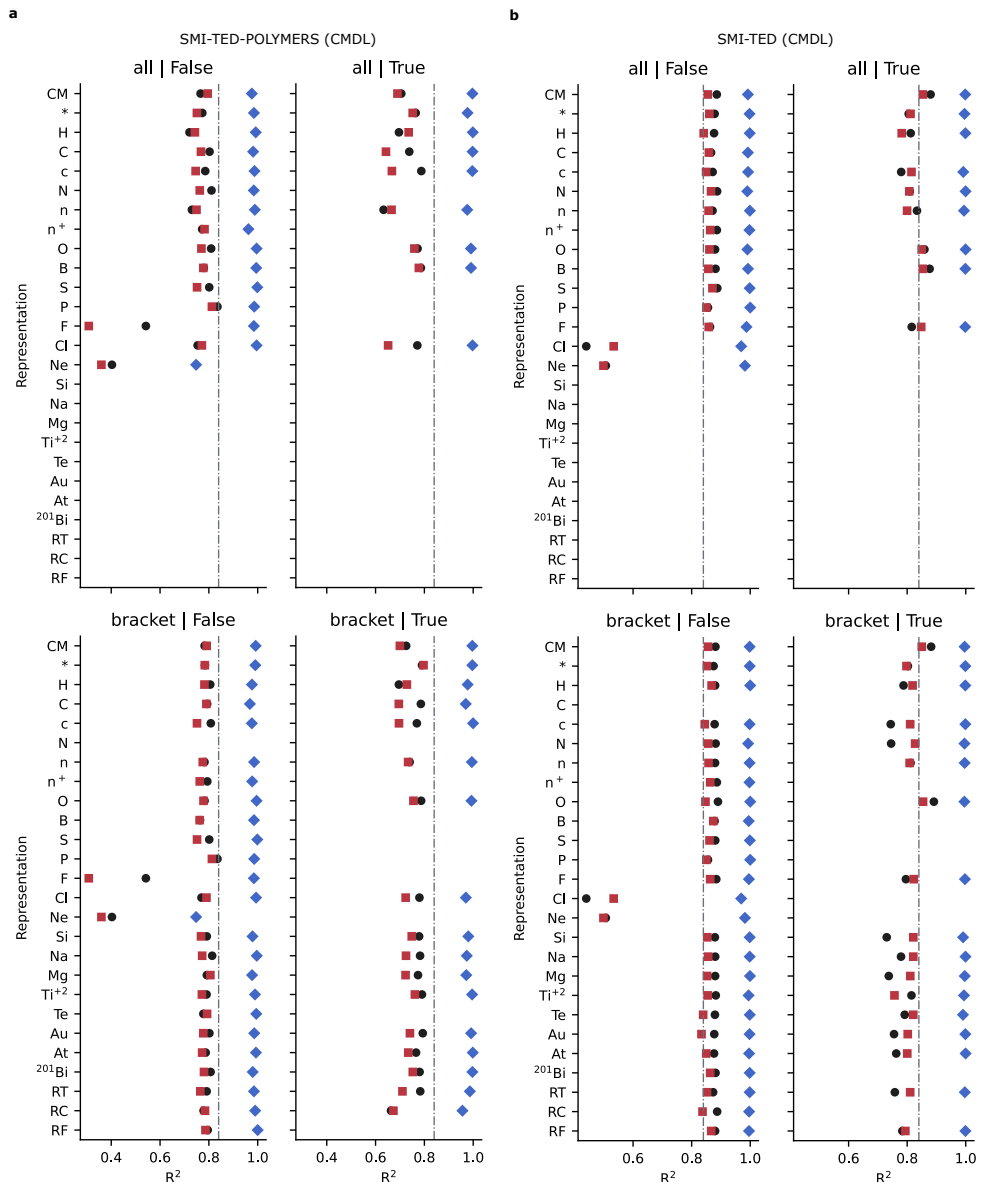


Fig. 133 Point plots for N_2 gas permeability benchmark experiments of R^2 using the base random train, valid, and test splits for SMI-TED-POLYMER (a) and SMI-TED (b) models fine-tuned using the CPG representation.

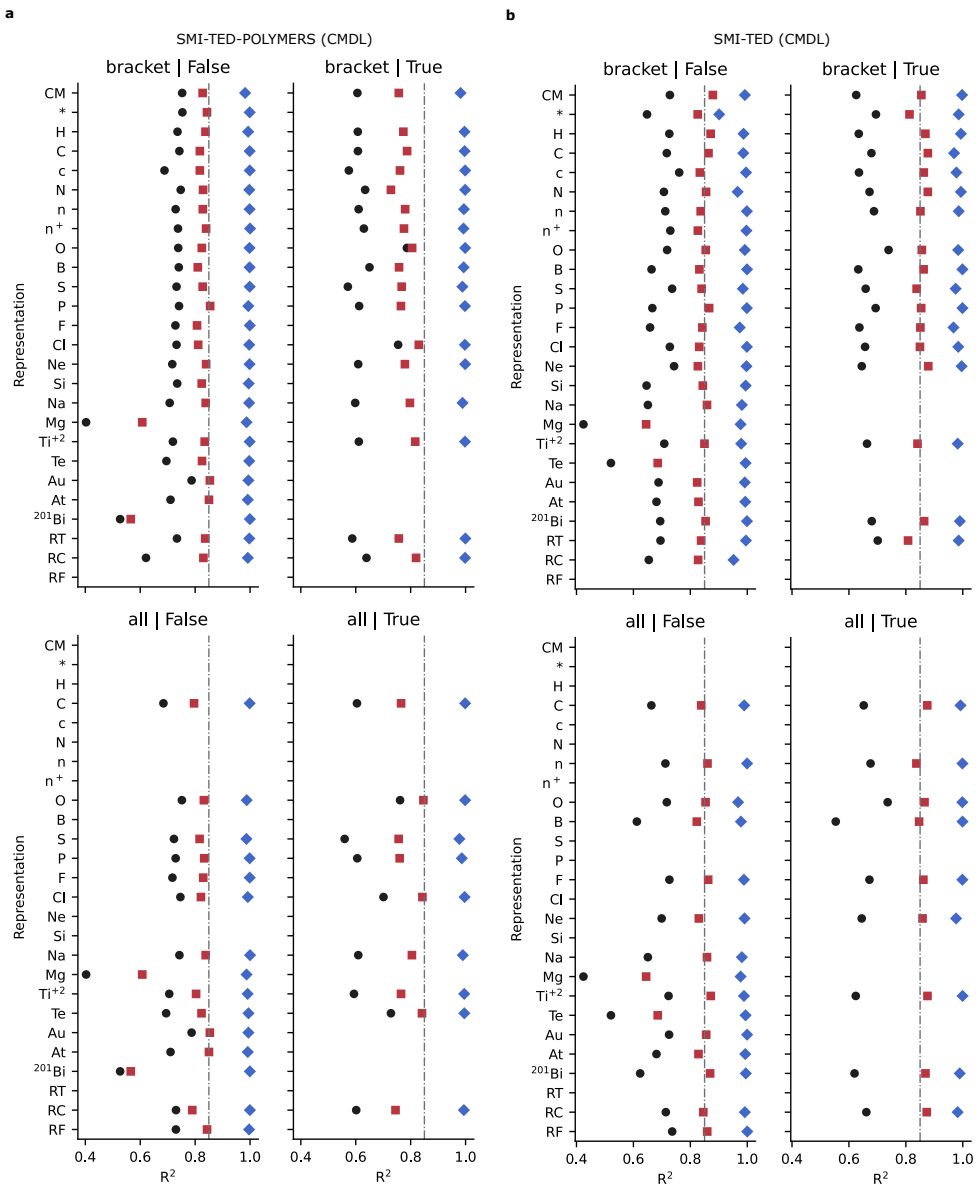


Fig. 141 Point plots for CH_4 gas permeability benchmark experiments of R^2 using the base random train, valid, and test splits for SMI-TED-POLYMER (a) and SMI-TED (b) models fine-tuned using the CPG representation.

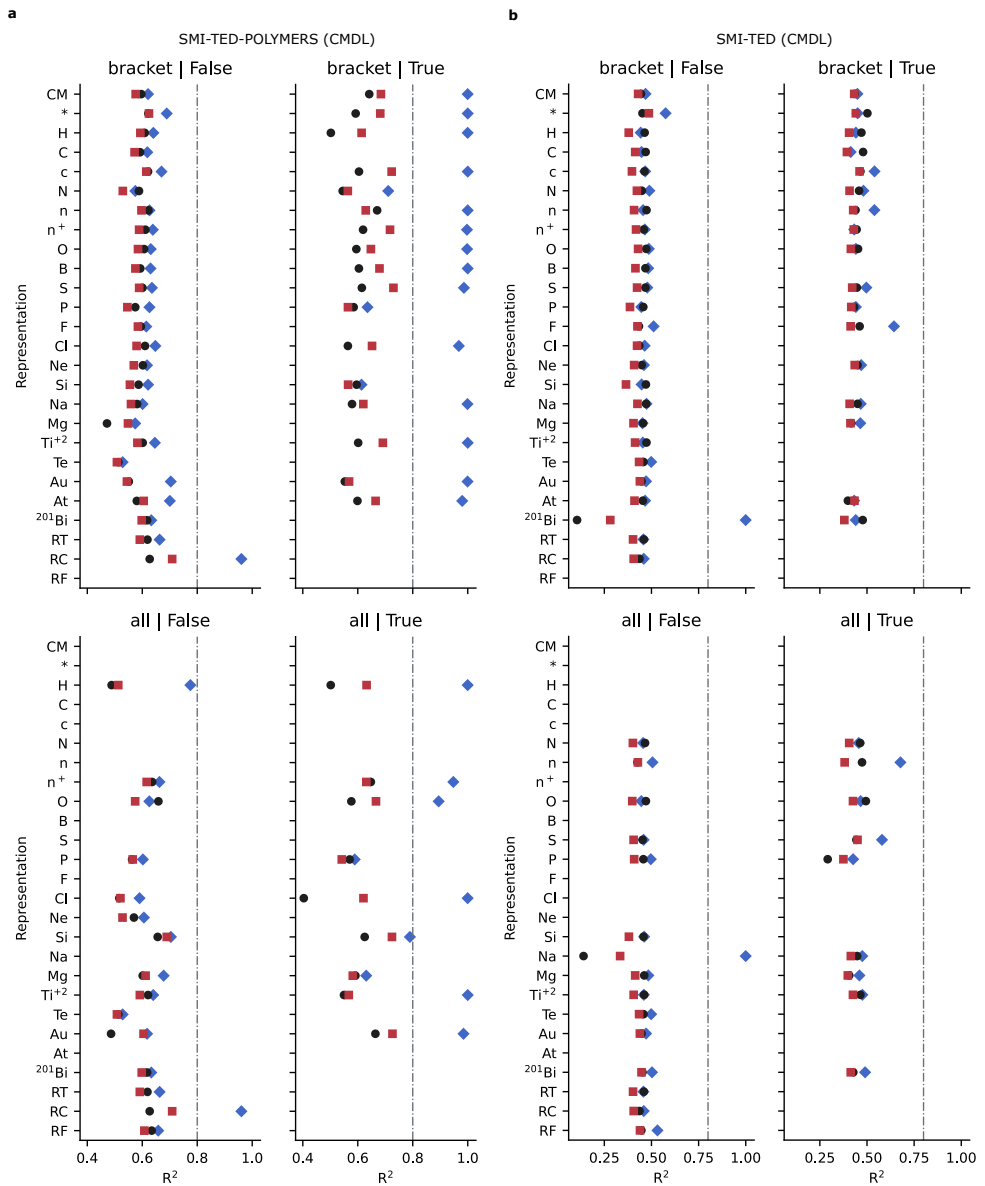


Fig. 149 Point plots for CO₂:CH₄ gas selectivity benchmark experiments of R² using the base random train, valid, and test splits for SMI-TED-POLYMER (**a**) and SMI-TED (**b**) models fine-tuned using the CPG representation.

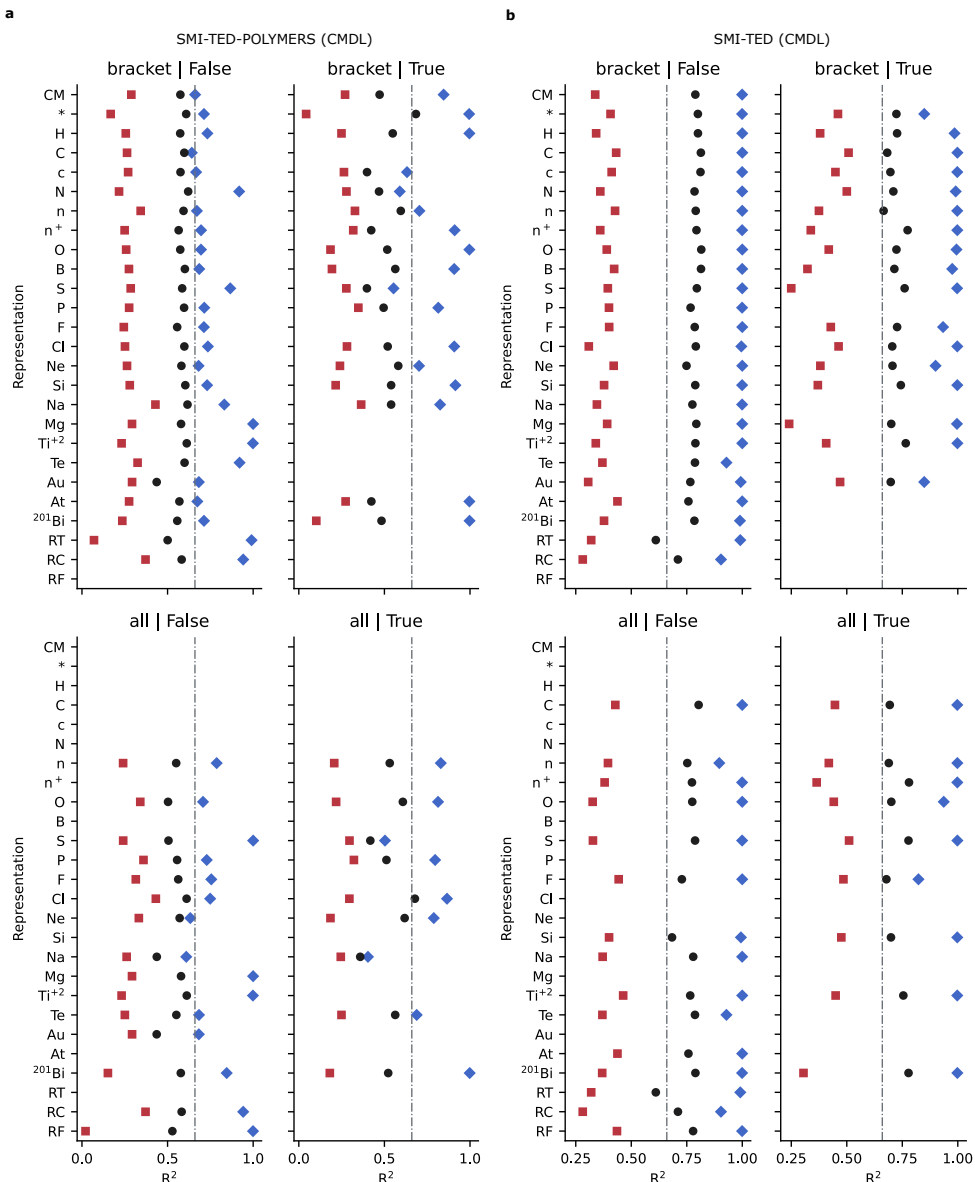


Fig. 157 Point plots for CO₂:N₂ gas selectivity benchmark experiments of R² using the base random train, valid, and test splits for SMI-TED-POLYMER (a) and SMI-TED (b) models fine-tuned using the CPG representation.